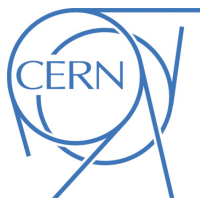




ATLAS NOTE

ATL-COM-PHYS-2016-1458

22nd August 2017



Draft version 1.1

1

2 Search for Neutral MSSM Higgs bosons H/A and Z' decaying to 3 $\tau_\ell \tau_h$ produced in 13 TeV Collisions with the ATLAS Detector

4 Adam Bailey^a, Will Davey^e, Eric Drechsler^c, Dirk Duschinger^f, Luca Fiorini^a, Lino Gerlach^c,
5 Michel Janus^c, Mohamed Gouighri^a, Guillermo Nicolas Hamityⁱ, Lorenz Hauswald^f, Hao Liu^j,
6 Samina Jabbar^k, Adomas Jelinskas^b, Karsten Koneke^l, Wolfgang Mader^f, Allison McCarn^j,
7 Roger Moore^k, Masahiro Morinaga^m, Verena Muckhoff^e, Bill Murray^b, Nikolaos Rompotis^h,
8 Pedro Henrique Sales De Bruin^o, Arno Straessner^f, Junichi Tanaka^m, Trevor Vickeyⁱ, Lei
9 Zhang^l, Zinonas Zinonos^q, Theodore Zorbasⁱ

10 ^a*Instituto de Fisica Corpuscular (IFIC), Centro Mixto Universidad de Valencia - CSIC*

11 ^b*University of Warwick, Coventry*

12 ^c*Georg-August-Universitat Goettingen, II. Physikalisches Institut*

13 ^e*University of Bonn*

14 ^f*Institut fuer Kern- und Teilchenphysik, Technische Universitaet Dresden*

15 ^h*University of Liverpool*

16 ⁱ*Department of Physics and Astronomy, University of Sheffield*

17 ^j*University of Michigan, Department of Physics*

18 ^k*University of Alberta*

19 ^l*Albert-Ludwigs-Universitaet Freiburg, Fakultaet fuer Mathematik und Physik*

20 ^m*International Center for Elementary Particle Physics and Department of Physics, The University of Tokyo*

21 ⁿ*Universite Hassan II, Ain Chock*

22 ^o*Uppsala University*

23 ^p*Universite de Paris-Sud 11*

24 ^q*Max-Planck-Institut fur Physik*

25

Abstract

26

27 We report a search for neutral MSSM Higgs bosons and Z' boson produced in proton-
28 proton collisions delivered by the Large Hadron Collider (LHC) at center-of-mass energy 13
29 TeV and recorded by the ATLAS detector. The data correspond to an integrated luminosity
30 of 36.1 fb^{-1} . The heavy resonance is produced via gluon-fusion or b-associated production
31 for the MSSM Higgs bosons or quark-antiquark annihilation for the Z' . The heavy resonance
32 is assumed to decay to a $\tau^+ \tau^-$ pair with one τ lepton decaying leptonically and the other
33 hadronically. The results are interpreted in a range of MSSM scenarios and in models that
include a Z' .

34 © 2017 CERN for the benefit of the ATLAS Collaboration.

35 Reproduction of this article or parts of it is allowed as specified in the CC-BY-4.0 license.

35 List of contributions

Adam Bailey	Hadhad analyzer and $Z' \rightarrow \tau\tau$ signal preparation.
Will Davey	Paper editor, Supervisor.
Eric Drechsler	xTau framework support
Dirk Duschinger	Analysis contact, hadhad main analyzer, in charge of $Z' \rightarrow \tau\tau$ signal preparation.
Luca Fiorini	Supervisor.
Lino Gerlach	Hadhad channel, fake background studies.
Michel Janus	Supervisor.
Mohamed Gouighri	$Z' \rightarrow \tau\tau$ signal preparation.
Guillermo Nicolas Hamity	Main analyzer of lephad, on the ntuple production, and final statistical analysis.
Lorenz Hauswald	Analysis contact, hadhad main analyzer, bbH signal validation.
Hao Liu	Lephad fake background from QCD multijet study.
Samina Jabbar	Lephad fake background from Wjets study
Adomas Jelinskas	Main analyzer of lephad, in charge of background estimation.
Karsten Koneke	Supervisor.
Wolfgang Mader	Supervisor.
Allison McCarn	LepHad channel QCD multijet estimation.
Roger Moore	Supervisor.
Masahiro Morinaga	Main analyzer of lephad, work on the ntuple production and produce the main lephad analysis and perform combination with hadhad.
Verena Muckhoff	Lephad, main analyzer on LepHad channel QCD multijet estimation.
Bill Murray	Supervisor.
Nikolaos Rompotis	LepHad Channel
Pedro Henrique Sales De Bruin	LepHad Channel and provide important cross check on hadhad
Arno Straessner	Supervisor
Junichi Tanaka	Supervisor
Trevor Vickey	Paper editor, Supervisor
Lei Zhang	Analysis contact, main analyzer of LepHad Channel.
Zinonas Zinonos	xtau framework support.
Theodore Zorbas	In charge of lephad on the ntuple production.

37

38 Contents

39 0 Notes for the reader	5
40 1 Introduction	5
41 2 Data Samples and Monte Carlo Simulation	8
42 2.1 Monte Carlo Event Samples	8
43 2.2 Data Samples	9
44 3 Object Reconstruction	9
45 3.1 Electrons	9

Not reviewed, for internal circulation only

46	3.2 Muons	9
47	3.3 Jets	10
48	3.4 τ leptons	10
49	3.5 Removal of objects with geometric overlaps	10
50	3.6 Missing transverse momentum	11
51	3.7 Di- τ mass reconstruction	11
52	4 Event Selection	12
53	4.1 Preselection	12
54	4.2 Event Selection	13
55	4.3 Final Categorization	13
56	4.4 Distributions of the key variables	16
57	5 Background Estimation	25
58	5.1 Background with correctly identified ℓ and jet misidentified as τ_{had}	26
59	5.1.1 Definition of the $W+\text{jets}$ control region	26
60	5.1.2 Calculation of the $W+\text{jets}$ jet $\rightarrow \tau$ tau fake factor	27
61	5.1.3 Fake factor validation	30
62	5.1.4 Systematic uncertainties in the $W+\text{jets}$ tau fake factors	31
63	5.2 Background with jets misidentified as ℓ and τ_{had}	35
64	5.2.1 Introduction	35
65	5.2.2 Multi-jet jet $\rightarrow \tau$ tau fake factor estimation	37
66	5.2.3 $\Delta\Phi(\tau, E_{\text{T}}^{\text{miss}})$ correction on QCD tau fake factor	40
67	5.2.4 Multi-jet jet $\rightarrow l$ lepton fake factor estimation	41
68	5.2.5 Measurement of multi-jet fraction	46
69	5.3 Combined background estimation	48
70	6 Systematic Uncertainties	48
71	6.1 Experimental uncertainties	48
72	6.2 Theoretical uncertainties on background modeling	49
73	6.3 Uncertainties on data-driven background estimations	49
74	6.4 Uncertainties on signal modeling	50
75	7 Results	52
76	7.1 Statistics Analysis	52
77	7.2 Fit check	53
78	7.3 Exclusion Limit	58
79	8 Combination of $\tau_{\ell}\tau_{\text{had}}$ and $\tau_{\text{had}}\tau_{\text{had}}$ channels	60
80	8.1 Fit study for combination	60
81	9 Conclusions	63
82	Auxiliary material	74
83	A Signal Samples	74
84	A.1 Validation of the bbH fast simulation	74

Not reviewed, for internal circulation only

85	A.2 $Z/\gamma^* \rightarrow Z'$ reweighting validation	76
86	B Signal width	81
87	C Details on Signal Acceptance Uncertainty Estimation	82
88	C.1 Event Selection	82
89	C.2 Uncertainty Evaluation	83
90	C.3 Negative Weight Fractions in b-associated events	83
91	D Signal theoretical uncertainty shape effect	91
92	D.1 $Z' \rightarrow \tau\tau$ interpretation of combination	94
93	E MC Samples	97
94	F Fake related studies	105
95	F.1 Details of QCD fake systematics treatment	105
96	F.2 Some investigation on the Fake lepton and Fake tau	109
97	F.3 Some investigation on the Fake tau from Wjets	112
98	F.4 muhad b -veto rQCD investigation	114
99	F.5 $W+jets$ control region with $\Delta\phi(\tau, E_T^{\text{miss}})$ corrected Fake	116
100	F.5.1 Discussion on the potential difference between ehad and muhad	116
101	F.6 Separated Intermediate Regions	121
102	F.7 Intermediate region with and without $\Delta\phi(\tau, E_T^{\text{miss}})$ corrected Fake	123
103	F.8 $W+jets$ Fake factor calculation: original input distribution	126
104	F.9 Lepton Fake factor calculation: original input distribution	130
105	F.10 Lepton fake factor study	133
106	G Debug stream data check	142
107	H Different MSSM exclusion limit interpolation schemes	143
108	I Central provided LPX systematics for Z+jets	146
109	J Impact of the systematics on the expected limit	147
110	K Fit study for Version (Latest production)	148
111	K.1 Some detailed investigation on the Fit results	161
112	L TES insitu systematics study	163
113	M Expected limit comparison between ICHEP and current analysis	168
114	N Extrap Plots	169
115	O New and old m_T^{tot} reconstruction comparison	170
116	P High MET category	171
117	Q Investigation on Nbjet = 2	177

118	R Useful plots and extra studies in paper	178
119	R.1 Background estimation	178
120	R.1.1 Jet background estimate in the $\tau_{\text{lep}} \tau_{\text{had}}$ channel	178
121	R.1.2 Jet background estimate in the $\tau_{\text{had}} \tau_{\text{had}}$ channel	180
122	R.2 Results	180
123	R.2.1 Cross-section limits	181
124	R.2.2 MSSM interpretation	184
125	R.2.3 Z' interpretations	184
126	R.3 Auxillary plots in paper	187

127 0. Notes for the reader

128 This is the lephad internal note with the full 2015 and 2016 data for the analysis for the publication around
 129 Summer 2017 time scale. This version is updated after unblinding data and the 2nd circulation of the
 130 paper draft:

- 131 • This version will document all the important changes and cross check after unblinding the data.
- 132 • Appendix ?? documents all the useful plots and table in the paper draft.

133 1. Introduction

134 The discovery of a scalar particle at the Large Hadron Collider (LHC) [1, 2] has provided important insight
 135 into the mechanism of electroweak symmetry breaking. Experimental studies of the new particle [3–7]
 136 demonstrate consistency with the Standard Model (SM) Higgs boson [8–13]. However, it remains possible
 137 that the discovered particle is part of an extended scalar sector, a scenario that is favoured by a number of
 138 theoretical arguments [14, 15].

139 The Minimal Supersymmetric Standard Model (MSSM) [16–20] is an extension of the SM, which provides
 140 a framework addressing naturalness, gauge coupling unification, and the existence of dark matter. The
 141 Higgs sector of the MSSM contains two Higgs doublets, which results in five physical Higgs bosons after
 142 electroweak symmetry breaking. The MSSM Higgs sector is CP-conserving at tree level and assuming
 143 that higher order corrections conserve CP the Higgs bosons are such that two are neutral and CP-even
¹(h , H), one is neutral and CP-odd (A), ¹ and the remaining two are charged (H^\pm). At tree level, the
 144 mass of the light scalar Higgs boson, m_h , is restricted to be smaller than the Z boson mass, m_Z . This
 145 bound is weakened due to radiative corrections up to a maximum allowed value of $m_h \sim 135$ GeV.
 146 Only two additional parameters are needed with respect to the SM at tree level to describe the MSSM
 147 Higgs sector. These can be chosen to be the mass of the CP-odd Higgs boson, m_A , and the ratio of the
 148 vacuum expectation values of the two Higgs doublets, $\tan \beta$. Beyond lowest order, the MSSM Higgs
 149 sector depends on additional parameters, which are fixed at specific values in various MSSM benchmark
 150 scenarios. For example, in the m_h^{\max} scenario the parameters that define the radiative corrections are

¹ By convention the lighter CP-even Higgs boson is denoted h , the heavier CP-even Higgs boson is denoted H . The masses of the three bosons are denoted in the following as m_h , m_H and m_A for h , H and A , respectively.

chosen such that m_h is maximised for a given $\tan \beta$ and M_{SUSY} [21, 22].² This results for $M_{\text{SUSY}} = 1$ TeV in $m_h \sim 130$ GeV for large m_A and $\tan \beta$. In addition, in the same region the heavy Higgs bosons, H , A and H^\pm , are approximately mass degenerate and h has properties very similar to a SM Higgs boson with the same mass. This feature is generic in the MSSM Higgs sector: a decoupling limit exists defined by $m_A \gg m_Z$ in which the heavy Higgs bosons have similar masses and the light CP-even Higgs boson in practice becomes identical to a SM Higgs boson with the same mass.

The discovery of a SM-like Higgs boson, with mass that is now measured to be 125.09 ± 0.21 (stat) ± 0.11 (syst) GeV [24], has prompted the definition of additional MSSM scenarios [23]. Most notably, the $m_h^{\text{mod}+}$ and $m_h^{\text{mod}-}$ scenarios are similar to the m_h^{max} scenario, apart from the fact that the choice of parameters that govern the radiative corrections is such that the maximum light CP-even Higgs boson mass is ~ 126 GeV. This choice increases the region of the parameter space that is compatible with the observed Higgs boson being the lightest CP-even Higgs boson of the MSSM with respect to the m_h^{max} scenario. A different approach is employed in the hMSSM scenario [25, 26] in which the measured value of m_h can be used, with certain assumptions, to predict the remaining masses and couplings of the MSSM Higgs bosons without explicit reference to the soft supersymmetry-breaking parameters. There are many other MSSM parameter choices beyond these scenarios that are also compatible with the observed SM Higgs boson, see for instance [27, 28].

In the MSSM Higgs sector the couplings of the MSSM Higgs bosons to down-type fermions are enhanced with respect to the SM for large $\tan \beta$ values resulting in increased branching fractions to τ leptons and b -quarks, as well as a higher cross section for Higgs boson production in association with b -quarks. This has motivated a variety of searches in $\tau\tau$ and bb final states at LEP [29], the Tevatron [30–32] and the LHC [33–36].

Additional heavy Z' gauge bosons appear in many models [37–41] and are “one of the best motivated extensions of the standard model (SM)” [42]. Z' bosons often arise in grand unified theories and while they are typically considered to obey lepton universality, this is not a necessary requirement. In particular, some models offering an explanation for the high mass of the top-quark, predict that such bosons preferentially couple to third-generation fermions, one of them is the Strong Flavour Model (SFM) [43, 44]. Non-universal Z' models can also explain the anomalous dimuon production observed at the D0 experiment [45] and the excess in semileptonic B -meson decays into τ -leptons observed at the Belle and BaBar experiments [46, 47]. Searches in the ditau channel are also sensitive to sgoldstino-like scalars in supersymmetric models [48, 49], hidden sector Z' models [50] and to the anomalous τ -lepton dipole moments and higher order τ -gluon couplings [51].

The Sequential Standard Model (SSM) contains a single additional Z' boson with the same couplings as the SM Z boson, and while not theoretically well motivated, serves as a benchmark. Direct searches for high-mass ditau resonances have been performed by the ATLAS and CMS collaborations at $\sqrt{s} = 13$ TeV. The latest results from ATLAS excludes Z'_{SSM} with masses below 1.9 TeV at 95% CL considering 3.2 fb^{-1} of integrated luminosity [52]. CMS results with 2.2 fb^{-1} are setting lower mass limits at 2.1 TeV at 95% CL in the SSM [53]. Indirect limits on Z' bosons with non-universal flavour couplings have been set using measurements from LEP and LEP II [54] and translate to a lower bound on the Z' mass of 1.09 TeV. For comparison, the most stringent limits on Z'_{SSM} in the dielectron and dimuon decay channels combined are 4.50 TeV from ATLAS [55] and 3.37 TeV from CMS [56]. While searches in these channels are in

² The supersymmetry scale, M_{SUSY} , is defined here as the geometric average of the mass of the third generation squarks following refs. [21–23].

Not reviewed, for internal circulation only

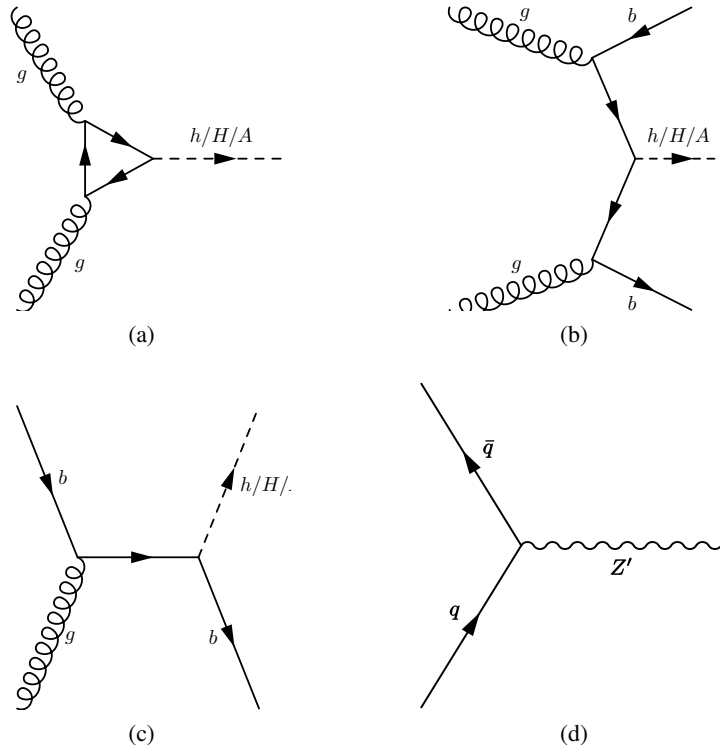


Figure 1: Lowest-order Feynman diagrams for (a) gluon-fusion and b -associated production in the (b) four-flavour and (c) five-flavour schemes of a neutral MSSM Higgs boson. Feynman diagram for Drell–Yan production of a Z' boson at lowest order (d).

193 general more sensitive than in the ditau channel, they may be evaded by models with weak couplings to
 194 electrons and muons.

195 This note presents the results of a search for a neutral MSSM Higgs boson as well as high-mass resonances
 196 decaying into two tau leptons using 36.1 fb^{-1} of proton–proton collision data collected with the ATLAS
 197 detector [57] in 2015 and 2016 at a centre-of-mass energy of 13 TeV. Tau leptons can decay into a charged
 198 lepton and two neutrinos ($\tau_{\text{lep}} = \tau_e$ or τ_μ), or hadronically (τ_{had}), predominantly into one or three charged
 199 pions, a neutrino and often additional neutral pions. The $\tau_{\text{lep}}\tau_{\text{had}}$ decay channel with a branching ratio of
 200 $\text{BR}=23\%$ is analysed in this document. Higgs boson production through gluon-fusion or in association
 201 with b -quarks is considered (see Figure 1), with the latter mode dominating for high $\tan\beta$ values. The
 202 results of the search are interpreted in various MSSM scenarios. Limits on the cross section times $\tau^+\tau^-$
 203 branching fraction of a generic neutral resonance are reported. The impact on the signal acceptance from
 204 altering Z' couplings is evaluated and limits are also placed on a particular model that exhibits enhanced
 205 couplings to tau-leptons.

206 2. Data Samples and Monte Carlo Simulation

207 2.1. Monte Carlo Event Samples

208 Monte Carlo samples used by this analysis are produced with the ATLAS simulation infrastructure [58] as
 209 part of the ATLAS *mc15c* production campaign. The samples and generators listed in Appendix E have
 210 been used.

211 Simulated samples are used for the following processes: $W+jets$, $Z+jets$, $t\bar{t}$, single top and diboson. The
 212 $W+jets$ process is modelled with **Sherpa 2.2** generator [59], while for the $Z+jets$ process the **POWHEG** [60]
 213 generator is used and the events are subsequently showered with **Pythia8** [61, 62]. For the $t\bar{t}$ and single
 214 top samples **POWHEG** is used as well, but the events are showered with **Pythia6** [61]. Diboson samples
 215 have been generated and showered with **Sherpa**. The $Z+jets$ samples are simulated in slices with different
 216 masses of the off-shell boson mass. In order to avoid overlap the inclusive samples are truncated keeping
 217 only events with $m^* < 120$ GeV, where m^* denotes the off-shell boson mass. The procedure used is in
 218 agreement with the physics modelling group recommendations.

219 Two production processes of heavy neutral MSSM Higgs bosons have relevant cross sections for this ana-
 220 lysis: gluon-fusion and b -associated production. Samples of b -associated production events at 18 different
 221 Higgs masses, from 150 GeV to 2.5 TeV, have been generated using the **MadGraph5_aMC@NLO 2.1.2**
 222 generator [63, 64]. Gluon-fusion samples with the same masses are generated using **POWHEG** [60]. The
 223 generation of parton shower, underlying event and hadronisation is performed using **Pythia 8.2** [65] for
 224 both signal processes. Due to the fact that the **MadGraph5_aMC@NLO 2.1.2** generator produces a lot of
 225 events with negative weights, much larger statistics with respect to the gluon-fusion samples have to be
 226 generated. For this reason the ALTFast-II simulation has been used to simulate these events. The fast
 227 simulation has been validated against full simulation for a single mass point and the results of this study
 228 are shown in Appendix A.

229 The contributions of the various Z' signal models are estimated by reweighting $Z/\gamma^* \rightarrow \tau\tau$ events using
 230 the TauSpinnerTool. This tool utilizes the TauSpinner algorithm [66], which correctly accounts for spin
 231 effects in the tau decays. The used $Z/\gamma^* \rightarrow \tau\tau$ sample, enriched in high-mass events, is generated
 232 with PYTHIA 8.165 [62]. A leading-order generator is chosen for the $Z/\gamma^* \rightarrow \tau\tau$ process since this
 233 is a requirement for the matrix element reweighting done in TauSpinnerTool. The A14 tune is used
 234 together with the NNPDF2.3LO PDF set [67]. A detailed description of the reweighting procedure is given
 235 in Appendix A.2. Interference of the Z' signals with the SM Z/γ^* is not included since we can take
 236 the $Z/\gamma^* \rightarrow \tau\tau$ modelling directly from POWHEG+Pythia8 sample. For each signal model, 18 mass
 237 hypotheses are considered, ranging from 500 to 1000 GeV in steps of 100 GeV and up to 4000 GeV in
 238 steps of 125 GeV.

239 Each sample is passed through the full GEANT4 [58, 68] simulation of the ATLAS detector and is
 240 reconstructed with the same software as used for data. The only exception are the bbH signal samples that
 241 have used the fast simulation.

242 For this analysis the DAOD_HIGG4D2 derivation and the xTau framework are used sequentially to
 243 produce the ntuples for the final analysis. The xTau framework is being officially used for the ATLAS
 244 Tau CP Working group, the charged Higgs analysis $H^\pm \rightarrow \tau\nu$ and it is the recommended framework of
 245 the HLeptons Higgs sub-group.

246 2.2. Data Samples

247 The data used for this version of the note corresponds to 36.1 fb^{-1} , recorded by ATLAS detector at LHC
 248 in 2015 and 2016.

249 Events for which the trigger is unable to process in time or causing errors in the online reconstruction are
 250 redirected to the debug stream. These events are taken into account in the analysis to avoid bias in the
 251 event selection. The events from the debug stream are processed and only 1 event passes the analysis
 252 pre-selection criteria as shown in Appendix G. So the effect is negligible.

253 Data where the IBL was not fully operational have not been used, since we use b -tagging to define signal
 254 region categories. Data from the 50ns configuration are not used as well, since they correspond to a small
 255 fraction of the data without a visible impact in sensitivity.

256 3. Object Reconstruction

257 The ATLAS detector [69] consists of an inner tracking detector with an acceptance $|\eta| < 2.5$ surrounded
 258 by a thin 2 T superconducting solenoid, a calorimeter system extending up to $|\eta| = 4.9$ that uses a variety
 259 of technologies to detect electrons, photons and hadronic jets, as well as a large muon spectrometer using
 260 superconducting toroids arranged with an eight-fold azimuthal coil symmetry.

261 3.1. Electrons

262 An electron object is made of clustered energy deposits in the electromagnetic calorimeter that are matched
 263 to a track in the inner detector. Electron candidates are required to pass a “medium” likelihood-based
 264 identification selection point, have $E_T > 30 \text{ GeV}$, where $E_T = E_{\text{cluster}} / \cosh(\eta_{\text{track}})$, and to be in the fiducial
 265 volume of the detector, $|\eta| < 2.47$. The transition region between the barrel and end-cap calorimeters
 266 ($1.37 < |\eta| < 1.52$) is excluded. The exclusion of the crack region is done because of the very large
 267 uncertainty in the electron to tau fake rate in that region (see also Ref. [70]). Electron candidates must
 268 fulfill quality requirements based on the expected shower shape [71]. A gradient isolation requirement is
 269 applied which is expected to be 90(99)% efficient for electrons of $p_T = 25$ (60) GeV.

270 3.2. Muons

271 Objects are considered as muon candidates if an inner detector track matches a track reconstructed in the
 272 muon spectrometer [72]. Muon candidates are required to have $p_T > 30 \text{ GeV}$ and $|\eta| < 2.5$. Muons
 273 must be reconstructed with a variety of muon reconstruction algorithms³, and pass a gradient isolation
 274 criterion that is expected to be 90(99)% efficient for muons of $p_T = 25$ (60) GeV. The “medium” muon
 275 identification selection point is required.

³ See also the muon twiki for more details: https://twiki.cern.ch/twiki/bin/viewauth/Atlas/MuonSelectionTool#Quality_definition

276 3.3. Jets

277 Jets are reconstructed from topological clusters in the calorimeters using the anti- k_T algorithm [73, 74]
 278 with a size parameter value of $R = 0.4$. Jets are calibrated using the EM+JES+GSC calibration scheme.
 279 Corrections, derived from simulations and based on jet areas [75], are then applied in order to reduce
 280 the effects of pile-up on the jet calibration [76]. Only jets with a transverse momentum $p_T > 25$
 281 GeV and a direction within $|\eta| < 2.5$ are considered in the following. A method that allows for the
 282 identification and selection of jets originating from the hard-scatter interaction through the use of tracking
 283 and vertexing information is used [76]. It is referred to as the “JVT”, where JVT is the output of the
 284 jet vertex tagger algorithm. Jets whose $p_T < 60$ GeV and $|\eta| < 2.4$ are required to have a $JVT > 0.59$.
 285 In order to suppress jets from instrumental effects or non-collision backgrounds, the LooseBad cleaning
 286 requirement is imposed [77]. In order to identify the jets initiated by b quarks, the MV2c10 algorithm
 287 is used [78], which uses variables constructed by the IP2D, IP3D, SV1 and JetFitter algorithms into a
 288 multivariate discriminant score, w_{MV2C10} , with values between minus and plus one. A working point that
 289 corresponds to an average efficiency of 70% for b-jets in $t\bar{t}$ events is chosen (corresponding to a weight
 290 $w_{MV2C10} > 0.824$). Tagging and mis-tagging efficiency scale factors relate efficiencies as determined
 291 in various data samples to their counterparts in simulation. They are used in all simulated events, after
 292 having applied the b-tagging algorithm to the jets. Note that the b-tagged jets are required to pass the
 293 same p_T , η and JVT selection as all other jets.

294 3.4. τ leptons

295 Hadronic decays of τ leptons (τ_{had}) are characterized by the presence of mostly one or three charged tracks,
 296 accompanied by a neutrino and possibly neutral pions. This results in a collimated shower profile in the
 297 calorimeter and only a few nearby tracks. Before the object selection and identification, candidates for
 298 hadronic τ lepton decays are seeded by jets. In order to reconstruct hadronically decaying τ leptons [70], all
 299 anti- k_T jets depositing at least $p_T > 10$ GeV in the calorimeter are considered as τ_{had} candidates. A boosted
 300 decision tree is used for the discrimination of τ_{had} from quark or gluon initiated jets (BDT(τ_{had} ID)). This
 301 is based on shower shape and track multiplicity properties of the true τ_{had} objects. There are also electrons
 302 that may be reconstructed as τ_{had} . In order to reduce this background the τ_{had} is matched geometrically
 303 to a reconstructed electron passing a very loose electron identification requirement. If the matching is
 304 successful the candidate is rejected. The electron identification requirement is based on the likelihood
 305 discriminant that the egamma group provides and the value uses is tuned by the tau WG such that 95%
 306 efficiency on τ_{had} from $Z \rightarrow \tau\tau$ decays is achieved. Only candidates with one or three associated tracks
 307 reconstructed in the inner detector are considered. The hadronic decay products of the τ are required to
 308 have a visible transverse momentum (p_T^τ) of at least 20 GeV, to be within $|\eta| < 2.5$ and to not be within
 309 the transition region between the barrel and end-cap calorimeters ($1.37 < |\eta| < 1.52$). The “medium”
 310 τ_{had} identification criterion is used based on a $p_T(\tau_{had})$ dependent cut on BDT(τ_{had} ID). For the muons
 311 faking τ_{had} there is no separate discriminant, as it was in Run-I, but it depends on an optimized overlap
 312 removal with muons.

313 3.5. Removal of objects with geometric overlaps

314 Objects that have a geometric overlap (based on $\Delta R \equiv \sqrt{\Delta\phi^2 + \Delta\eta^2}$) are removed by the following
 315 priority:

- Jets within a $\Delta R = 0.2$ cone of the leading $p_T \tau_{\text{had}}$ are excluded.
- Jets within a $\Delta R = 0.4$ cone of an electron or muon are excluded.
- τ_{hadS} within a $\Delta R = 0.2$ cone of electrons or muons are excluded.
- Electrons within a $\Delta R = 0.2$ cone of muons are excluded.

For this overlap removal objects with loosened object selection are considered: no isolation, loose lepton identification, electron $p_T > 15$ GeV and muon $p_T > 7$ GeV. The choice of $\Delta R = 0.4$ cone for jet-lepton separation follows optimization in examining the $\Delta R(\text{jet}, \text{lepton})$ distributions in signal and background samples.

3.6. Missing transverse momentum

The missing transverse momentum vector \vec{E}_T^{miss} is measured as the negative vector sum of the transverse momenta of the reconstructed objects (jets, electrons, muon, τ_{had} , and photons) with the corresponding calibrations, and soft terms which are not associated to the reconstructed objects [79]. Different algorithms have been explored to improve the soft term measurement. The default algorithm in this note is Track-based Soft Term (TST) [80] due to its outstanding resolution performance and pileup robustness. In this algorithm the momentum of the soft terms are calculated based on inner detector measurements.

One complication is in the anti-isolation control region, described in Section 5.2, which is used for the multi-jet estimation. This region selects events with an electron or a muon that fail the isolation requirements. In the original E_T^{miss} reconstruction this lepton would have been calibrated to the jet energy scale and this was shown to lead to a bias in the control region. In order to avoid this bias the E_T^{miss} algorithm is run again for this particular control region considering these anti-isolated leptons with the lepton energy scale instead.

3.7. Di- τ mass reconstruction

The $\tau_{\text{lep}}\tau_{\text{had}}$ mass reconstruction is critical in achieving good performance, however, it is challenging due to the number of neutrinos from the τ lepton decays in the final state. For this reason, dedicated algorithms have been developed. The missing mass calculator, MMC, [81] uses a simulation-based parametrization of the angle between the neutrinos and the visible decay products. MOSAIC is based on a matrix element technique, as discussed in Ref. [82].

A simpler mass reconstruction, which was used for both $\tau_{\text{lep}}\tau_{\text{had}}$ and $\tau_{\text{had}}\tau_{\text{had}}$ channel in the 2015 paper analysis, is the total transverse mass:

$$m_T^{\text{tot}} = \sqrt{m_T^2(E_T^{\text{miss}}, \tau_{\text{lep}}) + m_T^2(E_T^{\text{miss}}, \tau_{\text{had}}) + m_T^2(\tau_{\text{lep}}, \tau_{\text{had}})},$$

where the notation $m_T(\vec{a}, \vec{b})$ is defined such that:

$$m_T(\vec{a}, \vec{b}) = \sqrt{2p_T(\vec{a})p_T(\vec{b})(1 - \cos \Delta\phi(\vec{a}, \vec{b}))}$$

This mass reconstruction has the property that the contribution of events with jets faking taus tends to be reconstructed to lower masses than MMC or MOSAIC.

345 The visible mass of the τ_{had} and τ_{lep} is another simple mass reconstruction. It is simply the invariant mass
 346 of the reconstructed lepton (electron or muon) 4-vector and the reconstructed $\tau_{\text{had-vis}}$ 4-vector.

347 The analysis uses $m_{\text{T}}^{\text{tot}}$ as the final variable, in part due to its simplicity and the fact that it does not take a
 348 lot of computation time. It was also suggested in studies for the 2015 data paper that $m_{\text{T}}^{\text{tot}}$ had similar or
 349 better performance at high mass compared to MMC and MOSAIC.

350 4. Event Selection

351 4.1. Preselection

352 Events are selected by two trigger categories: single electron and single muon trigger. The real treatment
 353 is more complicated due to the different trigger strategies under different luminosity conditions. In
 354 order to mimic the different trigger conditions for 2015 and 2016, a random run number has been
 355 generated according to the luminosity of each run for the MC events. At least one of the triggers
 356 `e24_lhmedium_L1EM20VH` for 2015 (`e26_lhtight_nod0_ivarloose` for 2016), `e60_lhmedium` and
 357 `e120_lhloose` (`e140_lhloose_nod0` for 2016) are required to be passed for the electron channel, and at
 358 least one of the triggers `mu20_iloose_L1MU15` for 2015 (`HLT_mu26_ivarmedium` for 2016) and `mu50`
 359 are required to be passed for the muon channel.

Table 1: Trigger list for lephad analysis.

period	Single-Electron-Trigger	Single-Muon-Trigger
data15	<code>e24_lhmedium_L1EM20VH</code> OR <code>e60_lhmedium</code> OR <code>e120_lhloose</code>	<code>mu20_iloose_L1MU15</code> OR <code>mu50</code>
data16	<code>e26_lhtight_nod0_ivarloose</code> OR <code>e60_lhmedium_nod0</code> OR <code>e140_lhloose_nod0</code>	<code>mu26_ivarmedium</code> OR <code>mu50</code>

360 The primary vertex of each event is chosen as the proton–proton vertex candidate with the highest sum
 361 of the squared transverse momenta of all associated tracks. Events must have at least one identified τ_{had}
 362 candidate and one electron or one muon candidate. Events with more than one lepton (electron with
 363 $p_{\text{T}} > 15 \text{ GeV}$ or muon with $p_{\text{T}} > 7 \text{ GeV}$) passing the loose identification criterion are rejected (“dilepton
 364 veto”) in order to reduce Z/γ^* events. The electron or the muon in the event are required to match
 365 geometrically with the HLT object that triggered the event. For simplicity, for different muon p_{T} different
 366 triggers are considered: $p_{\text{T}} > 55 \text{ GeV} \rightarrow \text{mu50}$; ($p_{\text{T}} > 30 \text{ GeV}$) `mu20_iloose_L1MU15` for 2015 and
 367 `HLT_mu26_ivarmedium` for 2016. For the electrons, a combined scale factor is used for the logical OR
 368 of the three triggers for 2015 and 2016, so it is not possible to consider the triggers separately. The τ_{had}
 369 candidate is required to have $p_{\text{T}} > 25 \text{ GeV}$ and pass medium identification requirements. In case of more
 370 than one τ_{had} candidates the candidate with the highest p_{T} is selected. After that, a $\eta < 2.3$ cut on τ_{had} is
 371 applied. This is because the high η area is mostly background and, in addition, there is a large systematics
 372 on the electron to τ_{had} fake rate. Finally, the lepton (e or μ , also denoted and as ℓ) and the τ_{had} are required
 373 to have opposite sign charge.

374 This preselection is defined in such a way that is orthogonal to the $\tau_{\text{had}}\tau_{\text{had}}$ channel, in which events are
 375 rejected if they contain an electron or a muon. Events in which τ_{lep} is an electron (muon) are referred to
 376 as belonging to the electron (muon) channel.

377 4.2. Event Selection

378 The analysis strategy is heavily based on the previous 2015 data analysis (paper analysis). In the ICHEP
 379 2016 analysis, a dedicated high $E_{\text{T}}^{\text{miss}}$ category was created, in order to retrieve some efficiency loss for
 380 the inefficiency of the single lepton trigger by adding the $E_{\text{T}}^{\text{miss}}$ trigger. However, we have decided to drop
 381 the high $E_{\text{T}}^{\text{miss}}$ category in this analysis due two reasons: Firstly, the sensitive parameter space for the
 382 high $E_{\text{T}}^{\text{miss}}$ category is the high Higgs mass region where the hadhad channel has more sensitivity. This
 383 means that the improvement from the high $E_{\text{T}}^{\text{miss}}$ category to the final combined results is not significant.
 384 Secondly, we do not have the dedicated manpower on the high $E_{\text{T}}^{\text{miss}}$ category.

385 The event selection consists of the following requirements:

- 386 • $\Delta\phi(\tau, \ell) > 2.4$
- 387 • $m_{\text{T}}(\ell, E_{\text{T}}^{\text{miss}}) < 40 \text{ GeV}$, where $m_{\text{T}}(\ell, E_{\text{T}}^{\text{miss}}) \equiv \sqrt{2p_{\text{T}}(\ell)E_{\text{T}}^{\text{miss}}(1 - \cos \Delta\phi(\ell, E_{\text{T}}^{\text{miss}}))}$

388 The $m_{\text{T}}(\ell, E_{\text{T}}^{\text{miss}})$ is an upper cut in order to reduce $W+\text{jets}$. The $W+\text{jets}$ background features a Jacobian
 389 peak in $m_{\text{T}}(\ell, E_{\text{T}}^{\text{miss}})$ at about 80 GeV. However, the signal signature is from a heavy Higgs boson that
 390 is produced with typically low p_{T} and decays to two boosted tau leptons. The leptonically decaying tau
 391 lepton has one more neutrino with respect to the hadronically decaying tau lepton, and hence one would
 392 expect the $E_{\text{T}}^{\text{miss}}$ to be aligned to the lepton direction leading to small $m_{\text{T}}(\ell, E_{\text{T}}^{\text{miss}})$.

393 In addition to these requirements, it was found that there is a significant number of electrons faking τ_{had}
 394 from $Z \rightarrow ee$ events. For this reason in the electron channel only, the region defined by the visible mass
 395 of the τ_{had} and the lepton $80 < m_{\text{vis}} < 110 \text{ GeV}$ is vetoed from the signal region.

396 4.3. Final Categorization

397 We further categorize events into the b -tag and b -veto regions, in order to explore the b -quark initiated
 398 jet in the b -associated production signal, by the following requirement:

- 399 • b-veto: $N_{\text{bjet}} = 0$
- 400 • b-tag: $N_{\text{bjet}} \geq 1$.

401 Here, N_{bjet} is the number of b -tagged jet in the event.

402 In the b -tag signal region, Top events with the truth tau are the dominant background source. In order to
 403 control the Top (truth tau) background, a Top CR is defined by requiring $m_{\text{T}}(\ell, E_{\text{T}}^{\text{miss}}) > 110(100) \text{ GeV}$
 404 for electron (muon) channel and used in the final fit.

405 Besides the signal and control regions defined above, many other control regions are defined to estimate
 406 the background contribution. Table 2 briefly summarises the regions that are used in this analysis. The
 407 detailed definition of each region can be found in the corresponding sections.

Table 2: Summary of categories used in this analysis.

Regions	Usages	Final fit	Key selection	Reference
Signal region	Extract signal	Yes	$m_T(\ell, E_T^{\text{miss}}) < 40 \text{ GeV}$	4.2
Intermediate CR	Validate background modeling and derive extrapolation uncertainty	No	$40 < m_T(\ell, E_T^{\text{miss}}) < 60(70) \text{ GeV}$ for muhad (ehad)	5.1
W+jets CR	Derive fake factor for W+jets (Top) by requiring b-veto (b-tag)	No	$60(70) < m_T(\ell, E_T^{\text{miss}}) < 150 \text{ GeV}$ for muhad (ehad)	5.1
Top CR	Constrain Top with truth tau background	Yes	$100(110) < m_T(\ell, E_T^{\text{miss}}) \text{ GeV}$ for muhad (ehad)	4.2
QCD fake tau CR	Derive fake factor for QCD Multi-jets	No	Invert lepton isolation	5.2.2
QCD fake lepton CR	Derive jet to lepton fake factor	No	No lepton isolation and $m_T(\ell, E_T^{\text{miss}}) < 30 \text{ GeV}$	5.2.4

Table 3: Yield table for each category. The numbers correspond to an integrated luminosity of 36.1 fb^{-1} . The quoted uncertainties only contain the statistical uncertainty .

Regions	Data	Total bkg	$Z \rightarrow ll$	$Z \rightarrow \tau\tau$	Top	Diboson	Jet $\rightarrow \tau$
muhad $\Delta\phi > 2.4$	294011	277294 ± 612	19409 ± 218	73550 ± 484	14198 ± 246	2548 ± 29	167589 ± 177
muhad $m_T < 40 \text{ GeV}$	114013	108078 ± 471	9040 ± 150	54075 ± 412	2181 ± 147	511 ± 11	42271 ± 88
muhad b-veto	110109	104835 ± 470	9079 ± 153	54038 ± 414	650 ± 135	514 ± 11	40554 ± 86
muhad b-tag	3904	3632 ± 56	51 ± 12	373 ± 41	1528 ± 26	3 ± 1	1678 ± 25
muhad TCR	6205	6322 ± 107	2 ± 1	11 ± 5	5595 ± 104	15 ± 2	699 ± 28
ehad Zee mvis veto	404064	369658 ± 560	12603 ± 128	67271 ± 456	26634 ± 215	3737 ± 65	259413 ± 198
ehad $\Delta\phi > 2.4$	226847	209535 ± 448	10865 ± 119	51616 ± 398	12023 ± 73	2123 ± 61	132909 ± 141
ehad $m_T < 40 \text{ GeV}$	96195	90769 ± 360	6683 ± 93	37846 ± 338	1671 ± 27	370 ± 11	44198 ± 79
ehad b-veto	93256	88163 ± 360	6737 ± 94	37775 ± 338	397 ± 13	371 ± 11	42883 ± 78
ehad b-tag	2939	2906 ± 53	35 ± 8	296 ± 45	1275 ± 24	4 ± 1	1296 ± 13
ehad TCR	5653	5885 ± 51	3 ± 1	4 ± 1	5222 ± 49	15 ± 2	641 ± 14

408 The number of events of backgrounds passing final selections are shown in Table 3 while that of signals
 409 are shown in Table 4. The normalization in the tables corresponds to the total luminosity 36.1 fb^{-1} . The
 410 signal cross section is assumed to be 1 pb. The quoted uncertainties are statistical uncertainty only. The
 411 signal region is still blinded, hence data is not shown. Here, $Z \rightarrow \tau\tau$ is mainly (true τ) with negligible
 412 contribution from $l \rightarrow \tau$, $Z \rightarrow ll$ is all $l \rightarrow \tau$, Top includes true τ and some ($\approx 10\%$) $l \rightarrow \tau$, Diboson
 413 true τ and some ($\approx 7\%$) $l \rightarrow \tau$. From these tables, it can be seen that the high mass signal contamination
 414 in Top CR is non-negligible. However, due to the high $m_T(\ell, E_T^{\text{miss}})$ requirement in Top CR, the signal
 415 to background ratio in Top CR is not comparable to the signal region in the high region of the final
 416 discriminant, m_T^{tot} .

417 Due to the fact that the analysis is still blind at this moment, no data-MC comparison plot is shown in
 418 the signal regions. Instead, a data-MC comparison plots in the validation regions, $40 < m_T(\ell, E_T^{\text{miss}}) <$
 419 $60(70) \text{ GeV}$ for muhad (ehad), in Section 5.1.3, are shown in Figures 20, 21, 22, 23, 24, 25. The signal
 420 ratio of this validation region to the signal region is about 20% for 200 GeV signal and 10% for 1500 GeV
 421 signal. This validation region has similar event composition as the signal region. The good modeling in the
 422 validation region proves the validity of the background modeling strategy. Here, the jet $\rightarrow \tau$ is an estimate
 423 of τ_{had} fakes from the anti- τ_{had} region events scaled by the jet $\rightarrow \tau$ fake factors measured in a W+jets and

Table 4: Yield table for each category. The numbers correspond to the integrated luminosity of 36.1 fb^{-1} for signal regions. The signal normalization corresponds to an assumed cross section of 1 pb. The quoted uncertainties only contain the statistical uncertainty. Note: the sum of the number of events in the b -tag and b -veto is not exactly equal to the yield before applying b -tagging categorization. This is due to the b -tagging efficiency calibration correction factors applied in b -tag and b -veto categories; It is a known feature, so-called *non-closure*, which is typically about 1% level.

Regions	ggH200	ggH600	ggH1000	ggH1500	bbH200	bbH600	bbH1000	bbH1500
muhad $\Delta\phi > 2.4$	697 ± 19	1816 ± 32	1865 ± 31	1726 ± 27	672 ± 19	1745 ± 20	1780 ± 31	1580 ± 32
muhad $m_T < 40 \text{ GeV}$	468 ± 16	1132 ± 25	1095 ± 24	948 ± 21	429 ± 15	1029 ± 15	1002 ± 22	809 ± 23
muhad b-veto	468 ± 16	1126 ± 26	1078 ± 24	914 ± 21	319 ± 13	640 ± 12	600 ± 18	483 ± 18
muhad b-tag	4 ± 1	17 ± 3	28 ± 4	42 ± 6	110 ± 7	393 ± 10	411 ± 15	335 ± 15
muhad TCR	0	9 ± 2	14 ± 2	16 ± 2	9 ± 2	160 ± 6	235 ± 11	238 ± 13
ehad Zee mvis veto	556 ± 16	1952 ± 35	1916 ± 34	1492 ± 27	528 ± 17	1807 ± 21	1659 ± 31	1361 ± 31
ehad $\Delta\phi > 2.4$	466 ± 14	1880 ± 35	1863 ± 33	1450 ± 26	474 ± 16	1734 ± 21	1606 ± 30	1318 ± 30
ehad $m_T < 40 \text{ GeV}$	304 ± 11	1136 ± 27	1056 ± 25	767 ± 18	282 ± 12	976 ± 16	850 ± 22	646 ± 21
ehad b-veto	303 ± 11	1132 ± 27	1037 ± 25	752 ± 18	217 ± 11	625 ± 13	501 ± 17	399 ± 16
ehad b-tag	3 ± 1	11 ± 2	29 ± 4	20 ± 3	65 ± 6	356 ± 10	352 ± 14	253 ± 14
ehad TCR	0	8 ± 2	16 ± 4	13 ± 2	9 ± 2	182 ± 6	215 ± 11	210 ± 12

⁴²⁴ a multi-jet control regions. *fakes* represents the jet $\rightarrow \tau$ from $W+\text{jets}$ and Top events while *qcd* represents
⁴²⁵ the jet $\rightarrow \tau$ from QCD multi-jet events. Note: here, the fake from $W+\text{jets}$ and QCD are separated. But in
⁴²⁶ the final analysis, for simplicity, these two components are merged. These two approaches are equivalent.
⁴²⁷ The whole procedure is described in Section 5. This procedure takes into account the fact that fakes from
⁴²⁸ multi-jets behave differently due to the different ratio of quark-initiated jets over gluon-initiated jets. The
⁴²⁹ rest of the histograms are taken from simulation and they include cases with a true lepton and a true tau
⁴³⁰ or tau that is faked by an electron or a muon.

Not reviewed, for internal circulation only

431 4.4. Distributions of the key variables

432 Figures 2 to 4 show the data-MC comparison for the Top CR. Figures 5 and 6 show the events composition
 433 and the data-MC comparison of the important kinematics variables in the signal region b -veto channel.
 434 Figure 7 shows the final discriminating mass variable, m_T^{tot} , that is used to derive the final result of
 435 this search. Similar as b -veto channel, figures 8 and 9 show the events composition and the data-MC
 436 comparison of the important kinematics variables in the signal region b -tag channel. Figure 10 shows the
 437 final discriminating mass variable, m_T^{tot} , that is used to derive the final result of this search.

438 Generally, the data-MC agreement in these plots are good and the discrepancy is within the one-sigma
 439 error band. It is worth to notice that there is a negative slope in the Top CR. This trend also can be seen
 440 in the b -tag signal region where top events are enriched. The discrepancy is covered by the dedicated
 441 top systematic uncertainties described in Section 6.2. About 5-10% discrepancy is observed in the b -veto
 442 categories and is covered mainly by Fake systematics, described in Section 5.1.4 and 5.2, and $Z \rightarrow \tau\tau$
 443 related systematics: “LPX”, tau reco, ID and TES, as described in Section 6.

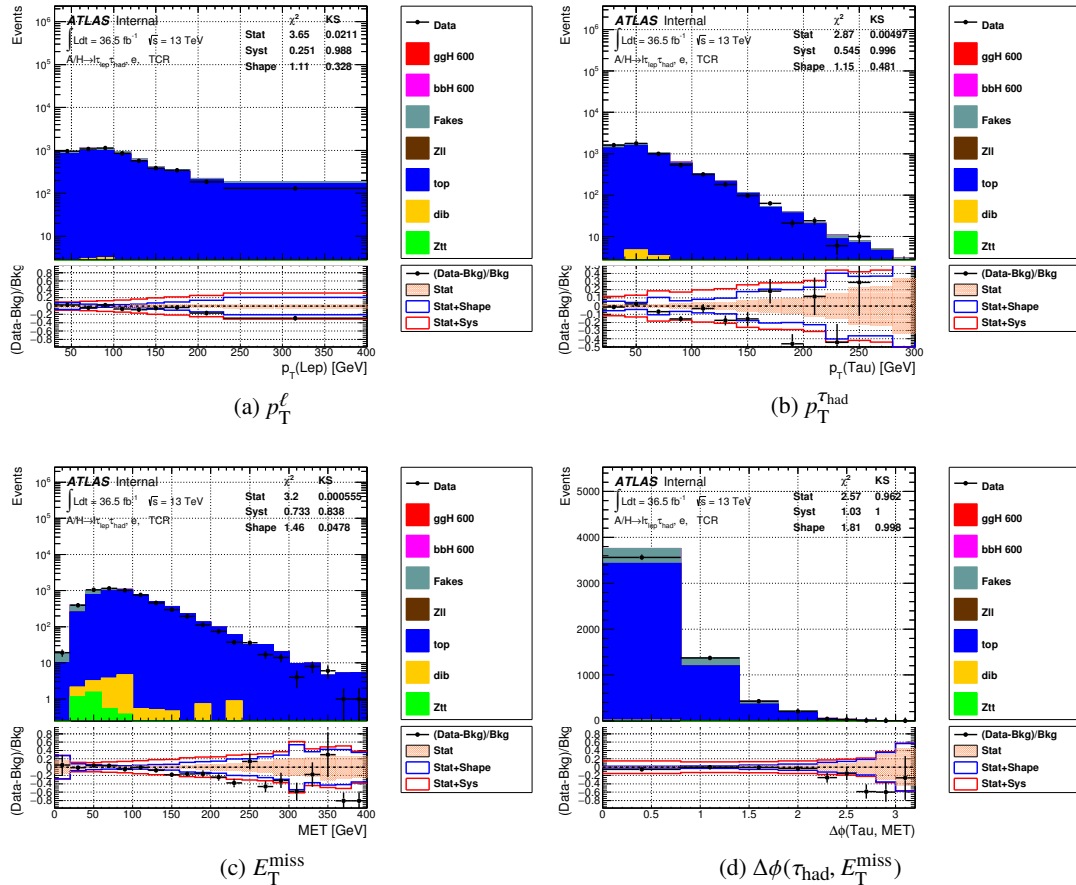


Figure 2: Electron channel variable distribution after the top CR full selection. Here, *fakes* only includes jet to tau fake from non-QCD multijet events. *qcd* includes jet to tau fake from QCD multijet events. The signals are normalized to 1 pb. “*qcd*” is estimated by using the lepton fake factor and tau fake factor described in Section 5.2.

Not reviewed, for internal circulation only

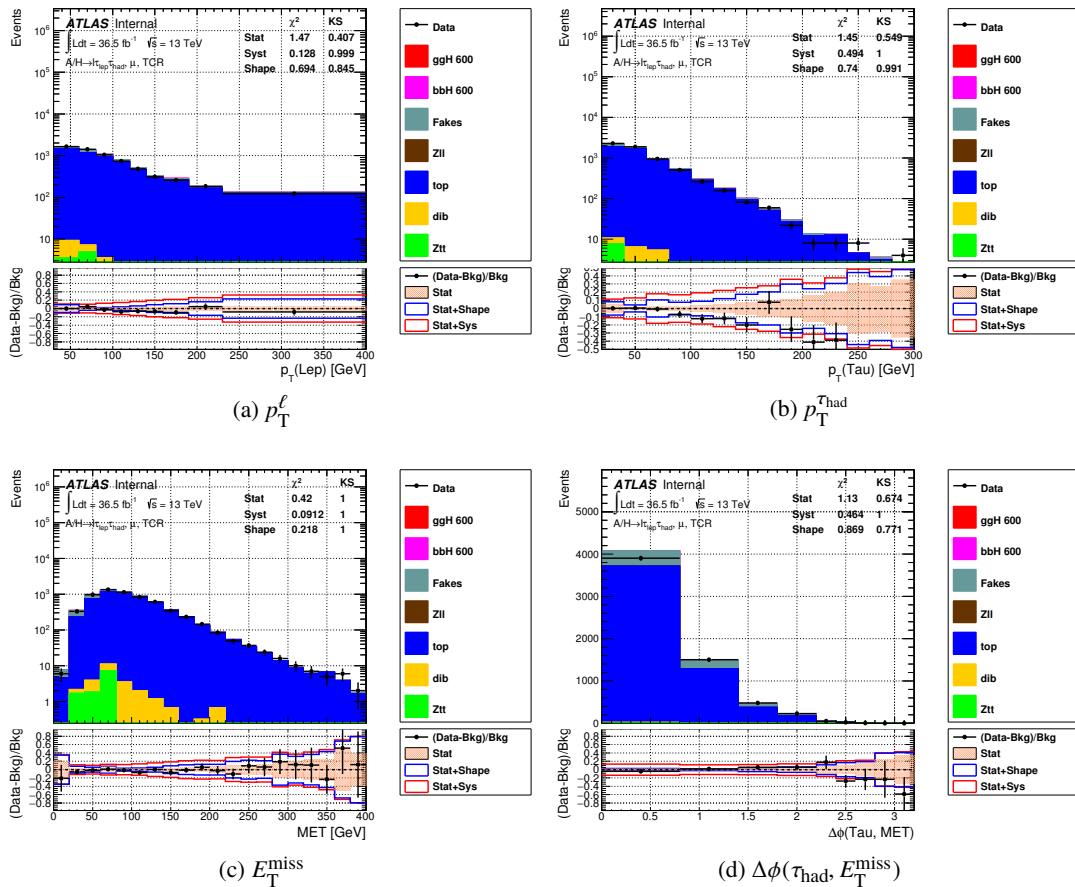


Figure 3: Muon channel variable distribution after the top CR full selection. Here, *fakes* only includes jet to tau fake from non-QCD multijet events. *qcd* includes jet to tau fake from QCD multijet events. The signals are normalized to 1 pb. “*qcd*” is estimated by using the lepton fake factor and tau fake factor described in Section 5.2.

Not reviewed, for internal circulation only

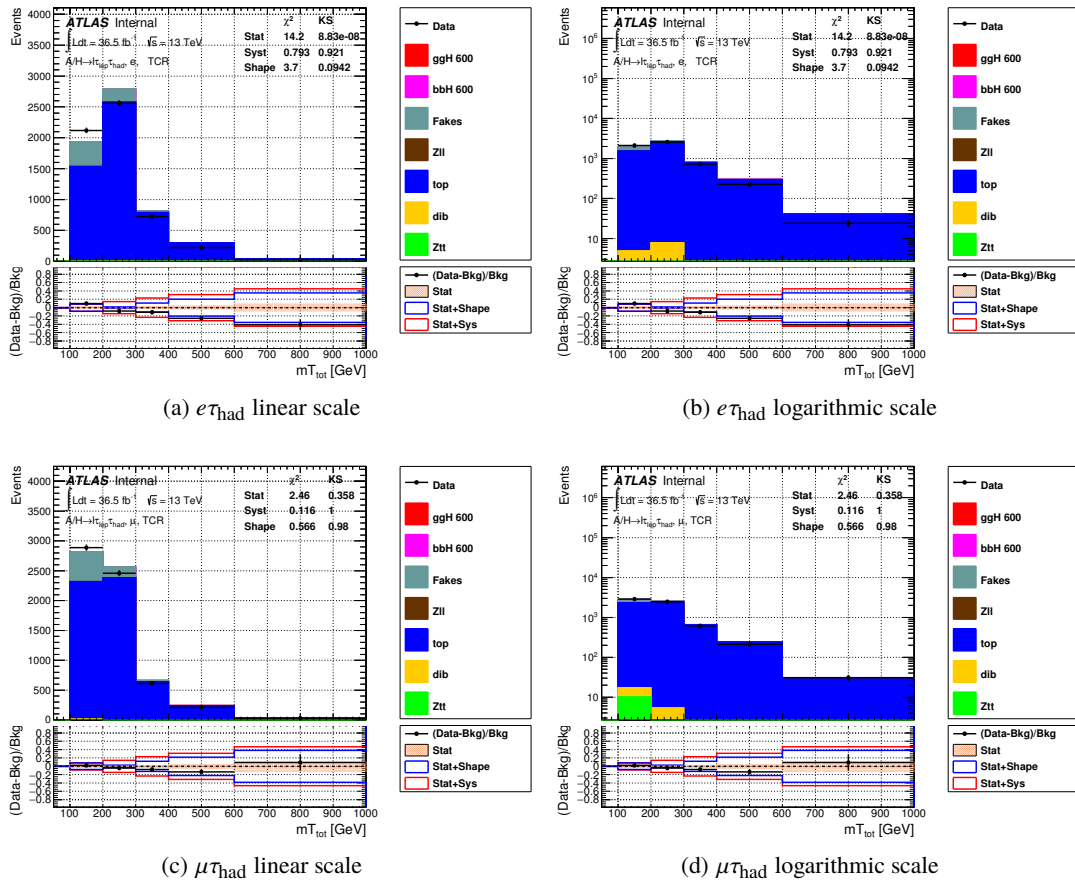


Figure 4: The final mass discriminant distribution: m_T^{tot} for electron (a,b) and muon (c,d) channel after the top CR full selection. Here, *fakes* only includes jet to tau fake from non-QCD multijet events. *qcd* includes jet to tau fake from QCD multijet events. The signals are normalized to 1 pb. “*qcd*” is estimated by using the lepton fake factor and tau fake factor described in Section 5.2.

Not reviewed, for internal circulation only

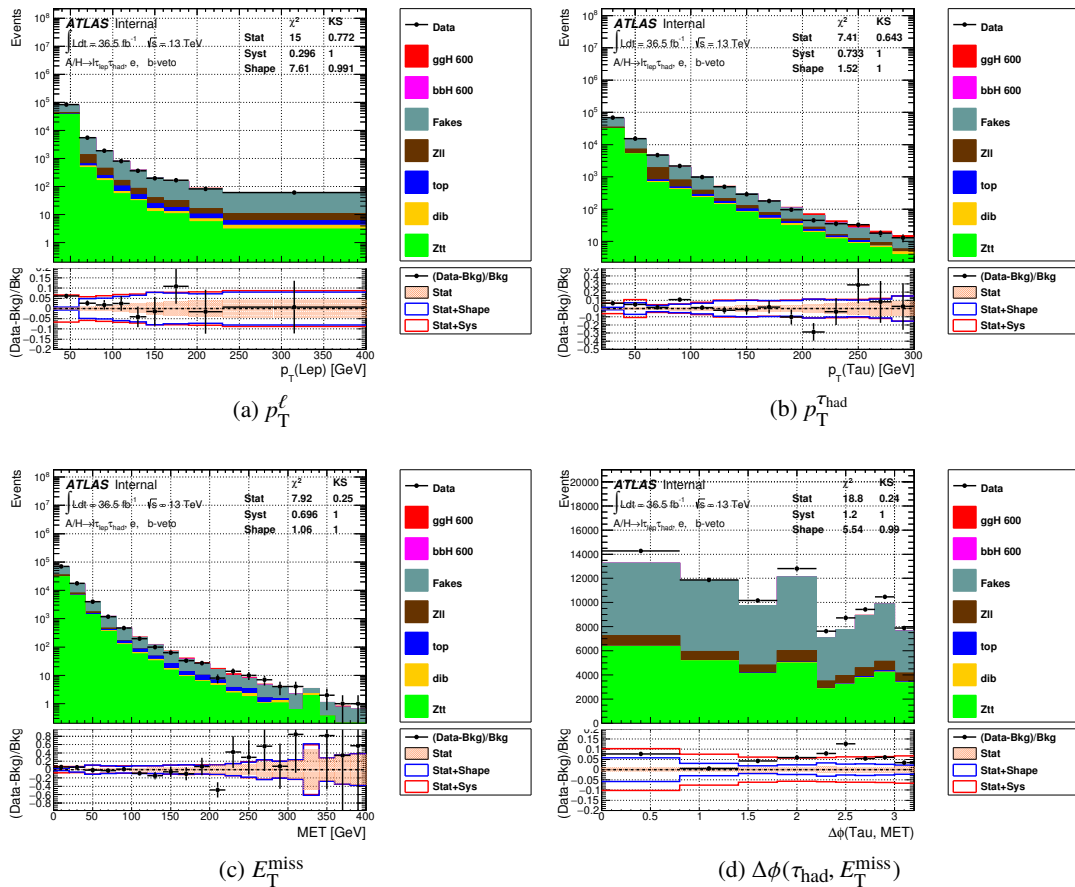


Figure 5: Electron channel variable distribution after the b-veto signal region full selection. Here, *fakes* only includes jet to tau fake from non-QCD multijet events. *qcd* includes jet to tau fake from QCD multijet events. The signals are normalized to 1 pb.

Not reviewed, for internal circulation only

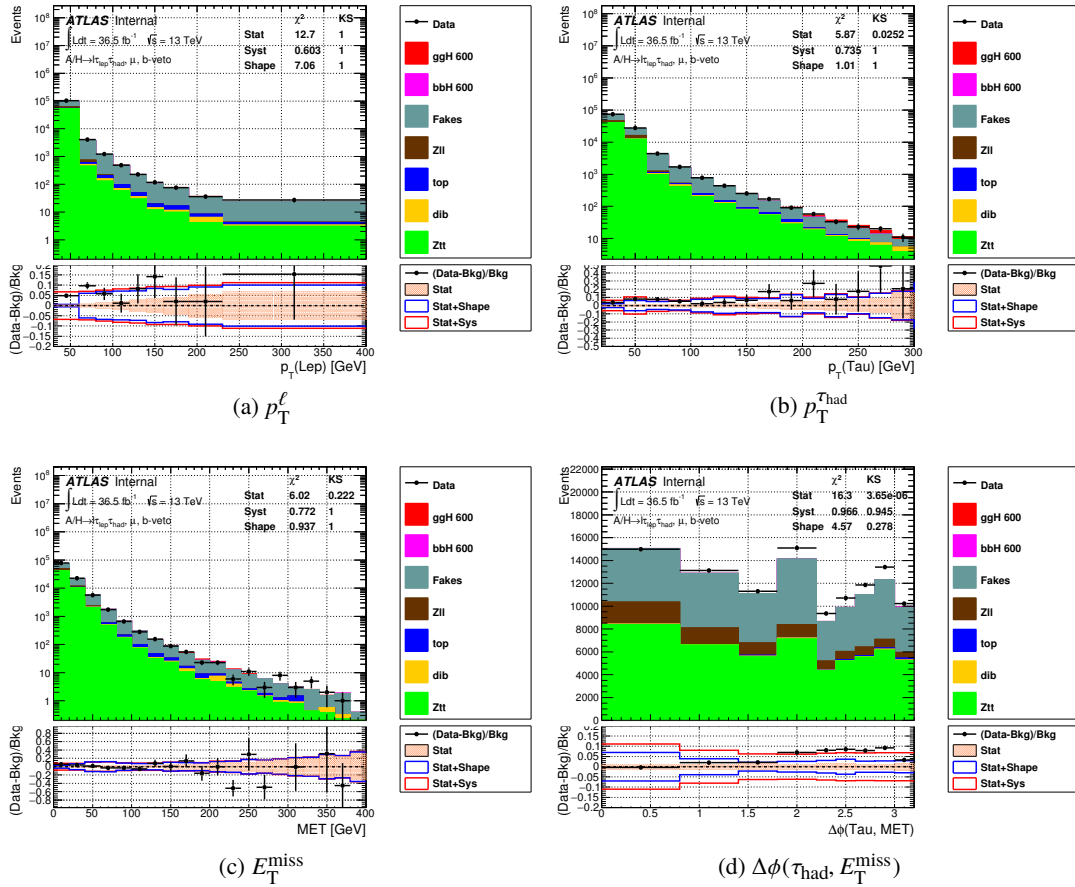


Figure 6: Muon channel variable distribution after the b-veto signal region full selection. Here, *fakes* only includes jet to tau fake from non-QCD multijet events. *qcd* includes jet to tau fake from QCD multijet events. The signals are normalized to 1 pb. “*qcd*” is estimated by using the lepton fake factor and tau fake factor described in Section 5.2.

Not reviewed, for internal circulation only

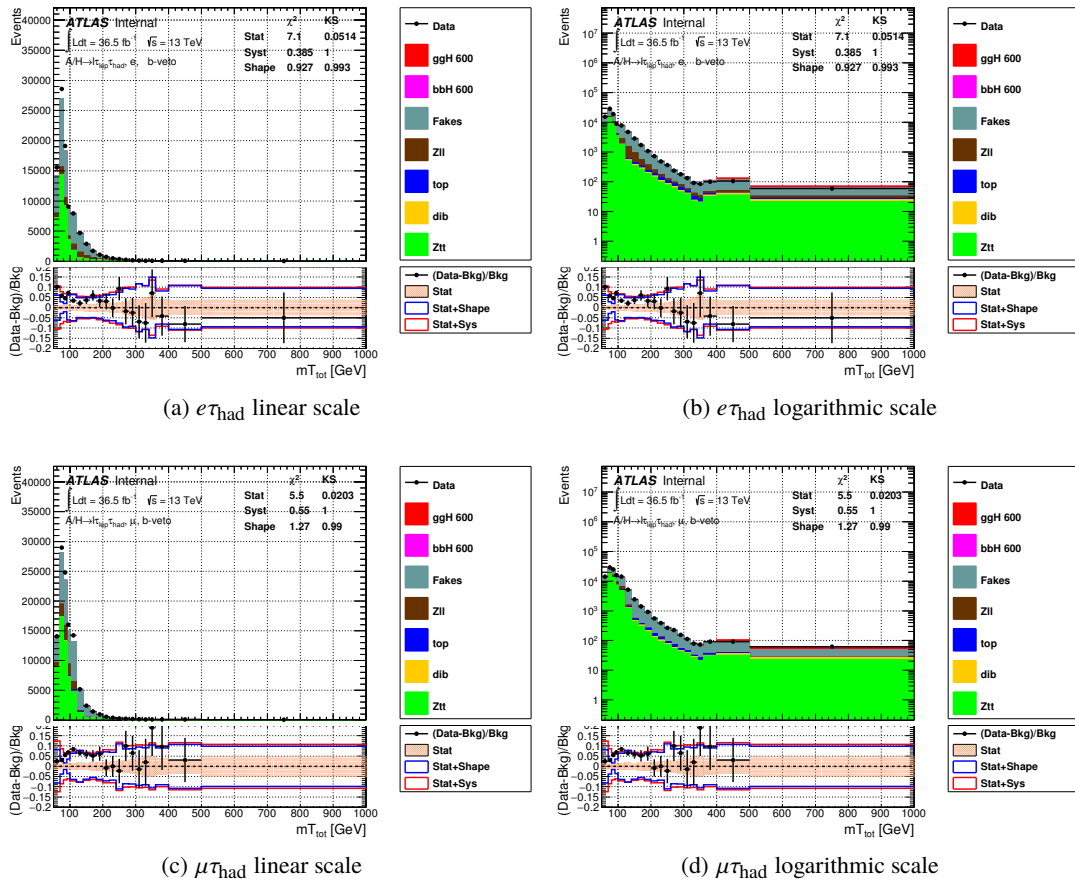


Figure 7: The final mass discriminant distribution: m_T^{tot} for electron (a,b) and muon (c,d) channel after the b-veto signal region full selection. Here, *fakes* only includes jet to tau fake from non-QCD multijet events. *qcd* includes jet to tau fake from QCD multijet events. The signals are normalized to 1 pb. “*qcd*” is estimated by using the lepton fake factor and tau fake factor described in Section 5.2.

Not reviewed, for internal circulation only

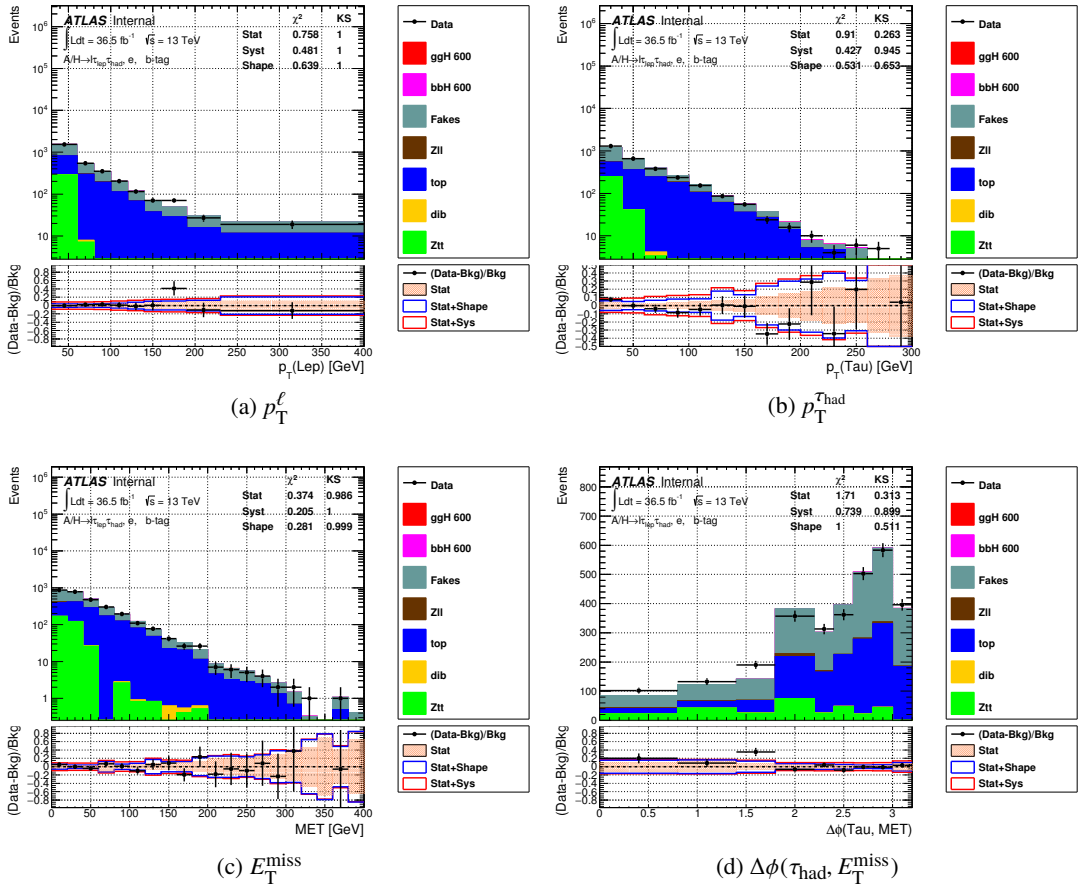


Figure 8: Electron channel variable distribution after the b-tag signal region full selection. Here, *fakes* only includes jet to tau fake from non-QCD multijet events. *qcd* includes jet to tau fake from QCD multijet events. The signals are normalized to 1 pb. “qcd” is estimated by using the lepton fake factor and tau fake factor described in Section 5.2.

Not reviewed, for internal circulation only

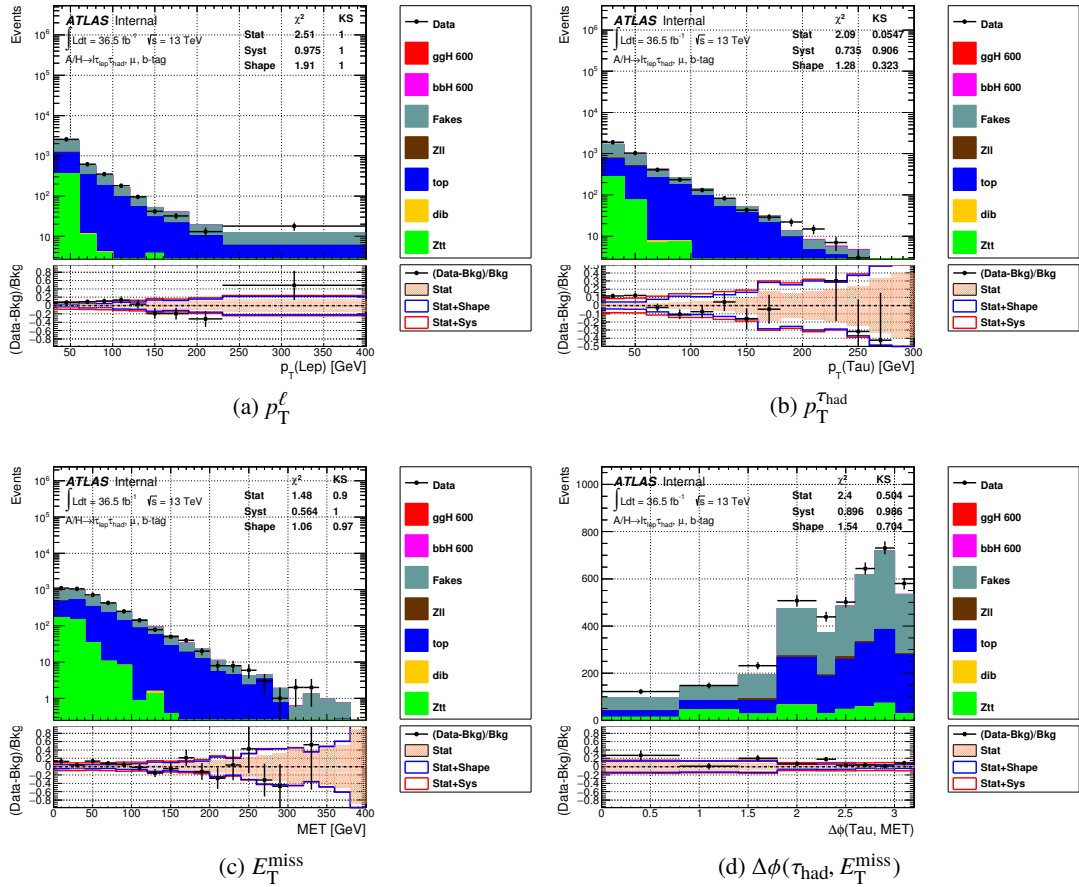


Figure 9: Muon channel variable distribution after the b-tag signal region full selection. Here, *fakes* only includes jet to tau fake from non-QCD multijet events. *qcd* includes jet to tau fake from QCD multijet events. The signals are normalized to 1 pb. “*qcd*” is estimated by using the lepton fake factor and tau fake factor described in Section 5.2.

Not reviewed, for internal circulation only

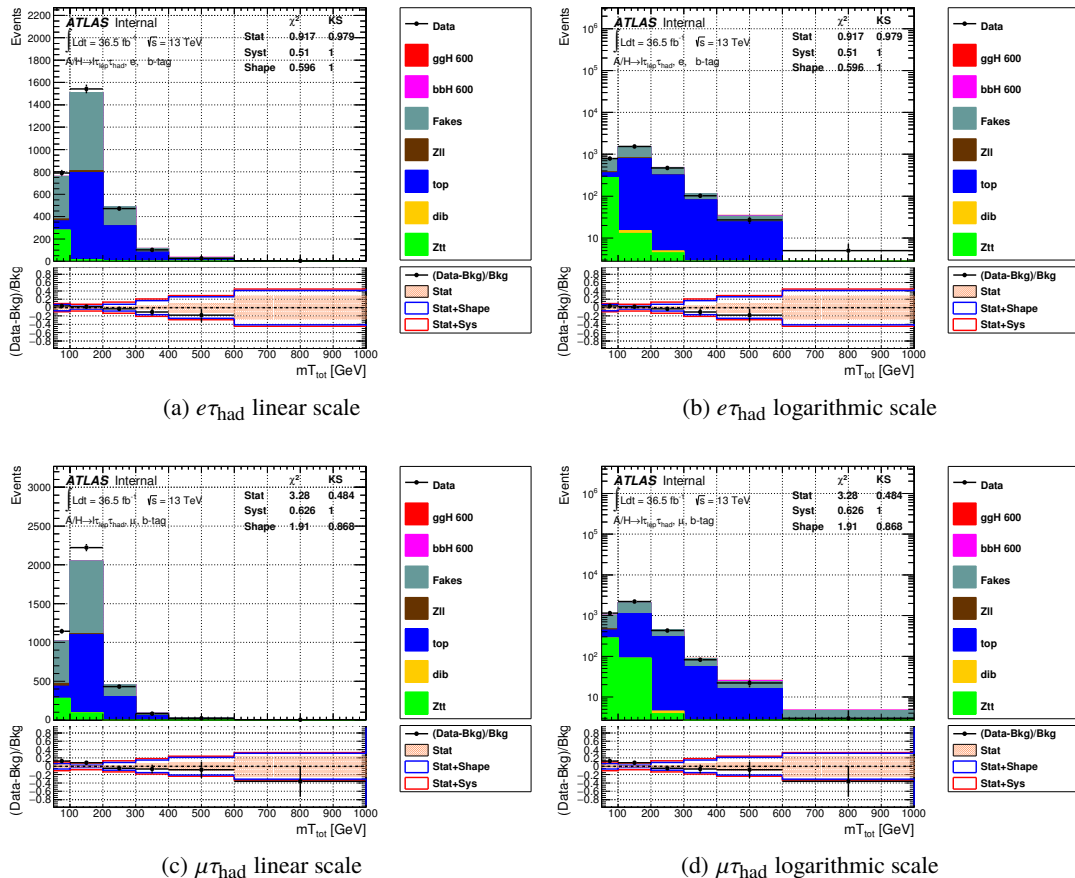


Figure 10: The final mass discriminant distribution: m_T^{tot} for electron (a,b) and muon (c,d) channel after the b-tag signal region full selection. Here, *fakes* only includes jet to tau fake from non-QCD multijet events. *qcd* includes jet to tau fake from QCD multijet events. The signals are normalized to 1 pb. “*qcd*” is estimated by using the lepton fake factor and tau fake factor described in Section 5.2.

Not reviewed, for internal circulation only

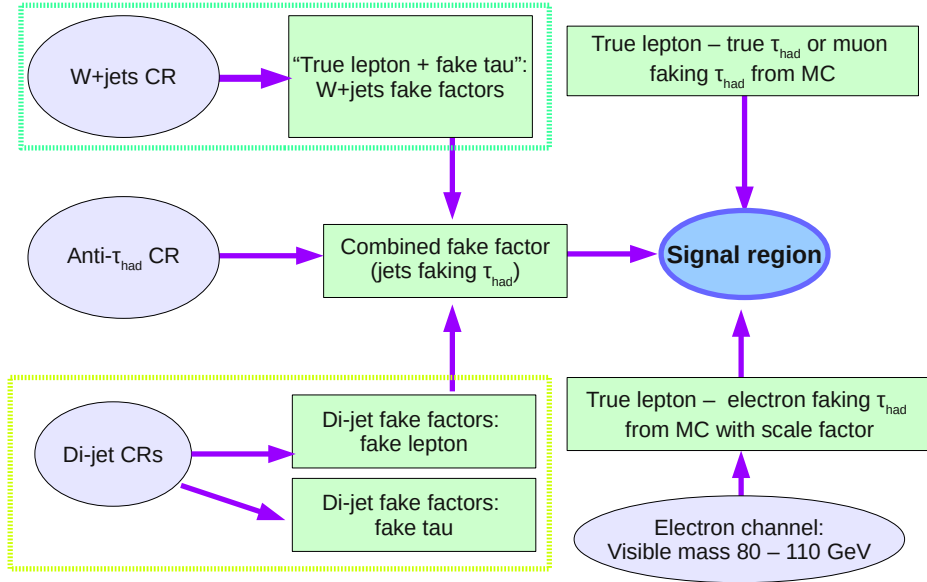


Figure 11: A schematic overview of the background estimation used in this analysis.

444 5. Background Estimation

445 The backgrounds can be separated into four categories, based on whether the lepton and/or τ_{had} are correctly
446 identified. An overview of the background estimation concept is shown schematically in Fig. 11.

447 In the first category, the lepton and τ_{had} candidates are a true lepton and a true τ_{had} . Events in this category
448 can originate from $Z/\gamma^* \rightarrow \tau\tau$, where one τ decays leptonically and the other hadronically, or from
449 Top events (e.g. $t\bar{t} \rightarrow W^-W^+ b\bar{b} \rightarrow \tau_{\text{had}}\ell\nu b\bar{b}$). In the second category, the τ_{had} is faked by a lepton,
450 whereas the lepton is genuine. The main source for this background is $Z/\gamma^* \rightarrow \ell\ell$ events. The above two
451 background sources are estimated from simulation, corrected by using the recommended data-driven scale
452 factors, from ATLAS tau working group, for reconstruction and identification efficiencies, as described
453 in Ref. [83]. The μ channel of the analysis has some contribution (about 4%) from events with muons
454 faking τ_{had} . With the current data statistics, these background events appear to be well-modeled and are
455 therefore taken from simulation.

456 In the third category, the lepton candidate is a true lepton, but the τ_{had} candidate originates from a quark
457 or gluon initiated jet. This background is dominated by W -jets processes in the b-veto category and Top
458 events in the b-tag category, with smaller contributions from Z/γ^*+j jets backgrounds. The last category
459 of background is the case where both lepton and τ_{had} candidates are quark or gluon initiated jets. This
460 background is dominated by multi-jet processes. The estimation method for each of these background
461 categories is described in the remaining of this section. The third and fourth categories are so called *Fakes*
462 which indicates the τ_{had} candidate originated from a quark or gluon initiated jet.

463 5.1. Background with correctly identified ℓ and jet misidentified as τ_{had}

464 In the b -veto category this background category is dominated by $W+\text{jets}$ events, where the W decays into
 465 the identified lepton and an additional jet is misidentified as the τ_{had} . However, in the b -tag category this
 466 background category also has a large amount of top events: $t\bar{t}$ and single top, where the W comes from a
 467 top quark decay or is produced in association with a top quark. The cut on $m_T(\ell, E_T^{\text{miss}}) < 40 \text{ GeV}$ targets
 468 the rejection of these processes.

469 Since the jet $\rightarrow \tau_{\text{had}}$ fake rate is not modeled well in Sherpa samples and the statistics of simulated samples
 470 is not enough, a data-driven “fake factor” method is used to estimate this background. In $W+\text{jets}$ events
 471 the jets that are misidentified as a τ_{had} are dominated by light-quark initiated jets. In top events, while
 472 light-quark initiated jets are still dominant, the fraction of b -quark initiated jets that are misidentified as a
 473 τ_{had} is significantly increased. The fake rate can be different for different jet flavour compositions.

474 The fake factor method is based on the following idea. A $W+\text{jets}$ control region (WCR) is defined,
 475 which contains $\ell\tau_{\text{had}}$ events with kinematics similar to the signal region. These events contain a τ_{had} that
 476 originates from a misidentified jet. From this set of fake τ_{had} objects the following ratio is calculated,
 477 referred in the following as the fake factor:

$$\text{FF}^{W+\text{jets}} = \frac{N(\text{pass “medium” tau ID})}{N(\text{fail “medium” tau ID and jet BDT score } > 0.35)}, \quad (1)$$

478 where the number in the nominator (denominator) is the number of events in which the selected τ_{had}
 479 candidates pass (fail) the “medium” τ_{had} identification criterion of the signal region. The fake factors are
 480 parametrized in $p_T(\tau_{\text{had}})$ and number of τ_{had} tracks, without separated into electron and muon channels.

481 The fake factors are subsequently used to derive an estimate of the background events with a true ℓ and a
 482 fake τ_{had} from another control region, so called “Anti- τ_{had} ” control region. It is defined to be the same as
 483 the signal region, except requiring the τ_{had} candidate to fail the “medium” τ_{had} identification criterion.

484 5.1.1. Definition of the $W+\text{jets}$ control region

485 The $W+\text{jets}$ control region is defined by the same selection as the signal region except:

- 486 • Leading $p_T \tau_{\text{had}}$ candidate with $\text{BDT}(\tau_{\text{had}} \text{ ID}) > 0.35$;
- 487 • $60 < m_T(\ell, E_T^{\text{miss}}) < 150 \text{ GeV}$ in the muon channel;
- 488 • $70 < m_T(\ell, E_T^{\text{miss}}) < 150 \text{ GeV}$ in the electron channel;

489 The lower cut on $\text{BDT}(\tau_{\text{had}} \text{ ID})$ of the τ_{had} candidate is applied in order to remove those jets far from
 490 signal region and with very different kinematic properties from signal region. The low end of m_T cut in
 491 the electron channel is higher to reduce QCD contamination. The high end of m_T cut is to reduce the top
 492 backgrounds with true τ_{had} which dominate at high m_T . This control region, when it is used in the b -veto
 493 category, includes also the b -veto requirement and it includes b -tag requirement when it is used in the
 494 b -tag category.

495 Figure 12 show some basic distributions of the $W+\text{jets}$ control region. Contributions of each physics
 496 process are presented. jet $\rightarrow \tau_{\text{had}}$ fakes from electroweak and top processes are modeled with MC
 497 simulation. Large disagreement between data and MC prediction in events where the τ_{had} passes medium

Not reviewed, for internal circulation only

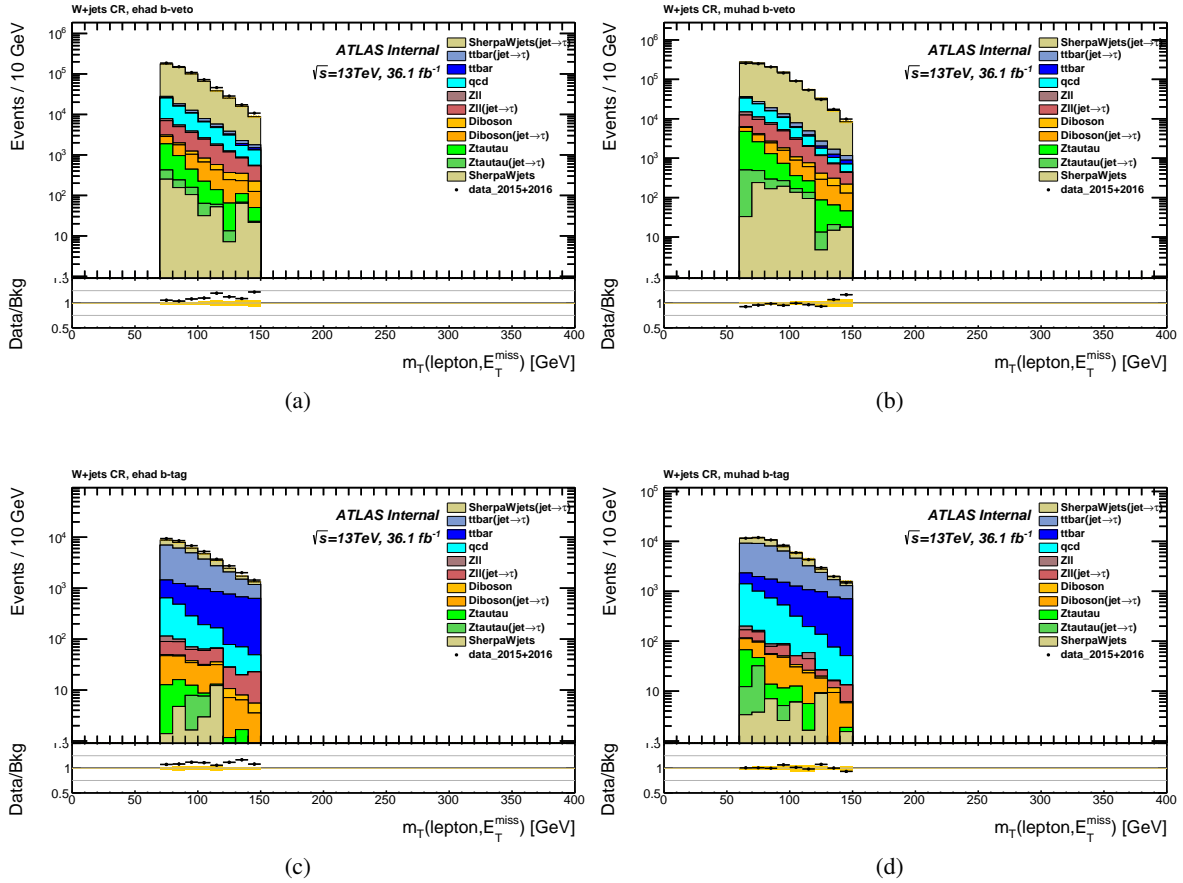


Figure 12: $m_T(\ell, E_T^{\text{miss}})$ distribution of the $W+\text{jets}$ control region, before any τ_{had} identification requirement, after the m_T cut with the b -veto requirement in (a) electron and (b) muon channel, and the b -tag requirement in (c) electron and (d) muon channel. The error band contains only the statistical uncertainty. Here, the components in the legend without jet $\rightarrow \tau$ are with the tau candidate from the generated tau or lepton fake. “qcd” is estimated by using the lepton fake factor and tau fake factor described in Section 5.2.

identification criterion, Figure 13, shows that one can not use simulation for the fake τ_{had} but a data-driven estimation is needed.

5.1.2. Calculation of the $W+\text{jets}$ jet $\rightarrow \tau$ tau fake factor

- The fake factors are calculated from Eq. (1) using leading τ_{had} candidates in the $W+\text{jets}$ control region events. Backgrounds from true ℓ and τ_{had} , as well as leptons faking τ_{had} , are subtracted using simulation. Multi-jet contribution is subtracted using the data-driven lepton fake factor method, as described in Section 5.2.4. Note that since QCD contribution is estimated from events where jets fake leptons, the selected lepton in the simulated event has to be truth matched to a true lepton.
- The distribution used in calculating the fake factors are shown in Appendix F.8. The fake factors for 1 and 3 prong τ_{had} candidates as a function of $p_T(\tau_{\text{had}})$ are shown in Figs. 14 (a) and (b). The fake factors

Not reviewed, for internal circulation only

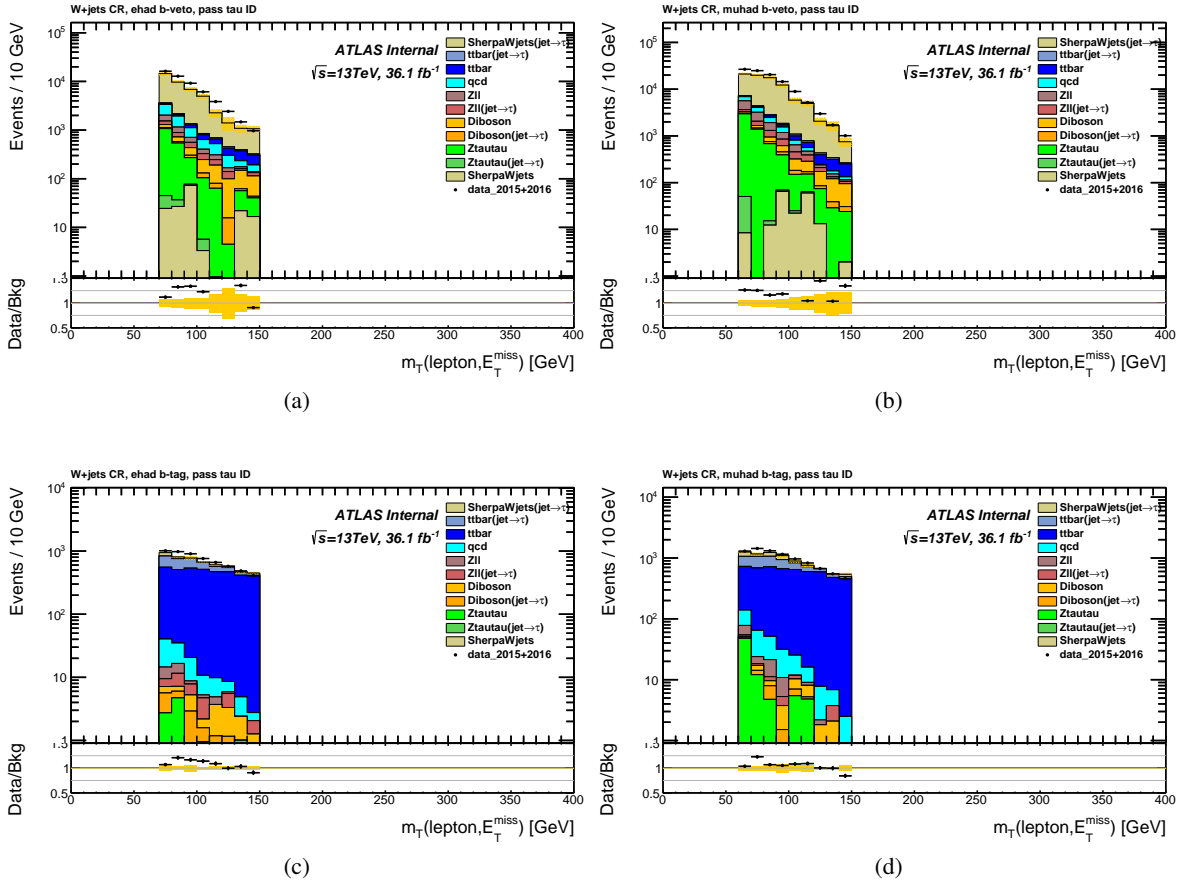


Figure 13: $m_T(\ell, E_T^{\text{miss}})$ distribution of events that pass “medium” τ_{had} identification requirement in the $W+\text{jets}$ control region after the m_T cut with the b -veto requirement in (a) electron and (b) muon channel, and the b -tag requirement in (c) electron and (d) muon channel. The error band contains only the statistical uncertainty. Here, the components in the legend without jet $\rightarrow\tau$ are with the tau candidate from the generated tau or lepton fake. “qcd” is estimated by using the lepton fake factor and tau fake factor described in Section 5.2.

508 for the combined electron and muon channels are used, since there is no significant difference observed
509 between the factors measured in the two channels, as shown in figure 86 in appendix F.3.

510 As discussed, the fake factors can be different in the b -tag and b -veto categories due to a different jet
511 composition. However, after requiring at least 1 b -tagged jet and subtracting huge true background
512 contamination, the statistical uncertainty is too large to describe any shape effect. Figure 15 shows the
513 comparison of the fake factor between b -veto and b -tag categories. Except the first bin, the difference
514 is overwhelmed by the huge uncertainty in the b -tag category. In this case, the fake factor from the
515 b -veto category is used to describe the shape and a normalization correction factor is derived for the b -tag
516 category as a ratio of fake factors without binning in p_T . The b -tag correction factor for 1-prong (3-prong)
517 tau is 0.80 ± 0.10 (0.66 ± 0.17) as half of the correction is assigned as systematics.

518 Due to limited sample statistics, the fake factors are only parametrized as a function of $p_T(\tau_{\text{had}})$ and the
519 number of core tracks. To evaluate the modeling of other important variables, a closure test is performed
520 by applying the fake factors to the control region where the factors are derived. Indeed, several variables,

Not reviewed, for internal circulation only

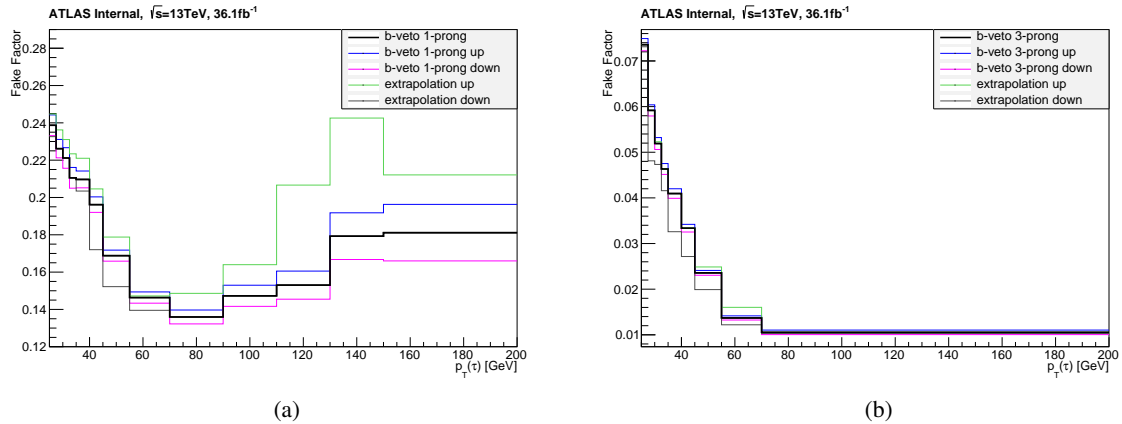


Figure 14: Fake factors from the $W+jets$ control region (with b -veto requirement) as a function of $p_T(\tau_{\text{had}})$ calculated for (a) 1-prong and (b) 3-prong τ_{had} candidates. Thin blue lines include statistical, MC subtraction and QCD background errors while extrapolation uncertainties are explained in Section 5.1.4. All systematics are added together in quadrature for up and down variations, respectively.

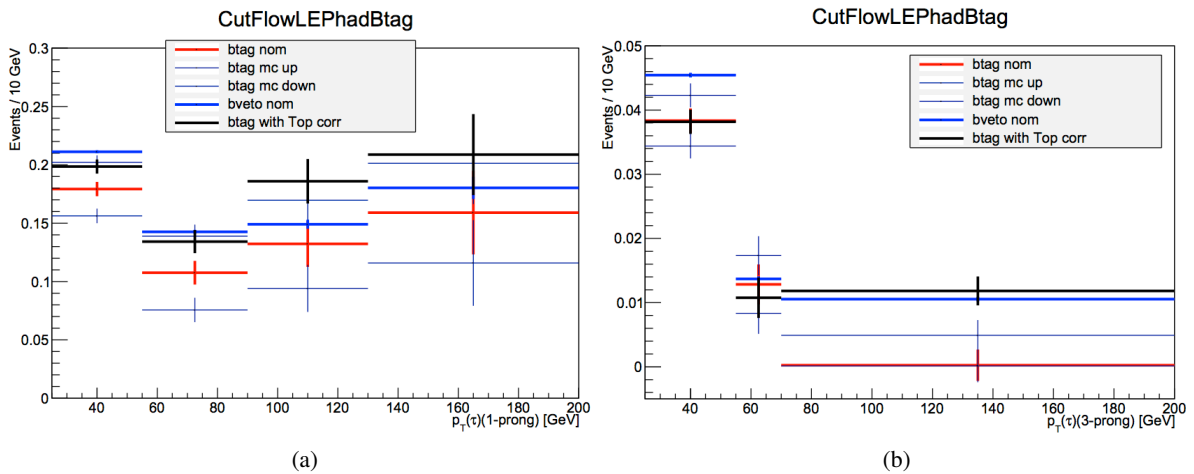


Figure 15: Comparison of Fake factors in b -veto region and that in b -tagged region with various MC subtracted background systematics: (a) 1-prong and (b) 3-prong τ_{had} candidates.

521 e.g. $\Delta\phi(\tau, E_T^{\text{miss}})$, are found to be not modeled well, as shown in figure 16. It is found that a sequential
522 reweighting on $\Delta\phi(\tau, E_T^{\text{miss}})$ distribution after applying the fake factor can improve the modeling in the
523 validation regions.

524 Therefore, the data over background ratio as a function of $\Delta\phi(\tau, E_T^{\text{miss}})$ in Figure 16 is taken as a correction
525 to the fake factors. Dedicated corrections are derived for different $p_T(\tau_{\text{had}})$ range, as shown in Fig. 17. The
526 associated uncertainty estimated by comparing the difference between the correction of nearby p_T slices
527 is 30% of the correction. For example, in Figure 17 (a), at $\Delta\phi(\tau, E_T^{\text{miss}}) = 0$, the correction is about 1.1,
528 so the assigned uncertainty will be 0.03. The b -tag category does not show significant non-closure on
529 the $\Delta\phi(\tau, E_T^{\text{miss}})$ distribution in both control region and validation region. So, the $\Delta\phi(\tau, E_T^{\text{miss}})$ correction
530 is not applied in the b -tagged category but the same amount of systematics is applied as in the b -veto

Not reviewed, for internal circulation only

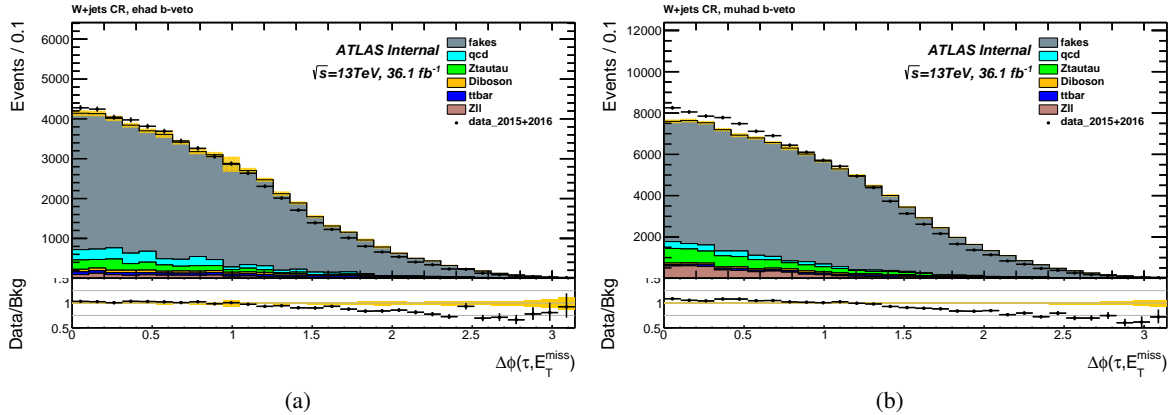


Figure 16: Closure test on $\Delta\phi(\tau, E_T^{\text{miss}})$ in $W+\text{jets}$ control region. Here, the fake background is modeled using the fake factors derived from $W+\text{jets}$ control region and parameterized in $p_T(\tau_{\text{had}})$ and the number of core tracks.

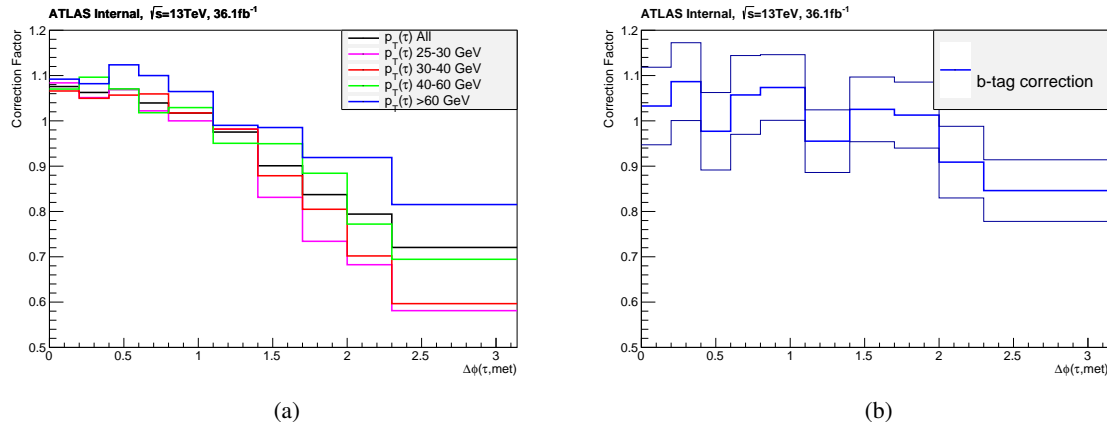


Figure 17: Correction values (a), in different $p_T(\tau_{\text{had}})$ slices, that are multiplied to the $W+\text{jets}$ fake factors as a function of $\Delta\phi(\tau, E_T^{\text{miss}})$ calculated without split into different prongs and lepton flavor, since no significant difference is found between channels, as shown in the internal note of the previous analysis. The non-closure of $\Delta\phi(\tau, E_T^{\text{miss}})$ distribution (b) with b-tagged jets only show deviation from one in the last two bins where the statistical uncertainty is large. Here, the light blue is the nominal correction while the two grey histograms are the up/down statistical uncertainty variations.

531 category.

532 5.1.3. Fake factor validation

533 Figures 18 and 19 show the data-background comparison on the $m_T(\ell, E_T^{\text{miss}})$ distributions where the jet
 534 to tau fake is modeled with the fake factor method. The “qcd” component in these plots is estimated by
 535 using the lepton fake factor and tau fake factor described in Section 5.2. Furthermore, a validation region
 536 for jet to tau fake modeling is defined by requiring $40 < m_T(\ell, E_T^{\text{miss}}) < 60(70)$ GeV for muon(electron)
 537 channel, as shown in Figs. 20–25. The data-background agreement is generally good in all distributions,

Not reviewed, for internal circulation only

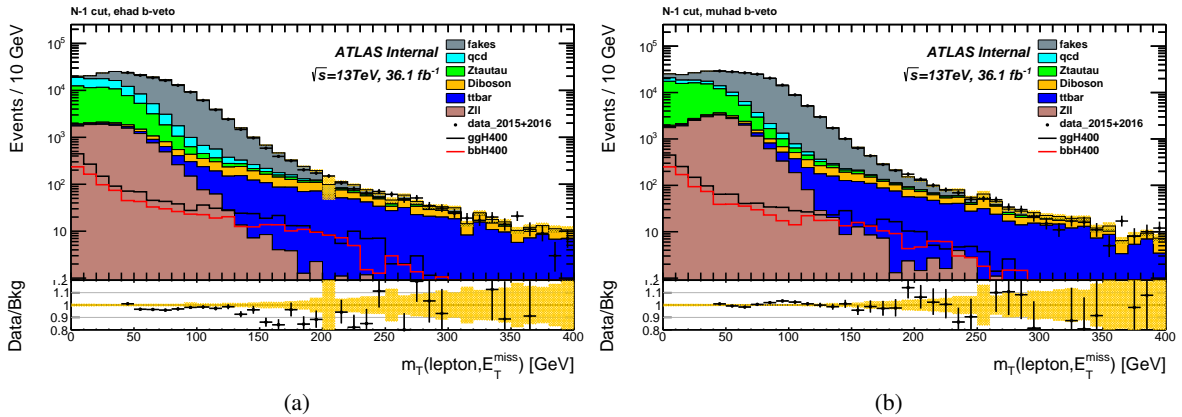


Figure 18: Transverse mass, $m_T(\ell, E_T^{\text{miss}})$ distributions before $m_T(\ell, E_T^{\text{miss}})$ cut in the b -veto (left) electron and (right) muon channel. Note: the data in the signal region $m_T(\ell, E_T^{\text{miss}}) < 40$ GeV are blinded. Backgrounds estimated from MC samples are truth matched.

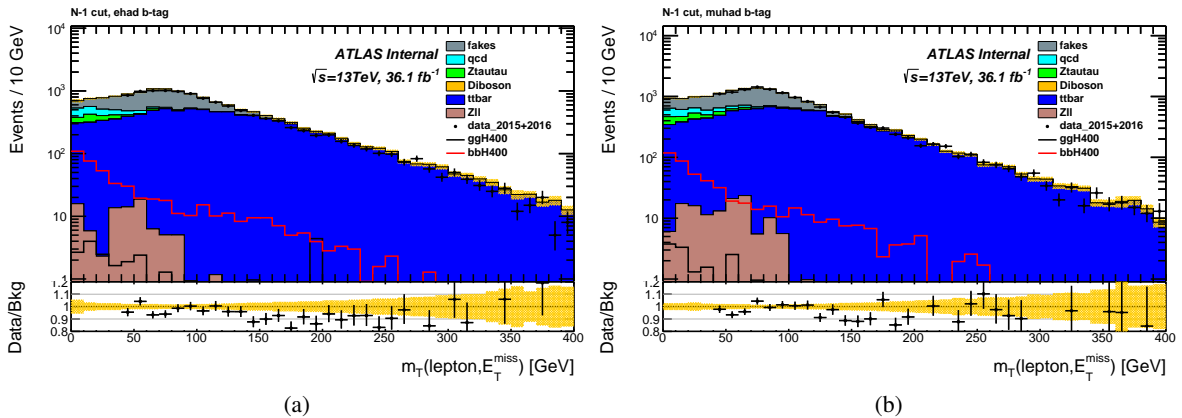


Figure 19: Transverse mass, $m_T(\ell, E_T^{\text{miss}})$, distributions before $m_T(\ell, E_T^{\text{miss}})$ cut in the b -tag (left) electron and (right) muon channel. Note: the data in the signal region $m_T(\ell, E_T^{\text{miss}}) < 40$ GeV are blinded. Backgrounds estimated from MC samples are truth matched.

538 but some discrepancies are observed in the key distributions, e.g. m_T^{tot} , $p_T(\tau_{\text{had}})$, etc. Hence, the residual
 539 discrepancy in the b -veto tau p_T distribution, as shown in Figure 22, is taken as a systematics for the fake
 540 factors to cover the potential mis-modeling due to the extrapolation from the control regions to the signal
 541 region. Technically, the electron and muon channels are checked separately and the maximum up or down
 542 deviation are taken as up or down systematics variation, respectively. The systematics effect is shown in
 543 Figure 14.

544 5.1.4. Systematic uncertainties in the $W + \text{jets}$ tau fake factors

545 The following systematic uncertainties are studied in order to cover the potential uncertainties of the
 546 method.

Not reviewed, for internal circulation only

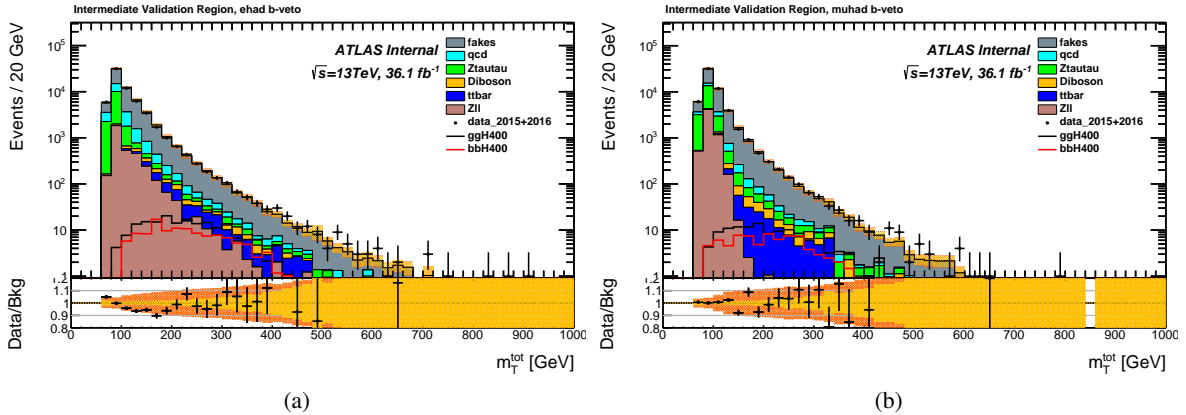


Figure 20: m_T^{tot} distributions in the b -veto (left) electron and (right) muon channel with requiring $40 < m_T(\ell, E_T^{\text{miss}}) < 60(70)$ GeV for muon(electron) channel. Backgrounds estimated from MC samples are truth matched.

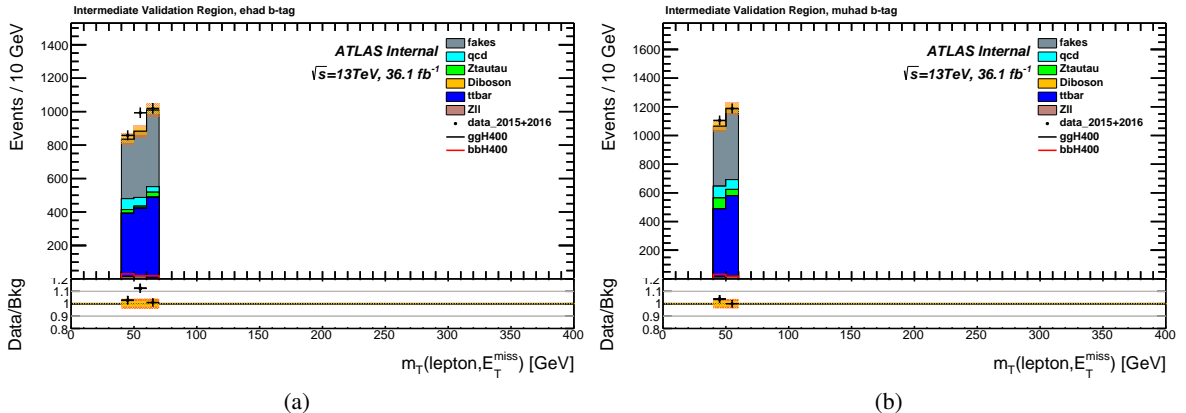


Figure 21: m_T^{tot} distributions in the b -tag (left) electron and (right) muon channel with requiring $40 < m_T(\ell, E_T^{\text{miss}}) < 60(70)$ GeV for muon(electron) channel. Backgrounds estimated from MC samples are truth matched. Figures 154 shows the x-axis zoomed in plot.

547 1. Contamination from other backgrounds

548 Fake factors have been derived in the high $m_T(\ell, E_T^{\text{miss}})$ region with additional requirements to enrich
 549 $W+jets$ (b -veto) events and top (b -tag) events. As shown in Fig. 12, backgrounds in the $W+jets$ control
 550 region that come from events with a true lepton and a true τ_{had} or a true lepton and a τ_{had} faked by a lepton
 551 are estimated purely with MC samples. Multi-jet background with the lepton faked by a jet is estimated
 552 with the lepton fake factor method. In addition, there are backgrounds with a τ_{had} faked by a jet that
 553 may come from $Z+jets$, diboson and top production. MC simulation shows that in b -veto category this
 554 contamination amounts to up to 5% of total $W+jets$ events. In the b -tag category top processes dominate
 555 and therefore the fake factors measured in this region are actually more to describe the jet to tau fake in
 556 the top events. In general, the fake factors measured are suitable for that particular mixture of events from
 557 different processes and quark or gluon initiated jets.

558 The true background assumes a 10% uncertainty in its subtraction from the data. This 10% value is

Not reviewed, for internal circulation only

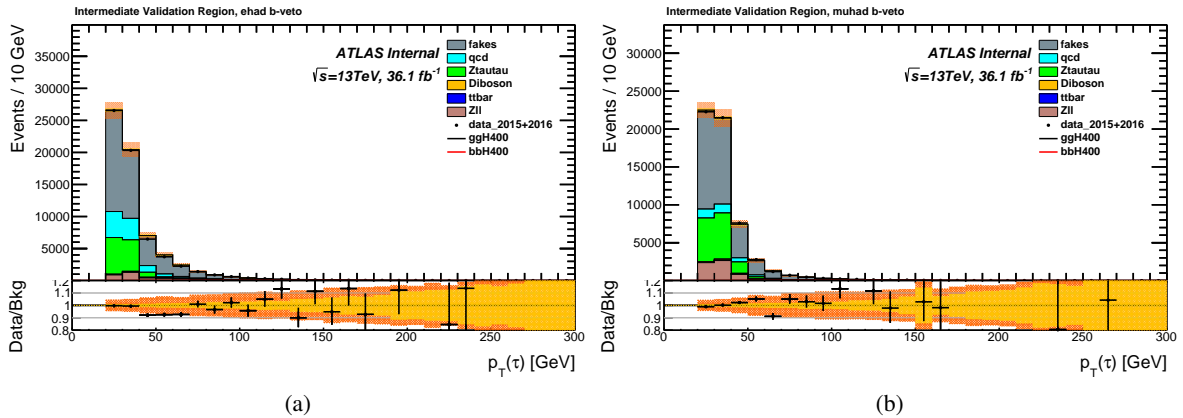


Figure 22: $p_T(\tau_{\text{had}})$ distributions in the b -veto (left) electron and (right) muon channel with requiring $40 < m_T(\ell, E_T^{\text{miss}}) < 60(70)$ GeV for muon(electron) channel. Backgrounds estimated from MC samples are truth matched. Figures 155 shows the x-axis zoomed in plot.

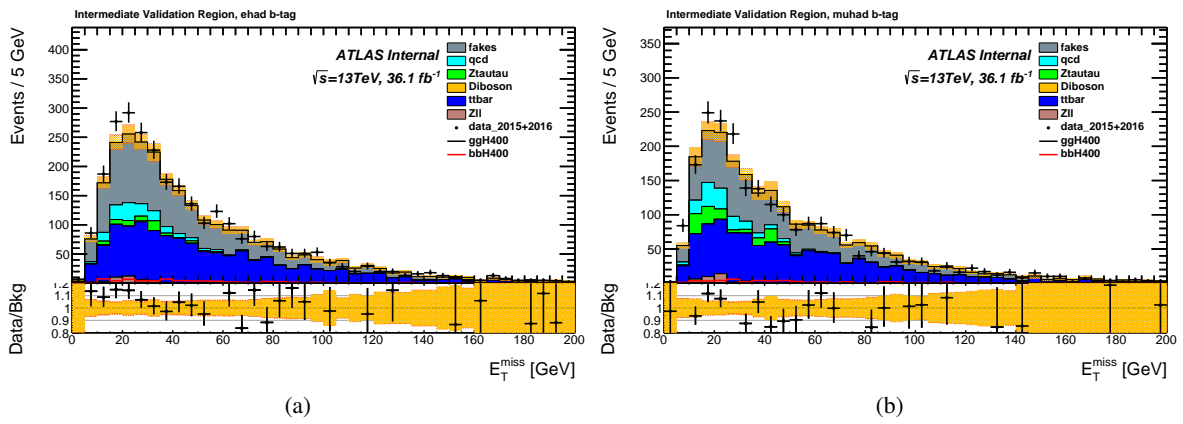


Figure 23: $p_T(\tau_{\text{had}})$ distributions in the b -tag (left) electron and (right) muon channel with requiring $40 < m_T(\ell, E_T^{\text{miss}}) < 60(70)$ GeV for muon(electron) channel. Backgrounds estimated from MC samples are truth matched.

Not reviewed, for internal circulation only

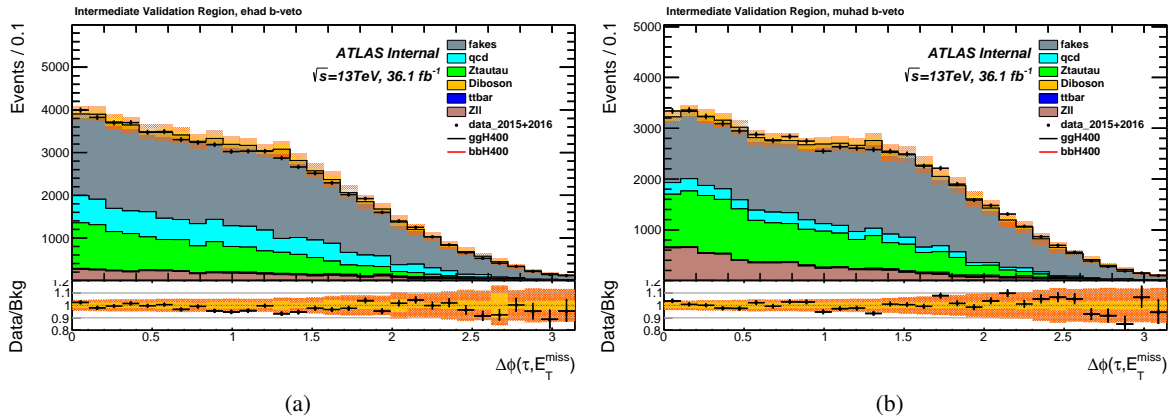


Figure 24: $\Delta\phi(\tau, E_T^{\text{miss}})$ distributions in the b -veto (left) electron and (right) muon channel with requiring $40 < m_T(\ell, E_T^{\text{miss}}) < 60(70)$ GeV for muon(electron) channel. Backgrounds estimated from MC samples are truth matched.

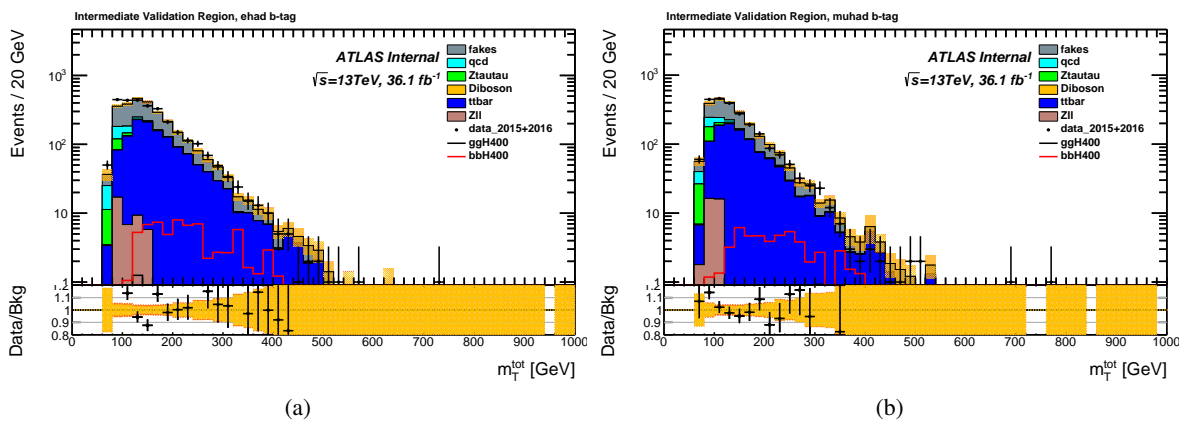


Figure 25: $\Delta\phi(\tau, E_T^{\text{miss}})$ distributions in the b -tag (left) electron and (right) muon channel with requiring $40 < m_T(\ell, E_T^{\text{miss}}) < 60(70)$ GeV for muon(electron) channel. Backgrounds estimated from MC samples are truth matched.

estimated conservatively according to the theoretical cross section precision and the precision of the in-situ measurements on electron, muon and τ_{had} performance at ATLAS. Note: this systematics is not correlated with the theoretical cross section uncertainties, described in Section 6.2. Uncertainty on the multi-jet contamination is estimated as described in Section 5.2 and is taken into account when subtracting this background from the data. The uncertainties due to the backgrounds with true tau, e.g. $Z/\gamma^* \rightarrow \tau\tau$ and $t\bar{t}$, are not significant in b -veto category. The uncertainties due to the true background and multi-jet background are added in quadrature and the total amount is about 2-3%. For the Top background, some non-negligible discrepancies are found in the Top CR, as shown in Figures 2 and 3. So, according the discrepancy found in Top CR, a reweighting is applied to the b -tag $W+\text{jets}$ CR to estimate the impact on the b -tag FF correction. In the end, half of the b -tag FF correction is assigned as the systematics.

More details on the background composition of the b -veto and b -tag $W+\text{jets}$ control regions can be found in Tables 5-6. The label "truth-matched" includes both true τ_{had} and τ_{had} faked by a lepton. The label "fakes" include all that are not truth matched.

2. Uncertainty on the $\Delta\phi(\tau, E_T^{\text{miss}})$ correction

30% of the $\Delta\phi(\tau, E_T^{\text{miss}})$ correction, i.e. $0.3 \times (\text{SF}_{\Delta\phi(\tau, E_T^{\text{miss}})} - 1)$, is taken as the systematics uncertainty, which is motivated by the difference between the correction functions from the nearby p_T slices, as shown in Figure 17.

3. Extrapolation from high to low m_T

The control region definition assumes that the fake factors calculated in the high- $m_T(\ell, E_T^{\text{miss}})$ region can be used as they are for the low- $m_T(\ell, E_T^{\text{miss}})$ signal region. This assumption is tested in the Intermediate control region which is in between SR and WCR, $40 < m_T(\ell, E_T^{\text{miss}}) < 60(70)$ GeV for muon(electron) channel, as shown in Figure 18. Disagreement between data and model in $p_T(\tau_{\text{had}})$ distribution, as shown in Figure 22 is taken as a systematic uncertainty of the $W+\text{jets}$ fake factors. This systematics is designed to cover any sample dependence of fake factors between signal regions and control regions and is consistent with a MC test, as shown in Figure 87.

Conclusion

The total uncertainty on the $W+\text{jets}$ fake factor is in the range from 2 to 15% below 100 GeV and up to 25% above 100 GeV, for the 1-prong τ_{had} and 2–20% for the 3-prong τ_{had} , depending on the τ_{had} p_T . Finally, the uncertainty of the $\Delta\phi(\tau, E_T^{\text{miss}})$ correction is about 3–10%.

5.2. Background with jets misidentified as ℓ and τ_{had}

5.2.1. Introduction

This section describes the data-driven methods that are used for the estimation of the multi-jet background, and how they are incorporated into the overall estimation of the backgrounds with jets misidentified as τ_{had} . The three subsections describe the method:

1. Section 5.2.2 describes the measurement of τ_{had} fake factors in a multi-jet control region. These fake factors are used in the combined fake factor method, described in Section 5.3.
2. In the combined fake factor method (Section 5.3), τ_{had} fake factors are applied to the Anti- τ_{had} region. In order to take into account the correct mixture of multi-jet and $W+\text{jets}$ events, a data-driven method using lepton fake factors, described in Section 5.2.4, is used to predict the total multi-jet contribution to the Anti- τ_{had} region.

Table 5: $W+jets$ b-veto control region composition for 1-prong and 3-prong τ_{had} . The numbers correspond to an integrated luminosity of 36.1 fb^{-1} . The quoted uncertainties only contain the statistical uncertainty .

	1-prong τ_{had}							
channel	$e\tau_{had}$				$\mu\tau_{had}$			
tau ID	pass		fail		pass		fail	
	fake	truth-matched	fake	truth-matched	fake	truth-matched	fake	truth-matched
$Z \rightarrow \tau\tau$	24 ± 7	1405 ± 69	123 ± 19	483 ± 42	54 ± 10	4000 ± 110	378 ± 37	1459 ± 76
$Z \rightarrow \ell\ell$	584 ± 28	1024 ± 38	4462 ± 74	647 ± 33	1391 ± 66	4340 ± 110	8970 ± 150	978 ± 53
Diboson	141 ± 7	639 ± 14	1110 ± 23	183 ± 8	269 ± 11	890 ± 15	1872 ± 28	231 ± 7
Top	352 ± 13	764 ± 17	2530 ± 32	270 ± 10	635 ± 17	1063 ± 21	4266 ± 41	414 ± 13
$W+jets$	23500 ± 1500	-	165000 ± 3800	-	49700 ± 2300	-	329100 ± 5800	-
QCD	2169 ± 28	-	15420 ± 190	-	2934 ± 19	-	20960 ± 130	-
Data	40410		202034		81625		356687	

	3-prong τ_{had}							
channel	$e\tau_{had}$				$\mu\tau_{had}$			
tau ID	pass		fail		pass		fail	
	fake	truth-matched	fake	true τ_{had}	fake	true τ_{had}	fake	true τ_{had}
$Z \rightarrow \tau\tau$	10 ± 5	419 ± 37	184 ± 22	338 ± 40	9 ± 7	1291 ± 67	518 ± 44	1101 ± 69
$Z \rightarrow \ell\ell$	122 ± 17	35 ± 7	7820 ± 100	328 ± 21	257 ± 29	22 ± 6	12720 ± 180	164 ± 26
Diboson	47 ± 6	203 ± 8	2079 ± 33	178 ± 8	92 ± 7	266 ± 8	3423 ± 42	240 ± 8
Top	86 ± 6	267 ± 10	5865 ± 48	354 ± 11	200 ± 9	344 ± 12	9832 ± 62	522 ± 13
$W+jets$	8150 ± 890	-	292300 ± 51000	-	16300 ± 1300	-	577600 ± 7800	-
QCD	540 ± 7	-	18710 ± 220	-	792 ± 6	-	30510 ± 150	-
Data	12078		357962		24919		596405	

Not reviewed, for internal circulation only

Table 6: $W+jets$ b-tag control region composition for 1-prong and 3-prong τ_{had} . The numbers correspond to an integrated luminosity of 36.1 fb^{-1} . The quoted uncertainties only contain the statistical uncertainty .

	1-prong τ_{had}							
channel	$e\tau_{had}$				$\mu\tau_{had}$			
tau ID	pass		fail		pass		fail	
	fake	truth-matched	fake	truth-matched	fake	truth-matched	fake	truth-matched
$Z \rightarrow \tau\tau$	0 ± 0	5 ± 2	9 ± 5	7 ± 7	0 ± 0	77 ± 20	9 ± 5	5 ± 5
$Z \rightarrow \ell\ell$	10 ± 3	12 ± 3	74 ± 9	18 ± 5	10 ± 4	47 ± 10	77 ± 14	21 ± 10
Diboson	6 ± 2	9 ± 2	46 ± 6	2 ± 1	9 ± 2	11 ± 2	72 ± 5	2 ± 1
Top	872 ± 20	2557 ± 34	6600 ± 53	872 ± 20	1392 ± 24	3590 ± 38	10514 ± 65	1217 ± 22
$W+jets$	155 ± 70	-	2590 ± 320	-	550 ± 150	-	4130 ± 440	-
QCD	46 ± 3	-	435 ± 26	-	168 ± 3	-	1620 ± 25	-
Data	4364		11458		6532		17292	

	3-prong τ_{had}							
channel	$e\tau_{had}$				$\mu\tau_{had}$			
tau ID	pass		fail		pass		fail	
	fake	truth-matched	fake	truth-matched	fake	truth-matched	inclusive	fail truth-matched
$Z \rightarrow \tau\tau$	0 ± 0	5 ± 4	1 ± 4	18 ± 12	0 ± 0	4 ± 4	46 ± 39	10 ± 5
$Z \rightarrow \ell\ell$	3 ± 2	1 ± 1	115 ± 13	15 ± 8	1 ± 1	0 ± 0	125 ± 17	0 ± 0
Diboson	2 ± 1	2 ± 1	82 ± 6	4 ± 2	3 ± 1	5 ± 1	138 ± 7	3 ± 1
Top	222 ± 11	883 ± 19	12963 ± 74	956 ± 20	357 ± 13	1207 ± 22	19885 ± 90	1269 ± 22
$W+jets$	111 ± 36	-	4450 ± 350	-	244 ± 76	-	7760 ± 650	-
QCD	12 ± 1	-	641 ± 31	-	45 ± 1	-	2344 ± 30	-
Data	1393		22292		2137		33308	

599 3. Section 5.2.5 describes how the result from Section 5.2.4 provides the fraction of multi-jet events
600 in the Anti- τ_{had} control region.

601 The background estimation methods used for the b -tag and b -veto categories are the same, though separate
602 values of fake factors and multi-jet fractions are calculated for the different signal region categories.

603 **5.2.2. Multi-jet jet $\rightarrow\tau$ tau fake factor estimation**

604 It is known that the jet to τ_{had} fake rate depends significantly on the quark/gluon fraction of the jets.
 605 The $W+\text{jets}$ events are mostly composed of light quark jets. The jets from multi-jet processes are more
 606 gluon-initiated jets though, which tend to have lower fake rates to τ_{had} with respect to quark-initiated jets.
 607 Hence, the multi-jet fake factors are expected to be smaller than the $W+\text{jets}$ control region fake factors
 608 previously estimated. Since the background of the signal region is expected to include both $W+\text{jets}$ and
 609 multi-jet events, it is important to take both possible sources of background into account in the combined
 610 fake factor method (Section 5.3). For this purpose, τ_{had} fake factors are measured in a multi-jet control
 611 region.

612 The fake factors are measured in a region that is the same as the signal region, except that the isolation
 613 cut for the electron or muon in the event is inverted. This provides an event sample with a high purity of
 614 QCD multi-jet events. Then, the fake factor is defined the same as in equation 1.

615 These fake factors are parameterized in the number of prongs in the τ decay (one or three) and the p_T of
 616 the τ . Since the lepton isolation requirement of the lepton trigger was looser in 2015 than that in 2016,
 617 the fraction of 2015 data in the anti-isolated region will be higher than it in the isolated signal region. Due
 618 to the different pileup condition between 2015 and 2016, which leads to the different fake factor, it will
 619 cause a potential bias on the total fake background estimation. In such a case, the separated QCD tau fake
 620 factor are derived and shown in Figures 26 and 27.

621 The systematic uncertainties that are considered for the fake factor measurement are:

- 622 • Uncertainty on the subtraction of simulated events with true τ_{had} , by varying the subtraction by 50%.
 623 Events with true τ_{had} contribute at a very low level to the anti-isolated region where the fake factors
 624 are measured. The QCD jet fake control region uses the anti-isolated lepton which is understood as
 625 well as the region with the isolated lepton. Moreover, the simulated events are also used to model
 626 the jet $\rightarrow\tau$ fake. That is why 50% variation is applied, instead of 10% in $W+\text{jets}$ control region.
- 627 • The QCD τ fake factor is measured in a region with inverted isolation cuts on the leptons. A
 628 systematic is considered to take into account whether the inverted lepton isolation cut biases the τ
 629 fake factors. In order to test this, a control region with a tau and lepton of same sign charge and an
 630 isolated lepton is defined. The differences between the fake factors measured in this region and in
 631 the nominal control region are taken as a systematic uncertainty.
- 632 • Another closure test is performed in an alternative QCD MJ enriched control region with same
 633 selection except requiring same charge sign (SS).

634 The total uncertainty is determined that a combined uncertainty of 20% on the nominal fake factor
 635 histogram is conservative enough to cover 68% of the population of measurements listed in Figures 26
 636 and 27. More details on systematics uncertainty estimation for QCD jet to tau fake factor are shown in
 637 appendix F.1.

Not reviewed, for internal circulation only

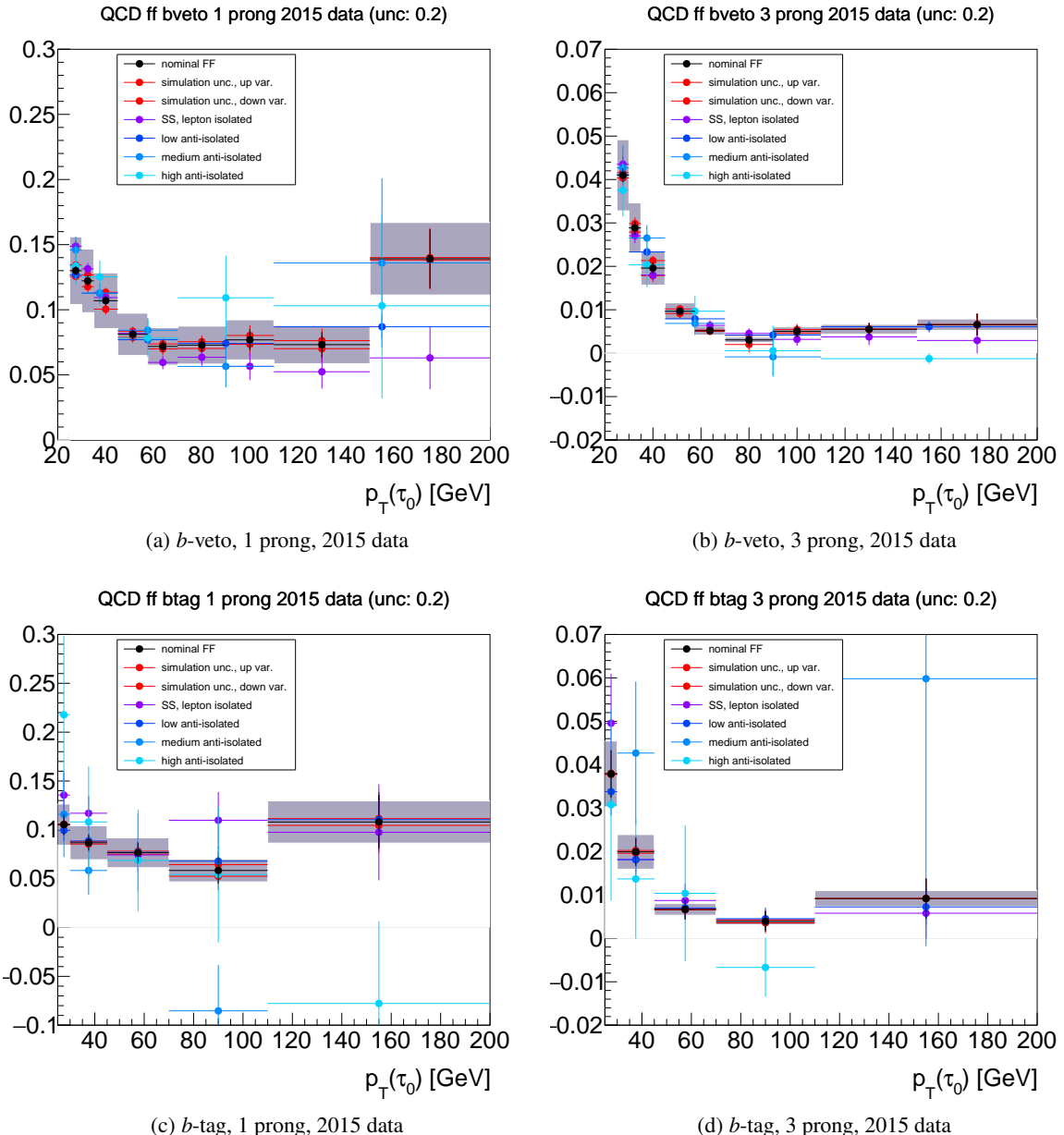


Figure 26: Nominal multi-jet τ_{had} fake factor histograms and variations for the 2015 data taking period. The uncertainty band shown corresponds to a combined uncertainty of 20% on the nominal histogram. In the plots, “simulation unc., up/down var.” are the systematics variations due to the simulated background subtraction; “SS, lepton isolated” is FF from the same sign charged region; “low/medium/high anti-isolated” are FFs from different isolation requirement.

Not reviewed, for internal circulation only

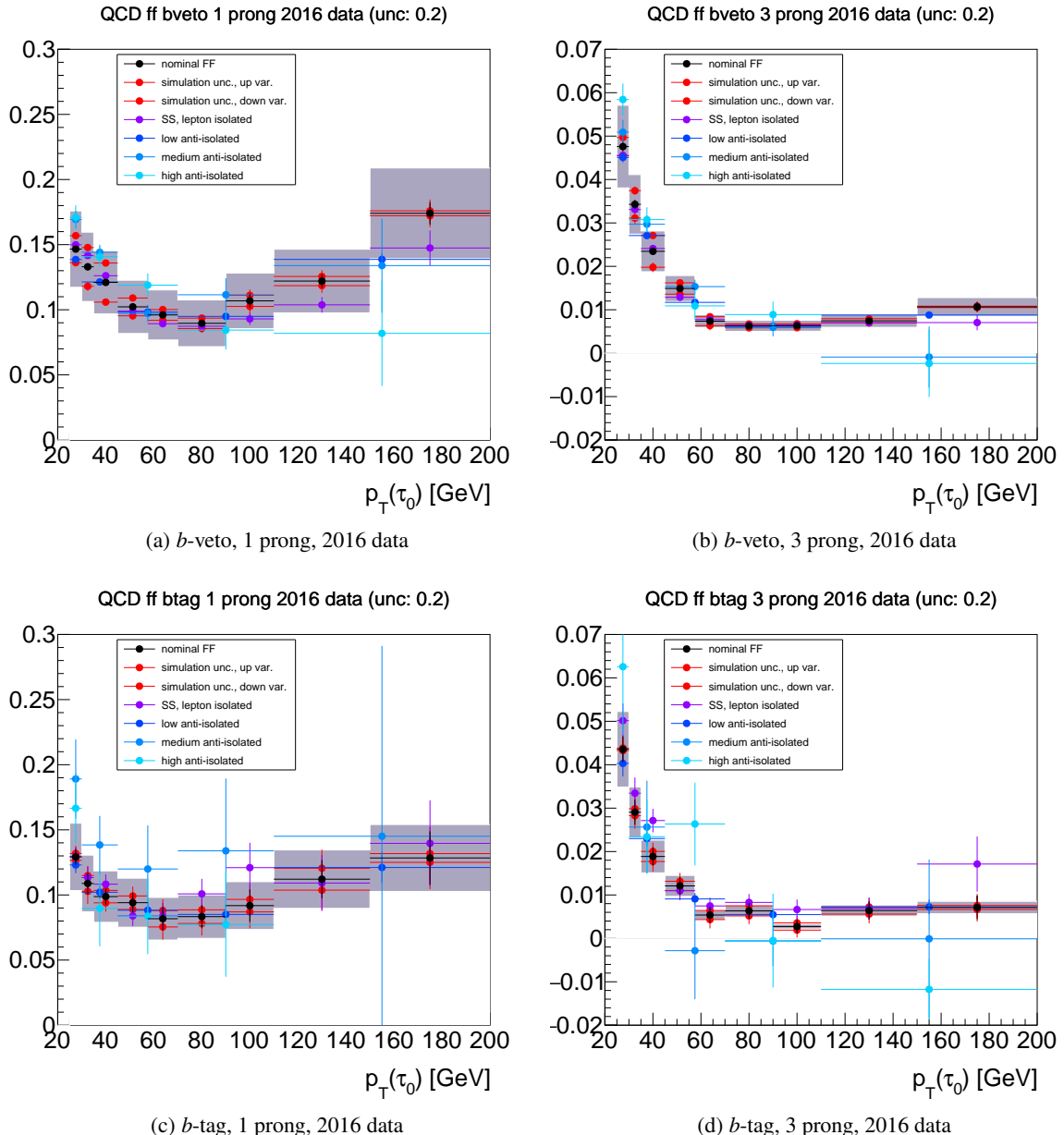


Figure 27: Nominal multi-jet τ_{had} fake factor histograms and variations for the 2016 data taking period. The uncertainty band shown corresponds to a combined uncertainty of 20% on the nominal histogram. In the plots, “simulation unc., up/down var.” are the systematics variations due to the simulated background subtraction; “SS, lepton isolated” is FF from the same sign charged region; “low/medium/high anti-isolated” are FFs from different isolation requirement.

638 **5.2.3. $\Delta\Phi(\tau, E_T^{\text{miss}})$ correction on QCD tau fake factor**

639 Like $W+\text{jets}$ FF, since the fake factor is parameterized only on τp_T due to the limited statistics, it could
 640 lead to some imperfectness in modeling some other variables. A closure test is performed by applying the
 641 fake factor back to the same region where it has been derived. Figure 28 shows the ratio of events passing
 642 Tau identification to those anti-tau region with applying the fake factor for the $\Delta\Phi(\tau, E_T^{\text{miss}})$ distribution.
 643 From Fig.28, the b -veto low p_T shows a significant trend and the rest are consistent with 1 within the
 644 statistical uncertainty. In this analysis, the ratio curve of b -veto low p_T is used as the correction and is
 645 applied to the b -veto low p_T events, and half of the correction is assigned as systematics. The b -veto
 646 high p_T and b -tag events have no correction but are assigned half of the b -veto low p_T correction as
 647 systematics.

Not reviewed, for internal circulation only

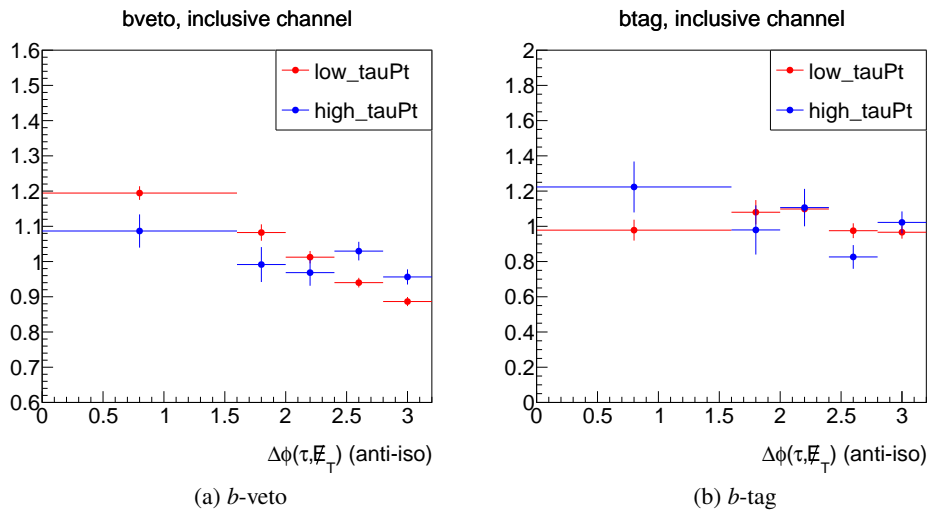


Figure 28: $\Delta\Phi(\tau, E_T^{\text{miss}})$ distribution ratio plots of events passing Tau identification to those anti-tau region with applying the fake factor: (a) b -veto, (b) b -tag. Here, the high τp_T means p_T higher than 60 GeV while the low τp_T means p_T lower than 60 GeV.

648 5.2.4. Multi-jet jet→ l lepton fake factor estimation

649 The primary source of background with jets misidentified as both the lepton and τ_{had} of the event is multi-jet
 650 events. Since the misidentification probabilities of jets from multi-jets being identified as leptons and τ_{had}
 651 are not modelled well in simulation, data-driven methods must be used to estimate this background. An
 652 additional complication arises from the extremely large cross sections and small event selection acceptance
 653 for multi-jet events. It is impossible to simulate a sufficient number of events to model this background
 654 adequately, so the data-driven estimation method is performed using data. The methodology described
 655 here to estimate this background is similar to that of the previous section, and is similarly referred to as a
 656 lepton “fake factor” method.

657 For this lepton fake factor method, a fake lepton control region is defined, which contains events with jets
 658 misidentified as leptons. Since the low $E_{\text{T}}^{\text{miss}}$ region is poorly modeled in simulation, a cut on $E_{\text{T}}^{\text{miss}}$ can
 659 not be used to reduce contribution from $W+\text{jets}$ events. Instead, a cut on $m_{\text{T}}(\ell, E_{\text{T}}^{\text{miss}})$ and number of jets
 660 is used for both electron and muon channels. Also, it is found that the lepton fake factors have a strong
 661 dependence on the b -tagged jet multiplicity in the region, so the factors are split into b -tag and b -veto
 662 regions, as in the signal region. The event selection is defined as:

- 663 • a single lepton trigger
- 664 • exactly one lepton, no offline isolation required
- 665 • at least one (two) selected jets for the b -veto (b -tag) categories
- 666 • no selected loose τ_{had}
- 667 • $m_{\text{T}}(\ell, E_{\text{T}}^{\text{miss}}) < 30 \text{ GeV}$

668 The event selection is designed to reduce the contamination of true leptons in the numerator of the lepton
 669 fake factor without dramatically reducing the number of events, and to bring the selection of the control
 670 region close to that of the signal region. The cut on the transverse mass primarily reduces the large $W+\text{jets}$
 671 background, while also shifting the control region closer to the selection of the final signal region. The
 672 requirement of at least one selected jet (in addition to the b -tagged jet of the b -tag region) also rejects true
 673 lepton background in favor of di-jet events and brings the control region close to the signal region. The
 674 contributions of various backgrounds to this control region are shown in Table 7.

Table 7: Events in the fake lepton region. The numbers correspond to an integrated luminosity of 36.1 fb^{-1} . The quoted uncertainties are due to the finite number of generated events in the simulated samples.

Regions	muhad b -tag	ehad b -tag	muhad b -veto	ehad b -veto
real lepton background events	58366 ± 792	133253 ± 1140	1560552 ± 5650	4992532 ± 8160
lepton isolated	54233 ± 756	127658 ± 1130	1436601 ± 5410	4762534 ± 7940
lepton anti-isolated	4133 ± 239	5595 ± 201	123950 ± 1630	22998 ± 1880
data	569192	798626	5261392	14668019
lepton isolated	193515	434040	2658343	10166358
lepton anti-isolated	375677	364586	2603049	4501661

675 After subtracting the true lepton contamination from this region using simulation, the following ratio for
 676 fake leptons is calculated, referred to hereafter as the lepton fake factor:

$$677 FF = \frac{N(\text{pass “gradient” lepton isolation})}{N(\text{fail “gradient” lepton isolation})}, \quad (2)$$

677 where $N(\text{pass “gradient” lepton isolation})$ ($N(\text{fail “gradient” lepton isolation})$) is the number of lepton
 678 candidates passing (failing) the “gradient” lepton isolation criterion of the signal region.

679 This lepton fake factor is parameterized in lepton η , while separated into two lepton p_T bins for the muon
 680 channel and also separated into b -tag and b -veto categories, where there is at least one or exactly zero
 681 tagged b -jets found in the region, respectively. The different lepton p_T binning between electron and muon
 682 channels is because a combined scale factor is provided for all electron triggers used in this analysis, while
 683 separated scale factors are provided for muon triggers.

684 The main systematics sources for the lepton fake factor are listed below:

- 685 • Statistical uncertainty of backgrounds and data,
- 686 • Uncertainty on the true lepton subtraction, taken by varying the normalization of the subtracted
 687 simulated events by 20%. Note: The lepton fake control region uses the lepton before isolation
 688 which has not been studied as much as the isolated lepton in $W+\text{jets}$ control region. That is why
 689 20% variation is applied, instead of 10% in $W+\text{jets}$ control region.
- 690 • Uncertainty that takes into account potential selection bias by varying the m_T cut,

691 The final lepton fake factors, as a function of lepton η , can be seen in Figure 29, 30 and 31.

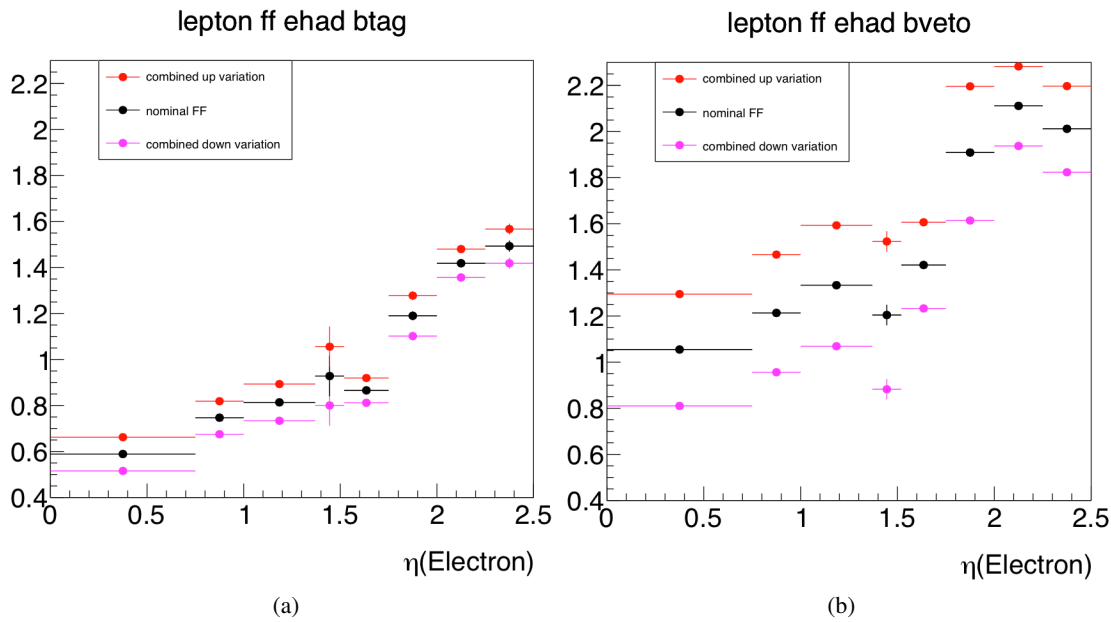


Figure 29: Fake factors from the ehad fake lepton control region as a function of lepton η for (a) b -tagged and (b) b -veto. Note, the crack region about 1.4–1.5 is not used in this analysis.

692 These lepton fake factors can be used to derive an estimate for the background events with a misidentified
 693 τ_{had} and lepton. In the current analysis, this method is used to predict the contribution of multi-jet events
 694 to the anti- τ_{had} region, so that this information can be used in the combined fake factor method that will
 695 be described in Section 5.3. To predict the multi-jet contribution to this region, the lepton fake factors
 696 are applied to data with the same event selection as the Anti- τ_{had} region, except that the electron and
 697 muon isolation requirements are inverted. Contributions to this anti-isolated region from events with true

Not reviewed, for internal circulation only

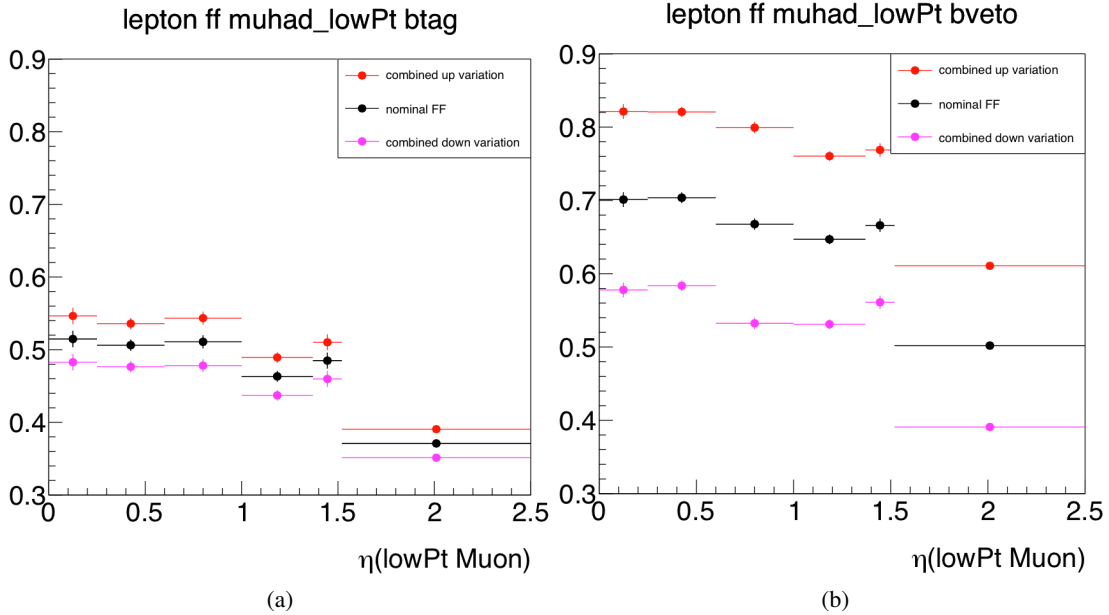


Figure 30: Fake factors from the muhad fake lepton control region with $p_T < 55$ GeV as a function of lepton η for (a) b -tagged and (b) b -veto.

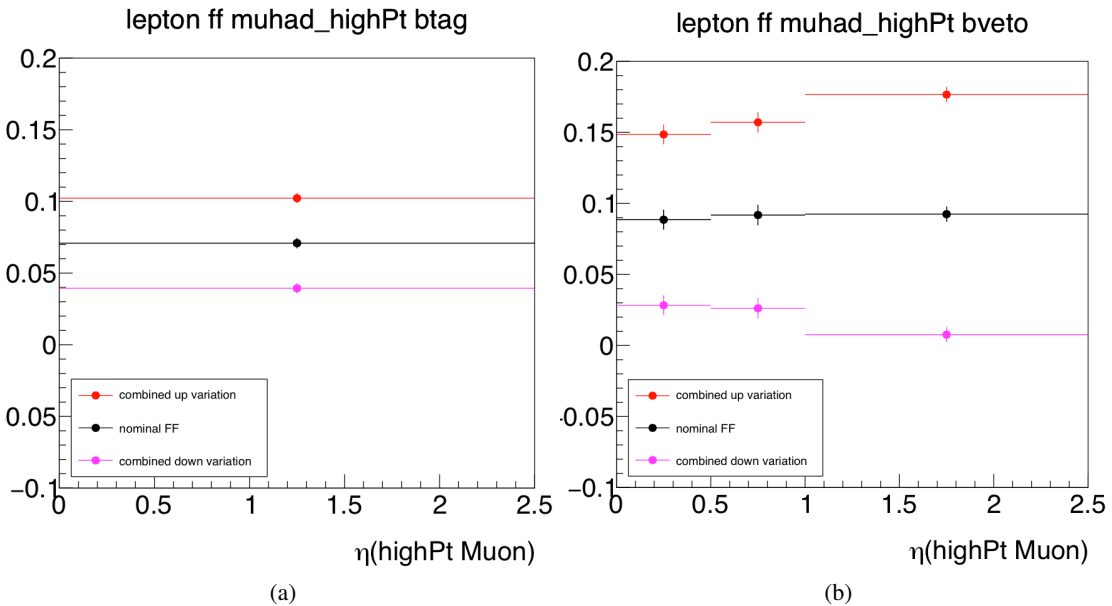


Figure 31: Fake factors from the muhad fake lepton control region with $p_T > 55$ GeV as a function of lepton η for (a) b -tagged and (b) b -veto.

698 electrons or muons are very small, but are subtracted using simulation. The estimate for the Anti- τ region
699 is shown in Figure 32 and 33, for the b -veto and b -tag channels, respectively.

700 From Figure 32 (b), a significant discrepancy is found in the muhad b -veto channel. In Appendix F.4, a
701 detailed study is performed to investigate this discrepancy, which indicates the fact that the leading p_T jet
702 is not well modeled in the lepton fake control region. The underlying reason is not clear yet. To estimate
703 the final impact on fake backgrounds in the signal region, a test has been performed by scaling the rQCD
704 to match the data in anti-ID region. The estimated impact in the signal region is negligible due to the
705 smallness of the difference on fake factor between QCD and $W+jets$. In such a case, no further procedure
706 is taken on the muhad b -veto rQCD in this analysis. The followup study will be performed in the future
707 analysis.

Not reviewed, for internal circulation only

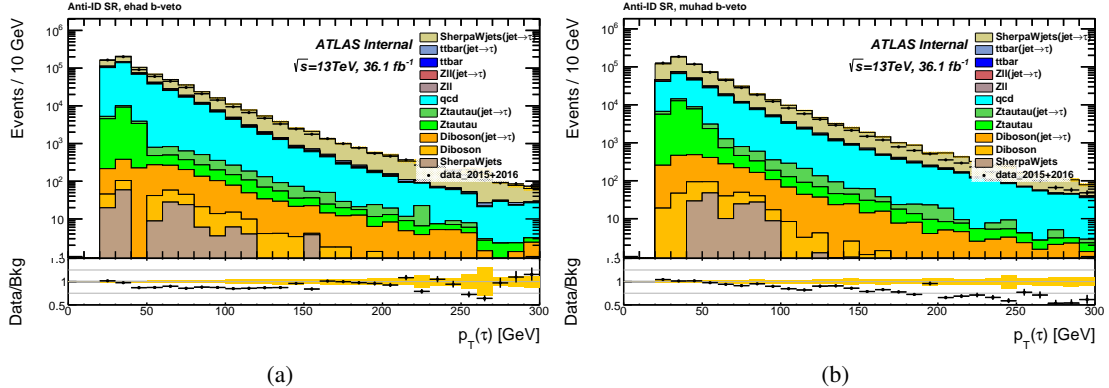


Figure 32: Distributions of τp_T for the b -veto electron (a) and muon (b) channels, after all selection in the Anti- τ_{had} region. The only uncertainties shown are the statistical uncertainties of the sample.

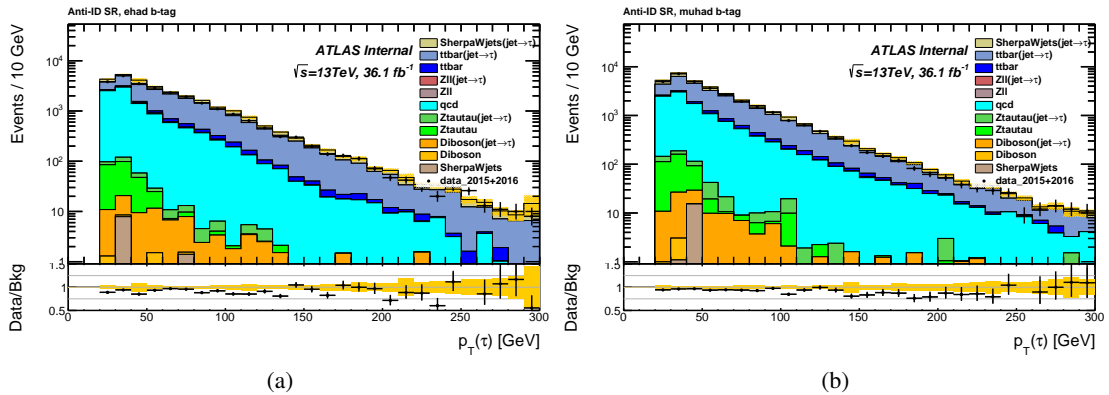


Figure 33: Distributions of τp_T for the b -tag electron (a) and muon (b) channels, after all selection in the Anti- τ_{had} region. The only uncertainties shown are the statistical uncertainties of the sample.

708 5.2.5. Measurement of multi-jet fraction

709 In order to predict r_{QCD} , the fraction of events that arise from QCD multi-jet sources, a prediction of
 710 the contribution of multi-jet backgrounds is performed for the Anti- τ region of data. The r_{QCD} fraction
 711 is then determined as a function of the τp_{T} , separately for b -tag and b -veto categories, as well as for
 712 electron and muon channels. For the calculation of this fraction, simulation is used to predict the number
 713 of events with a true τ_{had} , and the lepton fake factor data-driven method is used to predict the contribution
 714 of multi-jet events. In each bin of the two parameterizing variables (p_{T} and number of tracks), the factor
 715 is defined as:

$$r_{\text{QCD}} = \frac{N(\text{multi-jet, data-driven})}{N(\text{data}) - N(\text{true } \tau_{\text{had}}, \text{MC})}, \quad (3)$$

716 The values of r_{QCD} as a function of τp_{T} for the b -tag and b -veto categories at the end of the cutflow can
 717 be seen in Fig. 34 and 35, separately for electron and muon channels as well as b -tag and b -veto.

718 The uncertainties are symmetrized, and constrained to never allow the r_{QCD} factor to go below zero or
 719 above one. The uncertainties included in Figures 34 and 35 are:

- 720 • Uncertainty propagated from the lepton fake facotr uncertainty in Section 5.2.4.
- 721 • Statistical uncertainty in the Anti- τ_{had} region.
- 722 • Uncertainty on the true lepton and true τ contribution to the Anti- τ_{had} region.

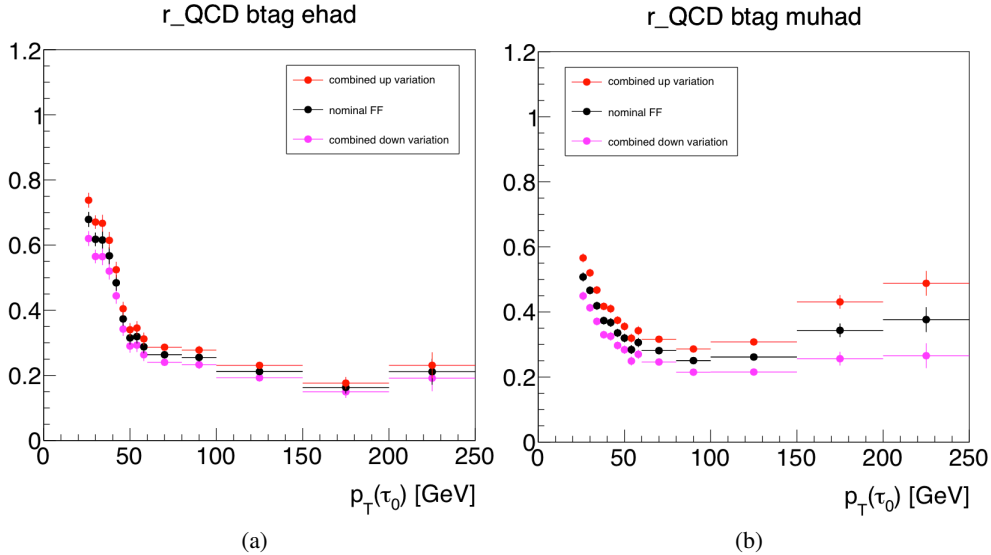


Figure 34: The evolution of r_{QCD} for the b -tag category as a function of τp_{T} at the end of the event selection, along with the total up and down shifts for the uncertainties, shown separately for the electron (a) and the muon (b) channels,

Not reviewed, for internal circulation only

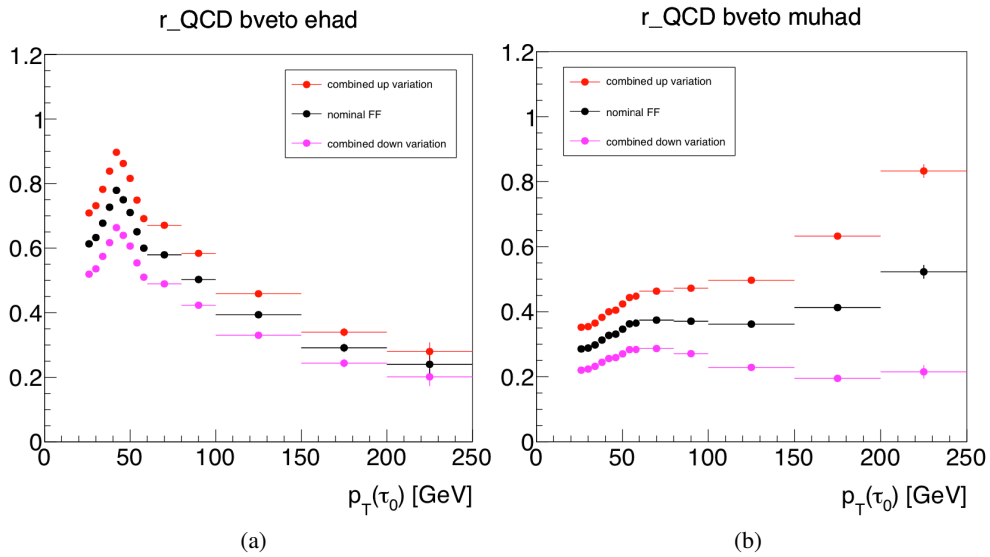


Figure 35: The evolution of r_{QCD} for the b -veto category as a function of τp_T at the end of the event selection, along with the total up and down shifts for the uncertainties, shown separately for the electron (a) and the muon (b) channels.

723 5.3. Combined background estimation

724 The final fake τ_{had} background estimation uses a combined fake factor method similar to what was used
 725 in the Standard Model $H \rightarrow \tau\tau$ search in [84]. The fake τ_{had} background is estimated by re-weighting
 726 events in the anti- τ_{had} control region using a combined fake factor FF(comb), which is defined as follows:

$$727 \quad \text{FF(comb)} = \text{FF}(W + \text{jets}) \times (1 - r_{\text{QCD}}) + \text{FF(QCD)} \times r_{\text{QCD}} \quad (4)$$

728 where the parameter r_{QCD} is calculated in a data-driven method described in the previous section and it
 729 is parameterised as a function of the channel (electron or muon) and the τ_{had} p_{T} . $1 - r_{\text{QCD}}$ denotes the
 730 fraction of contributions from all electroweak processes, such as Z , top and $W + \text{jets}$. The events from
 731 processes with true τ_{had} or a τ_{had} faked by a lepton are subtracted from the anti- τ_{had} region, leaving there
 732 only events with jets faking tau.

733 The following list summarizes the uncertainties and the approximated order of the effect associated to the
 734 combined fake factor method:

- 735 • Systematics of fake factor for FF($W + \text{jets}$) (3–6%) and FF(QCD) (3–5%),
- 736 • Systematics of $\Delta\Phi(\tau, E_{\text{T}}^{\text{miss}})$ correction for both FF($W + \text{jets}$) (2–3%) and FF(QCD) (3–6%),
- 737 • Systematics of b -tag correction of FF($W + \text{jets}$) (10% for b -tag region),
- 738 • Systematics of r_{QCD} (1–2%),

739 The fake factors are correlated between the electron and the muon channels, since they are in common.
 740 The r_{QCD} is taken uncorrelated between electron and muon channel.

741 6. Systematic Uncertainties

742 6.1. Experimental uncertainties

743 Uncertainties relating to the detector simulation and the integrated luminosity measurement (3.2%) are
 744 included for signal and for backgrounds that are estimated using simulated samples. This version of the
 745 analysis note uses the final 2015+2016 CP recommendations. These systematics are summarized in Table
 746 8.

747 The impact of the systematics can be found in the NP ranking plots in Sec. 7.2.

748 In order to decrease the impact of the statistical fluctuation and small systematics variations, the smoothing-
 749 and pruning procedure used in ATLAS VHbb Run 1 analysis [85] are applied to the systematics
 750 uncertainties, especially the detector related ones.

Table 8: Summary table for the experimental systematics: NP name start with “”, brief description, Scheme (how many in fit).

NP name	Description	Scheme (How many NPs)
“Lumi”	Integrated luminosity measurement	1
“TAU”	τ_{had} reconstruction, identification and electron-veto efficiencies	6
“TES”	τ_{had} energy scale	3
“MUON”	muon systematics, including trigger, reconstruction, isolation, identification and energy scale	13
“ELE or EG”	electron systematics, including trigger, reconstruction, isolation, identification and energy scale	6
“METSoft”	E_T^{miss} soft terms	2
“JER, JES, Jvt”	jet energy scale and resolution	7
“btag”	flavor-tagging	14
“PRW”	pile-up	1

Not reviewed, for internal circulation only

751 6.2. Theoretical uncertainties on background modeling

752 Theoretical cross section uncertainties have been used for the main MC samples that are in use in this
 753 analysis. For $t\bar{t}$, single top production and diboson production the uncertainty is taken 6% following the
 754 twiki recommendations [86–88]. The theoretical systematic uncertainties on Z+jets have been estimated
 755 by using the *LPX* weight provided by ATLAS PMG group. The uncertainties due to PDF, parton shower
 756 model and α_s are considered. The detailed study is discussed in Appendix I.

757 Furthermore, the top events with truth τ in the final state are modeled by MC simulation prediction. The
 758 modeling uncertainties are studied by comparing the MC samples with different configurations, according
 759 to the ATLAS official recommendation: The modeling uncertainty of the initial/final state radiation is
 760 estimated by comparing the MC samples generated with enhanced or reduced initial/final state radiation;
 761 the modeling uncertainty of showering and underlying events is estimated by comparing Pythia and
 762 Herwig; the systematics uncertainty on hard processes is estimated by comparing between aMcAtNLO
 763 and Powheg. The uncertainties applied in the analysis are shown in Figures 36 and 37. Table 9 summarises
 764 the normalization effect.

Table 9: Summary of the modeling systematics on top normalization

Source	Showering	Hard Proc.
Unc.	2%	0.5%

765 6.3. Uncertainties on data-driven background estimations

766 These are described when the data-driven techniques are explained in Section 5.

767 All the background modeling systematics are summarized in Table 10.

Not reviewed, for internal circulation only

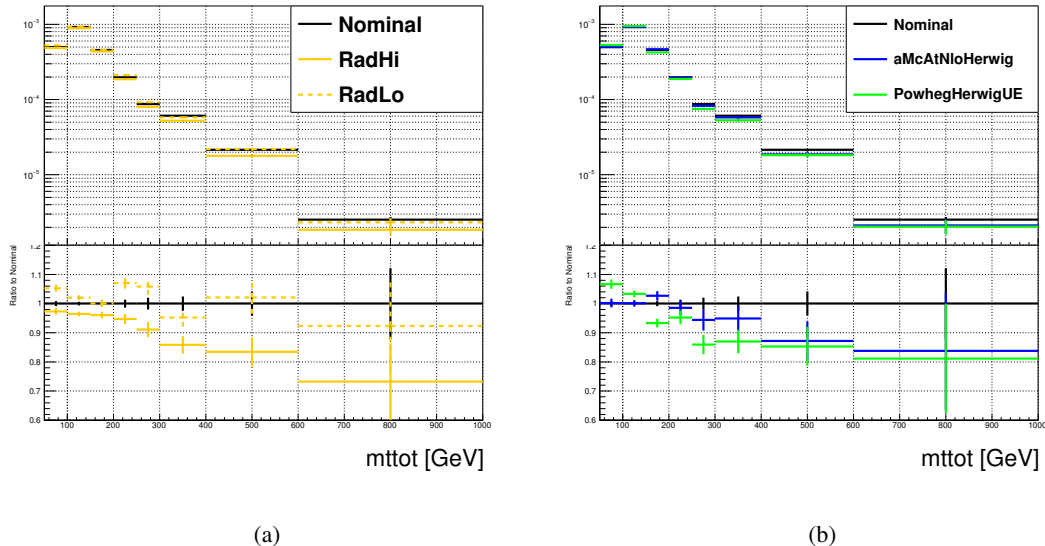


Figure 36: m_T^{tot} without b-tagging requirement: (a) is the comparison between the nominal sample and with the enhanced or reduced initial/final state radiation. (b) is the comparison between different shower models and hard process generators.

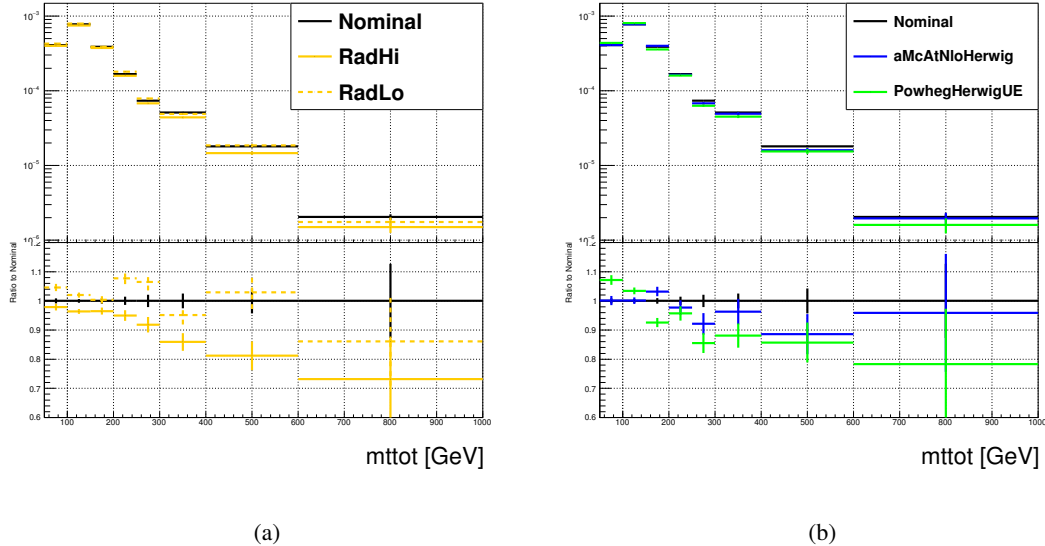


Figure 37: m_T^{tot} with b-tagging requirement: (a) is the comparison between the nominal sample and with the enhanced or reduced initial/final state radiation. (b) is the comparison between different shower models and hard process generators.

768 6.4. Uncertainties on signal modeling

769 Uncertainties related to signal modeling include the uncertainties associated with the initial and final state
 770 radiation, the modeling of multi-parton interactions, the renormalisation and factorisation scale, and the

Table 10: Summary table for the background modeling: NP name start with “”, brief description, Scheme (how many in fit), approximated order of magnitude if available.

NP name	Description	Scheme (How many NPs)	Order
“LPX”	(Mainly on Z+jets) systematics on PDF choose, QCD scale, strong interaction coefficient	10	-
“xsec_Diboson or top”	Cross section prediction uncertainty	2	6%
“TTBAR”	Top modeling sys (mainly shape sys)	2	-
“Fakes_Dphi”	FF dphi correction sys, decorrelated between e and μ channel	4	-
“Fakes_Shape_QCD or Wjets”	Fake QCD or Wjets FF sys, decorrelated between e and μ channel	4	-
“Fakes_Shape_WjetsBtag”	Fake Wjets btag FF sys	1	-
“Fakes_Shape_rQCD”	Fake rQCD sys	2	-

category	200 GeV	500 GeV	1000 GeV
<i>b</i> -associated production			
<i>b</i> -tag	3.9	2.0	1.0
<i>b</i> -veto	2.7	1.3	1.5
gluon fusion			
<i>b</i> -tag	15.7	7.3	7.4
<i>b</i> -veto	4.2	2.2	1.5

Table 11: Relative signal acceptance uncertainties (in percent)

⁷⁷¹ parton distribution functions.

⁷⁷² The combined uncertainties are listed in Tab. 11. More details are found in App. C.

⁷⁷³ Tables 12 and 13 show the expected limit changes when a given type of systematics is removed from the fit.

Table 12: Summary of the impact of the grouped systematics items for ggH signal(in %). The definition of impact is $(\text{Limit}_{\text{Default}} - \text{Limit}_{\text{New}})/\text{Limit}_{\text{Default}}$. “Default” is with the full default systematics, “all” means that all systematics are removed. “Fake” is all of the jet fake related sys, “AU” is signal acceptance uncertainties, “LPX sec” is background theoretical uncertainties, the meaning of the rest can be told from the names.

Mass	all	Fake	AU	TES	LPX sec	Tau	TTBAR	JET PRW	JER LUMI	MET Jvt	btag	EG
												ELE MU
200	41	28	8	1	0	0	0	1			0	0
300	36	5	8	15	1	0	0	0			1	0
400	36	3	9	19	1	0	1	1			1	0
500	33	4	10	19	1	0	1	1			0	0
600	30	4	12	15	3	0	1	0			0	0
700	26	3	12	12	3	0	1	1			0	0
800	22	2	13	8	3	0	1	1			0	0
1000	20	2	14	5	3	0	0	1			0	0
1200	20	1	15	4	3	0	0	1			0	0

Table 13: Summary of the impact of the grouped systematics items for bbH signal (in %). The definition of impact is $(Limit_{Default} - Limit_{New})/Limit_{Default}$. “Default” is with the full default systematics, “all” means that all systematics are removed. “Fake” is all of the jet fake related sys, “AU” is signal acceptance uncertainties, “LPX sec” is background theoretical uncertainties, the meaning of the rest can be told from the names.

Mass	all	Fake	AU	TES	LPX sec	Tau	TTBAR	JET PRW LUMI Jvt			btag	EG ELE MU
								JET	JER	MET		
200	57	25	30	1	0	0	0	1			1	0
300	58	4	28	25	0	0	1	1	1		0	0
400	53	1	27	25	0	0	1	1	1		0	0
500	44	2	26	17	0	0	1	1	1		0	0
600	38	1	26	12	1	0	0	0	0		0	0
700	33	1	26	7	1	0	0	0	0		0	0
800	31	1	25	5	1	0	0	0	0		0	0
1000	28	1	24	3	1	0	0	0	0		0	0
1200	27	1	23	3	2	0	1	0	0		0	0

Not reviewed, for internal circulation only

7. Results

7.1. Statistics Analysis

The results from the channels studied in this search are combined to improve the sensitivity to MSSM Higgs boson and Z' production. The parameter of interest in this search is the signal strength, μ , defined as the ratio of the fitted signal cross section times branching fraction to the signal cross section times branching fraction predicted by the particular MSSM signal assumption. The value $\mu = 0$ corresponds to the absence of signal, whereas the value $\mu = 1$ suggests signal presence as predicted by the theoretical model under study. The statistical analysis of the data employs a binned likelihood function constructed as the product of Poisson probability terms. Signal and background predictions depend on systematic uncertainties, which are parameterized as nuisance parameters and are constrained using Gaussian functions. The binned likelihood function is constructed in bins of the m_T^{tot} mass.

A simultaneous fit of the binned likelihood function is performed with 4 signal regions and 2 control regions, i.e. (b -tag, b -veto)×(ehad, muhad)+Top CR (ehad, muhad). The Top CR used in the fit constrains the Top related systematics uncertainty. The binning for the m_T^{tot} that has been used for these binned likelihood function for the b -veto and b -tag categories are the following:

- b -veto $e\tau_{\text{had}}$: (50, 70, 80, 90, 100, 120, 140, 160, 180, 200, 220, 240, 260, 280, 300, 320, 340, 360, 400, 500, 5000)
- b -veto $\mu\tau_{\text{had}}$: (50, 70, 8, 0.9, 0.1, 00, 120, 140, 160, 180, 200, 220, 240, 260, 280, 300, 500, 5000)
- b -tag $e\tau_{\text{had}}$: (50, 100, 150, 200, 250, 300, 350, 400, 500, 5000)
- b -tag $\mu\tau_{\text{had}}$: (50, 100, 150, 200, 250, 300, 400, 5000)
- TCR $e\tau_{\text{had}}$: (100, 150, 200, 250, 300, 350, 400, 500, 5000)
- TCR $\mu\tau_{\text{had}}$: (100, 150, 200, 250, 300, 350, 400, 450, 500, 5000)

Note, the overflow bin is included in the highest bin.

For the Z' analysis, we optimize the binning of the high mass region dedicatedly:

Not reviewed, for internal circulation only

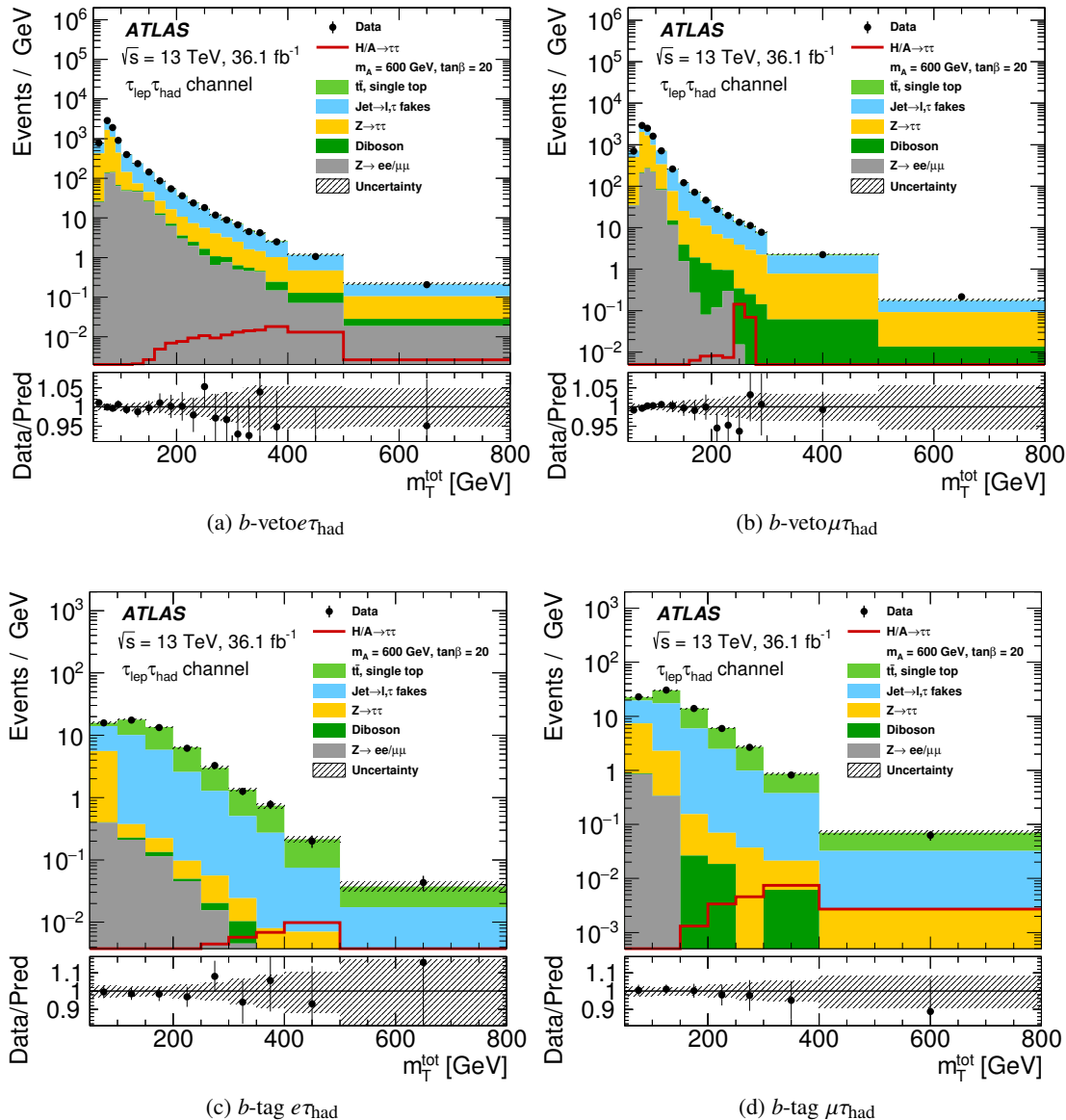


Figure 38: Post-fit m_T^{tot} distribution for b-veto and b-tag channel.

- b -inclusive $e\tau_{\text{had}}$: (50, 70, 80, 90, 100, 120, 140, 160, 180, 200, 220, 240, 260, 280, 300, 320, 340, 360, 400, 500, 600, 700, 800, 5000)
- b -inclusive $\mu\tau_{\text{had}}$: (50, 70, 80, 90, 100, 120, 140, 160, 180, 200, 220, 240, 260, 280, 300, 500, 600, 700, 800, 5000)

7.2. Fit check

The post-fit plots for each of the channels are shown in Fig. 38–39.

Not reviewed, for internal circulation only

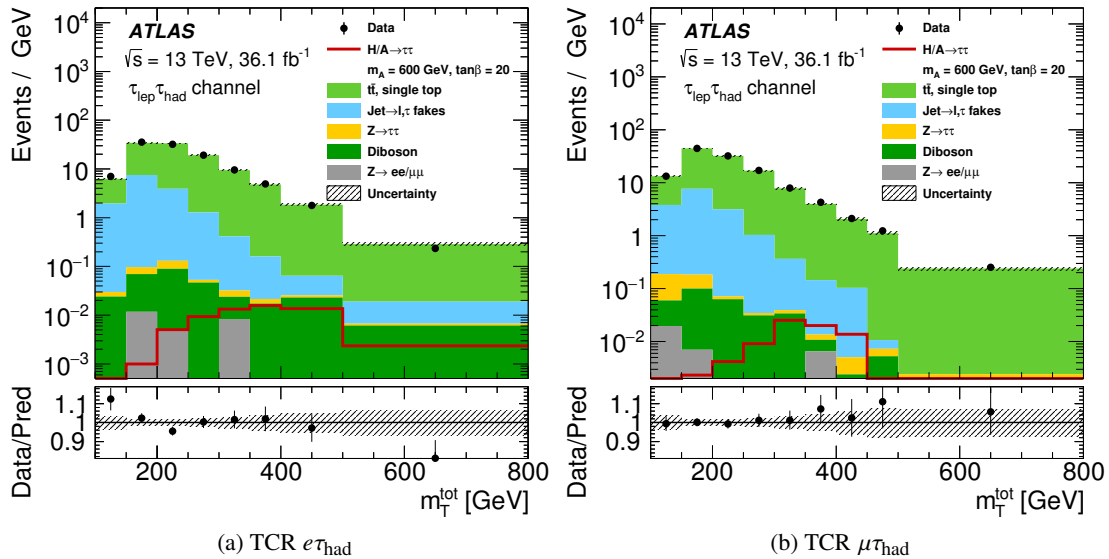


Figure 39: Post-fit m_T^{tot} distribution for the top control region.

The fit is done using both the Asimov datasets and real collision data for each category. Several studies are performed to check the fit model. The systematic effect for these important systematics are shown in Appendix K. Figure 40 shows the fit results of the full NPs. Those strongly constrained NPs, i.e. *MET-SoftTrkResoPerp*, *Fakes_Dphi_QCD*, *Fakes_Shape_QCD*, *Fakes_Shape_Wjets*, *Fakes_Shape_WjetsBtag*, *TESDETECTOR*, *TESINSITU*, *TTBAR_RADIATION*, *TTBAR_SHOWERGEN*, have been looked in detail, as shown in Appendix K. The behavior of the fit is generally understandable: The top systematics is constrained quite a lot, which is due to the high purity and high statistics top control region. The tau related systematics are also constrained and pulled. TauWG confirms that the systematics are bit overestimated. Additionally, the *TESINSITU* has been studied in detail, as shown in Appendix L. Some background modeling uncertainties, e.g. *Fake_DPhi* and *Fake_Shape*, are pulled, as these systematics are designed to cover the potential residual mismodeling. The e and μ channels are decorrelated for *Fake_DPhi*, *Fake_Shape*, because part of these systematics are introduced to cover the difference observed between e and μ channels during deriving them from the control regions or validation regions. Figures 42 and 41 show the correlation matrix of the NPs. No suspicious correlation is found.

Not reviewed, for internal circulation only

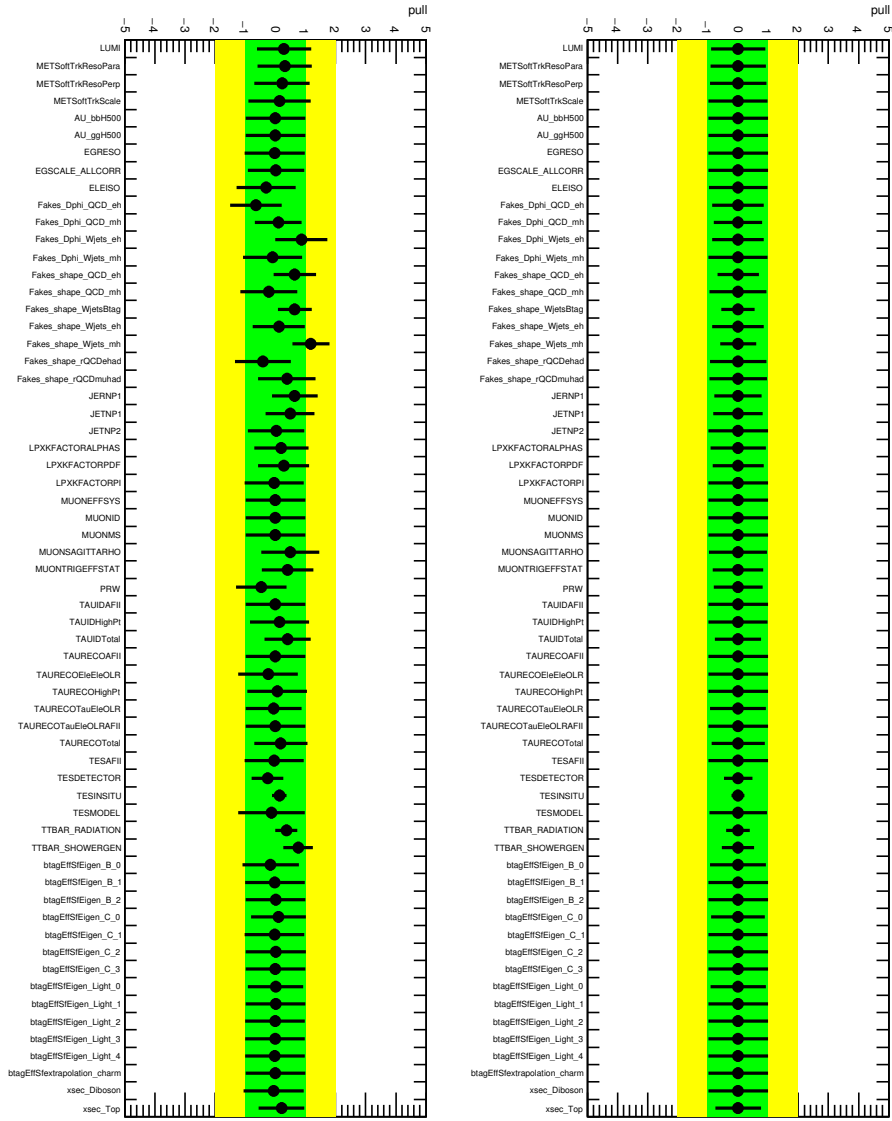


Figure 40: Pull plots for all nuisance parameters of the combined $\tau_{\text{lep}}\tau_{\text{had}}$ fit on (left) real data and (right) Asimov data.

Not reviewed, for internal circulation only

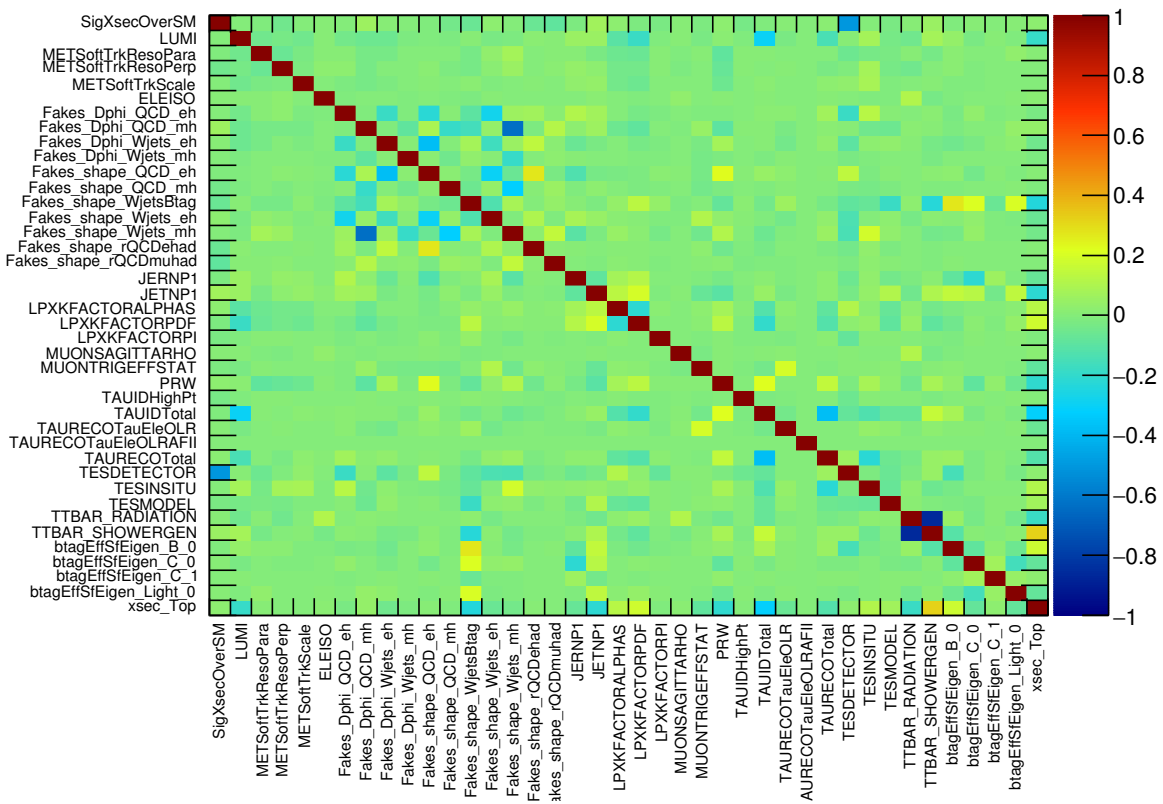


Figure 41: Correlation matrix of the highest correlated nuisance parameters of the combined $\tau_{\text{lep}}\tau_{\text{had}}$ fit on Asimov data.

Not reviewed, for internal circulation only

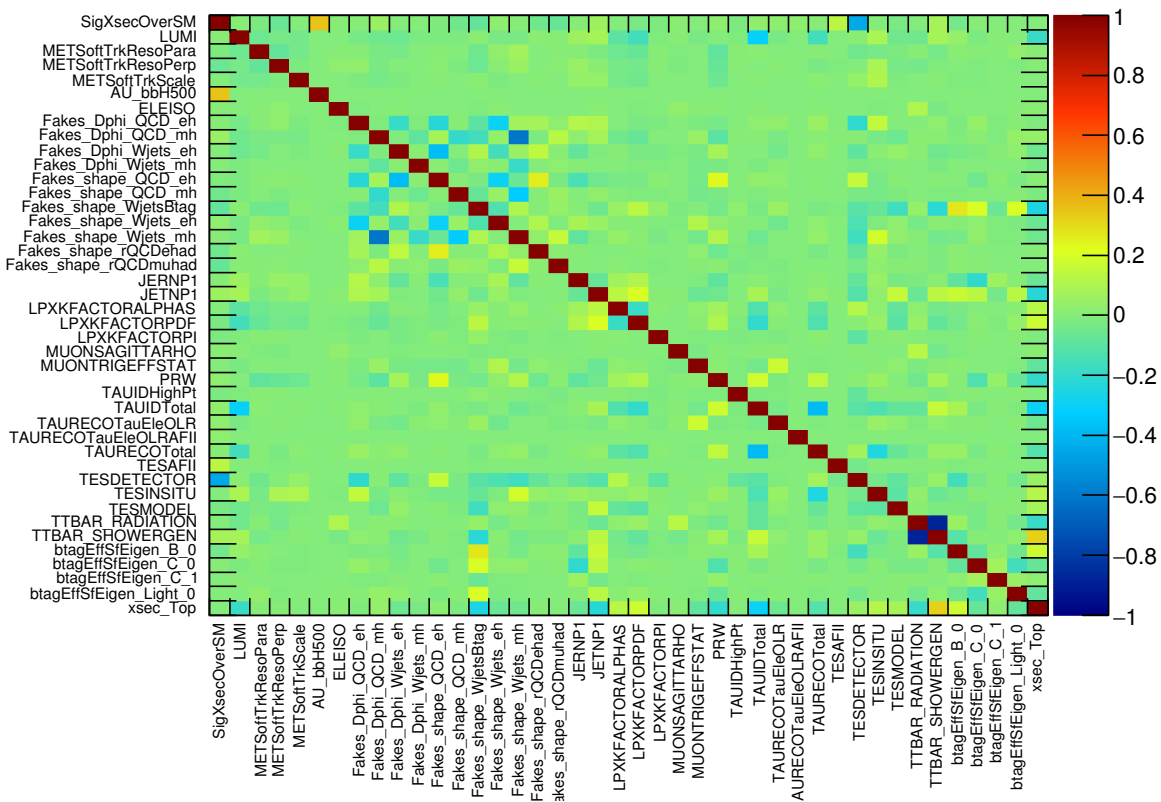


Figure 42: Correlation matrix of the highest correlated nuisance parameters of the combined $\tau_{\text{lep}}\tau_{\text{had}}$ fit on real data.

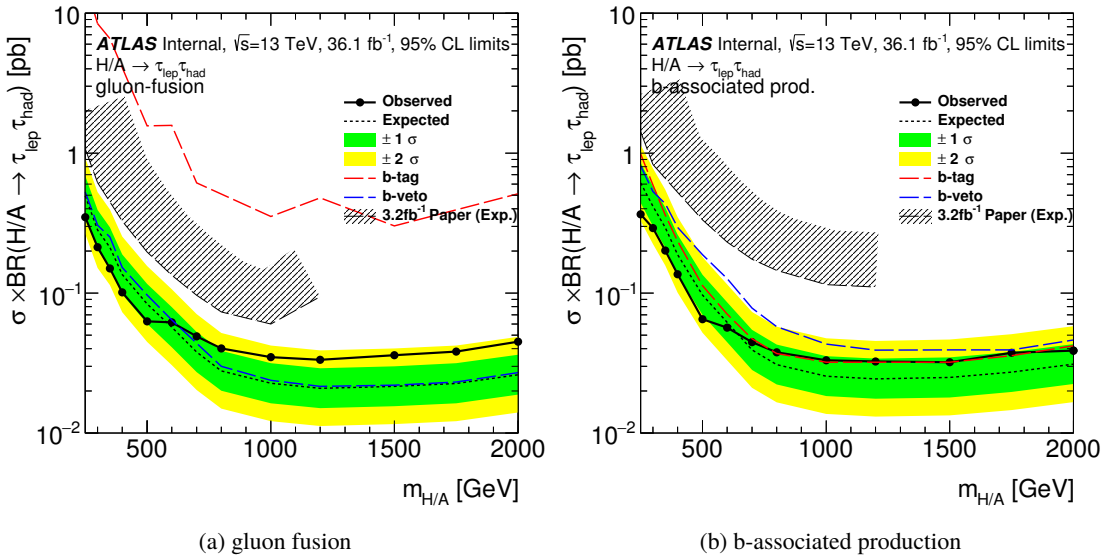


Figure 43: The 95% CL upper limit on the production times branching ratio to $\tau\tau$ of a single scalar boson produced via gluon fusion or b-associated production for 36.1 fb^{-1} of integrated luminosity at 13 TeV. Each category is shown separately.

7.3. Exclusion Limit

The significance of any small observed excess in data is evaluated by quoting p -values to quantify the level of consistency of the data with the $\mu = 0$ hypothesis. Exclusion limits use the modified frequentist method known as CL_s [89]. Both the exclusion limits and p -values are calculated using the asymptotic approximation [90]. The test statistic used for the exclusion limits derivation is the \tilde{q}_μ test statistic and for the p -values the q_0 test statistic [90]. The definition of the test statistics used in this search is the following:

$$\tilde{q}_\mu = \begin{cases} -2 \ln(\mathcal{L}(\mu, \hat{\theta}) / \mathcal{L}(0, \hat{\theta})) & \text{if } \hat{\mu} < 0 \\ -2 \ln(\mathcal{L}(\mu, \hat{\theta}) / \mathcal{L}(\hat{\mu}, \hat{\theta})) & \text{if } 0 \leq \hat{\mu} \leq \mu \\ 0 & \text{if } \hat{\mu} > \mu \end{cases}$$

and

$$q_0 = \begin{cases} -2 \ln(\mathcal{L}(0, \hat{\theta}) / \mathcal{L}(\hat{\mu}, \hat{\theta})) & \text{if } \hat{\mu} \geq 0 \\ 0 & \text{if } \hat{\mu} < 0 \end{cases}$$

where $\mathcal{L}(\mu, \theta)$ denotes the binned likelihood function, μ is the parameter of interest (i.e. the signal strength parameter), and θ denotes the nuisance parameters. The pair $(\hat{\mu}, \hat{\theta})$ corresponds to the global maximum of the likelihood, whereas $(x, \hat{\theta})$ corresponds to a conditional maximum in which μ is fixed to a given value x .

The signal mass range is considered up to Higgs boson mass 2.0 TeV. The model independent cross section times branching ratio limits for both ggH or bbH production are shown in Fig. 43.

Their interpretation in various scenarios is shown in Figs. 44.

Not reviewed, for internal circulation only

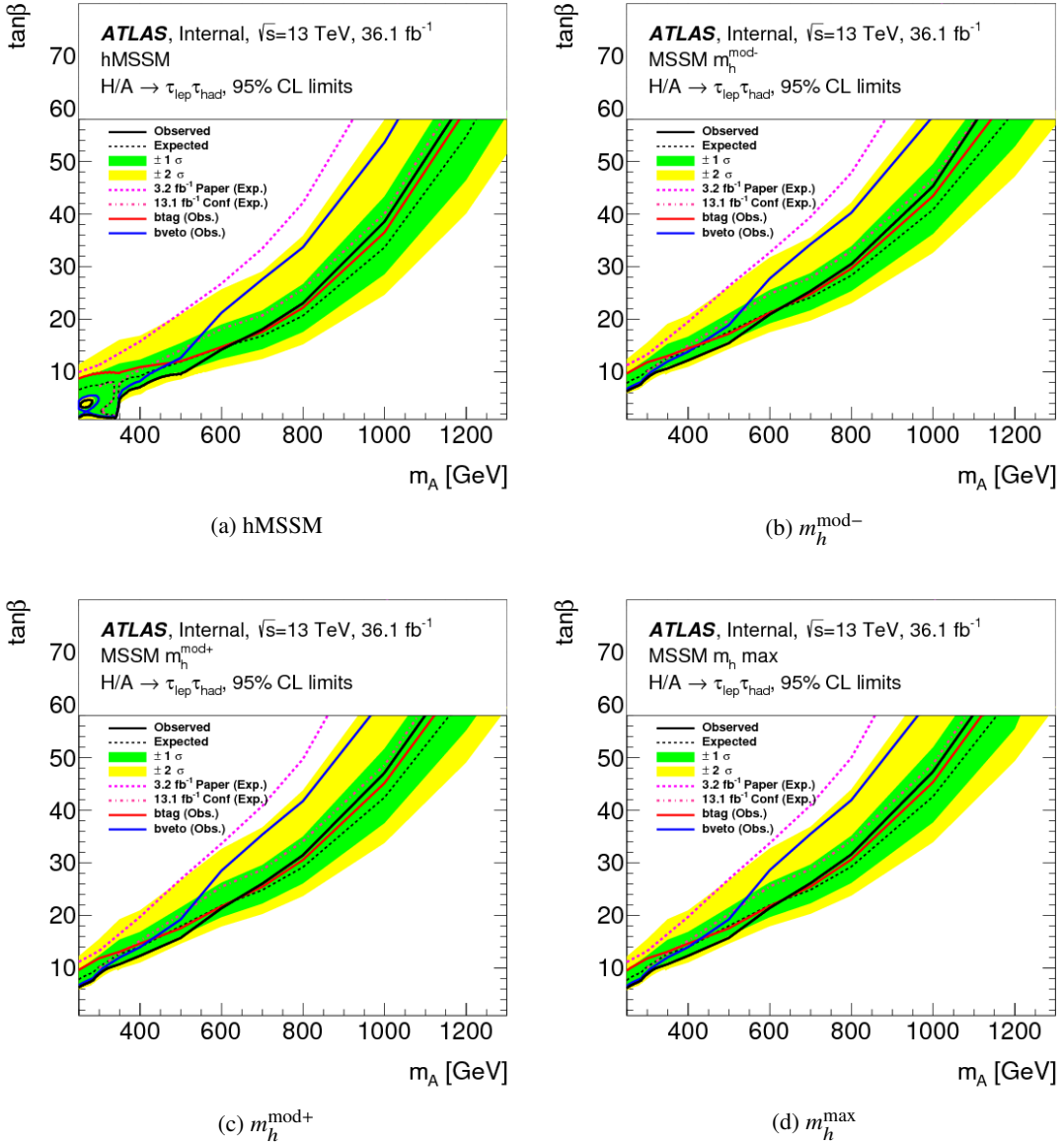


Figure 44: The 95% CL upper limit on the m_A - $\tan\beta$ plane of the MSSM parameter space in various scenarios for 36.1 fb^{-1} of integrated luminosity at 13 TeV.

8. Combination of $\tau_\ell \tau_{\text{had}}$ and $\tau_{\text{had}} \tau_{\text{had}}$ channels

This is the combination of the $\tau_\ell \tau_{\text{had}}$ and $\tau_{\text{had}} \tau_{\text{had}}$ channels.

The cross section limit combination is shown in Fig. 45. The combination of the MSSM limits are shown in Fig. 46.

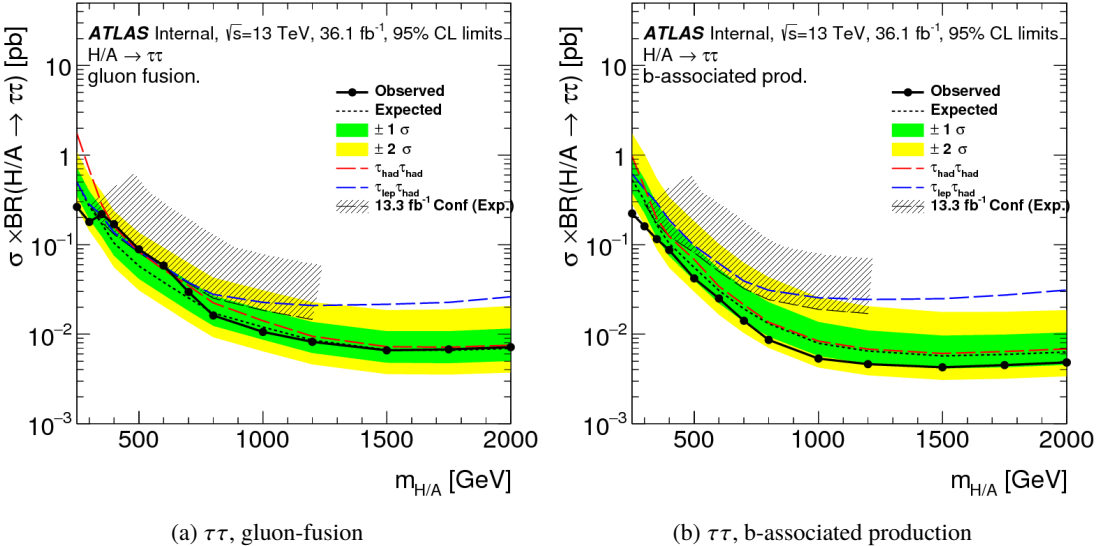


Figure 45: The 95% CL upper limit on the production times branching ratio to $\tau\tau$ of a single scalar boson produced via gluon-fusion or b -associated production for 36.1 fb^{-1} of integrated luminosity at 13 TeV. The combination of the channels is shown along with a comparison of the expected limits for each channel separately.

The exclusion limits are calculated in dependence of Higgs mass and the relative magnitude of the production processes (gluon fusion and b -associated production). Using the MSSM prediction of this fraction of the production cross sections, these limits can be expressed in dependence of m_A and $\tan \beta$ instead. The exclusion lines in this parameter space are then obtained by comparison of the limits with the MSSM cross section prediction. Non-linear exclusion lines between the tested signal mass points arise, because a bilinear interpolation is employed in the parameter space of m_{Higgs} and production process composition. In the plots shown in this section this interpolation is only performed for $\tan \beta < 10$, while for the rest of the parameter space the limits at the considered signal masses are only connected linearly in the $m_A - \tan \beta$ parameter space. A discussion of this interpolation scheme is included in Appendix H.

8.1. Fit study for combination

This section presents the fit results for the combined $\tau_{\text{lep}} \tau_{\text{had}}$ and $\tau_{\text{had}} \tau_{\text{had}}$ channels. The pull plot for the individual $\tau_{\text{lep}} \tau_{\text{had}}$ and $\tau_{\text{had}} \tau_{\text{had}}$ unconditional fits to data are shown in Fig. 47. The correlations of the most correlated systematics are shown in Fig. 48. The pull plot and correlation plot of combined $\tau_{\text{lep}} \tau_{\text{had}}$ and $\tau_{\text{had}} \tau_{\text{had}}$ unconditional fit to data is shown in Figs. 49 and 50.

Post-fit m_T^{tot} distribution plots from the unconditional fit, with a signal scaled to the expected cross-section from a $\tan \beta = 10$ and $m_A = 500 \text{ GeV}$ hMSSM signal, are shown in Fig. 51 for the different signal

Not reviewed, for internal circulation only

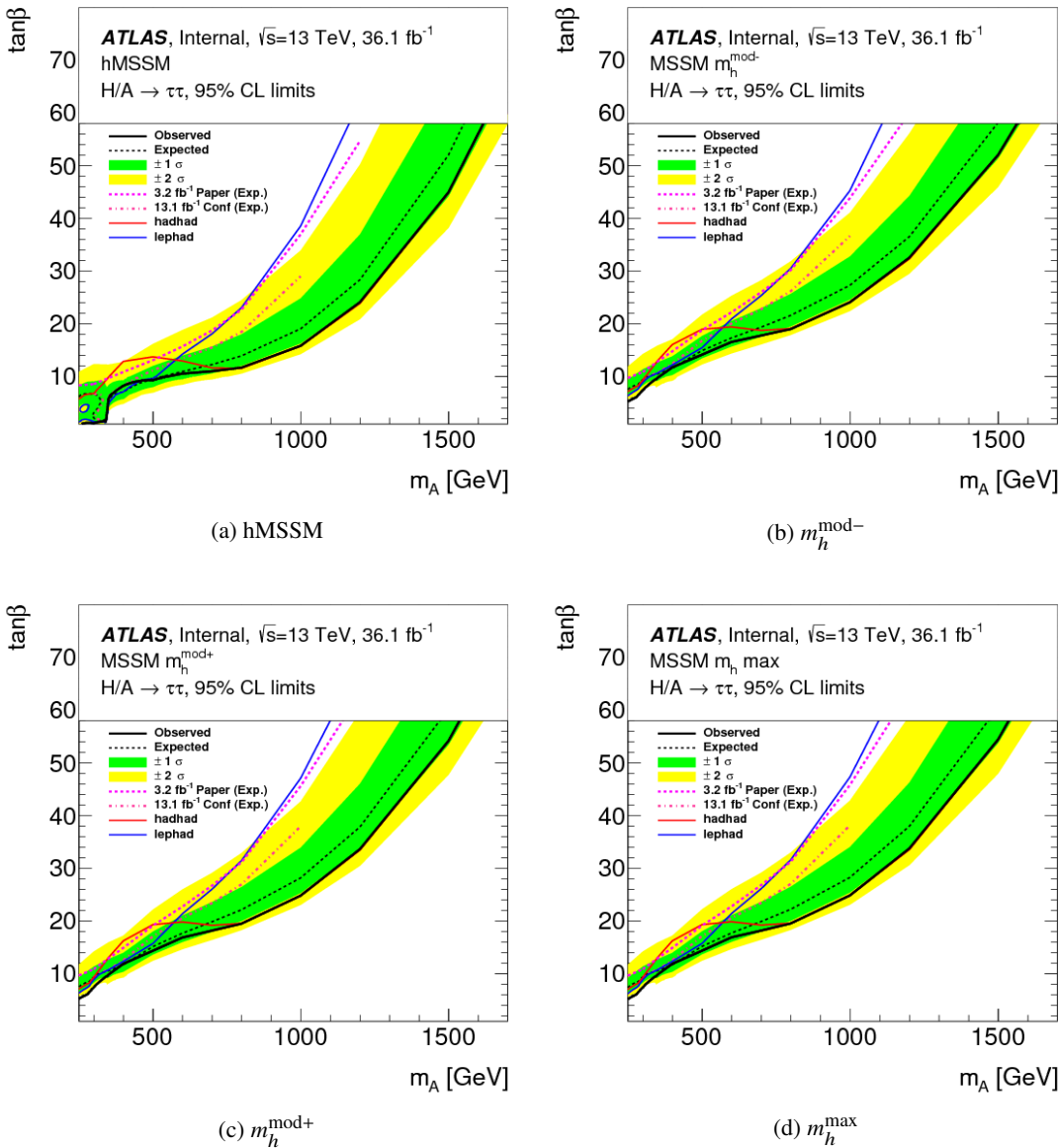


Figure 46: The 95% CL upper limit on the m_A - $\tan \beta$ plane of the MSSM parameter space in various scenarios for 36.1 fb^{-1} of integrated luminosity at 13 TeV.

regions. The best signal strength estimation is found as $\hat{\mu} = -0.07^{+0.33}_{-0.30}$, consistent with the background only hypothesis.

Post-fit m_T^{tot} distribution plots from the conditional background only fit are shown in Fig. 52 for the different signal regions.

Not reviewed, for internal circulation only

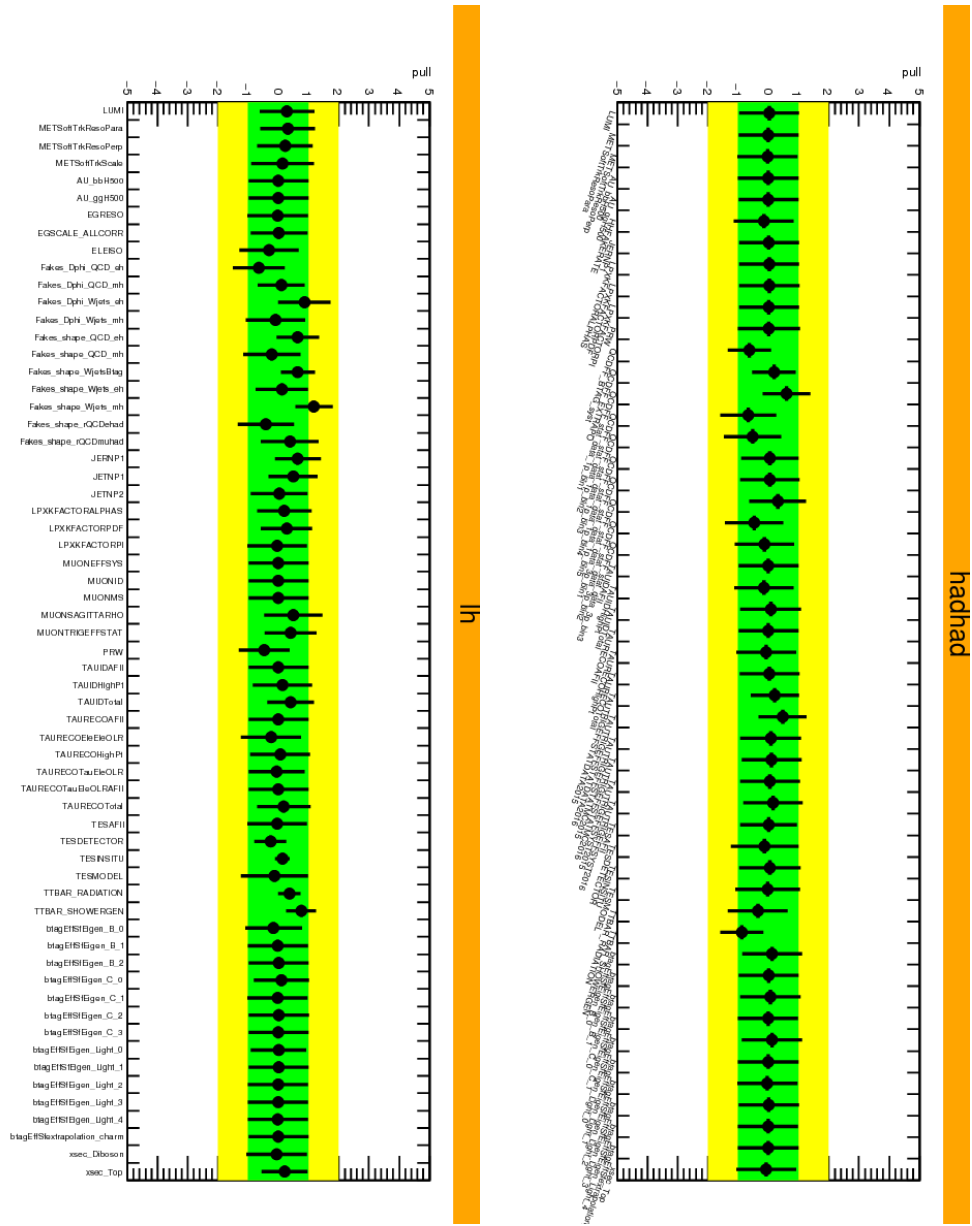


Figure 47: Pull plots for all nuisance parameters of the $\tau_{\text{lep}} \tau_{\text{had}}$ (left) and $\tau_{\text{had}} \tau_{\text{had}}$ (right) unconditional fit on data.

Not reviewed, for internal circulation only

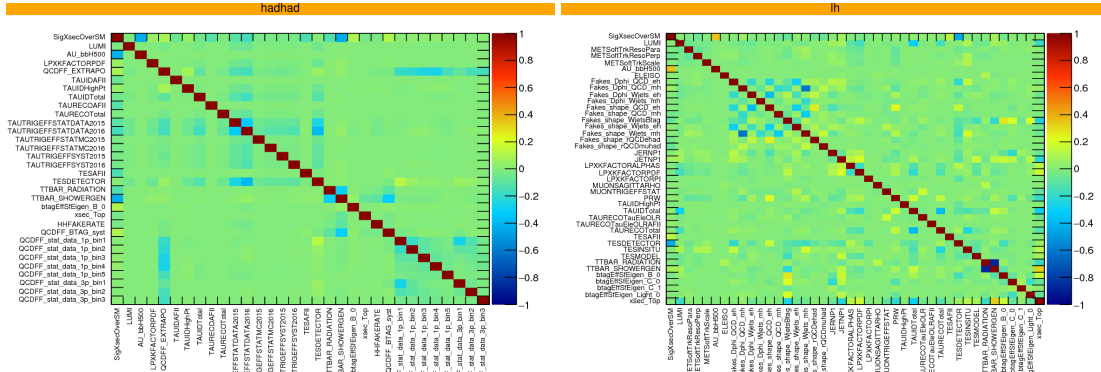


Figure 48: Correlation matrix of the highest correlated nuisance parameters of the $\tau_{\text{lep}} \tau_{\text{had}}$ (left) and $\tau_{\text{had}} \tau_{\text{had}}$ (right) unconditional fit on data.

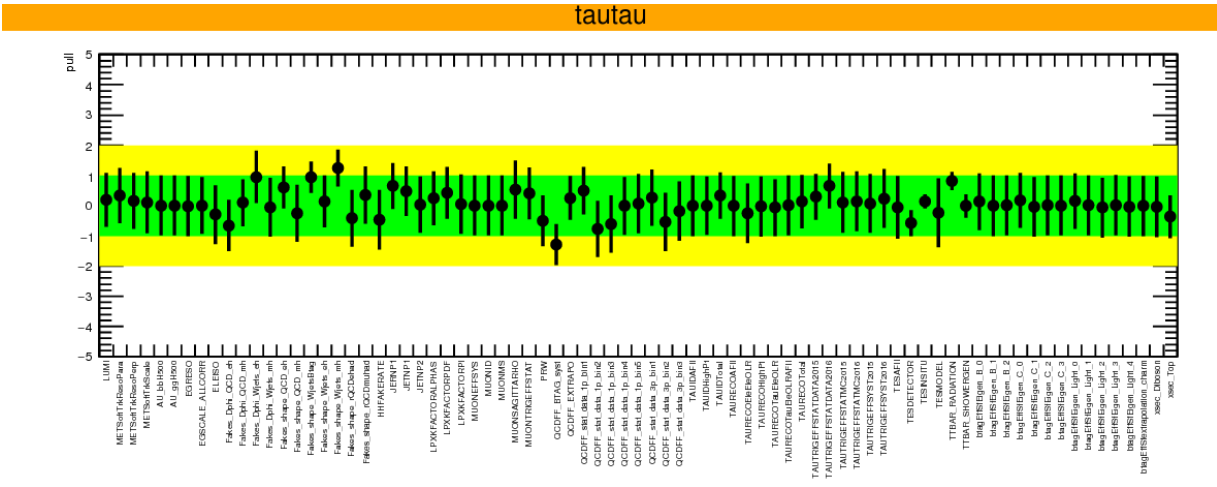


Figure 49: Pull plots for all nuisance parameters of the combined $\tau_{\text{lep}} \tau_{\text{had}}$ and $\tau_{\text{had}} \tau_{\text{had}}$ unconditional fit on data.

9. Conclusions

This is an update of the ATLAS search for a heavy $\tau\tau$ resonance with the full 2015 and 2016 data. The note describes the event selection and the methods for the background estimations for the $\tau_{\text{lep}} \tau_{\text{had}}$ channel.

Not reviewed, for internal circulation only

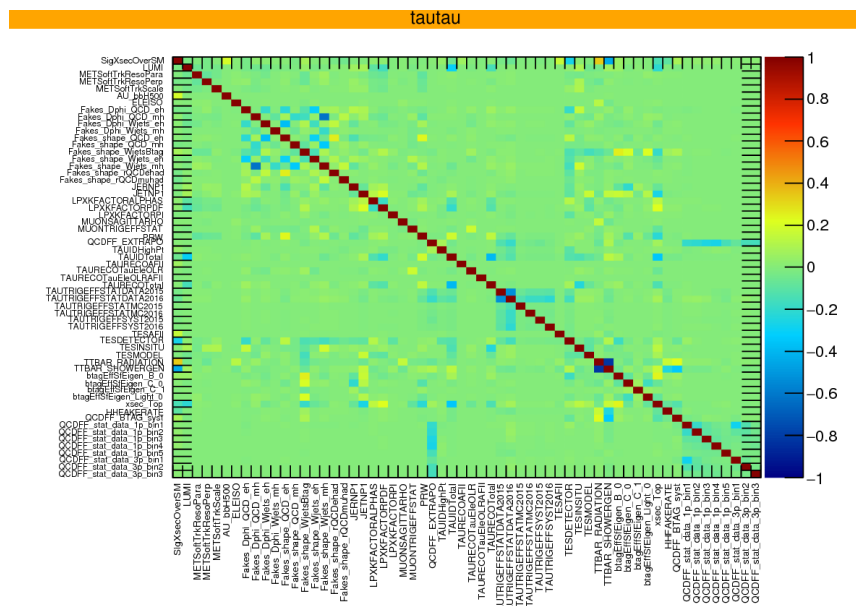


Figure 50: Correlation matrix of the highest correlated nuisance parameters of the combined $\tau_{\text{lep}} \tau_{\text{had}}$ and $\tau_{\text{had}} \tau_{\text{had}}$ unconditional on data.

Not reviewed, for internal circulation only

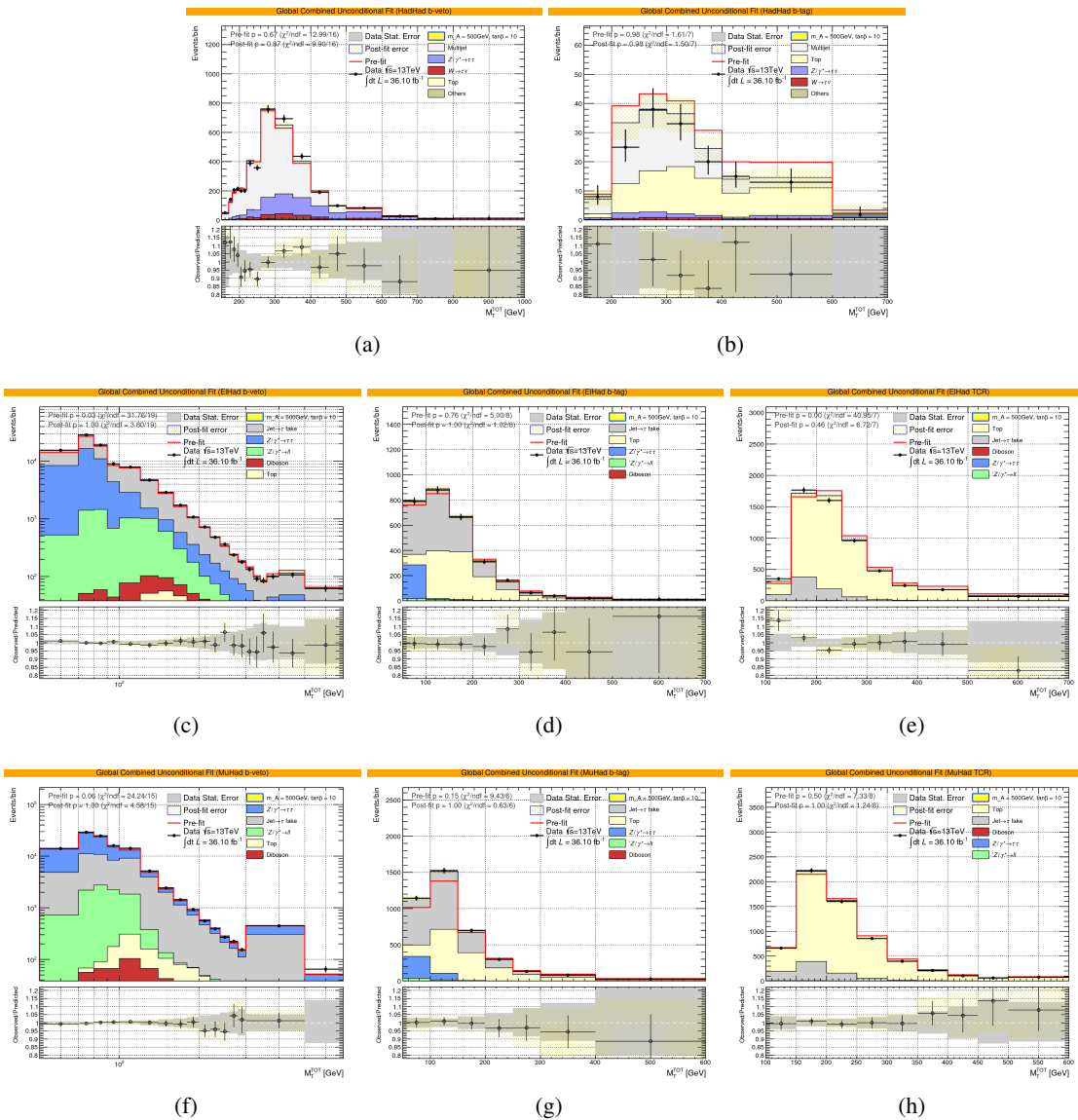


Figure 51: Post-fit m_T^{tot} distributions for the combined $\tau_{\text{had}}\tau_{\text{had}} + \tau_{\text{lep}}\tau_{\text{had}}$ unconditional fit for a hMSSM signal of $\tan \beta = 10$ and $m_A = 500$ GeV in the; $\tau_{\text{had}}\tau_{\text{had}}$ (a) b -veto, (b) b -tag; $\tau_e\tau_{\text{had}}$ (c) b -veto, (d) b -tag, (e) top-CR ; and $\tau_\mu\tau_{\text{had}}$ (c) b -veto, (d) b -tag, and (e) top-CR regions. The pre-fit histogram contains both the total pre-fit background and the scaled signal.

Not reviewed, for internal circulation only

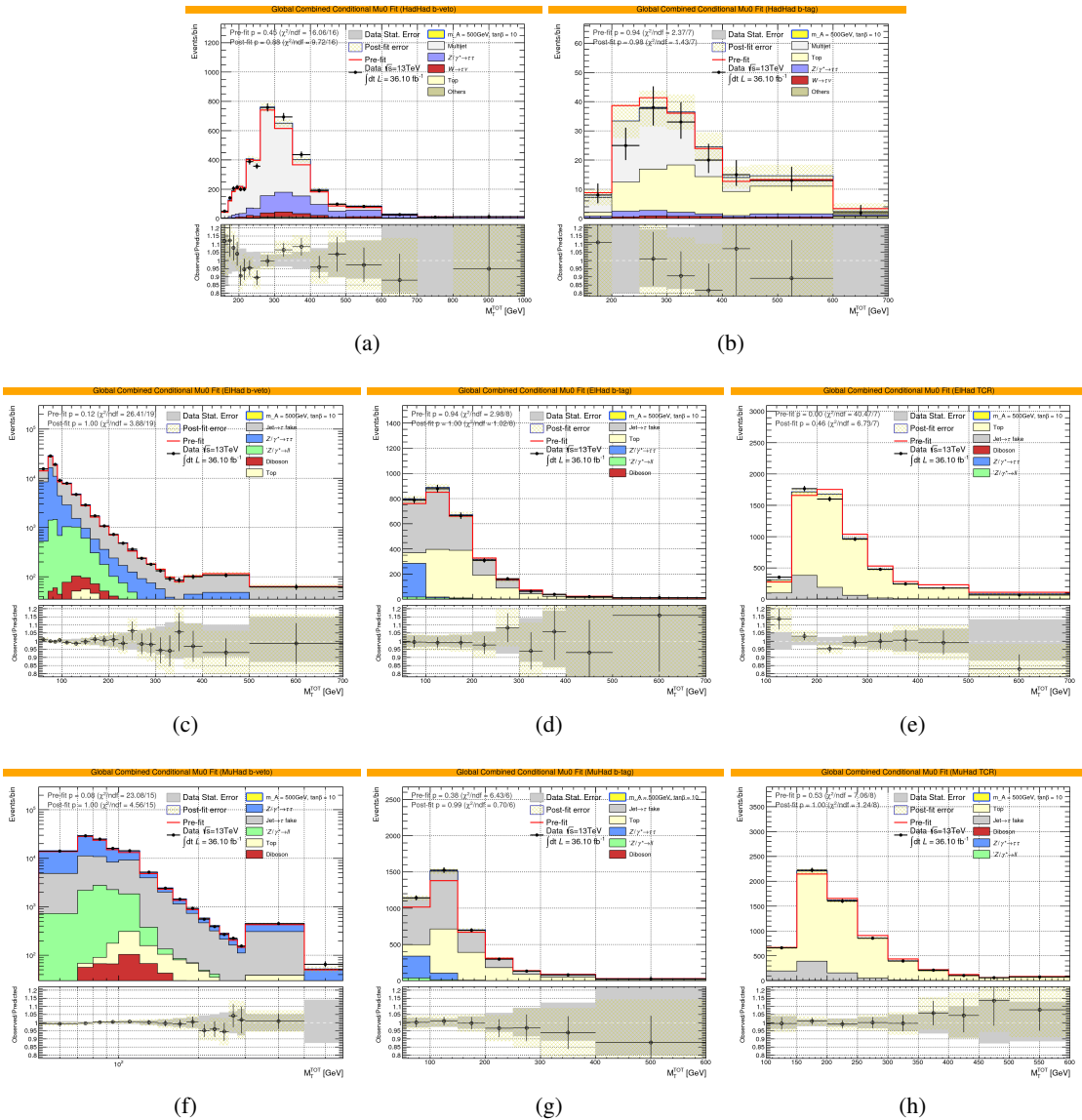


Figure 52: Post-fit m_T^{tot} distributions for the combined $\tau_{\text{had}}\tau_{\text{had}} + \tau_{\text{lep}}\tau_{\text{had}}$ conditional ($\mu = 0$) background only fit in the; $\tau_{\text{had}}\tau_{\text{had}}$ (a) b -veto, (b) b -tag; $\tau_e\tau_{\text{had}}$ (c) b -veto, (d) b -tag, (e) top-CR ; and $\tau_\mu\tau_{\text{had}}$ (c) b -veto, (d) b -tag, and (e) top-CR regions. The pre-fit histogram contains the total pre-fit background only.

860 References

- [1] ATLAS Collaboration, *Observation of a new particle in the search for the Standard Model Higgs boson with the ATLAS detector at the LHC*, *Phys. Lett. B* **716** (2012) 1, arXiv: [1207.7214 \[hep-ex\]](#).
- [2] CMS Collaboration, *Observation of a new boson at a mass of 125 GeV with the CMS experiment at the LHC*, *Phys. Lett. B* **716** (2012) 30, arXiv: [1207.7235 \[hep-ex\]](#).
- [3] ATLAS Collaboration, *Measurements of Higgs boson production and couplings in diboson final states with the ATLAS detector at the LHC*, *Phys. Lett. B* **726** (2013) 88, arXiv: [1307.1427 \[hep-ex\]](#).
- [4] ATLAS Collaboration, *Evidence for the spin-0 nature of the Higgs boson using ATLAS data*, *Phys. Lett. B* **726** (2013) 120, arXiv: [1307.1432 \[hep-ex\]](#).
- [5] CMS Collaboration, *Evidence for the direct decay of the 125 GeV Higgs boson to fermions*, *Nature Phys.* **10** (2014), arXiv: [1401.6527 \[hep-ex\]](#).
- [6] CMS Collaboration, *Measurement of the properties of a Higgs boson in the four-lepton final state*, *Phys. Rev. D* **89** (2014) 092007, arXiv: [1312.5353 \[hep-ex\]](#).
- [7] CMS Collaboration, *Measurement of Higgs boson production and properties in the WW decay channel with leptonic final states*, *JHEP* **01** (2014) 096, arXiv: [1312.1129 \[hep-ex\]](#).
- [8] F. Englert and R. Brout, *Broken symmetry and the mass of gauge vector mesons*, *Phys. Rev. Lett.* **13** (1964) 321.
- [9] P. W. Higgs, *Broken symmetries, massless particles and gauge fields*, *Phys. Lett.* **12** (1964) 132.
- [10] P. W. Higgs, *Broken symmetries and the masses of gauge bosons*, *Phys. Rev. Lett.* **13** (1964) 508.
- [11] P. W. Higgs, *Spontaneous symmetry breakdown without massless bosons*, *Phys. Rev.* **145** (1966) 1156.
- [12] G. Guralnik, C. Hagen and T. Kibble, *Global conservation laws and massless particles*, *Phys. Rev. Lett.* **13** (1964) 585.
- [13] T. Kibble, *Symmetry breaking in non-Abelian gauge theories*, *Phys. Rev.* **155** (1967) 1554.
- [14] A. Djouadi, *The Anatomy of electro-weak symmetry breaking. II. The Higgs bosons in the minimal supersymmetric model*, *Phys. Rept.* **459** (2008) 1, arXiv: [hep-ph/0503173 \[hep-ph\]](#).
- [15] G. Branco et al., *Theory and phenomenology of two-Higgs-doublet models*, *Phys. Rept.* **516** (2012) 1, arXiv: [1106.0034 \[hep-ph\]](#).
- [16] P. Fayet, *Supersymmetry and Weak, Electromagnetic and Strong Interactions*, *Phys. Lett. B* **64** (1976) 159.
- [17] P. Fayet, *Spontaneously Broken Supersymmetric Theories of Weak, Electromagnetic and Strong Interactions*, *Phys. Lett. B* **69** (1977) 489.
- [18] G. R. Farrar and P. Fayet, *Phenomenology of the Production, Decay, and Detection of New Hadronic States Associated with Supersymmetry*, *Phys. Lett. B* **76** (1978) 575.
- [19] P. Fayet, *Relations Between the Masses of the Superpartners of Leptons and Quarks, the Goldstino Couplings and the Neutral Currents*, *Phys. Lett. B* **84** (1979) 416.

- [20] S. Dimopoulos and H. Georgi, *Softly Broken Supersymmetry and SU(5)*, Nucl. Phys. **B 193** (1981) 150.
- [21] S. Heinemeyer, W. Hollik and G. Weiglein, *Constraints on tan Beta in the MSSM from the upper bound on the mass of the lightest Higgs boson*, JHEP **06** (2000) 009, arXiv: [hep-ph/9909540 \[hep-ph\]](#).
- [22] M. Carena, S. Heinemeyer, C. E. M. Wagner and G. Weiglein, *Suggestions for benchmark scenarios for MSSM Higgs boson searches at hadron colliders*, Eur. Phys. J. **C 26** (2003) 601, arXiv: [hep-ph/0202167 \[hep-ph\]](#).
- [23] M. Carena et al., *MSSM Higgs Boson Searches at the LHC: Benchmark Scenarios after the Discovery of a Higgs-like Particle*, Eur. Phys. J. **C 73** (2013) 2552, arXiv: [1302.7033 \[hep-ph\]](#).
- [24] G. Aad et al., *Combined Measurement of the Higgs Boson Mass in pp Collisions at $\sqrt{s} = 7$ and 8 TeV with the ATLAS and CMS Experiments*, Phys. Rev. Lett. **114** (2015) 191803, arXiv: [1503.07589 \[hep-ex\]](#).
- [25] A. Djouadi et al., *The post-Higgs MSSM scenario: Habemus MSSM?*, Eur. Phys. J. **C73** (2013) 2650, arXiv: [1307.5205 \[hep-ph\]](#).
- [26] E. Bagnaschi et al., *Benchmark scenarios for low tan β in the MSSM*, LHCHXSWG-2015-002, URL: <https://cds.cern.ch/record/2039911>.
- [27] P. Bechtle et al., *MSSM Interpretations of the LHC Discovery: Light or Heavy Higgs?*, Eur. Phys. J. **C 73** (2013) 2354, arXiv: [1211.1955 \[hep-ph\]](#).
- [28] A. Arbey et al., *The Higgs sector of the phenomenological MSSM in the light of the Higgs boson discovery*, JHEP **09** (2012) 107, arXiv: [1207.1348 \[hep-ph\]](#).
- [29] DELPHI, OPAL, ALEPH, LEP Working Group for Higgs Boson Searches, L3, *Search for neutral MSSM Higgs bosons at LEP*, Eur. Phys. J. **C47** (2006) 547, arXiv: [hep-ex/0602042 \[hep-ex\]](#).
- [30] D. Benjamin et al., *Combined CDF and D0 Upper Limits on MSSM Higgs Boson Production in tau-tau Final States with up to 2.2 fb-1*, (2010), arXiv: [1003.3363 \[hep-ex\]](#).
- [31] CDF Collaboration, T. Aaltonen et al., *Search for Higgs bosons predicted in two-Higgs-doublet models via decays to τ lepton pairs in 1.96 TeV proton–antiproton collisions*, Phys. Rev. Lett. **103** (2009) 201801, arXiv: [0906.1014 \[hep-ex\]](#).
- [32] D0 Collaboration, V. M. Abazov et al., *Search for Higgs bosons decaying to τ pairs in $p\bar{p}$ collisions with the D0 detector*, Phys. Rev. Lett. **101** (2008) 071804, arXiv: [0805.2491 \[hep-ex\]](#).
- [33] ATLAS Collaboration, *Search for neutral Higgs bosons of the minimal supersymmetric standard model in pp collisions at $\sqrt{s} = 8$ TeV with the ATLAS detector*, JHEP **1411** (2014) 056, arXiv: [1409.6064 \[hep-ex\]](#).
- [34] ATLAS Collaboration, *Search for the neutral Higgs bosons of the minimal supersymmetric standard model in pp collisions at $\sqrt{s} = 7$ TeV with the ATLAS detector*, JHEP **02** (2013) 095, arXiv: [1211.6956 \[hep-ex\]](#).
- [35] CMS Collaboration, *Search for neutral MSSM Higgs bosons decaying to a pair of tau leptons in pp collisions*, JHEP **10** (2014) 160, arXiv: [1408.3316 \[hep-ex\]](#).

- [36] LHCb Collaboration, R. Aaij et al.,
Limits on neutral Higgs boson production in the forward region in pp collisions at $\sqrt{s} = 7$ TeV,
JHEP **05** (2013) 132, arXiv: [1304.2591 \[hep-ex\]](#).
- [37] J. L. Hewett and T. G. Rizzo, *Low-energy phenomenology of superstring-inspired E₆ models*,
Phys. Rept. **183** (1989) 193.
- [38] M. Cvetic and S. Godfrey, *Discovery and identification of extra gauge bosons*, (1995),
arXiv: [hep-ph/9504216](#).
- [39] A. Leike, *The Phenomenology of extra neutral gauge bosons*, *Phys. Rept.* **317** (1999) 143,
arXiv: [hep-ph/9805494](#).
- [40] T. G. Rizzo, *Z' phenomenology and the LHC*,
(2006) 537, Published in Boulder, 2006, Colliders and Neutrinos (TASI 2006),
arXiv: [hep-ph/0610104](#).
- [41] R. Diener, S. Godfrey and T. A. Martin,
Unravelling an Extra Neutral Gauge Boson at the LHC using Third Generation Fermions,
PRD **83** (2011) 115008, arXiv: [1006.2845 \[hep-ph\]](#).
- [42] P. Langacker, *The Physics of Heavy Z' Gauge Bosons*,
Reviews Of Modern Physics **81** (2009) 1199, arXiv: [0801.1345 \[hep-ph\]](#).
- [43] K. R. Lynch et al.,
Finding Z' bosons coupled preferentially to the third family at LEP and the Tevatron,
PRD **63** (2001) 035006, arXiv: [hep-ph/0007286](#).
- [44] E. Malkawi, T. Tait and C.-P. Yuan, *A model of strong flavor dynamics for the top quark*,
PLB **385** (1996) 304, arXiv: [hep-ph/9603349](#).
- [45] H. D. Kim, S.-G. Kim and S. Shin,
D0 dimuon charge asymmetry from B_s system with Z' couplings and the recent LHCb result,
PRD **88** (2013) 015005, arXiv: [1205.6481 \[hep-ph\]](#).
- [46] X.-G. He and G. Valencia, *B decays with τ leptons in nonuniversal left-right models*,
PRD **87** (2013) 014014, arXiv: [1211.0348 \[hep-ph\]](#).
- [47] R. Aaij et al.,
Measurement of the ratio of branching fractions $\mathcal{B}(\bar{B}^0 \rightarrow D^{+}\tau^-\bar{\nu}_\tau)/\mathcal{B}(\bar{B}^0 \rightarrow D^{*+}\mu^-\bar{\nu}_\mu)$* ,
Phys. Rev. Lett. **115** (2015) 111803, [Addendum: *Phys. Rev. Lett.* 115,no.15,159901(2015)],
arXiv: [1506.08614 \[hep-ex\]](#).
- [48] E. Dudas, C. Petersson and R. Torre,
Collider signatures of low scale supersymmetry breaking: A Snowmass 2013 White Paper,
The Snowmass 2013 Proceedings (2013), arXiv: [1309.1179 \[hep-ph\]](#).
- [49] C. Petersson, A. Romagnoni and R. Torre, *Liberating Higgs couplings in supersymmetry*,
PRD **87**, 013008 (2013) 013008, arXiv: [1211.2114 \[hep-ph\]](#).
- [50] V. Barger, D. Marfatia and A. Peterson, *LHC and dark matter signals of Z' bosons*,
PRD **87**, 015026 (2013) 015026, arXiv: [1206.6649 \[hep-ph\]](#).
- [51] A. Hayreter and G. Valencia,
Constraining τ -lepton dipole moments and gluon couplings at the LHC,
PRD **88**, 013015 (2013) 013015, arXiv: [1305.6833 \[hep-ph\]](#).

- [52] ATLAS Collaboration, *Search for Minimal Supersymmetric Standard Model Higgs bosons H/A and for a Z' boson in the $\tau\tau$ final state produced in pp collisions at $\sqrt{s} = 13$ TeV with the ATLAS Detector*, *Eur. Phys. J. C* **76** (2016) 585, arXiv: [1608.00890 \[hep-ex\]](https://arxiv.org/abs/1608.00890).
- [53] CMS Collaboration, *Search for heavy resonances decaying to tau lepton pairs in proton-proton collisions at $\sqrt{s} = 13$ TeV*, *JHEP* **02** (2017) 048, arXiv: [1611.06594 \[hep-ex\]](https://arxiv.org/abs/1611.06594).
- [54] R. S. Chivukula and E. H. Simmons, *Electroweak limits on nonuniversal Z' bosons*, *PRD* **66** (1 2002) 015006, arXiv: [hep-ph/0205064](https://arxiv.org/abs/hep-ph/0205064).
- [55] ATLAS Collaboration, *Search for new high-mass phenomena in the dilepton final state using 36.1 fb^{-1} of proton-proton collision data at $\sqrt{s} = 13$ TeV with the ATLAS detector*, ATLAS-CONF-2017-027 (Apr. 2017), URL: <https://cds.cern.ch/record/2259039>.
- [56] CMS Collaboration, *Search for narrow resonances in dilepton mass spectra in proton-proton collisions at $\sqrt{s} = 13$ TeV and combination with 8 TeV data*, *Phys. Lett. B* **768** (2017) 57, arXiv: [1609.05391 \[hep-ex\]](https://arxiv.org/abs/1609.05391).
- [57] ATLAS Collaboration, *The ATLAS experiment at the CERN Large Hadron Collider*, *JINST* **3** (2008) S08003.
- [58] ATLAS Collaboration, *The ATLAS simulation infrastructure*, *Eur. Phys. J. C* **70** (2010) 823, arXiv: [1005.4568 \[physics.ins-det\]](https://arxiv.org/abs/1005.4568).
- [59] T. Gleisberg et al., *Event generation with SHERPA 1.1*, *JHEP* **02** (2009) 007, arXiv: [0811.4622 \[hep-ph\]](https://arxiv.org/abs/0811.4622).
- [60] S. Alioli et al., *NLO Higgs boson production via gluon fusion matched with shower in POWHEG*, *JHEP* **04** (2009) 002, arXiv: [0812.0578 \[hep-ph\]](https://arxiv.org/abs/0812.0578).
- [61] T. Sjöstrand, S. Mrenna and P. Skands, *PYTHIA 6.4 physics and manual*, *JHEP* **05** (2006) 026, arXiv: [hep-ph/0603175 \[hep-ph\]](https://arxiv.org/abs/hep-ph/0603175).
- [62] T. Sjöstrand, S. Mrenna and P. Skands, *A Brief Introduction to PYTHIA 8.1*, *Comput. Phys. Commun.* **178** (2008) 852, arXiv: [0710.3820 \[hep-ph\]](https://arxiv.org/abs/0710.3820).
- [63] J. Alwall et al., *The automated computation of tree-level and next-to-leading order differential cross sections, and their matching to parton shower simulations*, *JHEP* **07** (2014) 079, arXiv: [1405.0301 \[hep-ph\]](https://arxiv.org/abs/1405.0301).
- [64] M. Wiesemann et al, *Higgs production in association with bottom quarks*, *JHEP* **02** (2015) 132, arXiv: [1409.5301 \[hep-ph\]](https://arxiv.org/abs/1409.5301).
- [65] T. Sjöstrand et al., *An Introduction to PYTHIA 8.2*, *Comput. Phys. Commun.* **191** (2015) 159, arXiv: [1410.3012 \[hep-ph\]](https://arxiv.org/abs/1410.3012).
- [66] Z. Czyczula, T. Przedzinski and Z. Was, *TauSpinner Program for Studies on Spin Effect in tau Production at the LHC*, *epjc* **72** (2012) 1988, arXiv: [1201.0117 \[hep-ph\]](https://arxiv.org/abs/1201.0117).
- [67] R. D. Ball et al., *Parton distributions with LHC data*, *Nucl. Phys. B* **867** (2013) 244, arXiv: [1207.1303 \[hep-ph\]](https://arxiv.org/abs/1207.1303).
- [68] GEANT4 Collaboration, S. Agostinelli et al., *GEANT4 - a simulation toolkit*, *Nucl. Instrum. Meth. A* **506** (2003) 250.

- Not reviewed, for internal circulation only
- [69] ATLAS Collaboration, *The ATLAS Experiment at the CERN Large Hadron Collider*, JINST **3** (2008) S08003.
 - [70] ATLAS Tau Group, *Tau Recommendations*, (2017), URL: <https://twiki.cern.ch/twiki/bin/view/AtlasProtected/TauRecommendationsMoriond2017>.
 - [71] ATLAS E/Gamma Group, *E/Gamma Recommendations*, (2017), URL: <https://twiki.cern.ch/twiki/bin/view/AtlasProtected/EGammaRecommendations>.
 - [72] ATLAS Muon Group, *Muon Recommendations*, (2017), URL: https://twiki.cern.ch/twiki/bin/view/AtlasProtected/MCPAnalysisGuidelinesMC15#NEW_Recommendations_for_Moriond.
 - [73] M. Cacciari, G. P. Salam and G. Soyez, *The Anti- k_t jet clustering algorithm*, JHEP **0804** (2008) 063, arXiv: [0802.1189 \[hep-ph\]](https://arxiv.org/abs/0802.1189).
 - [74] M. Cacciari and G. P. Salam, *Dispelling the $N^{**}3$ myth for the k_t jet-finder*, Phys.Lett. **B641** (2006) 57, arXiv: [hep-ph/0512210 \[hep-ph\]](https://arxiv.org/abs/hep-ph/0512210).
 - [75] M. Cacciari, G. P. Salam and G. Soyez, *The Catchment Area of Jets*, JHEP **04** (2008) 005, arXiv: [0802.1188 \[hep-ph\]](https://arxiv.org/abs/0802.1188).
 - [76] ATLAS Collaboration, *Pile-up subtraction and suppression for jets in ATLAS*, (2013), URL: <http://cds.cern.ch/record/1570994..>
 - [77] ATLAS JetEtMiss Group, *ATLAS JetEtMiss group recommendation*, (2017), URL: <https://twiki.cern.ch/twiki/bin/view/AtlasProtected/JetEtmissRecommendationsMC15>.
 - [78] ATLAS Flavour Tagging Group, *ATLAS Flavour Tagging group recommendation*, (2017), URL: <https://twiki.cern.ch/twiki/bin/view/AtlasProtected/BTagCalib2015>.
 - [79] ATLAS Etmiss Subgroup, *Etmiss Recommendations*, (2017), URL: <https://twiki.cern.ch/twiki/bin/view/AtlasProtected/EtmissSubgroup>.
 - [80] ATLAS Collaboration, *Reconstruction of Soft Missing Transverse Momentum with Inner Detector Tracks*, ATL-COM-PHYS-2015-209, URL: [https://cds.cern.ch/record/2002888](http://cds.cern.ch/record/2002888).
 - [81] A. Elagin et al., *A New Mass Reconstruction Technique for Resonances Decaying to di-tau*, (2010), * Temporary entry *, arXiv: [1012.4686 \[hep-ex\]](https://arxiv.org/abs/1012.4686).
 - [82] ATLAS Collaboration, *Search for neutral MSSM Higgs bosons H/A to taulep tauhad and Z' to taulep tauhad produced in 13 TeV collisions with the ATLAS detector*, ATL-COM-PHYS-2015-604, URL: [https://cds.cern.ch/record/2030187](http://cds.cern.ch/record/2030187).
 - [83] ATLAS Collaboration, *Measurement of the tau lepton reconstruction and identification performance in the ATLAS experiment using pp collisions at $\sqrt{s} = 13$ TeV*, ATL-COM-PHYS-2016-929, URL: [https://cdsweb.cern.ch/record/2199788](http://cdsweb.cern.ch/record/2199788).
 - [84] ATLAS Collaboration, *Evidence for the Higgs-boson Yukawa coupling to tau leptons with the ATLAS detector*, JHEP **04** (2015) 117, arXiv: [1501.04943 \[hep-ex\]](https://arxiv.org/abs/1501.04943).
 - [85] ATLAS Collaboration, *Supporting Document for the Search for the bb decay of the Standard Model Higgs boson in associated (W/Z)H production with the ATLAS detector*, ATL-COM-PHYS-2014-051, URL: [https://cds.cern.ch/record/1645654](http://cds.cern.ch/record/1645654).

- [86] LHC Top Physics Working Group, *ATLAS-CMS recommended predictions for single-top cross sections using the Hathor v2.1 program*, (2017),
URL: <https://twiki.cern.ch/twiki/bin/view/LHCPhysics/SingleTopRefXsec>.
- [87] LHC Top Physics Working Group, *ATLAS-CMS recommended predictions for top-quark-pair cross sections using the Top++v2.0 program*, (2017),
URL: <https://twiki.cern.ch/twiki/bin/view/LHCPhysics/TtbarNNLO>.
- [88] J. Butterworth et al.,
Single Boson and Diboson Production Cross Sections in pp Collisions at $\sqrt{s}=7$ TeV, ATL-COM-PHYS-2010-695 (Aug. 2010), URL: <https://cds.cern.ch/record/1287902>.
- [89] A. L. Read, *Presentation of search results: the CL_s technique*, *J. Phys. G* **28** (2002) 2693.
- [90] G. Cowan, K. Cranmer, E. Gross and O. Vitells,
Asymptotic formulae for likelihood-based tests of new physics, *Eur. Phys. J. C* **71** (2011) 1554, arXiv: [1007.1727 \[physics.data-an\]](https://arxiv.org/abs/1007.1727).
- [91] A. Kaczmarzka et al., *Application of TauSpinner for studies on tau-lepton polarization and spin correlations in Z, W and H decays at LHC*, (2014), arXiv: [1402.2068 \[hep-ph\]](https://arxiv.org/abs/1402.2068).
- [92] S. Banerjee et al.,
Ascertaining the spin for new resonances decaying into tau+ tau- at Hadron Colliders, *Eur.Phys.J. C* **73** (2013) 2313, arXiv: [1212.2873 \[hep-ph\]](https://arxiv.org/abs/1212.2873).
- [93] ATLAS Collaboration, *A search for high-mass resonances decaying to $\tau^+\tau^-$ in pp collisions at $\sqrt{s} = 8$ TeV with the ATLAS detector*, ATL-PHYS-INT-2015-006, URL: <https://cds.cern.ch/record/2006867>.
- [94] J. Butterworth et al., ‘THE TOOLS AND MONTE CARLO WORKING GROUP Summary Report from the Les Houches 2009 Workshop on TeV Colliders’, *Physics at TeV colliders. Proceedings, 6th Workshop, dedicated to Thomas Binoth, Les Houches, France, June 8-26, 2009*, 2010, arXiv: [1003.1643 \[hep-ph\]](https://arxiv.org/abs/1003.1643).
- [95] J. Butterworth et al., *PDF4LHC recommendations for LHC Run II*, *J. Phys. G* **43** (2016) 023001, arXiv: [1510.03865 \[hep-ph\]](https://arxiv.org/abs/1510.03865).
- [96] A. Buckley et al., *LHAPDF6: parton density access in the LHC precision era*, *Eur. Phys. J. C* **75** (2015) 132, arXiv: [1412.7420 \[hep-ph\]](https://arxiv.org/abs/1412.7420).
- [97] ATLAS Collaboration, *ATLAS Run I Pythia8 tunes*, ATL-PHYS-PUB-2014-021 (2014), URL: <http://cds.cern.ch/record/1966419>.
- [98] ATLAS Collaboration, *Measurement of the transverse momentum distribution of Z/gamma* bosons in proton-proton collisions at roots = 7 TeV with the ATLAS detector : Update with 4.7 fb-1 of the previous measurement at this energy.*, ATL-COM-PHYS-2013-117 (2013), URL: <https://cds.cern.ch/record/1513133>.
- [99] ATLAS Flavour Tagging WG, ‘Expected flavour tagging performance in release 20.7’, URL: <https://twiki.cern.ch/twiki/bin/view/AtlasProtected/BTaggingBenchmarksRelease20>.
- [100] Q.-H. Cao et al.,
Discovery and identification of W' and Z' in $SU(2)_1 \otimes SU(2)_2 \otimes U(1)_X$ models at the LHC, *PRD* **86**, 095010 (Nov. 2012) 095010, arXiv: [1205.3769 \[hep-ph\]](https://arxiv.org/abs/1205.3769).

- 1106 [101] K. Y. Lee, *Lepton flavor violation in a nonuniversal gauge interaction model*,
1107 PRD **82**, 097701 (Nov. 2010) 097701, arXiv: [1009.0104](https://arxiv.org/abs/1009.0104) [hep-ph].
- 1108 [102] K. Y. Lee, *Unitarity violation of the CKM matrix in a nonuniversal gauge interaction model*,
1109 PRD **71**, 115008 (June 2005) 115008, eprint: [hep-ph/0410381](https://arxiv.org/abs/hep-ph/0410381).

[Not reviewed, for internal circulation only]

1110 Auxiliary material

1111 A. Signal Samples

1112 A.1. Validation of the bbH fast simulation

1113 Signal samples for the bbH production process were generated using Altfast-II (AF2) in MadGraph5_aMC@NLO.
 1114 Validation tests were performed to ensure that AF2 and Full Simulation (FS) results were comparable.
 1115 Test samples of 280500(277348) events were generated using AF2(FS) at the 1 TeV mass point, with a
 1116 scale factor applied to FS samples to account for the difference in sample size.

1117 In the lep-had channel, the leading Tau p_T (Fig. 53 and 58), E_T^{miss} (Fig. 54 and 59), Visible Mass (Fig. 55
 1118 and 60), MOSAIC (m_H) mass reconstruction (Fig. 56 and 61) and MMC mass reconstruction (Fig. 57
 1119 and 62) variables were compared directly. For both samples, no scale factors (other than that accounting
 1120 for the event number discrepancy) or weights are included; raw numbers only are used. Variables are
 1121 compared both before the lep-had cutflow (with all high-level trigger cuts applied) (Fig. 53, 54, 55, 56 and
 1122 57) and after the full lep-had cutflow (Fig. 58, 59, 60, 61 and 62).

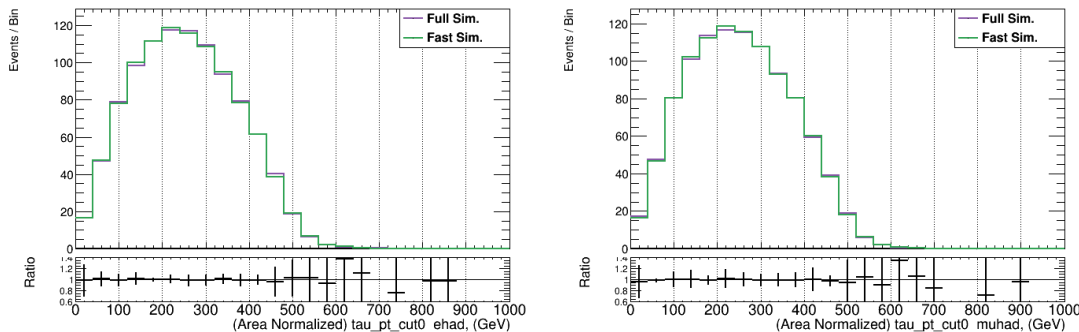


Figure 53: Tau p_T (HLT Cuts Only), separately for e -channel (left) and μ -channel (right).

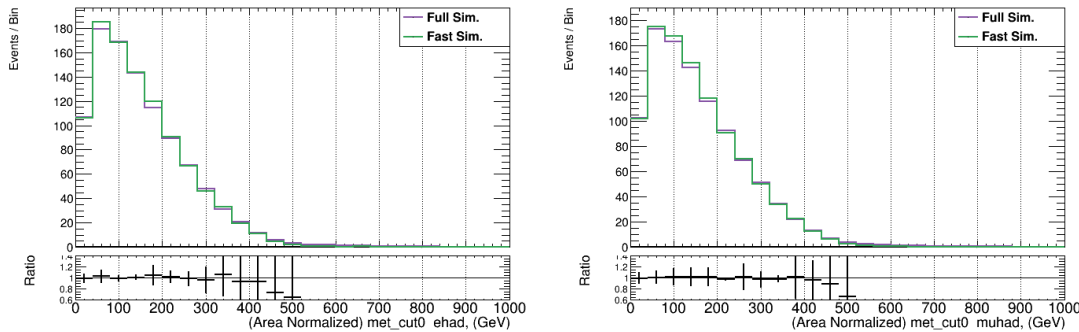


Figure 54: E_T^{miss} (HLT Cuts Only), separately for e -channel (left) and μ -channel (right).

1123 Variations between the fast and full simulation methods are minimal, with the exception of consistently
 1124 lower yields in E_T^{miss} in the fast simulation. In the e-had channel, the yield of the full (fast) simulation

Not reviewed, for internal circulation only

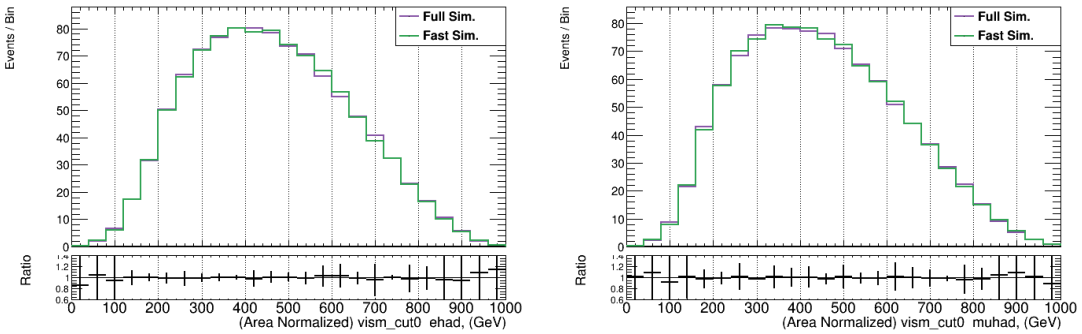


Figure 55: Visible Mass (HLT Cuts Only), separately for e -channel (left) and μ -channel (right).

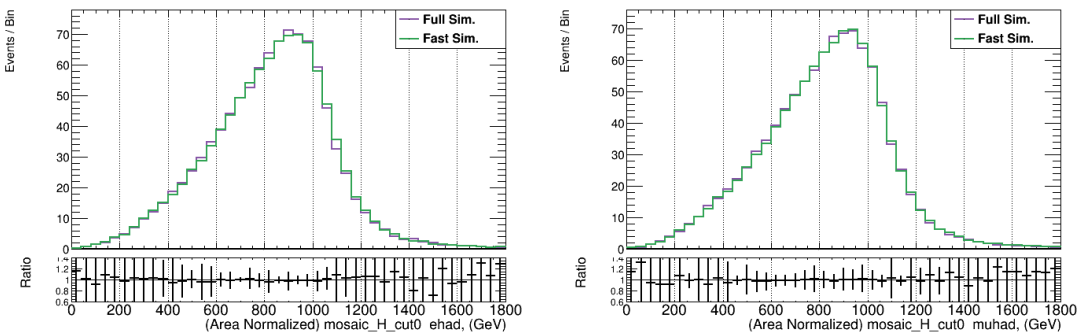


Figure 56: MOSAIC (m_H) (HLT Cuts Only), separately for e -channel (left) and μ -channel (right).

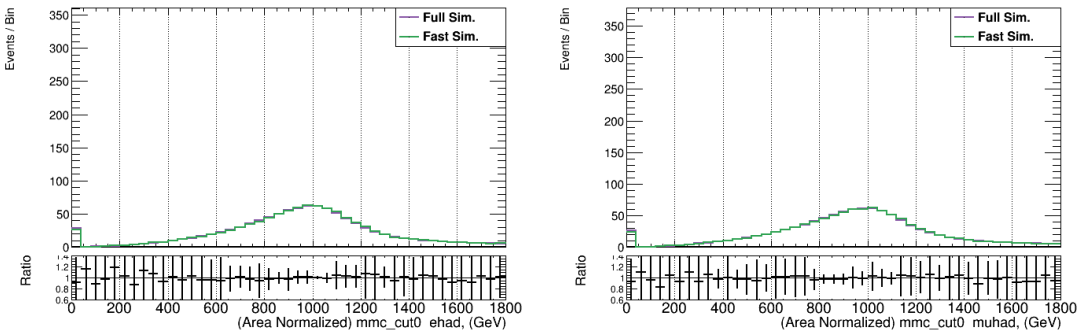


Figure 57: MMC (HLT Cuts Only), separately for e -channel (left) and μ -channel (right).

1125 is 40002.50 ± 201.14 (40089 ± 200.22) events, giving a discrepancy of 0.216%. In the mu-had channel,
 1126 the full (fast) yield is 45652 ± 214.87 (46331 ± 215.24), giving a discrepancy of 1.49%. These results
 1127 suggest that the fast simulation method is consistent with the full simulation method within approximately
 1128 2%.

Not reviewed, for internal circulation only

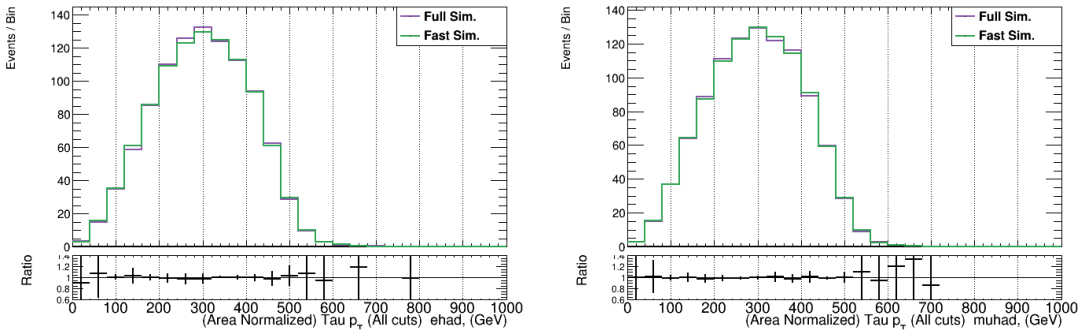


Figure 58: Tau p_T (All Cuts Applied), separately for e -channel (left) and μ -channel (right).

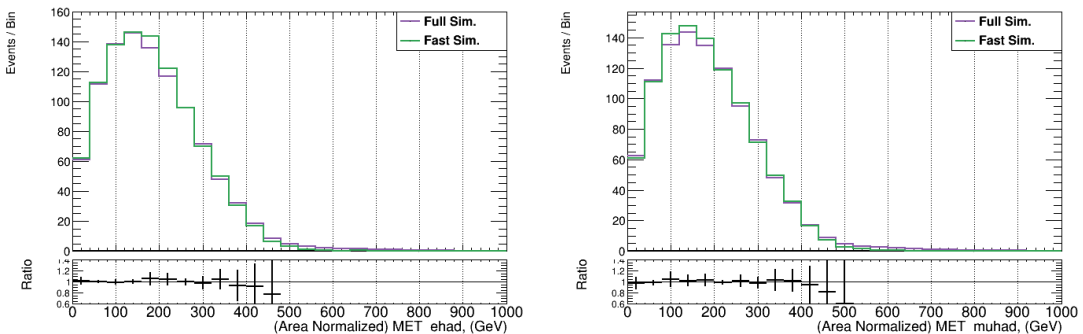


Figure 59: E_T^{miss} (All Cuts Applied), separately for e -channel (left) and μ -channel (right).

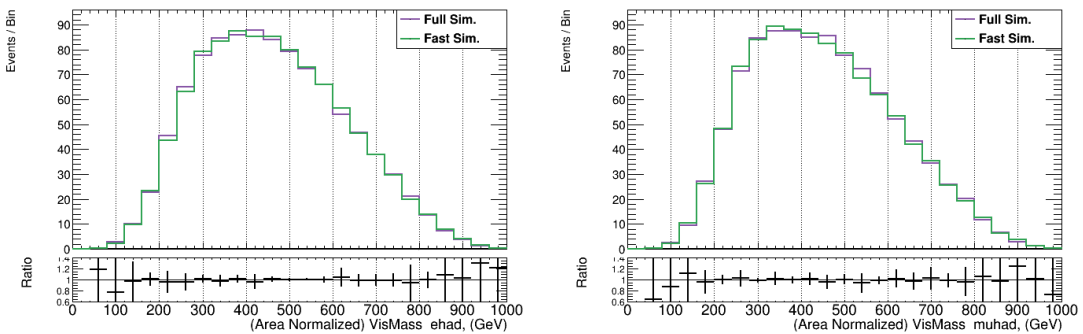


Figure 60: Visible Mass (All Cuts Applied), separately for e -channel (left) and μ -channel (right).

1129 A.2. $Z/\gamma^* \rightarrow Z'$ reweighting validation

1130 The reweighting provided by the TauSpinner algorithm, including the extension to allow reweighting for
 1131 BSM processes, has been extensively validated [66, 91–93]. In this section the validation of the Born-level
 1132 cross sections for Z' production that has been provided to TauSpinner is described.

1133 As an additional cross-check to validate the reweighting at 13 TeV a simulated Z' signal sample with a
 1134 resonance mass of 3 TeV is compared to $Z/\gamma^* \rightarrow \tau\tau$ reweighted to a signal with the same mass. The

Not reviewed, for internal circulation only

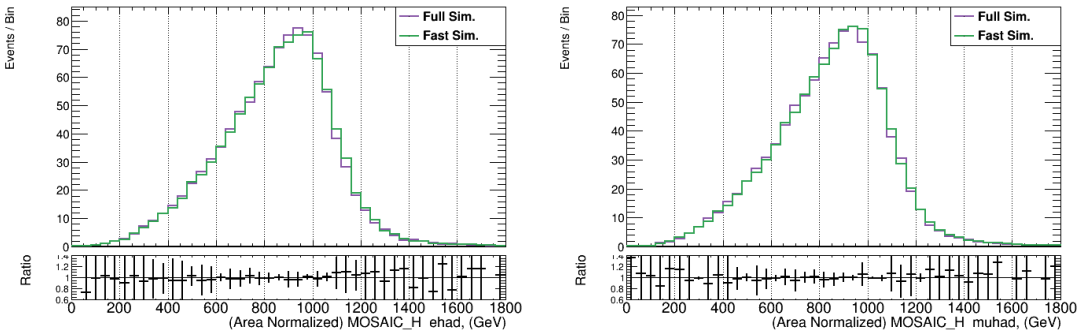


Figure 61: MOSAIC (m_H) (All Cuts Applied), separately for e -channel (left) and μ -channel (right).

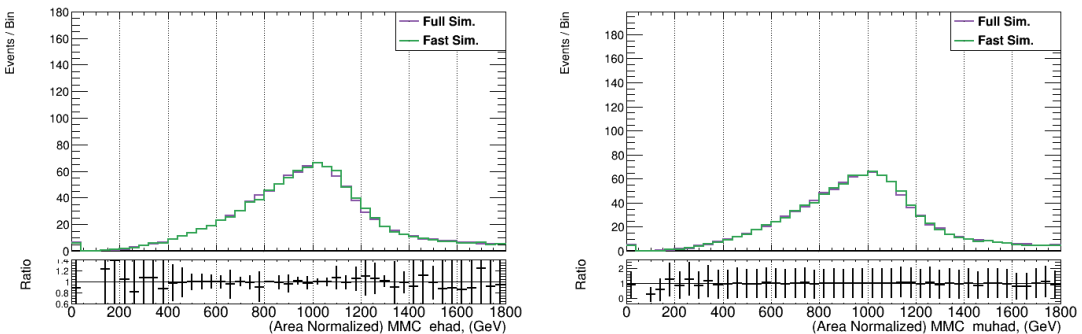


Figure 62: MMC (All Cuts Applied), separately for e -channel (left) and μ -channel (right).

1135 lowest available generated resonance mass for the $Z/\gamma^* \rightarrow \tau\tau$ slices is 70 GeV and so for consistency
 1136 events with a resonance mass below 70 GeV are not considered for the Z' signal sample. The simulated
 1137 Z' signal sample is generated without τ spin weights. This makes it necessary to use TauSpinner for
 1138 applying weights to correct for that. The effect can be seen in the Fig. 63, which shows the fraction of the
 1139 charged pion momentum with respect to the full tau momentum for $\tau^\pm \rightarrow \pi^\pm \nu$ decays.

1140 Fig. 64 depicts the generator level resonance mass. Reasonable agreement is found over the whole mass
 1141 range. Fig. 65 and 66 show various kinematic distributions of the tau leptons at generator level and the
 1142 mass variables of the missing transverse mass and the total transverse mass m_T^{tot} .

Not reviewed, for internal circulation only

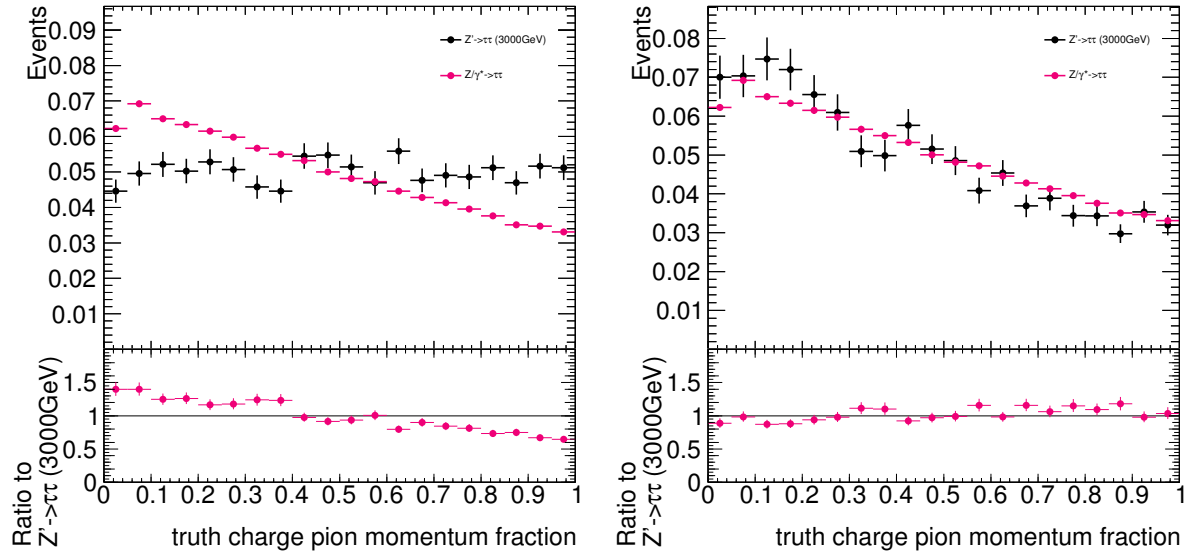


Figure 63: Fraction of the charged pion momentum with respect to the full tau momentum for $\tau^\pm \rightarrow \pi^\pm \nu$ decays. The black distribution shows the generated Z' without (left) and with (right) spin weights from TauSpinner applied.

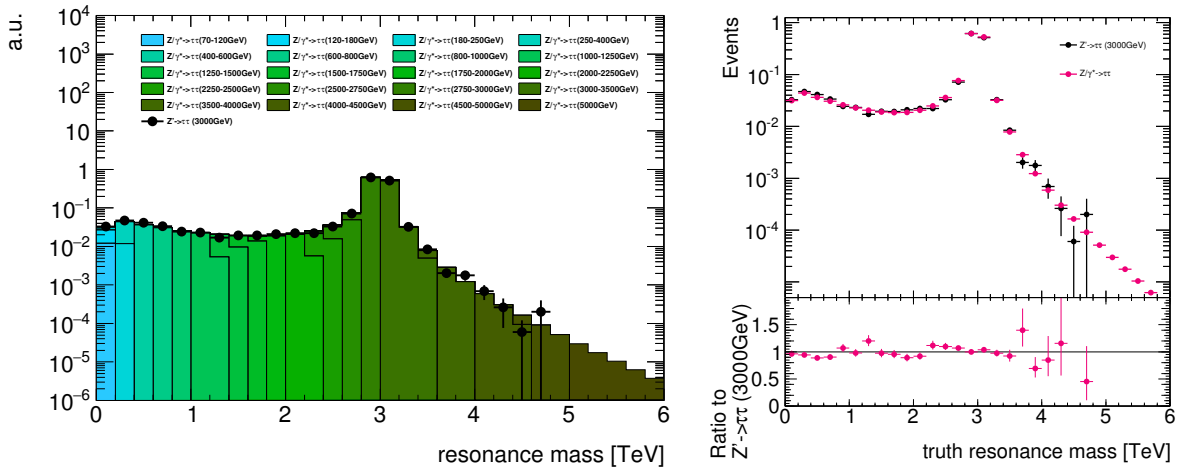


Figure 64: Generator-level resonance mass for Z' with $m_{Z'} = 3$ TeV events generated with Pythia8, and also for $Z/\gamma^* \rightarrow \tau\tau$ events generated with Pythia8 reweighted to the same mass. The left plot shows $Z/\gamma^* \rightarrow \tau\tau$ samples splitted in the various slices while the right plot shows the inclusive $Z/\gamma^* \rightarrow \tau\tau$.

Not reviewed, for internal circulation only

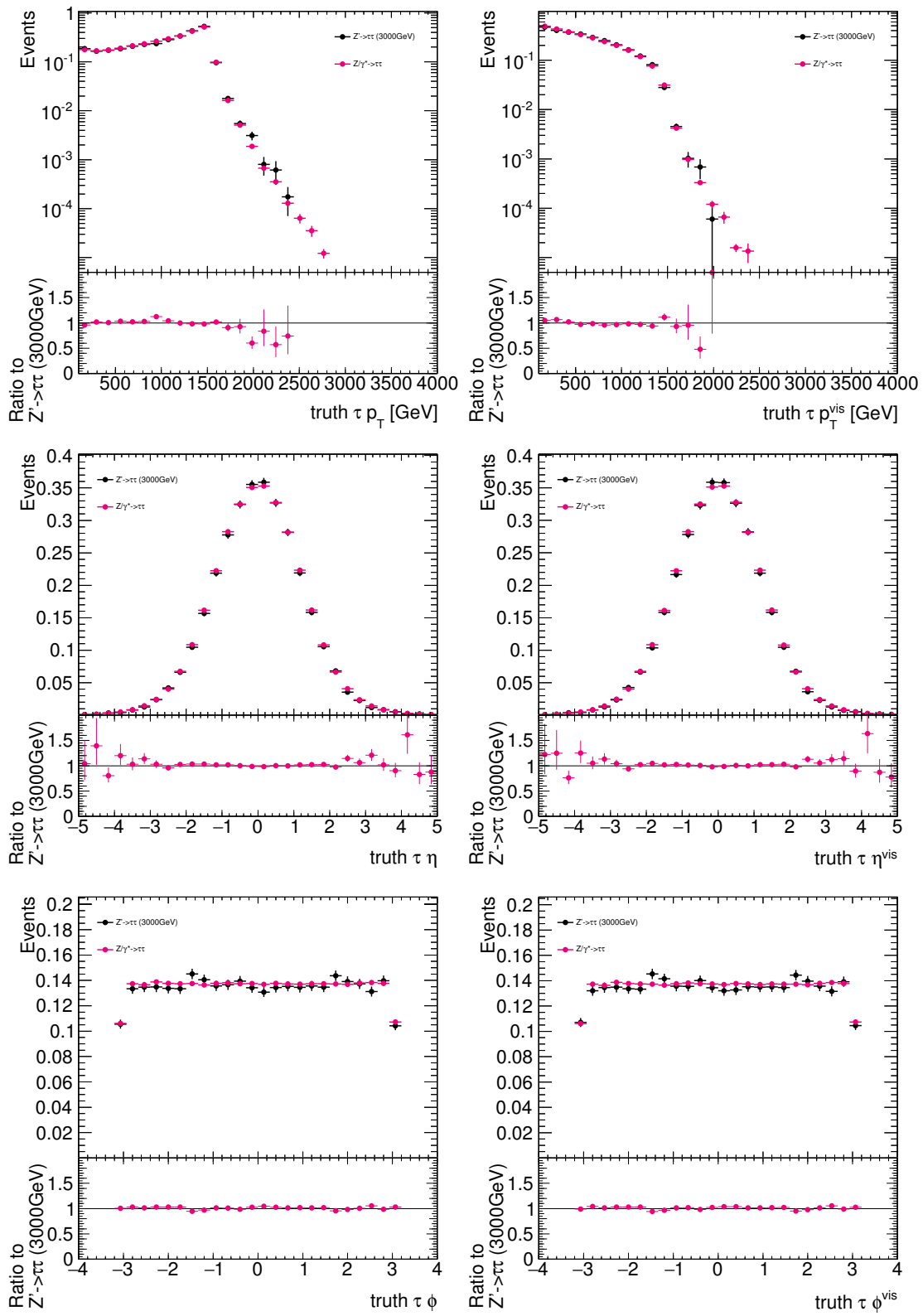


Figure 65: Generator-level full and visible kinematic variables of tau leptons from for Z' with $m_{Z'} = 3$ TeV events generated with Pythia8, and also for $Z/\gamma^* \rightarrow \tau\tau$ events generated with Pythia8 reweighted to the same mass.

Not reviewed, for internal circulation only

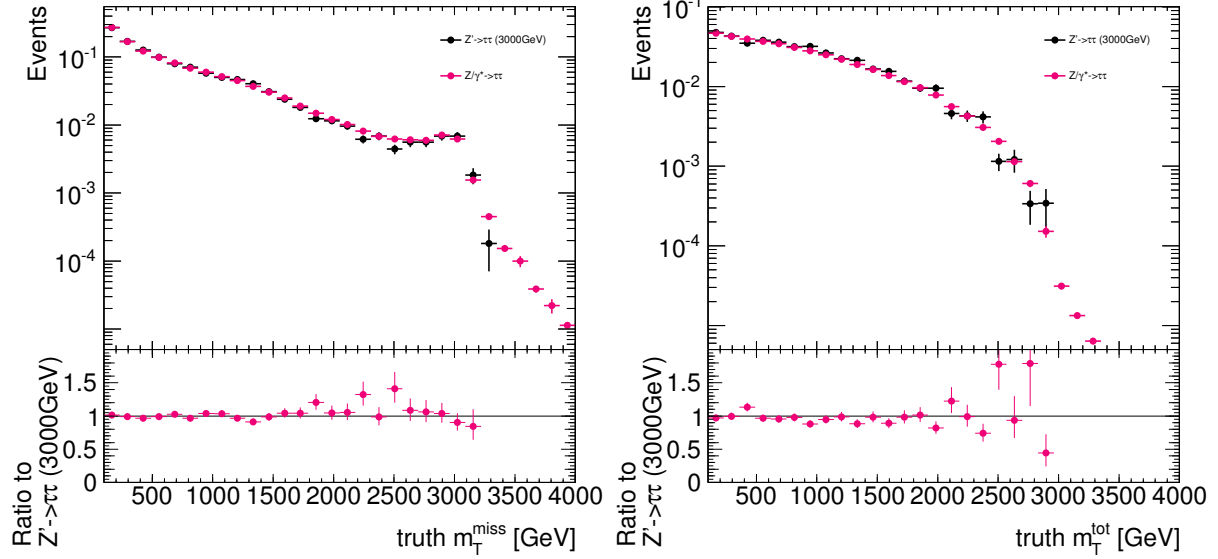


Figure 66: Generator-level event mass distributions E_T^{miss} and m_T^{tot} for Z' with $m_{Z'} = 3$ TeV events generated with Pythia8, and also for $Z/\gamma^* \rightarrow \tau\tau$ events generated with Pythia8 reweighted to the same mass.

1143 B. Signal width

1144 Figure 67 shows the relative width of the signal hypothesis in the hMSSM model. From these plots, it can
 1145 be seen that the width is generally less than 6% of the Higgs boson mass, which less than the resolution
 1146 of the final discriminant, m_T^{tot} .

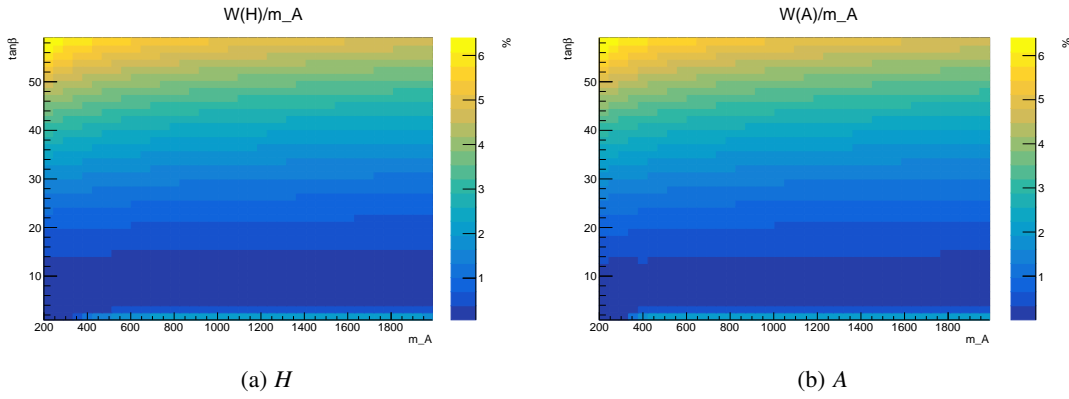


Figure 67: The relative width of (a) H and (b) A for the hMSSM model.

Not reviewed, for internal circulation only

1147 C. Details on Signal Acceptance Uncertainty Estimation

1148 To estimate the impact of uncertainties of factorisation and renormalisation scales, these were varied by a
 1149 factor of 2 up and down, including correlated and anti-correlated variations. The results of these variations
 1150 are provided by the respective matrix element generator (aMcAtNlo for the b -associated production signal
 1151 and Powheg for the gluon-fusion signal) as vector of weights stored per event in the LHEF event record [94]
 1152 and propagated to the showered samples. The largest deviation from the nominal in each direction was
 1153 taken as final scale uncertainty.

1154 To estimate the uncertainty due to the parton density function on the gluon-fusion signal samples, LHEF
 1155 weights vectors containing a weight for every PDF in PDF4LHC15_nlo_100 [95] are generated. For
 1156 the b -associated production sample the LHE reweighting approach is not possible, instead the LHAPDF
 1157 software package [96] was utilized to compute event weights for each PDF in the PDF4LC15_nlo_nf4_30.
 1158 The envelope of the resulting variations in acceptance was chosen as combined pdf uncertainty.

1159 For the estimation of uncertainties arising due to ISR, FSR and MPI modeling, tune variations of the
 1160 Pythia8 A14 tune [97] for the b -associated signal samples and of the AZNLO Pythia8 tune [98] for the
 1161 gluon-fusion samples were studied. The tune uncertainties are combined by quadratic summation for each
 1162 direction of acceptance change.

1163 None of the considered generator parameter variations resulted in a statistically significant effect on the
 1164 shape of the reconstructed mass distribution, so all the systematic effects are considered as normalisation
 1165 uncertainties. In the limit setting only the combined uncertainty per mass point will be considered.

1166 A selection close to the full analysis selection was implemented at particle level and the change in
 1167 acceptance due to the differently weighted events was evaluated.

1168 C.1. Event Selection

1169 Using release 20.1.8.3, the EVNT samples are converted to TRUTH1 derivations, which include prepro-
 1170 cessed truth particle containers, as well as truth jet collections and truth MET.

1171 The event selection in the $\tau_{\text{had}}\tau_{\text{had}}$ channel is as follows:

- 1172 • at least two $\tau_{\text{had-vis}}$ with $p_T > 40 \text{ GeV}$
- 1173 • no electron with $p_T > 15 \text{ GeV}$
- 1174 • no muon with $p_T > 7, \text{ GeV}$
- 1175 • leading $\tau_{\text{had-vis}} p_T > 85 \text{ GeV}$
- 1176 • subleading $\tau_{\text{had-vis}} p_T > 65 \text{ GeV}$
- 1177 • $\Delta\phi(\tau, \tau) > 2.7$
- 1178 • opposite charge

1179 An event weight is applied depending on the leading $\tau_{\text{had-vis}} p_T$ to emulate the different p_T thresholds. The
 1180 weight depends on the integrated luminosities of each lowest unprescaled single-tau trigger.

1181 The event selection in the $\tau_{\text{lep}}\tau_{\text{had}}$ channel is as follows:

- 1182 • at least one $\tau_{\text{had-vis}}$ with $p_T > 25 \text{ GeV}$
 1183 • exactly one muon or electron with $p_T > 30 \text{ GeV}$ (and none of the other respectively)
 1184 • $\Delta\phi(\ell, \tau) > 2.4$
 1185 • opposite charge
 1186 • $m_T(E_T^{\text{miss}}, \ell) < 40 \text{ GeV}$
 1187 • veto $80 < m_{\text{vis}}(e, \tau_{\text{had-vis}}) < 110 \text{ GeV}$
- 1188 Electrons, muons and $\tau_{\text{had-vis}}$ have to satisfy the same pseudorapidity selections as in the main analysis.
 1189 An overlap removal is performed, using the same ΔR and object priorities as described in Sec. ??.
- 1190 An event weight is calculated which corresponds to the probability of the event being b -tagged, w_{tag} . This
 1191 is based on the b -tagging performance benchmark for the working point used in the main analysis. For
 1192 each truth jet with $p_T > 20 \text{ GeV}$ and $|\eta| < 2.5$, the probability of the event not being tagged, $1 - \epsilon_{\text{tag}}$, which
 1193 depends on the jet flavor (utilizing HadronConeExclTruthLabelID), is multiplied to the event weight.
 1194 The values of the tagging efficiency ϵ_{tag} used are [99]: 0.6997 (b), 0.0822 (c), 0.0183 (τ) and 0.0026
 1195 (light jets). Events for the b -tag category are weighted by w_{tag} , for the b -veto category with $(1 - w_{\text{tag}})$.

Not reviewed, for internal circulation only

1196 **C.2. Uncertainty Evaluation**

The uncertainty on the acceptance due to systematic variation var_i is calculated as

$$\sigma(\text{var}_i) = \frac{N_{\text{selected}}(\text{var}_i) \times N_{\text{initial}}(\text{nominal})}{N_{\text{initial}}(\text{var}_i) \times N_{\text{selected}}(\text{nominal})} - 1,$$

1197 with N being the MC-weighted number of events before or after the selection.

1198 The uncertainties are listed in Tables 14–17. For the b -associated Higgs production samples, the absolute
 1199 value of the MC weight is used to reduce the statistical uncertainty. This approach is discussed further in
 1200 Sect. C.3.

1201 **C.3. Negative Weight Fractions in b-associated events**

1202 The b -associated Higgs production signal samples have a large fraction of negatively weighted events.
 1203 However, the distribution of the absolute MC weight has very little spread. Therefore, ignoring the sign
 1204 of the weight is a viable option in case the fraction of negatively weighted events is not significantly
 1205 changed by the systematic variations and the event selection. As listed in Table 18, the change in the
 1206 negative weight fraction due to the systematic variations is very small before the event selection. After the
 1207 event selection it is a bit bigger, but at this stage the statistical uncertainty is also significantly increased.
 1208 Furthermore, the magnitudes of the shifts in the negative weight fraction is still significantly smaller than
 1209 the acceptance uncertainties that are calculated when taking the sign of the MC weights into account
 1210 (Tables 19 and 20) and not even the sign of the shift seems to be correlated with the sign of the acceptance
 1211 uncertainty, suggesting that the small shift in negative weight fraction is not the cause of the majority of
 1212 the uncertainty effect.

syst. variation	<i>b</i> -tag			<i>b</i> -veto		
	400 GeV	700 GeV	1000 GeV	400 GeV	700 GeV	1000 GeV
fac up, ren def	0.11	0.35	0.41	0.40	0.14	0.01
fac down, ren def	-0.12	-0.39	-0.47	-0.51	-0.19	-0.04
fac def, ren up	0.35	0.13	0.16	-0.50	-0.41	-0.38
fac up, ren up	0.46	0.48	0.57	-0.09	-0.25	-0.36
fac down, ren up	0.22	-0.26	-0.30	-1.02	-0.60	-0.43
fac def, ren down	-0.45	-0.15	-0.15	0.59	0.46	0.41
fac up, ren down	-0.34	0.20	0.26	0.97	0.59	0.41
fac down, ren down	-0.56	-0.54	-0.62	0.09	0.29	0.38
Var1Down	-1.21	-0.29	-0.42	-0.54	0.49	-0.26
Var1Up	1.23	0.04	0.45	-0.66	0.56	-0.35
Var2Down	-0.29	0.39	0.09	-0.19	-0.34	-0.84
Var2Up	-2.09	-1.48	0.32	0.65	1.12	0.24
Var3aDown	0.16	-0.55	0.58	1.60	0.32	-0.35
Var3aUp	-1.12	-0.81	-0.38	0.55	1.14	-0.00
PDF variance	0.01	0.01	0.01	0.00	0.01	0.00
PDF mean	0.92	1.04	1.12	0.65	0.63	0.59
PDF max	1.16	1.32	1.35	0.83	0.91	0.68
PDF min	0.77	0.86	0.91	0.53	0.52	0.49
QCD scale	+0.46 -0.56	+0.48 -0.54	+0.57 -0.62	+0.97 -1.02	+0.59 -0.60	+0.41 -0.43
tune	+1.24 -2.68	+0.39 -1.80	+0.80 -0.57	+1.81 -0.87	+1.79 -0.34	+0.24 -1.01
pdf	+0.24 -0.15	+0.28 -0.18	+0.22 -0.21	+0.18 -0.12	+0.28 -0.11	+0.09 -0.10
combined	+1.34 -2.74	+0.68 -1.89	+1.01 -0.87	+2.06 -1.35	+1.91 -0.70	+0.48 -1.10
symmetric	± 2.04	± 1.28	± 0.94	± 1.70	± 1.30	± 0.79

Table 14: Relative signal acceptance uncertainties (in percent) for *b*-associated production in the $\tau_{\text{had}}\tau_{\text{had}}$ channel.

Not reviewed, for internal circulation only

syst. variation	<i>b</i> -tag			<i>b</i> -veto		
	200 GeV	500 GeV	1000 GeV	200 GeV	500 GeV	1000 GeV
fac up, ren def	-0.30	0.26	0.41	0.82	0.31	0.03
fac down, ren def	0.44	-0.29	-0.47	-1.03	-0.38	-0.07
fac def, ren up	0.88	0.32	0.16	-0.61	-0.47	-0.37
fac up, ren up	0.57	0.58	0.58	0.22	-0.15	-0.33
fac down, ren up	1.30	0.03	-0.30	-1.64	-0.87	-0.45
fac def, ren down	-0.76	-0.36	-0.22	0.73	0.51	0.38
fac up, ren down	-1.04	-0.10	0.21	1.54	0.81	0.39
fac down, ren down	-0.30	-0.65	-0.70	-0.30	0.13	0.32
Var1Down	-1.04	-0.27	-0.72	-1.11	-0.26	-0.29
Var1Up	2.67	1.37	0.71	-0.91	-0.23	-0.85
Var2Down	2.29	0.96	-0.01	-1.46	-1.14	-0.17
Var2Up	-3.50	1.41	-0.21	1.22	0.84	1.76
Var3aDown	0.89	2.34	0.36	0.52	-0.27	0.23
Var3aUp	0.79	0.39	0.28	1.90	0.08	0.51
PDF variance	0.01	0.01	0.01	0.01	0.00	0.00
PDF mean	0.89	1.03	1.05	0.64	0.74	0.55
PDF max	1.13	1.28	1.25	0.97	0.90	0.64
PDF min	0.67	0.87	0.86	0.44	0.62	0.45
QCD scale	+1.30 -1.04	+0.58 -0.65	+0.58 -0.70	+1.54 -1.64	+0.81 -0.87	+0.39 -0.45
tune	+3.71 -3.65	+3.23 -0.27	+0.85 -0.75	+2.32 -2.05	+0.85 -1.22	+1.84 -0.92
pdf	+0.24 -0.22	+0.24 -0.16	+0.20 -0.19	+0.34 -0.20	+0.17 -0.12	+0.09 -0.11
combined	+3.94 -3.80	+3.29 -0.72	+1.05 -1.04	+2.80 -2.63	+1.18 -1.50	+1.89 -1.03
symmetric	± 3.87	± 2.00	± 1.04	± 2.72	± 1.34	± 1.46

Table 15: Relative signal acceptance uncertainties (in percent) for *b*-associated production in the $\tau_{\text{lep}}\tau_{\text{had}}$ channel.

Not reviewed, for internal circulation only

syst. variation	<i>b</i> -tag			<i>b</i> -veto		
	400 GeV	700 GeV	1000 GeV	400 GeV	700 GeV	1000 GeV
fac def, ren down	2.42	1.71	1.04	-0.62	-0.71	-0.57
fac def, ren up	-1.90	-1.34	-0.81	0.48	0.55	0.45
fac down, ren def	0.45	0.51	0.60	-0.36	-0.42	-0.32
fac down, ren down	3.03	2.40	1.80	-1.02	-1.21	-0.97
fac down, ren up	-1.56	-0.95	-0.32	0.16	0.20	0.19
fac up, ren def	-0.53	-0.51	-0.54	0.33	0.38	0.28
fac up, ren down	1.72	1.03	0.36	-0.25	-0.25	-0.22
fac up, ren up	-2.31	-1.72	-1.26	0.78	0.88	0.68
Var1+	-0.86	-0.41	4.19	0.18	-0.78	0.71
Var1-	1.92	-0.46	7.01	0.38	-0.23	0.53
Var2+	7.21	-3.32	4.42	0.48	-0.54	-0.10
Var2-	3.44	2.07	5.51	-0.44	-0.15	-0.00
FSR+	-3.64	-7.66	-0.99	0.57	-0.04	0.29
FSR-	2.42	5.25	9.08	-0.34	-0.40	0.03
MPI+	7.77	-2.14	2.29	-0.26	-0.42	0.11
MPI-	8.06	-1.15	5.30	0.41	-0.52	0.07
PDF variance	0.00	0.00	0.00	0.00	0.00	0.00
PDF mean	0.97	0.75	0.50	0.74	0.76	0.74
PDF max	1.11	0.84	0.56	0.93	0.93	0.86
PDF min	0.79	0.59	0.39	0.54	0.61	0.58
QCD scale	+3.03 -2.31	+2.40 -1.72	+1.80 -1.26	+0.78 -1.02	+0.88 -1.21	+0.68 -0.97
tune	+14.10 -3.74	+5.64 -8.71	+15.24 -0.99	+0.95 -0.61	+0.00 -1.26	+0.95 -0.10
pdf	+0.14 -0.18	+0.09 -0.16	+0.05 -0.11	+0.19 -0.20	+0.17 -0.15	+0.12 -0.16
combined	+14.42 -4.40	+6.13 -8.88	+15.34 -1.61	+1.24 -1.20	+0.89 -1.76	+1.17 -0.99
symmetric	± 9.41	± 7.51	± 8.48	± 1.22	± 1.32	± 1.08

Table 16: Relative signal acceptance uncertainties (in percent) for gluon fusion in the $\tau_{\text{had}}\tau_{\text{had}}$ channel.

Not reviewed, for internal circulation only

syst. variation	<i>b</i> -tag			<i>b</i> -veto		
	200 GeV	500 GeV	1000 GeV	200 GeV	500 GeV	1000 GeV
fac def, ren down	1.86	2.02	1.19	-1.20	-0.69	-0.62
fac def, ren up	-1.46	-1.57	-0.93	0.94	0.54	0.49
fac down, ren def	0.10	0.26	0.26	-0.68	-0.40	-0.43
fac down, ren down	2.00	2.42	1.59	-1.91	-1.14	-1.14
fac down, ren up	-1.38	-1.42	-0.76	0.28	0.17	0.12
fac up, ren def	-0.29	-0.31	-0.25	0.64	0.37	0.38
fac up, ren down	1.50	1.56	0.82	-0.51	-0.26	-0.16
fac up, ren up	-1.69	-1.78	-1.09	1.54	0.87	0.81
Var1+	3.39	-2.22	-4.39	2.69	0.78	0.07
Var1-	-0.87	-3.63	-1.82	2.80	1.35	-0.17
Var2+	0.07	-0.99	-0.18	2.27	0.78	-1.00
Var2-	1.51	0.02	-5.99	1.48	1.78	-0.86
FSR+	1.21	-1.42	-9.85	2.30	1.04	0.23
FSR-	-10.51	6.68	0.09	2.72	0.16	-1.01
MPI+	3.65	-0.94	-2.88	1.10	-0.35	-0.54
MPI-	19.90	-5.65	-2.67	1.84	1.47	-0.08
PDF variance	0.00	0.00	0.00	0.01	0.00	0.00
PDF mean	0.78	1.14	1.05	0.46	0.85	0.82
PDF max	1.12	1.26	1.18	0.76	1.06	0.96
PDF min	0.50	0.93	0.83	0.12	0.66	0.64
QCD scale	+2.00 -1.69	+2.42 -1.78	+1.59 -1.09	+1.54 -1.91	+0.87 -1.14	+0.81 -1.14
tune	+20.61 -10.55	+6.68 -7.34	+0.09 -13.08	+6.30 -0.00	+3.08 -0.35	+0.24 -1.75
pdf	+0.33 -0.28	+0.12 -0.21	+0.13 -0.22	+0.30 -0.34	+0.21 -0.18	+0.14 -0.17
combined	+20.71 -10.69	+7.11 -7.56	+1.60 -13.12	+6.49 -1.94	+3.21 -1.21	+0.86 -2.10
symmetric	± 15.70	± 7.33	± 7.36	± 4.22	± 2.21	± 1.48

Table 17: Relative signal acceptance uncertainties (in percent) for gluon fusion in the $\tau_{\text{lep}}\tau_{\text{had}}$ channel.

Not reviewed, for internal circulation only

syst. variation	total		hh selected 400 GeV		lh selected 500 GeV	
	400 GeV hh	500 GeV lh	<i>b</i> -tag	<i>b</i> -veto	<i>b</i> -tag	<i>b</i> -veto
fac up, ren def	0.10	0.07	0.10	0.08	0.06	0.06
fac down, ren def	-0.05	-0.04	-0.05	-0.03	-0.05	-0.02
fac def, ren up	-0.11	-0.11	-0.13	-0.10	-0.11	-0.10
fac up, ren up	-0.07	-0.08	-0.09	-0.07	-0.10	-0.08
fac down, ren up	-0.19	-0.18	-0.21	-0.19	-0.19	-0.15
fac def, ren down	0.13	0.14	0.15	0.12	0.12	0.11
fac up, ren down	0.34	0.31	0.40	0.29	0.32	0.27
fac down, ren down	0.12	0.12	0.14	0.11	0.11	0.10
Var1Down	-0.33	-0.16	-0.85	0.68	-0.06	-2.41
Var1Up	-0.22	0.24	-0.73	-1.61	0.34	0.54
Var2Down	0.40	-0.39	0.00	0.13	-1.71	-0.46
Var2Up	0.17	-0.04	-0.65	-1.30	-0.71	-0.07
Var3aDown	-0.49	0.44	-1.51	-1.07	-0.35	0.62
Var3aUp	0.31	-0.23	-1.53	0.16	-0.33	-0.44
PDF variance	0.00	0.00	0.00	0.00	0.00	0.00
PDF mean	0.00	0.00	-0.03	-0.03	0.01	-0.00
PDF max	0.00	0.00	-0.01	-0.01	0.03	0.03
PDF min	0.00	0.00	-0.05	-0.05	-0.01	-0.02
QCD scale	+0.34 -0.19	+0.31 -0.18	+0.40 -0.21	+0.29 -0.19	+0.32 -0.19	+0.27 -0.15
tune	+0.53 -0.63	+0.50 -0.48	+0.00 -2.51	+0.71 -2.33	+0.34 -1.91	+0.83 -2.50
pdf	+0.00 -0.00	+0.00 -0.00	+0.02 -0.02	+0.02 -0.02	+0.02 -0.02	+0.03 -0.02
combined	+0.63 -0.66	+0.59 -0.51	+0.40 -2.52	+0.77 -2.33	+0.46 -1.92	+0.87 -2.50
symmetric	± 0.65	± 0.55	± 1.46	± 1.55	± 1.19	± 1.69

Table 18: Relative difference in the fraction of negatively weighted events for selected *b*-associated Higgs production mass points.

Not reviewed, for internal circulation only

syst. variation	<i>b</i> -tag			<i>b</i> -veto		
	400 GeV	700 GeV	1000 GeV	400 GeV	700 GeV	1000 GeV
fac up, ren def	-0.32	0.42	0.67	0.95	0.24	-0.06
fac down, ren def	0.41	-0.43	-0.74	-1.11	-0.31	0.05
fac def, ren up	0.70	0.95	0.90	-0.13	-0.72	-1.03
fac up, ren up	0.46	1.30	1.47	0.72	-0.45	-1.02
fac down, ren up	1.00	0.58	0.28	-1.12	-1.05	-1.07
fac def, ren down	-1.10	-1.46	-1.35	0.07	1.04	1.50
fac up, ren down	-1.52	-0.91	-0.50	1.19	1.22	1.28
fac down, ren down	-0.51	-2.03	-2.31	-1.25	0.78	1.74
Var1Down	0.58	-0.01	-4.90	-4.52	-2.49	2.13
Var1Up	3.07	-1.26	0.39	5.04	1.10	-1.53
Var2Down	1.21	2.55	2.04	0.78	-4.59	-1.06
Var2Up	0.88	-2.53	1.33	6.72	1.50	-0.48
Var3aDown	3.75	2.34	-0.61	4.13	4.17	-0.98
Var3aUp	5.65	3.32	0.34	1.09	2.18	0.76
PDF variance	0.01	0.08	0.01	0.01	0.08	0.00
PDF mean	0.98	1.09	1.29	0.70	0.81	0.86
PDF max	1.21	2.48	1.54	0.93	2.20	0.97
PDF min	0.81	0.72	1.08	0.56	0.46	0.70
QCD scale	+1.00 -1.52	+1.30 -2.03	+1.47 -2.31	+1.19 -1.25	+1.22 -1.05	+1.74 -1.07
tune	+7.61 -0.00	+4.79 -2.82	+2.49 -4.94	+9.46 -4.52	+5.06 -5.22	+2.26 -2.16
pdf	+0.23 -0.17	+1.39 -0.37	+0.25 -0.21	+0.23 -0.14	+1.39 -0.35	+0.11 -0.15
combined	+7.68 -1.53	+5.16 -3.49	+2.90 -5.46	+9.53 -4.69	+5.39 -5.34	+2.86 -2.42
symmetric	± 4.60	± 4.32	± 4.18	± 7.11	± 5.37	± 2.64

Table 19: Relative signal acceptance uncertainties (in percent) for *b*-associated production in the $\tau_{\text{had}}\tau_{\text{had}}$ channel. This version of the table considers the sign of the MC weights.

syst. variation	<i>b</i> -tag			<i>b</i> -veto		
	200 GeV	500 GeV	1000 GeV	200 GeV	500 GeV	1000 GeV
fac up, ren def	-1.37	0.22	0.65	1.40	0.61	-0.25
fac down, ren def	1.61	-0.17	-0.70	-1.58	-0.72	0.27
fac def, ren up	1.59	1.31	0.83	0.92	-0.58	-1.32
fac up, ren up	0.45	1.48	1.39	2.18	0.01	-1.44
fac down, ren up	2.91	1.16	0.23	-0.54	-1.26	-1.19
fac def, ren down	-2.67	-2.04	-1.24	-1.98	0.82	1.93
fac up, ren down	-4.43	-1.69	-0.42	-0.29	1.46	1.44
fac down, ren down	-0.55	-2.32	-2.14	-3.81	0.05	2.49
Var1Down	9.00	-0.66	-4.65	-4.91	8.73	0.67
Var1Up	-0.60	1.01	1.48	-1.45	-1.51	-0.79
Var2Down	4.91	5.88	0.48	-4.33	-0.74	0.29
Var2Up	22.65	3.94	1.99	3.79	0.97	1.81
Var3aDown	-0.02	5.41	-4.92	-5.02	-1.12	-5.70
Var3aUp	-0.05	0.78	1.69	4.52	0.98	-0.21
PDF variance	0.01	0.01	0.01	0.01	0.00	0.00
PDF mean	0.74	0.98	0.91	0.64	0.72	0.52
PDF max	0.95	1.19	1.12	1.06	0.90	0.59
PDF min	0.53	0.84	0.74	0.42	0.62	0.44
QCD scale	+2.91 -4.43	+1.48 -2.32	+1.39 -2.14	+2.18 -3.81	+1.46 -1.26	+2.49 -1.44
tune	+24.86 -0.60	+9.00 -0.66	+3.04 -6.76	+5.90 -8.37	+8.84 -2.02	+1.96 -5.76
pdf	+0.22 -0.21	+0.21 -0.14	+0.21 -0.17	+0.41 -0.23	+0.18 -0.11	+0.07 -0.08
combined	+25.03 -4.48	+9.13 -2.42	+3.34 -7.10	+6.30 -9.20	+8.96 -2.39	+3.17 -5.94
symmetric	± 14.75	± 5.77	± 5.22	± 7.75	± 5.67	± 4.55

Table 20: Relative signal acceptance uncertainties (in percent) for *b*-associated production in the $\tau_{\text{lep}}\tau_{\text{had}}$ channel. This version of the table considers the sign of the MC weights.

1213 D. Signal theoretical uncertainty shape effect

1214 Figures 68–73 show the potential systematics shape effect on bbH signal with $m_H=700$ GeV. From these
 1215 plots, it can be concluded that the shape effect is not significant. The situation is expected similar for ggH
 1216 signals.

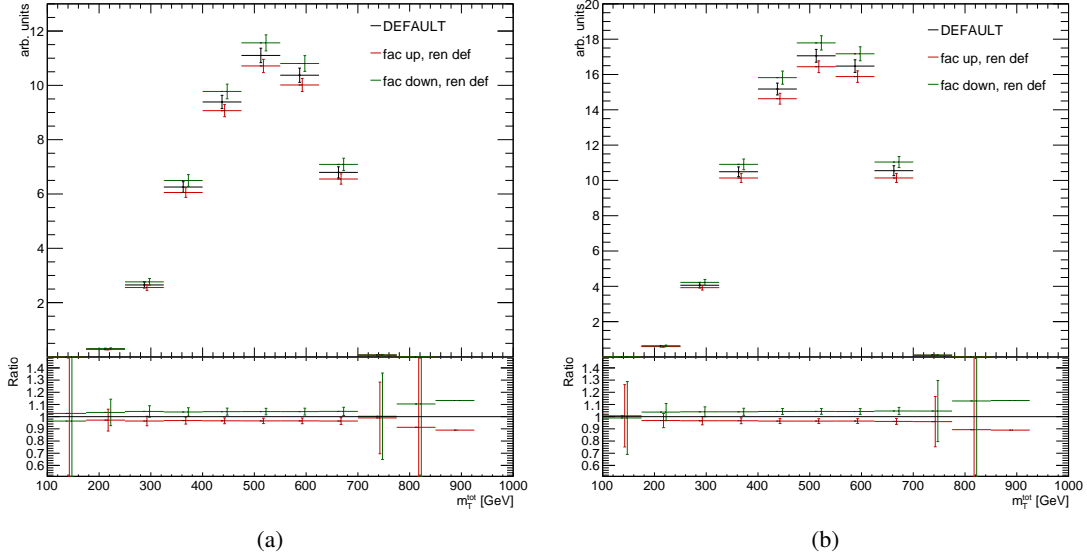


Figure 68: The uncertainty on the shape of bbH signal at $m_H=700$ GeV.

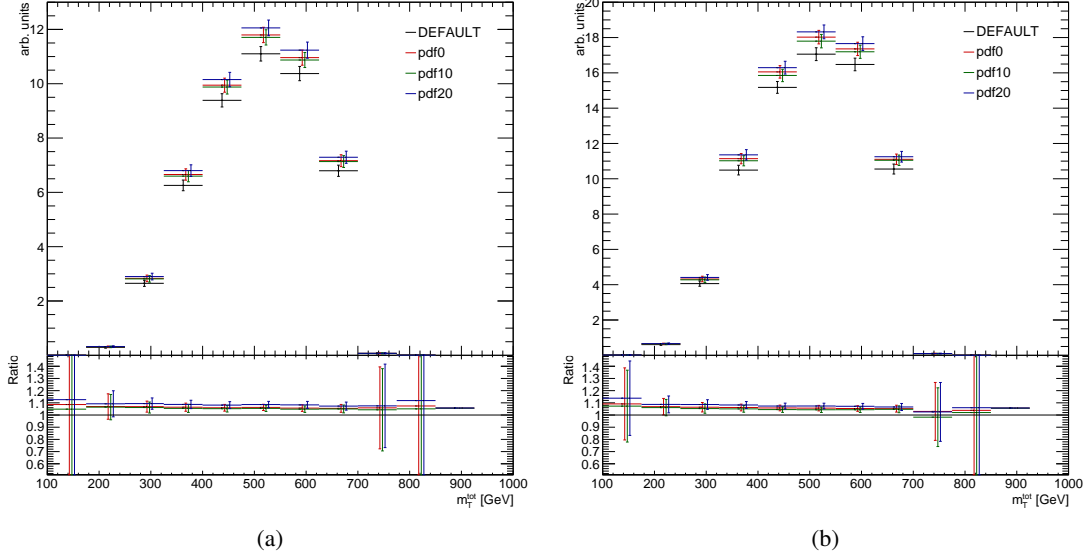


Figure 69: The uncertainty on the shape of bbH signal at $m_H=700$ GeV.

Not reviewed, for internal circulation only

Not reviewed, for internal circulation only

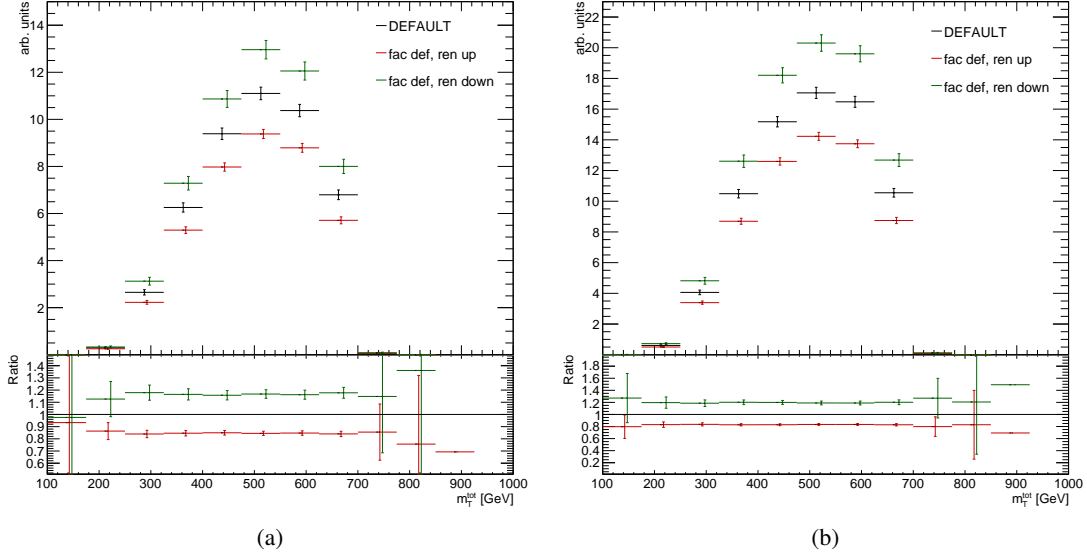


Figure 70: The uncertainty on the shape of bbH signal at $m_H=700$ GeV.

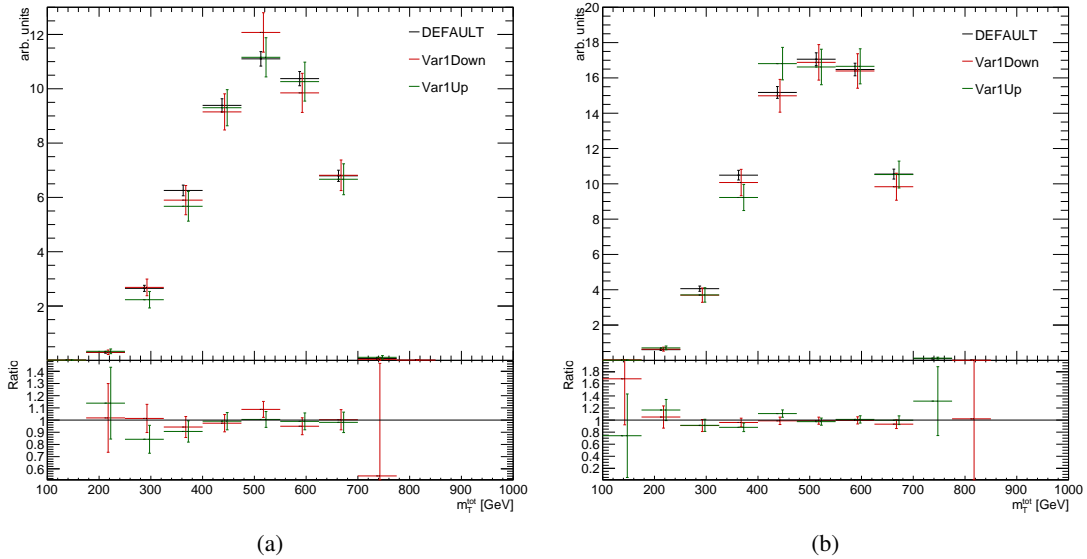


Figure 71: The uncertainty on the shape of bbH signal at $m_H=700$ GeV.

Not reviewed, for internal circulation only

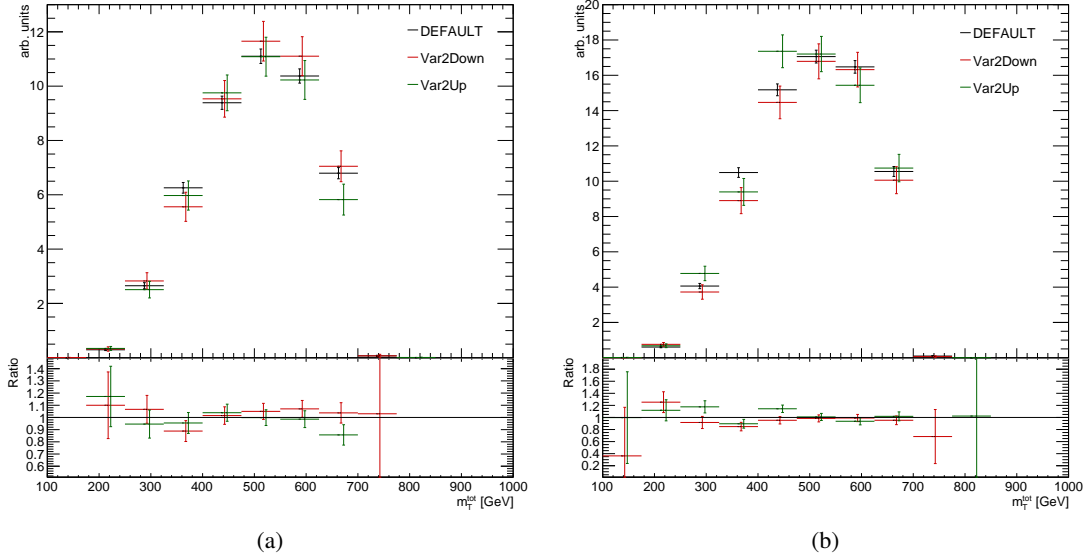


Figure 72: The uncertainty on the shape of bbH signal at $m_H=700$ GeV.

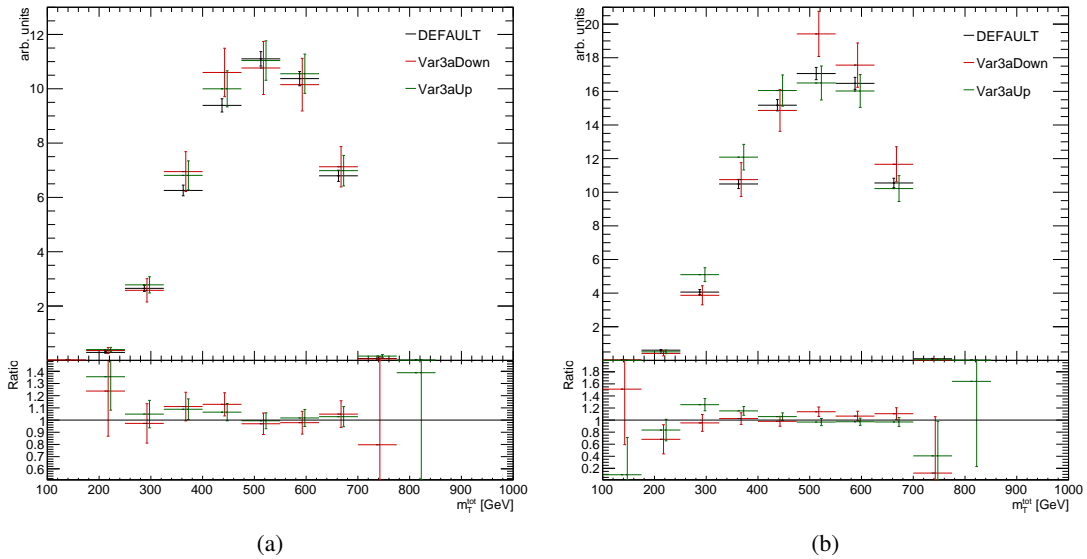


Figure 73: The uncertainty on the shape of bbH signal at $m_H=700$ GeV.

1217 **D.1. $Z' \rightarrow \tau\tau$ interpretation of combination**

1218 For the statistical analysis the same strategy as for $A/H \rightarrow \tau\tau$ is utilized. An inclusive category (b -tag
1219 + b -veto) is considered for the Z' fit, along with the original $\tau_{\text{lep}}\tau_{\text{had}}$ top control region which is used to
1220 constrain top systematics. The limits are interpreted in the SSM in Fig. 74 in the $\tau_{\text{lep}}\tau_{\text{had}}$ and $\tau_{\text{had}}\tau_{\text{had}}$
1221 channels. The combined limits are interpreted in the SSM in Fig. 75 and SFM in Fig. 76. The resulting
1222 95 % CL expected lower limit on the mass of a Z'_{SSM} is 1.99 TeV($\tau_{\text{lep}}\tau_{\text{had}}$), 2.41 TeV ($\tau_{\text{had}}\tau_{\text{had}}$), and
1223 2.48 TeV (combined).

Not reviewed, for internal circulation only

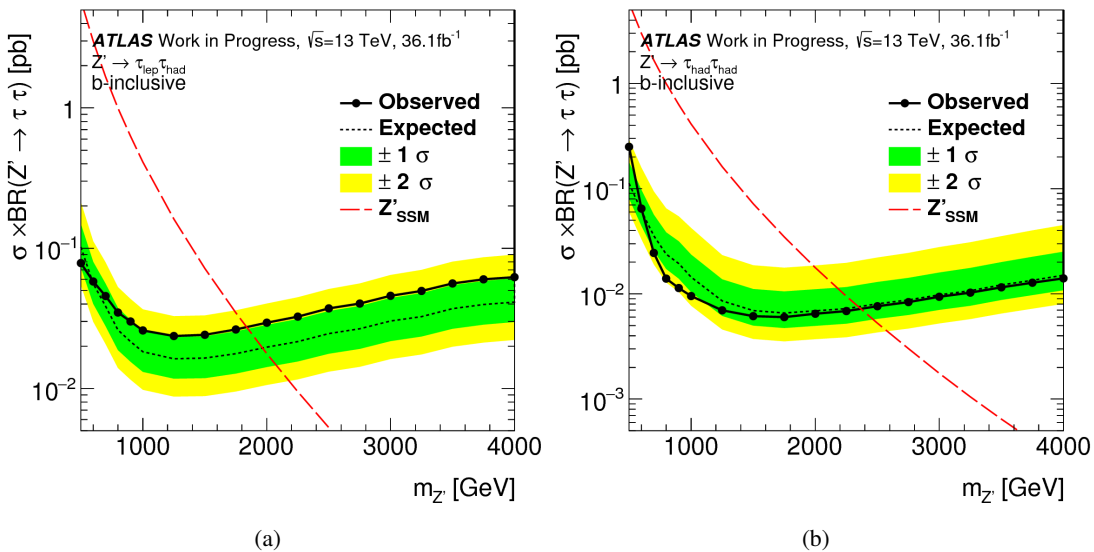


Figure 74: The 95 % CL upper limit on the cross section times ditau branching fraction for a $Z' \rightarrow \tau\tau$ in the Sequential Standard Model in the (a) $\tau_{\text{lep}}\tau_{\text{had}}$ and (b) $\tau_{\text{had}}\tau_{\text{had}}$ channel including the 1σ and 2σ uncertainty bands for 36.1 fb^{-1} of integrated luminosity at 13 TeV. The expected lower limits on the mass of a Z'_{SSM} are 1.99 TeV($\tau_{\text{lep}}\tau_{\text{had}}$) and 2.41 TeV ($\tau_{\text{had}}\tau_{\text{had}}$).

Not reviewed, for internal circulation only

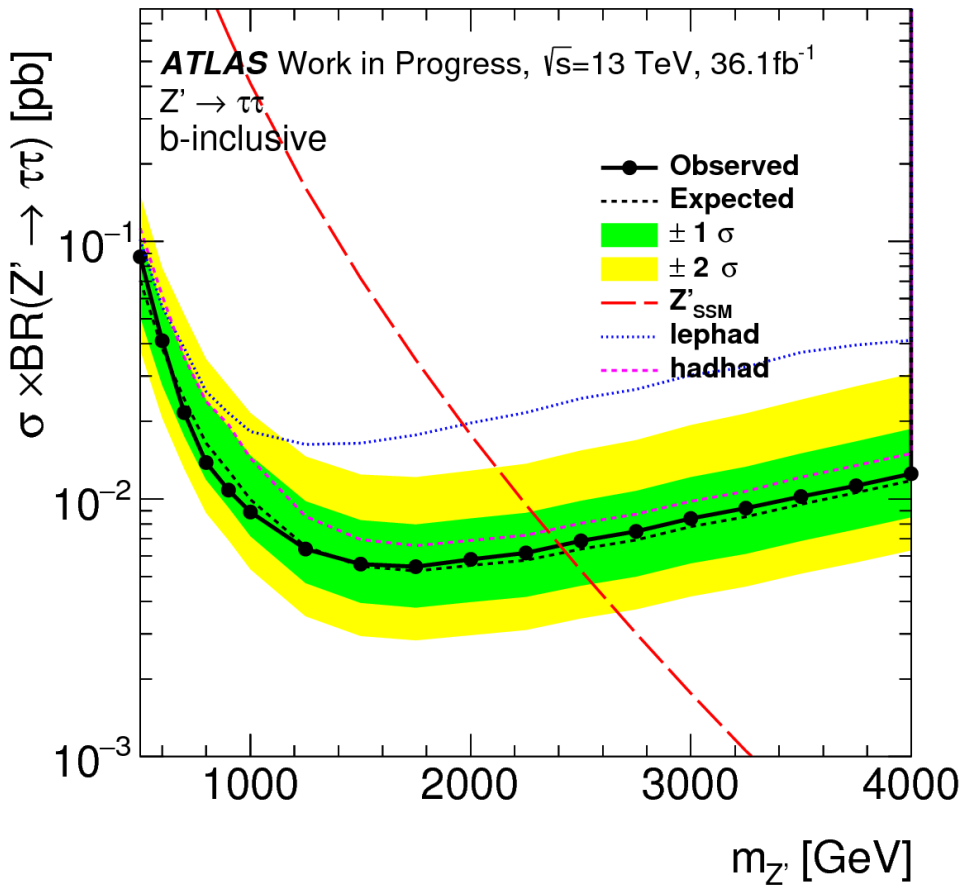


Figure 75: The 95 % CL upper limit on the cross section times ditau branching fraction for a $Z' \rightarrow \tau\tau$ in the Sequential Standard Model in the combined channel including the 1σ and 2σ uncertainty bands for 36.1 fb^{-1} of integrated luminosity at 13 TeV. The expected lower limits on the mass of a Z'_{SSM} is 2.48 TeV.

Not reviewed, for internal circulation only

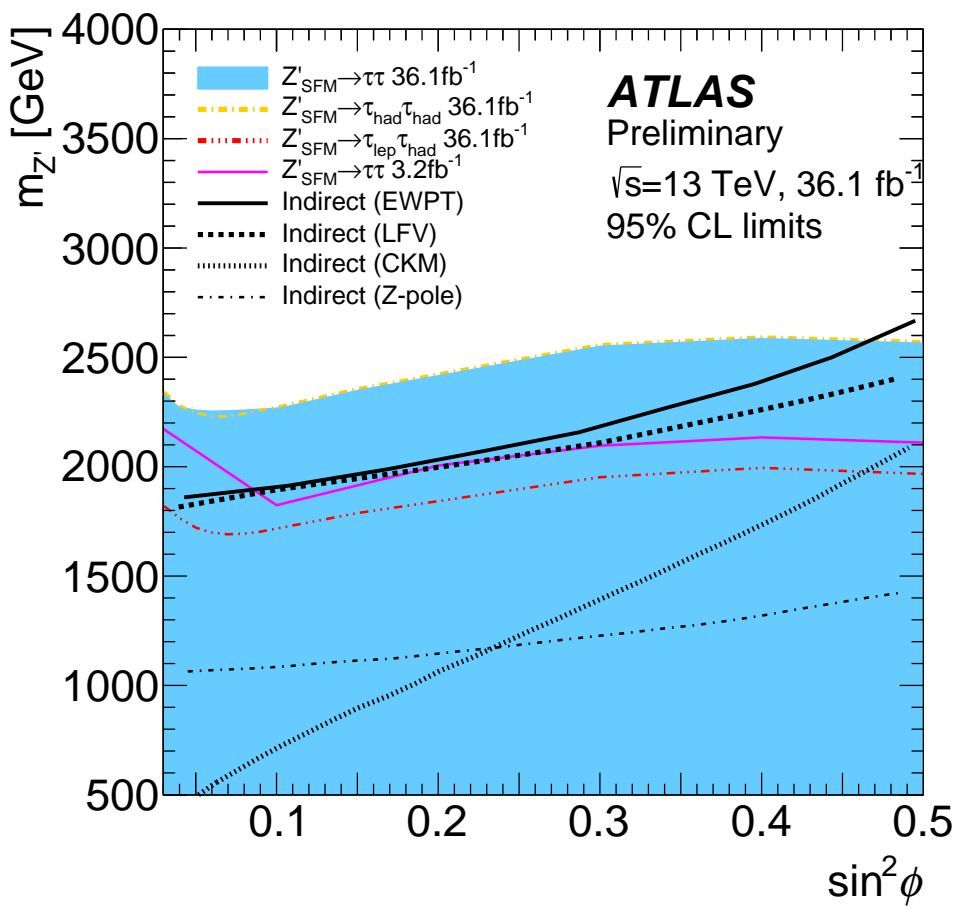


Figure 76: The observed 95% CL exclusion limits on $\sin^2 \phi$ and m_A in the Strong Flavor Model in $\tau^+\tau^-$ for 36.1 fb^{-1} of integrated luminosity at 13 TeV.

1224 E. MC Samples

1225 Table 21 shows the cross section of gluon-initiated and b-associated production modes in the hMSSM model.

Table 21: bbH and ggH cross section [pb] of different Higgs mass in hMSSM model at representative $\tan\beta$ value

$m_{A/H}$	$\tan\beta$	$gg \rightarrow H\tau\tau$	$gg \rightarrow A\tau\tau$	$bb \rightarrow H\tau\tau$	$bb \rightarrow A\tau\tau$	total
200	10	0.480236	0.259930	1.069625	1.165388	2.975180
250	10	0.175824	0.077584	0.502903	0.529303	1.285614
300	10	0.079154	0.033430	0.247117	0.265621	0.625323
350	10	0.048867	0.055091	0.137428	0.130616	0.372002
400	10	0.025828	0.034147	0.075288	0.069932	0.205195
500	10	0.006856	0.012118	0.027187	0.026046	0.072207
600	15	0.002094	0.004789	0.029696	0.029486	0.066065
700	15	0.000713	0.002050	0.014351	0.014275	0.031390
800	15	0.000275	0.000949	0.007434	0.007418	0.016076
1000	25	0.000119	0.000313	0.006804	0.006804	0.014041
1200	35	0.000073	0.000138	0.004870	0.004869	0.009950
1500	50	0.000033	0.000048	0.002615	0.002613	0.005309

1226

1227 This section contains the names of the MC samples used.

```

1228 mc15_13TeV:mc15_13TeV.301000.PowhegPythia8EvtGen_AZNLOCTEQ6L1_DYee_120M180.merge.DAOD_HIGG4D2.e3649_s2576_s2132_r7772_r7676_p2823
1229 mc15_13TeV:mc15_13TeV.301001.PowhegPythia8EvtGen_AZNLOCTEQ6L1_DYee_180M250.merge.DAOD_HIGG4D2.e3649_s2576_s2132_r7772_r7676_p2823
1230 mc15_13TeV:mc15_13TeV.301002.PowhegPythia8EvtGen_AZNLOCTEQ6L1_DYee_250M400.merge.DAOD_HIGG4D2.e3649_s2576_s2132_r7772_r7676_p2823
1231 mc15_13TeV:mc15_13TeV.301003.PowhegPythia8EvtGen_AZNLOCTEQ6L1_DYee_400M600.merge.DAOD_HIGG4D2.e3649_s2576_s2132_r7772_r7676_p2823
1232 mc15_13TeV:mc15_13TeV.301004.PowhegPythia8EvtGen_AZNLOCTEQ6L1_DYee_600M800.merge.DAOD_HIGG4D2.e3649_s2576_s2132_r7772_r7676_p2823
1233 mc15_13TeV:mc15_13TeV.301005.PowhegPythia8EvtGen_AZNLOCTEQ6L1_DYee_800M1000.merge.DAOD_HIGG4D2.e3649_s2576_s2132_r7772_r7676_p2823
1234 mc15_13TeV:mc15_13TeV.301006.PowhegPythia8EvtGen_AZNLOCTEQ6L1_DYee_1000M1250.merge.DAOD_HIGG4D2.e3649_s2576_s2132_r7772_r7676_p2823
1235 mc15_13TeV:mc15_13TeV.301007.PowhegPythia8EvtGen_AZNLOCTEQ6L1_DYee_1250M1500.merge.DAOD_HIGG4D2.e3649_s2576_s2132_r7772_r7676_p2823
1236 mc15_13TeV:mc15_13TeV.301008.PowhegPythia8EvtGen_AZNLOCTEQ6L1_DYee_1500M1750.merge.DAOD_HIGG4D2.e3649_s2576_s2132_r7772_r7676_p2823
1237 mc15_13TeV:mc15_13TeV.301009.PowhegPythia8EvtGen_AZNLOCTEQ6L1_DYee_1750M2000.merge.DAOD_HIGG4D2.e3649_s2576_s2132_r7772_r7676_p2823
1238 mc15_13TeV:mc15_13TeV.301010.PowhegPythia8EvtGen_AZNLOCTEQ6L1_DYee_2000M2250.merge.DAOD_HIGG4D2.e3649_s2576_s2132_r7772_r7676_p2823
1239 mc15_13TeV:mc15_13TeV.301011.PowhegPythia8EvtGen_AZNLOCTEQ6L1_DYee_2250M2500.merge.DAOD_HIGG4D2.e3649_s2576_s2132_r7772_r7676_p2823
1240 mc15_13TeV:mc15_13TeV.301012.PowhegPythia8EvtGen_AZNLOCTEQ6L1_DYee_2500M2750.merge.DAOD_HIGG4D2.e3649_s2576_s2132_r7772_r7676_p2823
1241 mc15_13TeV:mc15_13TeV.301013.PowhegPythia8EvtGen_AZNLOCTEQ6L1_DYee_2750M3000.merge.DAOD_HIGG4D2.e3649_s2576_s2132_r7772_r7676_p2823
1242 mc15_13TeV:mc15_13TeV.301014.PowhegPythia8EvtGen_AZNLOCTEQ6L1_DYee_3000M3500.merge.DAOD_HIGG4D2.e3649_s2576_s2132_r7772_r7676_p2823
1243 mc15_13TeV:mc15_13TeV.301015.PowhegPythia8EvtGen_AZNLOCTEQ6L1_DYee_3500M4000.merge.DAOD_HIGG4D2.e3649_s2576_s2132_r7772_r7676_p2823
1244 mc15_13TeV:mc15_13TeV.301016.PowhegPythia8EvtGen_AZNLOCTEQ6L1_DYee_4000M4500.merge.DAOD_HIGG4D2.e3649_s2576_s2132_r7772_r7676_p2823
1245 mc15_13TeV:mc15_13TeV.301017.PowhegPythia8EvtGen_AZNLOCTEQ6L1_DYee_4500M5000.merge.DAOD_HIGG4D2.e3649_s2576_s2132_r7772_r7676_p2823
1246 mc15_13TeV:mc15_13TeV.301018.PowhegPythia8EvtGen_AZNLOCTEQ6L1_DYee_5000M.merge.DAOD_HIGG4D2.e3649_s2576_s2132_r7772_r7676_p2823
1247 mc15_13TeV:mc15_13TeV.301020.PowhegPythia8EvtGen_AZNLOCTEQ6L1_DYmumu_120M180.merge.DAOD_HIGG4D2.e3649_s2576_s2132_r7772_r7676_p2823
1248 mc15_13TeV:mc15_13TeV.301021.PowhegPythia8EvtGen_AZNLOCTEQ6L1_DYmumu_180M250.merge.DAOD_HIGG4D2.e3649_s2576_s2132_r7772_r7676_p2823
1249 mc15_13TeV:mc15_13TeV.301022.PowhegPythia8EvtGen_AZNLOCTEQ6L1_DYmumu_250M400.merge.DAOD_HIGG4D2.e3649_s2576_s2132_r7772_r7676_p2823
1250 mc15_13TeV:mc15_13TeV.301023.PowhegPythia8EvtGen_AZNLOCTEQ6L1_DYmumu_400M600.merge.DAOD_HIGG4D2.e3649_s2576_s2132_r7772_r7676_p2823
1251 mc15_13TeV:mc15_13TeV.301024.PowhegPythia8EvtGen_AZNLOCTEQ6L1_DYmumu_600M800.merge.DAOD_HIGG4D2.e3649_s2576_s2132_r7772_r7676_p2823
1252 mc15_13TeV:mc15_13TeV.301025.PowhegPythia8EvtGen_AZNLOCTEQ6L1_DYmumu_800M1000.merge.DAOD_HIGG4D2.e3649_s2576_s2132_r7772_r7676_p2823
1253 mc15_13TeV:mc15_13TeV.301026.PowhegPythia8EvtGen_AZNLOCTEQ6L1_DYmumu_1000M1250.merge.DAOD_HIGG4D2.e3649_s2576_s2132_r7772_r7676_p2823
1254 mc15_13TeV:mc15_13TeV.301027.PowhegPythia8EvtGen_AZNLOCTEQ6L1_DYmumu_1250M1500.merge.DAOD_HIGG4D2.e3649_s2576_s2132_r7772_r7676_p2823

```

Not reviewed, for internal circulation only

1396 mc15_13TeV:mc15_13TeV.301176.PowhegPythia8EvtGen_AZNLOCTEQ6L1_Wmintaunu_4000M4500.merge.DAOD_HIGG4D2.e3663_s2608_s2183_r7772_r7676_p2823
 1397 mc15_13TeV:mc15_13TeV.301177.PowhegPythia8EvtGen_AZNLOCTEQ6L1_Wmintaunu_4500M5000.merge.DAOD_HIGG4D2.e3663_s2608_s2183_r7772_r7676_p2823
 1398 mc15_13TeV:mc15_13TeV.301178.PowhegPythia8EvtGen_AZNLOCTEQ6L1_Wmintaunu_5000M.merge.DAOD_HIGG4D2.e3663_s2608_s2183_r7772_r7676_p2823
 1399 mc15_13TeV:mc15_13TeV.341856.aMcAtNloPythia8EvtGen_A14NNPDF23L0_bbH125_yb2_tautaulh.merge.DAOD_HIGG4D2.e4482_a766_a821_r7676_p2823
 1400 mc15_13TeV:mc15_13TeV.341857.aMcAtNloPythia8EvtGen_A14NNPDF23L0_bbH150_yb2_tautaulh.merge.DAOD_HIGG4D2.e5686_a766_a821_r7676_p2823
 1401 mc15_13TeV:mc15_13TeV.341858.aMcAtNloPythia8EvtGen_A14NNPDF23L0_bbH200_yb2_tautaulh.merge.DAOD_HIGG4D2.e4482_a766_a821_r7676_p2823
 1402 mc15_13TeV:mc15_13TeV.341859.aMcAtNloPythia8EvtGen_A14NNPDF23L0_bbH250_yb2_tautaulh.merge.DAOD_HIGG4D2.e5686_a766_a821_r7676_p2823
 1403 mc15_13TeV:mc15_13TeV.341860.aMcAtNloPythia8EvtGen_A14NNPDF23L0_bbH300_yb2_tautaulh.merge.DAOD_HIGG4D2.e4482_a766_a821_r7676_p2823
 1404 mc15_13TeV:mc15_13TeV.341861.aMcAtNloPythia8EvtGen_A14NNPDF23L0_bbH350_yb2_tautaulh.merge.DAOD_HIGG4D2.e4482_a766_a821_r7676_p2823
 1405 mc15_13TeV:mc15_13TeV.341862.aMcAtNloPythia8EvtGen_A14NNPDF23L0_bbH400_yb2_tautaulh.merge.DAOD_HIGG4D2.e4298_a766_a821_r7676_p2823
 1406 mc15_13TeV:mc15_13TeV.341863.aMcAtNloPythia8EvtGen_A14NNPDF23L0_bbH500_yb2_tautaulh.merge.DAOD_HIGG4D2.e4482_a766_a821_r7676_p2823
 1407 mc15_13TeV:mc15_13TeV.341864.aMcAtNloPythia8EvtGen_A14NNPDF23L0_bbH600_yb2_tautaulh.merge.DAOD_HIGG4D2.e4482_a766_a821_r7676_p2823
 1408 mc15_13TeV:mc15_13TeV.341865.aMcAtNloPythia8EvtGen_A14NNPDF23L0_bbH700_yb2_tautaulh.merge.DAOD_HIGG4D2.e4482_a766_a821_r7676_p2823
 1409 mc15_13TeV:mc15_13TeV.341866.aMcAtNloPythia8EvtGen_A14NNPDF23L0_bbH800_yb2_tautaulh.merge.DAOD_HIGG4D2.e4482_a766_a821_r7676_p2823
 1410 mc15_13TeV:mc15_13TeV.341868.aMcAtNloPythia8EvtGen_A14NNPDF23L0_bbH1000_yb2_tautaulh.merge.DAOD_HIGG4D2.e4298_a766_a821_r7676_p2823
 1411 mc15_13TeV:mc15_13TeV.341870.aMcAtNloPythia8EvtGen_A14NNPDF23L0_bbH1200_yb2_tautaulh.merge.DAOD_HIGG4D2.e4482_a766_a821_r7676_p2823
 1412 mc15_13TeV:mc15_13TeV.341873.aMcAtNloPythia8EvtGen_A14NNPDF23L0_bbH1500_yb2_tautaulh.merge.DAOD_HIGG4D2.e5314_a766_a821_r7676_p2823
 1413 mc15_13TeV:mc15_13TeV.341925.aMcAtNloPythia8EvtGen_A14NNPDF23L0_bbH200_ybyt_tautaulh.merge.DAOD_HIGG4D2.e5686_a766_a821_r7676_p2823
 1414 mc15_13TeV:mc15_13TeV.342300.PowhegPythia8EvtGen_CT10_AZNLOCTEQ6L1_ggh125W02_tautaulh.merge.DAOD_HIGG4D2.e4284_s2608_s2183_r7772_r7676_p2823
 1415 mc15_13TeV:mc15_13TeV.342303.PowhegPythia8EvtGen_CT10_AZNLOCTEQ6L1_ggh150W03_tautaulh.merge.DAOD_HIGG4D2.e4284_s2608_s2183_r7772_r7676_p2823
 1416 mc15_13TeV:mc15_13TeV.342305.PowhegPythia8EvtGen_CT10_AZNLOCTEQ6L1_ggh200W1_tautaulh.merge.DAOD_HIGG4D2.e4284_s2608_s2183_r7772_r7676_p2823
 1417 mc15_13TeV:mc15_13TeV.342308.PowhegPythia8EvtGen_CT10_AZNLOCTEQ6L1_ggh250W1_tautaulh.merge.DAOD_HIGG4D2.e4284_s2608_s2183_r7772_r7676_p2823
 1418 mc15_13TeV:mc15_13TeV.342310.PowhegPythia8EvtGen_CT10_AZNLOCTEQ6L1_ggh300W2_tautaulh.merge.DAOD_HIGG4D2.e4284_s2608_s2183_r7772_r7676_p2823
 1419 mc15_13TeV:mc15_13TeV.342312.PowhegPythia8EvtGen_CT10_AZNLOCTEQ6L1_ggh350W3_tautaulh.merge.DAOD_HIGG4D2.e4284_s2608_s2183_r7772_r7676_p2823
 1420 mc15_13TeV:mc15_13TeV.342314.PowhegPythia8EvtGen_CT10_AZNLOCTEQ6L1_ggh400W5_tautaulh.merge.DAOD_HIGG4D2.e4284_s2608_s2183_r7772_r7676_p2823
 1421 mc15_13TeV:mc15_13TeV.342316.PowhegPythia8EvtGen_CT10_AZNLOCTEQ6L1_ggh500W5_tautaulh.merge.DAOD_HIGG4D2.e4284_s2608_s2183_r7772_r7676_p2823
 1422 mc15_13TeV:mc15_13TeV.342318.PowhegPythia8EvtGen_CT10_AZNLOCTEQ6L1_ggh600W10_tautaulh.merge.DAOD_HIGG4D2.e4284_s2608_s2183_r7772_r7676_p2823
 1423 mc15_13TeV:mc15_13TeV.342320.PowhegPythia8EvtGen_CT10_AZNLOCTEQ6L1_ggh700W20_tautaulh.merge.DAOD_HIGG4D2.e4284_s2608_s2183_r7772_r7676_p2823
 1424 mc15_13TeV:mc15_13TeV.342322.PowhegPythia8EvtGen_CT10_AZNLOCTEQ6L1_ggh800W20_tautaulh.merge.DAOD_HIGG4D2.e4284_s2608_s2183_r7772_r7676_p2823
 1425 mc15_13TeV:mc15_13TeV.342324.PowhegPythia8EvtGen_CT10_AZNLOCTEQ6L1_ggh900W20_tautaulh.merge.DAOD_HIGG4D2.e4284_s2608_s2183_r7772_r7676_p2823
 1426 mc15_13TeV:mc15_13TeV.342326.PowhegPythia8EvtGen_CT10_AZNLOCTEQ6L1_ggh1000W30_tautaulh.merge.DAOD_HIGG4D2.e4284_s2608_s2183_r7772_r7676_p2823
 1427 mc15_13TeV:mc15_13TeV.342328.PowhegPythia8EvtGen_CT10_AZNLOCTEQ6L1_ggh1100W40_tautaulh.merge.DAOD_HIGG4D2.e4284_s2608_s2183_r7772_r7676_p2823
 1428 mc15_13TeV:mc15_13TeV.342330.PowhegPythia8EvtGen_CT10_AZNLOCTEQ6L1_ggh1200W40_tautaulh.merge.DAOD_HIGG4D2.e4284_s2608_s2183_r7772_r7676_p2823
 1429 mc15_13TeV:mc15_13TeV.342332.PowhegPythia8EvtGen_CT10_AZNLOCTEQ6L1_ggh1300W50_tautaulh.merge.DAOD_HIGG4D2.e4284_s2608_s2183_r7772_r7676_p2823
 1430 mc15_13TeV:mc15_13TeV.342334.PowhegPythia8EvtGen_CT10_AZNLOCTEQ6L1_ggh1400W50_tautaulh.merge.DAOD_HIGG4D2.e4284_s2608_s2183_r7772_r7676_p2823
 1431 mc15_13TeV:mc15_13TeV.342336.PowhegPythia8EvtGen_CT10_AZNLOCTEQ6L1_ggh1500W60_tautaulh.merge.DAOD_HIGG4D2.e4284_s2608_s2183_r7772_r7676_p2823
 1432 mc15_13TeV:mc15_13TeV.345287.aMcAtNloPythia8EvtGen_A14NNPDF23L0_bbH1750_yb2_tautaulh.merge.DAOD_HIGG4D2.e5686_a766_a821_r7676_p2823
 1433 mc15_13TeV:mc15_13TeV.345289.aMcAtNloPythia8EvtGen_A14NNPDF23L0_bbH2000_yb2_tautaulh.merge.DAOD_HIGG4D2.e5686_a766_a821_r7676_p2823
 1434 mc15_13TeV:mc15_13TeV.345291.aMcAtNloPythia8EvtGen_A14NNPDF23L0_bbH2250_yb2_tautaulh.merge.DAOD_HIGG4D2.e5686_a766_a821_r7676_p2823
 1435 mc15_13TeV:mc15_13TeV.345293.aMcAtNloPythia8EvtGen_A14NNPDF23L0_bbH2500_yb2_tautaulh.merge.DAOD_HIGG4D2.e5686_a766_a821_r7676_p2823
 1436 mc15_13TeV:mc15_13TeV.345295.PowhegPythia8EvtGen_CT10_AZNLOCTEQ6L1_ggh1750W70_tautaulh.merge.DAOD_HIGG4D2.e5685_s2726_r7772_r7676_p2823
 1437 mc15_13TeV:mc15_13TeV.345297.PowhegPythia8EvtGen_CT10_AZNLOCTEQ6L1_ggh2000W80_tautaulh.merge.DAOD_HIGG4D2.e5685_s2726_r7772_r7676_p2823
 1438 mc15_13TeV:mc15_13TeV.345299.PowhegPythia8EvtGen_CT10_AZNLOCTEQ6L1_ggh2250W90_tautaulh.merge.DAOD_HIGG4D2.e5685_s2726_r7772_r7676_p2823
 1439 mc15_13TeV:mc15_13TeV.345301.PowhegPythia8EvtGen_CT10_AZNLOCTEQ6L1_ggh2500W100_tautaulh.merge.DAOD_HIGG4D2.e5685_s2726_r7772_r7676_p2823
 1440 mc15_13TeV:mc15_13TeV.345302.aMcAtNloPythia8EvtGen_A14NNPDF23L0_bbH150_ybyt_tautaulh.merge.DAOD_HIGG4D2.e5686_a766_a821_r7676_p2823
 1441 mc15_13TeV:mc15_13TeV.361063.Sherpa_CT10_llll.merge.DAOD_HIGG4D2.e3836_s2608_s2183_r7725_r7676_p2823
 1442 mc15_13TeV:mc15_13TeV.361064.Sherpa_CT10_lllvSFMinus.merge.DAOD_HIGG4D2.e3836_s2608_s2183_r7725_r7676_p2823

1443 mc15_13TeV:mc15_13TeV.361065.Sherpa_C10_lllvOFminus.merge.DAOD_HIGG4D2.e3836_s2608_s2183_r7725_r7676_p2823
 1444 mc15_13TeV:mc15_13TeV.361066.Sherpa_C10_lllvSFPlus.merge.DAOD_HIGG4D2.e3836_s2608_s2183_r7725_r7676_p2823
 1445 mc15_13TeV:mc15_13TeV.361067.Sherpa_C10_lllvOFplus.merge.DAOD_HIGG4D2.e3836_s2608_s2183_r7725_r7676_p2823
 1446 mc15_13TeV:mc15_13TeV.361068.Sherpa_C10_llvv.merge.DAOD_HIGG4D2.e3836_s2608_s2183_r7725_r7676_p2823
 1447 mc15_13TeV:mc15_13TeV.361091.Sherpa_C10_Wp1vWmqq_SHv21_improved.merge.DAOD_HIGG4D2.e4607_s2726_r7725_r7676_p2823
 1448 mc15_13TeV:mc15_13TeV.361092.Sherpa_C10_WpqqWmlv_SHv21_improved.merge.DAOD_HIGG4D2.e4607_s2726_r7725_r7676_p2823
 1449 mc15_13TeV:mc15_13TeV.361093.Sherpa_C10_WlvZqq_SHv21_improved.merge.DAOD_HIGG4D2.e4607_s2726_r7725_r7676_p2823
 1450 mc15_13TeV:mc15_13TeV.361094.Sherpa_C10_WqqZll_SHv21_improved.merge.DAOD_HIGG4D2.e4607_s2726_r7725_r7676_p2823
 1451 mc15_13TeV:mc15_13TeV.361095.Sherpa_C10_WqqZvv_SHv21_improved.merge.DAOD_HIGG4D2.e4607_s2726_r7725_r7676_p2823
 1452 mc15_13TeV:mc15_13TeV.361096.Sherpa_C10_ZqqZll_SHv21_improved.merge.DAOD_HIGG4D2.e4607_s2726_r7725_r7676_p2823
 1453 mc15_13TeV:mc15_13TeV.361097.Sherpa_C10_ZqqZvv_SHv21_improved.merge.DAOD_HIGG4D2.e4607_s2726_r7725_r7676_p2823
 1454 mc15_13TeV:mc15_13TeV.361100.PowhegPythia8EvtGen_AZNLOCTEQ6L1_Wplusenu.merge.DAOD_HIGG4D2.e3601_s2576_s2132_r7725_r7676_p2823
 1455 mc15_13TeV:mc15_13TeV.361101.PowhegPythia8EvtGen_AZNLOCTEQ6L1_Wplusmunu.merge.DAOD_HIGG4D2.e3601_s2576_s2132_r7725_r7676_p2823
 1456 mc15_13TeV:mc15_13TeV.361102.PowhegPythia8EvtGen_AZNLOCTEQ6L1_Wplustaunu.merge.DAOD_HIGG4D2.e3601_s2576_s2132_r7725_r7676_p2823
 1457 mc15_13TeV:mc15_13TeV.361103.PowhegPythia8EvtGen_AZNLOCTEQ6L1_Wminusenu.merge.DAOD_HIGG4D2.e3601_s2576_s2132_r7725_r7676_p2823
 1458 mc15_13TeV:mc15_13TeV.361104.PowhegPythia8EvtGen_AZNLOCTEQ6L1_Wminusmunu.merge.DAOD_HIGG4D2.e3601_s2576_s2132_r7725_r7676_p2823
 1459 mc15_13TeV:mc15_13TeV.361105.PowhegPythia8EvtGen_AZNLOCTEQ6L1_Wminusstaunu.merge.DAOD_HIGG4D2.e3601_s2576_s2132_r7725_r7676_p2823
 1460 mc15_13TeV:mc15_13TeV.361106.PowhegPythia8EvtGen_AZNLOCTEQ6L1_Zee.merge.DAOD_HIGG4D2.e3601_s2576_s2132_r7725_r7676_p2823
 1461 mc15_13TeV:mc15_13TeV.361107.PowhegPythia8EvtGen_AZNLOCTEQ6L1_Zmumu.merge.DAOD_HIGG4D2.e3601_s2576_s2132_r7725_r7676_p2823
 1462 mc15_13TeV:mc15_13TeV.361108.PowhegPythia8EvtGen_AZNLOCTEQ6L1_Ztautau.merge.DAOD_HIGG4D2.e3601_s2726_r7725_r7676_p2823
 1463 mc15_13TeV:mc15_13TeV.361468.Sherpa_C10_Zee_Mll10to40_Pt0_70_BVeto.merge.DAOD_HIGG4D2.e4198_s2608_s2183_r7725_r7676_p2823
 1464 mc15_13TeV:mc15_13TeV.361469.Sherpa_C10_Zee_Mll10to40_Pt0_70_BFilter.merge.DAOD_HIGG4D2.e4198_s2608_s2183_r7725_r7676_p2823
 1465 mc15_13TeV:mc15_13TeV.361470.Sherpa_C10_Zee_Mll10to40_Pt70_140_BVeto.merge.DAOD_HIGG4D2.e4198_s2608_s2183_r7725_r7676_p2823
 1466 mc15_13TeV:mc15_13TeV.361471.Sherpa_C10_Zee_Mll10to40_Pt70_140_BFilter.merge.DAOD_HIGG4D2.e4198_s2608_s2183_r7725_r7676_p2823
 1467 mc15_13TeV:mc15_13TeV.361472.Sherpa_C10_Zee_Mll10to40_Pt140_400_BVeto.merge.DAOD_HIGG4D2.e4198_s2608_s2183_r7725_r7676_p2823
 1468 mc15_13TeV:mc15_13TeV.361473.Sherpa_C10_Zee_Mll10to40_Pt140_400_BFilter.merge.DAOD_HIGG4D2.e4198_s2608_s2183_r7725_r7676_p2823
 1469 mc15_13TeV:mc15_13TeV.361474.Sherpa_C10_Zee_Mll10to40_Pt400_E_CMS_BVeto.merge.DAOD_HIGG4D2.e4198_s2608_s2183_r7725_r7676_p2823
 1470 mc15_13TeV:mc15_13TeV.361475.Sherpa_C10_Zee_Mll10to40_Pt400_E_CMS_BFilter.merge.DAOD_HIGG4D2.e4198_s2608_s2183_r7725_r7676_p2823
 1471 mc15_13TeV:mc15_13TeV.361476.Sherpa_C10_Zmumu_Mll10to40_Pt0_70_BVeto.merge.DAOD_HIGG4D2.e4198_s2608_s2183_r7725_r7676_p2823
 1472 mc15_13TeV:mc15_13TeV.361477.Sherpa_C10_Zmumu_Mll10to40_Pt0_70_BFilter.merge.DAOD_HIGG4D2.e4198_s2608_s2183_r7725_r7676_p2823
 1473 mc15_13TeV:mc15_13TeV.361478.Sherpa_C10_Zmumu_Mll10to40_Pt70_140_BVeto.merge.DAOD_HIGG4D2.e4198_s2608_s2183_r7725_r7676_p2823
 1474 mc15_13TeV:mc15_13TeV.361479.Sherpa_C10_Zmumu_Mll10to40_Pt70_140_BFilter.merge.DAOD_HIGG4D2.e4198_s2608_s2183_r7725_r7676_p2823
 1475 mc15_13TeV:mc15_13TeV.361480.Sherpa_C10_Zmumu_Mll10to40_Pt140_400_BVeto.merge.DAOD_HIGG4D2.e4198_s2608_s2183_r7725_r7676_p2823
 1476 mc15_13TeV:mc15_13TeV.361481.Sherpa_C10_Zmumu_Mll10to40_Pt140_400_BFilter.merge.DAOD_HIGG4D2.e4198_s2608_s2183_r7725_r7676_p2823
 1477 mc15_13TeV:mc15_13TeV.361482.Sherpa_C10_Zmumu_Mll10to40_Pt400_E_CMS_BVeto.merge.DAOD_HIGG4D2.e4198_s2608_s2183_r7725_r7676_p2823
 1478 mc15_13TeV:mc15_13TeV.361483.Sherpa_C10_Zmumu_Mll10to40_Pt400_E_CMS_BFilter.merge.DAOD_HIGG4D2.e4198_s2608_s2183_r7725_r7676_p2823
 1479 mc15_13TeV:mc15_13TeV.361484.Sherpa_C10_Ztautau_Mll10to40_Pt0_70_BVeto.merge.DAOD_HIGG4D2.e4198_s2608_s2183_r7725_r7676_p2823
 1480 mc15_13TeV:mc15_13TeV.361485.Sherpa_C10_Ztautau_Mll10to40_Pt0_70_BFilter.merge.DAOD_HIGG4D2.e4198_s2608_s2183_r7725_r7676_p2823
 1481 mc15_13TeV:mc15_13TeV.361486.Sherpa_C10_Ztautau_Mll10to40_Pt70_140_BVeto.merge.DAOD_HIGG4D2.e4198_s2608_s2183_r7725_r7676_p2823
 1482 mc15_13TeV:mc15_13TeV.361487.Sherpa_C10_Ztautau_Mll10to40_Pt70_140_BFilter.merge.DAOD_HIGG4D2.e4198_s2608_s2183_r7725_r7676_p2823
 1483 mc15_13TeV:mc15_13TeV.361488.Sherpa_C10_Ztautau_Mll10to40_Pt140_400_BVeto.merge.DAOD_HIGG4D2.e4198_s2608_s2183_r7725_r7676_p2823
 1484 mc15_13TeV:mc15_13TeV.361489.Sherpa_C10_Ztautau_Mll10to40_Pt140_400_BFilter.merge.DAOD_HIGG4D2.e4198_s2608_s2183_r7725_r7676_p2823
 1485 mc15_13TeV:mc15_13TeV.361490.Sherpa_C10_Ztautau_Mll10to40_Pt400_E_CMS_BVeto.merge.DAOD_HIGG4D2.e4198_s2608_s2183_r7725_r7676_p2823
 1486 mc15_13TeV:mc15_13TeV.361491.Sherpa_C10_Ztautau_Mll10to40_Pt400_E_CMS_BFilter.merge.DAOD_HIGG4D2.e4198_s2608_s2183_r7725_r7676_p2823
 1487 mc15_13TeV:mc15_13TeV.363331.Sherpa_NNPDF30NNLO_Wtaunu_Pt0_70_CVetoBVeto.merge.DAOD_HIGG4D2.e4709_s2726_r7725_r7676_p2823
 1488 mc15_13TeV:mc15_13TeV.363332.Sherpa_NNPDF30NNLO_Wtaunu_Pt0_70_CFilterBVeto.merge.DAOD_HIGG4D2.e4709_s2726_r7725_r7676_p2823
 1489 mc15_13TeV:mc15_13TeV.363333.Sherpa_NNPDF30NNLO_Wtaunu_Pt0_70_BFilter.merge.DAOD_HIGG4D2.e4709_s2726_r7725_r7676_p2823

1490 mc15_13TeV:mc15_13TeV.363334.Sherpa_NNPDF30NNLO_Wtaunu_Pt70_140_CVetoBVeto.merge.DAOD_HIGG4D2.e4709_s2726_r7725_r7676_p2823
 1491 mc15_13TeV:mc15_13TeV.363335.Sherpa_NNPDF30NNLO_Wtaunu_Pt70_140_CFilterBVeto.merge.DAOD_HIGG4D2.e4709_s2726_r7725_r7676_p2823
 1492 mc15_13TeV:mc15_13TeV.363336.Sherpa_NNPDF30NNLO_Wtaunu_Pt70_140_BFilter.merge.DAOD_HIGG4D2.e4779_s2726_r7725_r7676_p2823
 1493 mc15_13TeV:mc15_13TeV.363337.Sherpa_NNPDF30NNLO_Wtaunu_Pt140_280_CVetoBVeto.merge.DAOD_HIGG4D2.e4709_s2726_r7725_r7676_p2823
 1494 mc15_13TeV:mc15_13TeV.363338.Sherpa_NNPDF30NNLO_Wtaunu_Pt140_280_CFilterBVeto.merge.DAOD_HIGG4D2.e4709_s2726_r7725_r7676_p2823
 1495 mc15_13TeV:mc15_13TeV.363339.Sherpa_NNPDF30NNLO_Wtaunu_Pt140_280_BFilter.merge.DAOD_HIGG4D2.e4709_s2726_r7725_r7676_p2823
 1496 mc15_13TeV:mc15_13TeV.363340.Sherpa_NNPDF30NNLO_Wtaunu_Pt280_500_CVetoBVeto.merge.DAOD_HIGG4D2.e4709_s2726_r7725_r7676_p2823
 1497 mc15_13TeV:mc15_13TeV.363341.Sherpa_NNPDF30NNLO_Wtaunu_Pt280_500_CFilterBVeto.merge.DAOD_HIGG4D2.e4779_s2726_r7725_r7676_p2823
 1498 mc15_13TeV:mc15_13TeV.363342.Sherpa_NNPDF30NNLO_Wtaunu_Pt280_500_BFilter.merge.DAOD_HIGG4D2.e4779_s2726_r7725_r7676_p2823
 1499 mc15_13TeV:mc15_13TeV.363343.Sherpa_NNPDF30NNLO_Wtaunu_Pt500_700_CVetoBVeto.merge.DAOD_HIGG4D2.e4709_s2726_r7725_r7676_p2823
 1500 mc15_13TeV:mc15_13TeV.363344.Sherpa_NNPDF30NNLO_Wtaunu_Pt500_700_CFilterBVeto.merge.DAOD_HIGG4D2.e4709_s2726_r7725_r7676_p2823
 1501 mc15_13TeV:mc15_13TeV.363345.Sherpa_NNPDF30NNLO_Wtaunu_Pt500_700_BFilter.merge.DAOD_HIGG4D2.e4779_s2726_r7725_r7676_p2823
 1502 mc15_13TeV:mc15_13TeV.363346.Sherpa_NNPDF30NNLO_Wtaunu_Pt700_1000_CVetoBVeto.merge.DAOD_HIGG4D2.e4709_s2726_r7725_r7676_p2823
 1503 mc15_13TeV:mc15_13TeV.363347.Sherpa_NNPDF30NNLO_Wtaunu_Pt700_1000_CFilterBVeto.merge.DAOD_HIGG4D2.e4709_s2726_r7725_r7676_p2823
 1504 mc15_13TeV:mc15_13TeV.363348.Sherpa_NNPDF30NNLO_Wtaunu_Pt700_1000_BFilter.merge.DAOD_HIGG4D2.e4779_s2726_r7725_r7676_p2823
 1505 mc15_13TeV:mc15_13TeV.363349.Sherpa_NNPDF30NNLO_Wtaunu_Pt1000_2000_CVetoBVeto.merge.DAOD_HIGG4D2.e4709_s2726_r7725_r7676_p2823
 1506 mc15_13TeV:mc15_13TeV.363350.Sherpa_NNPDF30NNLO_Wtaunu_Pt1000_2000_CFilterBVeto.merge.DAOD_HIGG4D2.e4709_s2726_r7725_r7676_p2823
 1507 mc15_13TeV:mc15_13TeV.363351.Sherpa_NNPDF30NNLO_Wtaunu_Pt1000_2000_BFilter.merge.DAOD_HIGG4D2.e4779_s2726_r8129_r7676_p2823
 1508 mc15_13TeV:mc15_13TeV.363352.Sherpa_NNPDF30NNLO_Wtaunu_Pt2000_E_CMS_CVetoBVeto.merge.DAOD_HIGG4D2.e4709_s2726_r7725_r7676_p2823
 1509 mc15_13TeV:mc15_13TeV.363353.Sherpa_NNPDF30NNLO_Wtaunu_Pt2000_E_CMS_CFilterBVeto.merge.DAOD_HIGG4D2.e4709_s2726_r7725_r7676_p2823
 1510 mc15_13TeV:mc15_13TeV.363354.Sherpa_NNPDF30NNLO_Wtaunu_Pt2000_E_CMS_BFilter.merge.DAOD_HIGG4D2.e4709_s2726_r7725_r7676_p2823
 1511 mc15_13TeV:mc15_13TeV.363436.Sherpa_NNPDF30NNLO_Wmmunu_Pt0_70_CVetoBVeto.merge.DAOD_HIGG4D2.e4715_s2726_r7725_r7676_p2823
 1512 mc15_13TeV:mc15_13TeV.363437.Sherpa_NNPDF30NNLO_Wmmunu_Pt0_70_CFilterBVeto.merge.DAOD_HIGG4D2.e4715_s2726_r7725_r7676_p2823
 1513 mc15_13TeV:mc15_13TeV.363438.Sherpa_NNPDF30NNLO_Wmmunu_Pt0_70_BFilter.merge.DAOD_HIGG4D2.e4715_s2726_r7725_r7676_p2823
 1514 mc15_13TeV:mc15_13TeV.363439.Sherpa_NNPDF30NNLO_Wmmunu_Pt70_140_CVetoBVeto.merge.DAOD_HIGG4D2.e4715_s2726_r7725_r7676_p2823
 1515 mc15_13TeV:mc15_13TeV.363440.Sherpa_NNPDF30NNLO_Wmmunu_Pt70_140_CFilterBVeto.merge.DAOD_HIGG4D2.e4715_s2726_r7725_r7676_p2823
 1516 mc15_13TeV:mc15_13TeV.363441.Sherpa_NNPDF30NNLO_Wmmunu_Pt70_140_BFilter.merge.DAOD_HIGG4D2.e4715_s2726_r7725_r7676_p2823
 1517 mc15_13TeV:mc15_13TeV.363442.Sherpa_NNPDF30NNLO_Wmmunu_Pt140_280_CVetoBVeto.merge.DAOD_HIGG4D2.e4715_s2726_r7725_r7676_p2823
 1518 mc15_13TeV:mc15_13TeV.363443.Sherpa_NNPDF30NNLO_Wmmunu_Pt140_280_CFilterBVeto.merge.DAOD_HIGG4D2.e4715_s2726_r7725_r7676_p2823
 1519 mc15_13TeV:mc15_13TeV.363444.Sherpa_NNPDF30NNLO_Wmmunu_Pt140_280_BFilter.merge.DAOD_HIGG4D2.e4715_s2726_r7725_r7676_p2823
 1520 mc15_13TeV:mc15_13TeV.363445.Sherpa_NNPDF30NNLO_Wmmunu_Pt280_500_CVetoBVeto.merge.DAOD_HIGG4D2.e4715_s2726_r7725_r7676_p2823
 1521 mc15_13TeV:mc15_13TeV.363446.Sherpa_NNPDF30NNLO_Wmmunu_Pt280_500_CFilterBVeto.merge.DAOD_HIGG4D2.e4715_s2726_r7725_r7676_p2823
 1522 mc15_13TeV:mc15_13TeV.363447.Sherpa_NNPDF30NNLO_Wmmunu_Pt280_500_BFilter.merge.DAOD_HIGG4D2.e4715_s2726_r7725_r7676_p2823
 1523 mc15_13TeV:mc15_13TeV.363448.Sherpa_NNPDF30NNLO_Wmmunu_Pt500_700_CVetoBVeto.merge.DAOD_HIGG4D2.e4715_s2726_r7725_r7676_p2823
 1524 mc15_13TeV:mc15_13TeV.363449.Sherpa_NNPDF30NNLO_Wmmunu_Pt500_700_CFilterBVeto.merge.DAOD_HIGG4D2.e4715_s2726_r7725_r7676_p2823
 1525 mc15_13TeV:mc15_13TeV.363450.Sherpa_NNPDF30NNLO_Wmmunu_Pt500_700_BFilter.merge.DAOD_HIGG4D2.e4715_s2726_r7725_r7676_p2823
 1526 mc15_13TeV:mc15_13TeV.363451.Sherpa_NNPDF30NNLO_Wmmunu_Pt700_1000_CVetoBVeto.merge.DAOD_HIGG4D2.e4715_s2726_r7725_r7676_p2823
 1527 mc15_13TeV:mc15_13TeV.363452.Sherpa_NNPDF30NNLO_Wmmunu_Pt700_1000_CFilterBVeto.merge.DAOD_HIGG4D2.e4715_s2726_r7725_r7676_p2823
 1528 mc15_13TeV:mc15_13TeV.363453.Sherpa_NNPDF30NNLO_Wmmunu_Pt700_1000_BFilter.merge.DAOD_HIGG4D2.e4715_s2726_r7725_r7676_p2823
 1529 mc15_13TeV:mc15_13TeV.363454.Sherpa_NNPDF30NNLO_Wmmunu_Pt1000_2000_CVetoBVeto.merge.DAOD_HIGG4D2.e4715_s2726_r7725_r7676_p2823
 1530 mc15_13TeV:mc15_13TeV.363455.Sherpa_NNPDF30NNLO_Wmmunu_Pt1000_2000_CFilterBVeto.merge.DAOD_HIGG4D2.e4715_s2726_r7725_r7676_p2823
 1531 mc15_13TeV:mc15_13TeV.363456.Sherpa_NNPDF30NNLO_Wmmunu_Pt1000_2000_BFilter.merge.DAOD_HIGG4D2.e4715_s2726_r7725_r7676_p2823
 1532 mc15_13TeV:mc15_13TeV.363457.Sherpa_NNPDF30NNLO_Wmmunu_Pt2000_E_CMS_CVetoBVeto.merge.DAOD_HIGG4D2.e4715_s2726_r7725_r7676_p2823
 1533 mc15_13TeV:mc15_13TeV.363458.Sherpa_NNPDF30NNLO_Wmmunu_Pt2000_E_CMS_CFilterBVeto.merge.DAOD_HIGG4D2.e4715_s2726_r7725_r7676_p2823
 1534 mc15_13TeV:mc15_13TeV.363459.Sherpa_NNPDF30NNLO_Wmmunu_Pt2000_E_CMS_BFilter.merge.DAOD_HIGG4D2.e4715_s2726_r7725_r7676_p2823
 1535 mc15_13TeV:mc15_13TeV.363460.Sherpa_NNPDF30NNLO_Wenu_Pt0_70_CVetoBVeto.merge.DAOD_HIGG4D2.e4715_s2726_r7725_r7676_p2823
 1536 mc15_13TeV:mc15_13TeV.363461.Sherpa_NNPDF30NNLO_Wenu_Pt0_70_CFilterBVeto.merge.DAOD_HIGG4D2.e4715_s2726_r7725_r7676_p2823

Not reviewed, for internal circulation only

1537 mc15_13TeV:mc15_13TeV.363462.Sherpa_NNPDF30NNLO_Wenu_Pt0_70_BFilter.merge.DAOD_HIGG4D2.e4715_s2726_r7725_r7676_p2823
 1538 mc15_13TeV:mc15_13TeV.363463.Sherpa_NNPDF30NNLO_Wenu_Pt70_140_CVetoBVeto.merge.DAOD_HIGG4D2.e4715_s2726_r7725_r7676_p2823
 1539 mc15_13TeV:mc15_13TeV.363464.Sherpa_NNPDF30NNLO_Wenu_Pt70_140_CFilterBVeto.merge.DAOD_HIGG4D2.e4715_s2726_r7725_r7676_p2823
 1540 mc15_13TeV:mc15_13TeV.363465.Sherpa_NNPDF30NNLO_Wenu_Pt70_140_BFilter.merge.DAOD_HIGG4D2.e4715_s2726_r7725_r7676_p2823
 1541 mc15_13TeV:mc15_13TeV.363466.Sherpa_NNPDF30NNLO_Wenu_Pt140_280_CVetoBVeto.merge.DAOD_HIGG4D2.e4715_s2726_r7725_r7676_p2823
 1542 mc15_13TeV:mc15_13TeV.363467.Sherpa_NNPDF30NNLO_Wenu_Pt140_280_CFilterBVeto.merge.DAOD_HIGG4D2.e4715_s2726_r7725_r7676_p2823
 1543 mc15_13TeV:mc15_13TeV.363468.Sherpa_NNPDF30NNLO_Wenu_Pt140_280_BFilter.merge.DAOD_HIGG4D2.e4715_s2726_r7725_r7676_p2823
 1544 mc15_13TeV:mc15_13TeV.363469.Sherpa_NNPDF30NNLO_Wenu_Pt280_500_CVetoBVeto.merge.DAOD_HIGG4D2.e4715_s2726_r7725_r7676_p2823
 1545 mc15_13TeV:mc15_13TeV.363470.Sherpa_NNPDF30NNLO_Wenu_Pt280_500_CFilterBVeto.merge.DAOD_HIGG4D2.e4715_s2726_r7725_r7676_p2823
 1546 mc15_13TeV:mc15_13TeV.363471.Sherpa_NNPDF30NNLO_Wenu_Pt280_500_BFilter.merge.DAOD_HIGG4D2.e4715_s2726_r7725_r7676_p2823
 1547 mc15_13TeV:mc15_13TeV.363472.Sherpa_NNPDF30NNLO_Wenu_Pt500_700_CVetoBVeto.merge.DAOD_HIGG4D2.e4715_s2726_r7725_r7676_p2823
 1548 mc15_13TeV:mc15_13TeV.363473.Sherpa_NNPDF30NNLO_Wenu_Pt500_700_CFilterBVeto.merge.DAOD_HIGG4D2.e4715_s2726_r7725_r7676_p2823
 1549 mc15_13TeV:mc15_13TeV.363474.Sherpa_NNPDF30NNLO_Wenu_Pt500_700_BFilter.merge.DAOD_HIGG4D2.e4771_s2726_r7725_r7676_p2823
 1550 mc15_13TeV:mc15_13TeV.363475.Sherpa_NNPDF30NNLO_Wenu_Pt700_1000_CVetoBVeto.merge.DAOD_HIGG4D2.e4715_s2726_r7725_r7676_p2823
 1551 mc15_13TeV:mc15_13TeV.363476.Sherpa_NNPDF30NNLO_Wenu_Pt700_1000_CFilterBVeto.merge.DAOD_HIGG4D2.e4715_s2726_r7725_r7676_p2823
 1552 mc15_13TeV:mc15_13TeV.363477.Sherpa_NNPDF30NNLO_Wenu_Pt700_1000_BFilter.merge.DAOD_HIGG4D2.e4715_s2726_r7725_r7676_p2823
 1553 mc15_13TeV:mc15_13TeV.363478.Sherpa_NNPDF30NNLO_Wenu_Pt1000_2000_CVetoBVeto.merge.DAOD_HIGG4D2.e4715_s2726_r7725_r7676_p2823
 1554 mc15_13TeV:mc15_13TeV.363479.Sherpa_NNPDF30NNLO_Wenu_Pt1000_2000_CFilterBVeto.merge.DAOD_HIGG4D2.e4715_s2726_r7725_r7676_p2823
 1555 mc15_13TeV:mc15_13TeV.363480.Sherpa_NNPDF30NNLO_Wenu_Pt1000_2000_BFilter.merge.DAOD_HIGG4D2.e4715_s2726_r7725_r7676_p2823
 1556 mc15_13TeV:mc15_13TeV.363481.Sherpa_NNPDF30NNLO_Wenu_Pt2000_E_CMS_CVetoBVeto.merge.DAOD_HIGG4D2.e4715_s2726_r7725_r7676_p2823
 1557 mc15_13TeV:mc15_13TeV.363482.Sherpa_NNPDF30NNLO_Wenu_Pt2000_E_CMS_CFilterBVeto.merge.DAOD_HIGG4D2.e4715_s2726_r7722_r7676_p2823
 1558 mc15_13TeV:mc15_13TeV.363483.Sherpa_NNPDF30NNLO_Wenu_Pt2000_E_CMS_BFilter.merge.DAOD_HIGG4D2.e4715_s2726_r8084_r7676_p2823
 1559 mc15_13TeV:mc15_13TeV.410000.PowhegPythiaEvtGen_P2012_ttbar_hdamp172p5_nonallhad.merge.DAOD_HIGG4D2.e3698_s2608_s2183_r7725_r7676_p2823
 1560 mc15_13TeV:mc15_13TeV.410011.PowhegPythiaEvtGen_P2012_singletop_tchan_lept_top.merge.DAOD_HIGG4D2.e3824_s2608_s2183_r7725_r7676_p2823
 1561 mc15_13TeV:mc15_13TeV.410012.PowhegPythiaEvtGen_P2012_singletop_tchan_lept_antitop.merge.DAOD_HIGG4D2.e3824_s2608_s2183_r7725_r7676_p2823
 1562 mc15_13TeV:mc15_13TeV.410013.PowhegPythiaEvtGen_P2012_Wt_inclusive_top.merge.DAOD_HIGG4D2.e3753_s2608_s2183_r7725_r7676_p2823
 1563 mc15_13TeV:mc15_13TeV.410014.PowhegPythiaEvtGen_P2012_Wt_inclusive_antitop.merge.DAOD_HIGG4D2.e3753_s2608_s2183_r7725_r7676_p2823
 1564 mc15_13TeV:mc15_13TeV.410015.PowhegPythiaEvtGen_P2012_Wt_dilepton_top.merge.DAOD_HIGG4D2.e3753_s2608_s2183_r7725_r7676_p2823
 1565 mc15_13TeV:mc15_13TeV.410016.PowhegPythiaEvtGen_P2012_Wt_dilepton_antitop.merge.DAOD_HIGG4D2.e3753_s2608_s2183_r7725_r7676_p2823
 1566 mc15_13TeV:mc15_13TeV.410025.PowhegPythiaEvtGen_P2012_SingleTopSchan_noAllHad_top.merge.DAOD_HIGG4D2.e3998_s2608_s2183_r7725_r7676_p2823
 1567 mc15_13TeV:mc15_13TeV.410026.PowhegPythiaEvtGen_P2012_SingleTopSchan_noAllHad_antitop.merge.DAOD_HIGG4D2.e3998_s2608_s2183_r7725_r7676_p2823
 1568

Not reviewed, for internal circulation only

1569 **F. Fake related studies**

1570 **F.1. Details of QCD fake systematics treatment**

1571 Finally, the systematic uncertainty on the multi-jet τ_{had} fake factor has to be derived. One contribution to it is
 1572 rooted in the fact that the QCD control region is not pure, but contaminated with non-multi-jet background.
 1573 However, this contamination is small, see figure 77. An uncertainty on the background subtraction is
 1574 therefore derived by varying the MC normalization by 50%, that is, weighting the background subtracting
 1575 with a factor of 0.5 (1.5) for the upper (lower) simulation uncertainty.

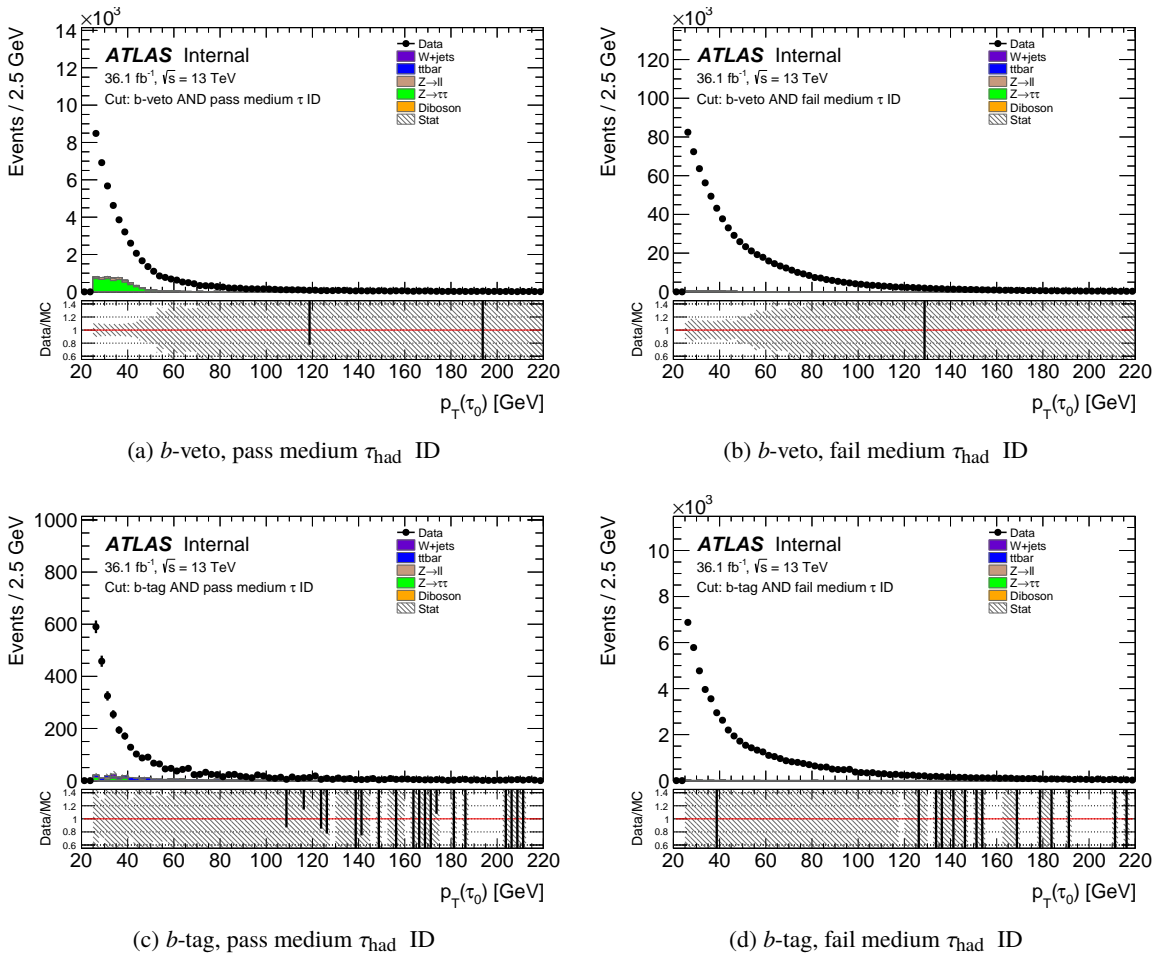


Figure 77: Observed data events and background contamination in the QCD control region.

1576 The derivation of the systematic uncertainty due to the selection of the control region itself is not so
 1577 straightforward, mainly because the datasets used for the calculation of the fake factors only contain one
 1578 variable with information about the lepton isolation. Figure 78 shows plots of this variable in the QCD
 1579 control region, for inclusive channel, category and number of charged tracks.

1580 The event's electron or muon passes the isolation requirement if the lepton isolation variable has a value
 1581 greater than 10,000. Unfortunately, separate information about track isolation in the inner detector and
 1582 isolation of hits in the electromagnetic calorimeter is not available.

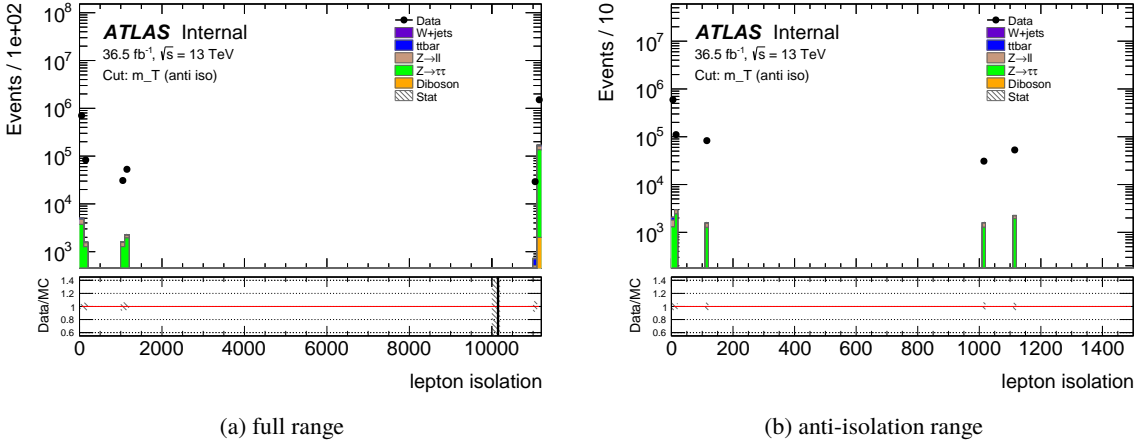


Figure 78: Lepton isolation variable available for this analysis, plotted after the cut on m_T in the QCD control region, inclusive channel, category and number of charged tracks.

1583 Thus, to get an estimate of the systematic uncertainty due to the definition of the QCD CR, two ways of
 1584 varying the fake factor calculation have been investigated. On the one hand, the control region has been
 1585 split into three ranges,

- 1586 • low: lepton isolation < 100
- 1587 • medium: 100 < lepton isolation < 1000
- 1588 • high: 1000 < lepton isolation < 10000

1589 and the FF_{MJ}^τ has been derived individually in each of those.

1590 On the other hand, an alternative QCD control region has been defined where the τ_{lep} passes the isolation
 1591 requirement and instead the cut on the electric charges of the two final state τ leptons is inverted, requiring
 1592 them to be of the same sign (SS). The idea behind that definition is that τ_{had} candidates faked by a jet
 1593 which stems from a $W+jets$ event or especially a $t\bar{t}$ pair are less likely to contain a τ_{lep} of same charge
 1594 than those come from a multi-jet event.

1595 Looking at all variation histograms, figures 79 and 80, it is determined that a combined uncertainty of
 1596 20% on the nominal fake factor histogram is conservative enough to cover 68% of the population of
 1597 measurements. These somewhat arbitrary variations of the fake factor calculation do not provide a strong
 1598 enough basis for arguing that the systematic uncertainty should be smaller.

1599 As the uncertainty on the multi-jet τ_{had} fake factor is not one of the dominant uncertainties of this analysis,
 1600 a more rigorous treatment to justify a stricter uncertainty is not necessary.

Not reviewed, for internal circulation only

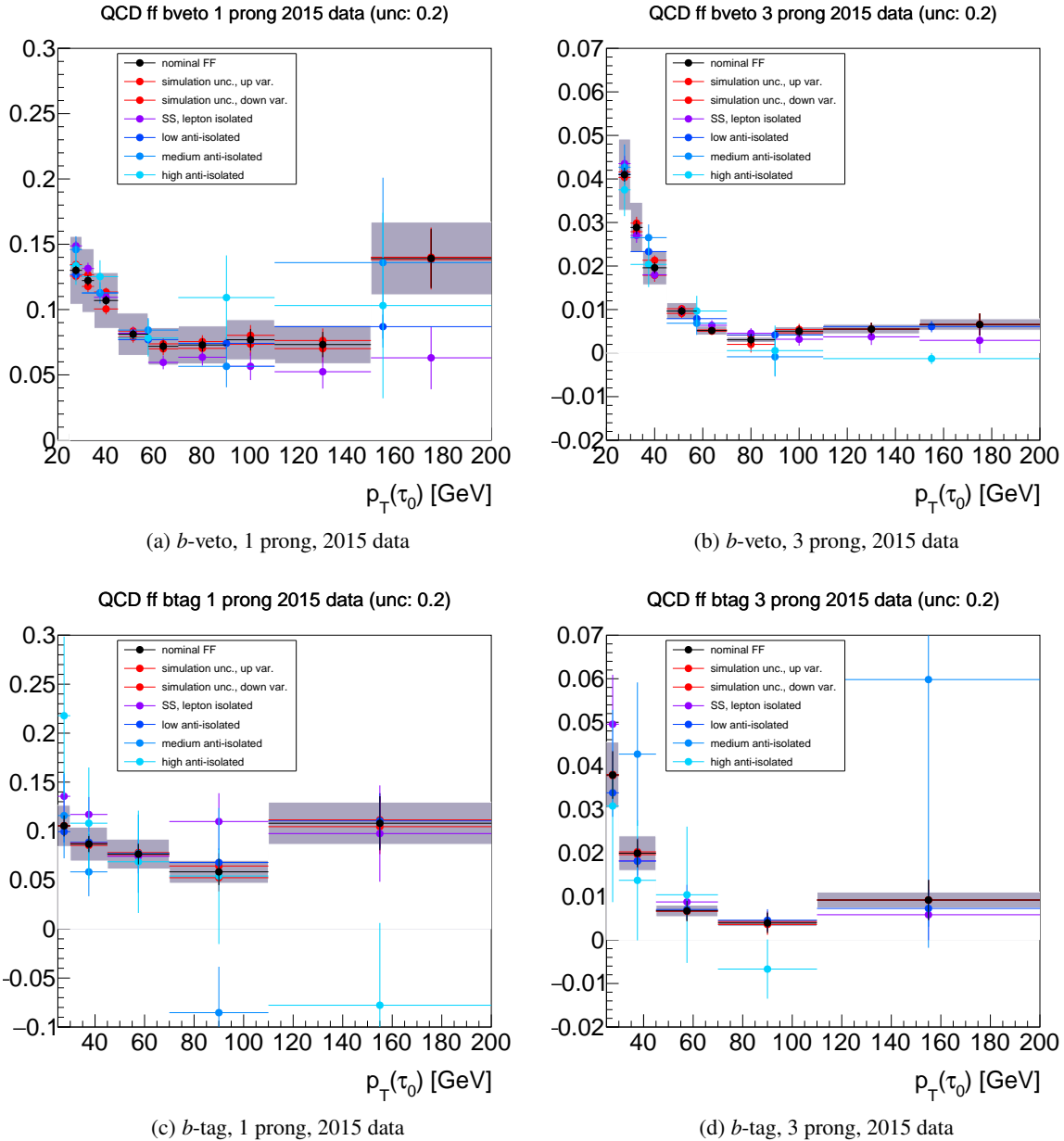


Figure 79: Nominal multi-jet τ_{had} fake factor histograms and variations for the 2015 data taking period. The uncertainty band shown corresponds to a combined uncertainty of 20% on the nominal histogram.

Not reviewed, for internal circulation only

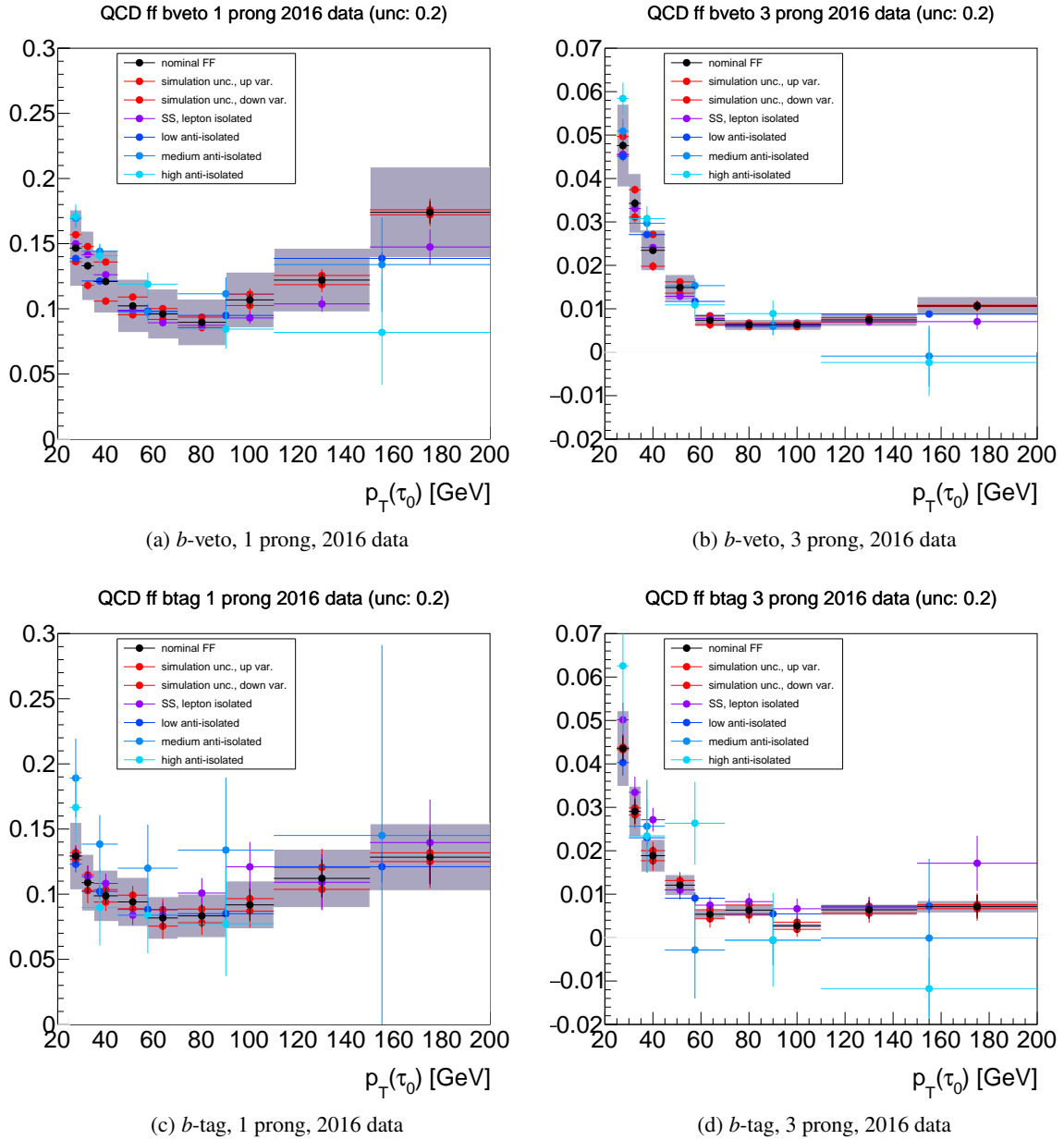


Figure 80: Nominal multi-jet τ_{had} fake factor histograms and variations for the 2016 data taking period. The uncertainty band shown corresponds to a combined uncertainty of 20% on the nominal histogram.

1601 F.2. Some investigation on the Fake lepton and Fake tau

1602 Figure 81 shows the fake factor as a function of tau pt in different pile up conditions. Figure 82 (a) show
 1603 the fake factors as a function of the average number of interactions per bunch crossing, also called pileup
 1604 or $\langle \mu \rangle$. It can be seen that there is a dependence between the fake factor and pileup. In 2015 data taking,
 1605 the isolation is not applied to the single lepton trigger but applied in the 2016 data taking due to the higher
 1606 instantaneous luminosity. The Multi-jet control region is selected by inverting isolation requirement. As
 1607 figure 82 (b) shows, the MJ CR selects relative more events with lower $\langle \mu \rangle$ in 2015 data. In such a case,
 1608 if we derive the fake factor with combined 2015 and 2016 data, the fake factor will be biased. Due to this
 1609 fact, we decide to derive the separated MJ fake factors for 2015 and 2016 data.

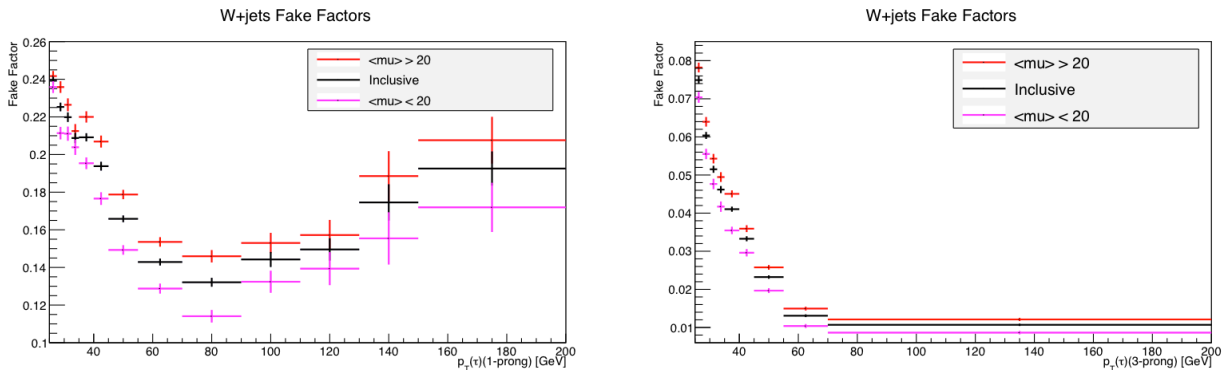


Figure 81: Fake factor comparison between high and low $\langle \mu \rangle$ for 1 prong (left) and 3 prong (right).

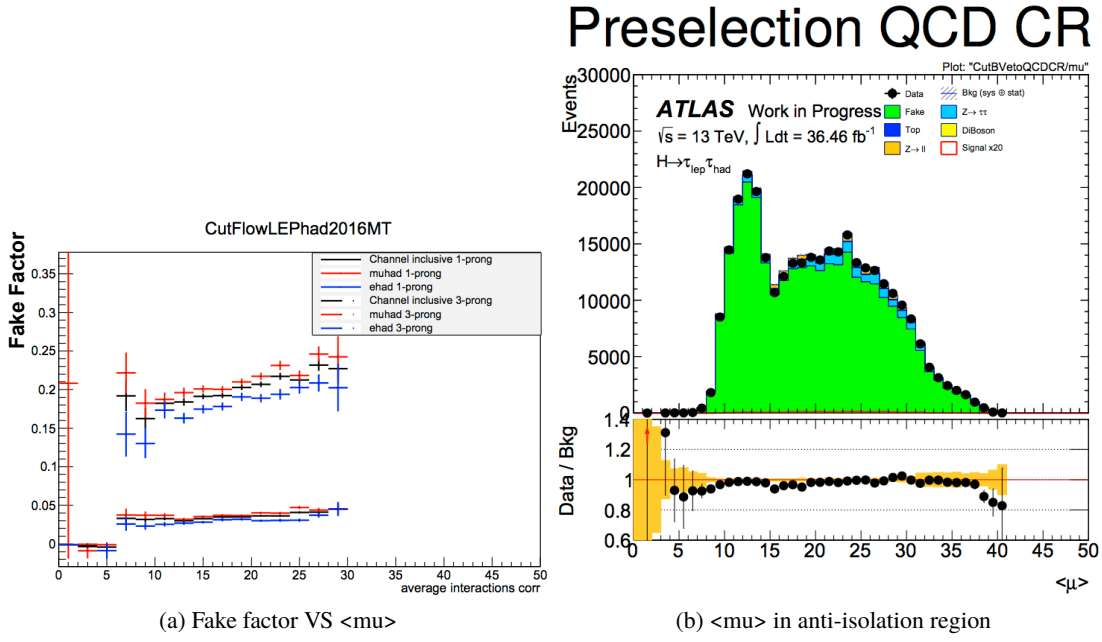


Figure 82

1610 For the Wjet fake factor, it is measured from Wjets control region where the same trigger as the signal
 1611 region is used. As demonstrated in figure 83, it is assumed that high $\langle \mu \rangle$ data has the larger fake rate

¹⁶¹² than the low $\langle \mu \rangle$ data. As $\langle \mu \rangle$ distribution is the same between the control region and the signal region, the common fake factor is still correct in the signal region.

Not reviewed, for internal circulation only

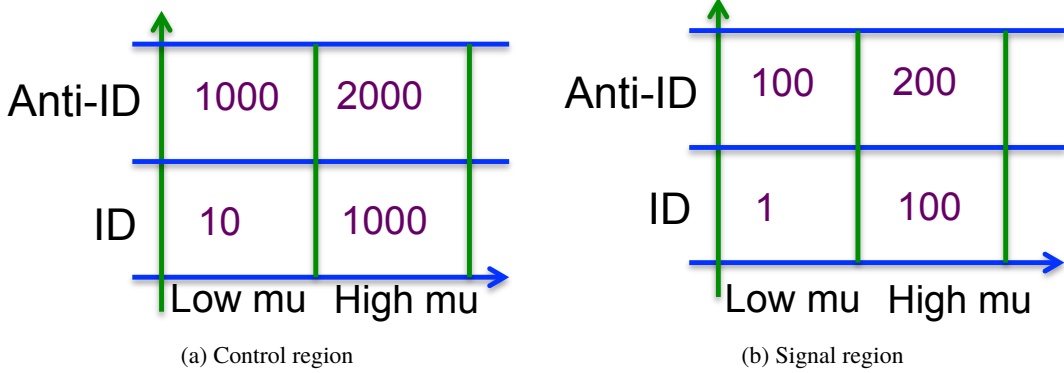


Figure 83: Illustrative plots for tau fake factor trigger selection dependence.

¹⁶¹³
¹⁶¹⁴ The similar argument is also valid for the lepton fake factor. As demonstrated in figure 81, the fraction for events pass or fail isolation is different between 2015 and 2016 due to the different trigger condition.
¹⁶¹⁵
¹⁶¹⁶ But as far as the situation is the same between the QCD fake lepton control region and signal region, the combined lepton fake factor is still valid.

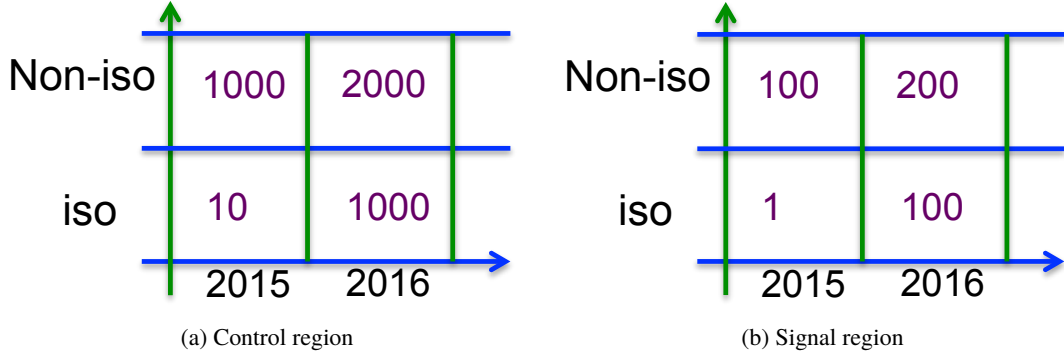


Figure 84: Illustrative plots for lepton fake factor trigger selection dependence.

¹⁶¹⁷
¹⁶¹⁸ Figure 85 shows the predicted Wjets fake background in signal region by using the combined fake factor
¹⁶¹⁹ and the annually separated fake factor. No significant difference is observed.

Not reviewed, for internal circulation only

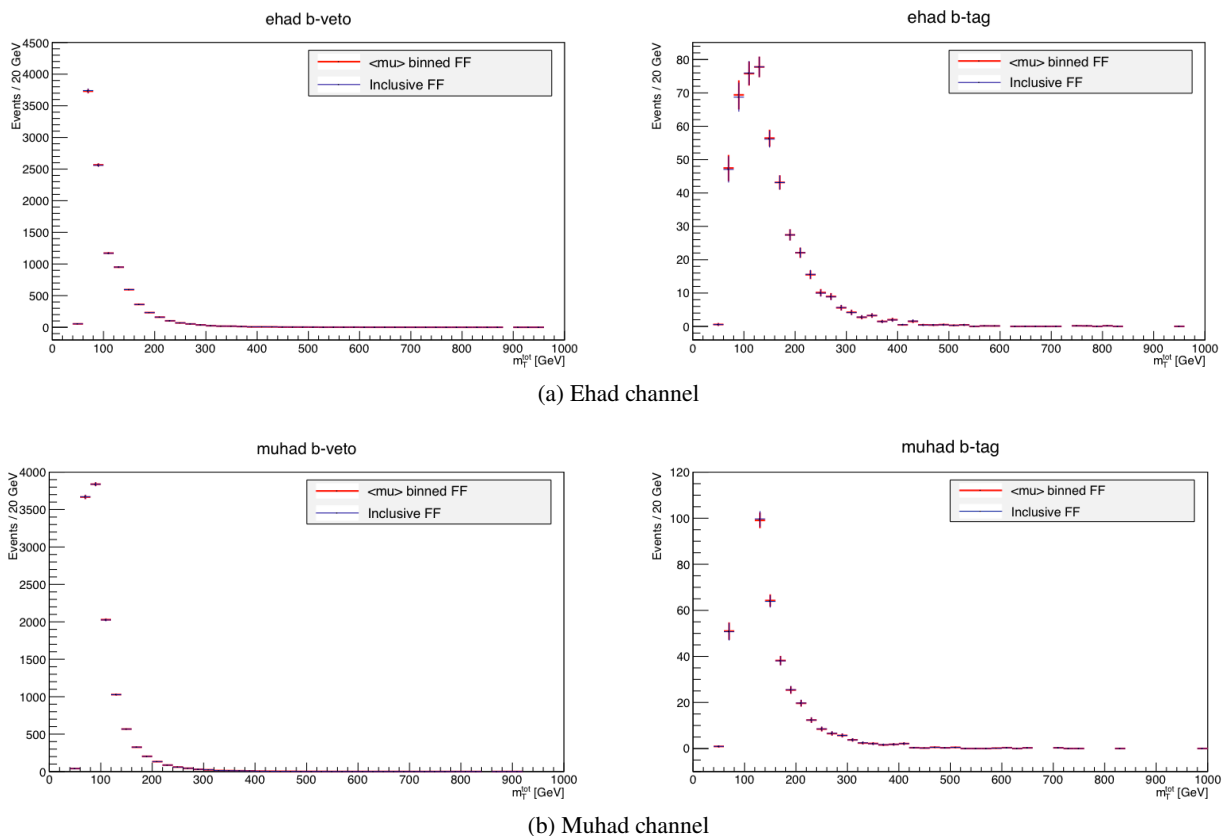


Figure 85: Wjets fake background comparison between combined fake factor and separated fake factor.

1620 F.3. Some investigation on the Fake tau from Wjets

1621 Figure 86 compares the fake factor measured with the selection of ehad, muhad and inclusive. It can be
 1622 seen that the difference between ehad and muhad is not significant.

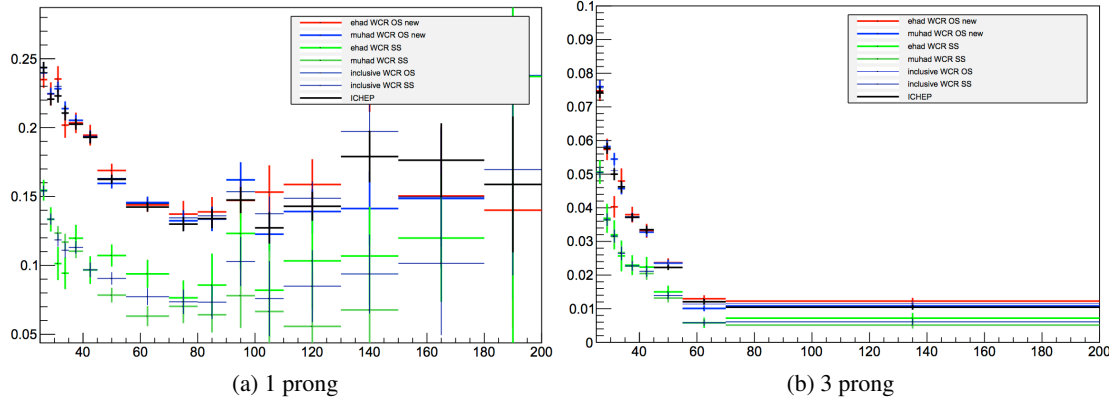


Figure 86: Fake factors comparison in different regions.

1623 Fake factors are derived from MC sample, measured in control regions, ICR, the SR, as shown in Fig. 87.
 1624 The statistical uncertainty is large due to the limited MC sample size. But it indicates that there is some
 1625 potential difference between different transverse mass regions.

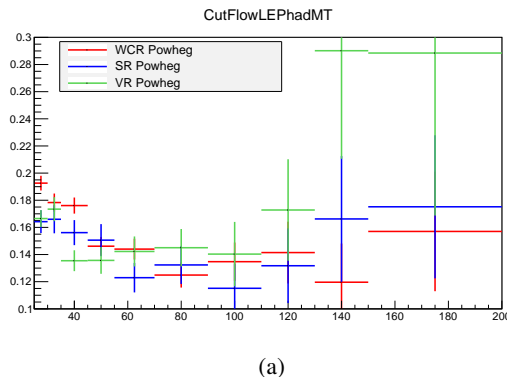


Figure 87: $W+jets$ fake factors measured with in MC simulation and compared in different regions (VR here is the ICR).

1626 Figures 88 and 89 show the data-MC comparison in the b -veto validation regions for 1 prong taus and 3
 1627 prong taus, respectively.

Not reviewed, for internal circulation only

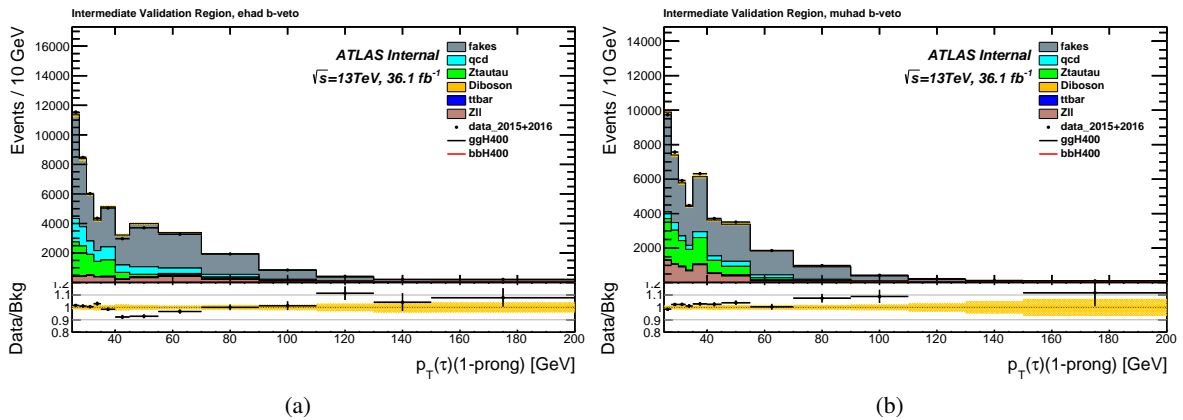


Figure 88: $p_T(\tau_{\text{had}})$ distributions of 1 prong tau in the b -veto (left) electron and (right) muon channel with requiring $40 < m_T(\ell, E_T^{\text{miss}}) < 60(70)$ GeV for muon(electron) channel. Backgrounds estimated from MC samples are truth matched.

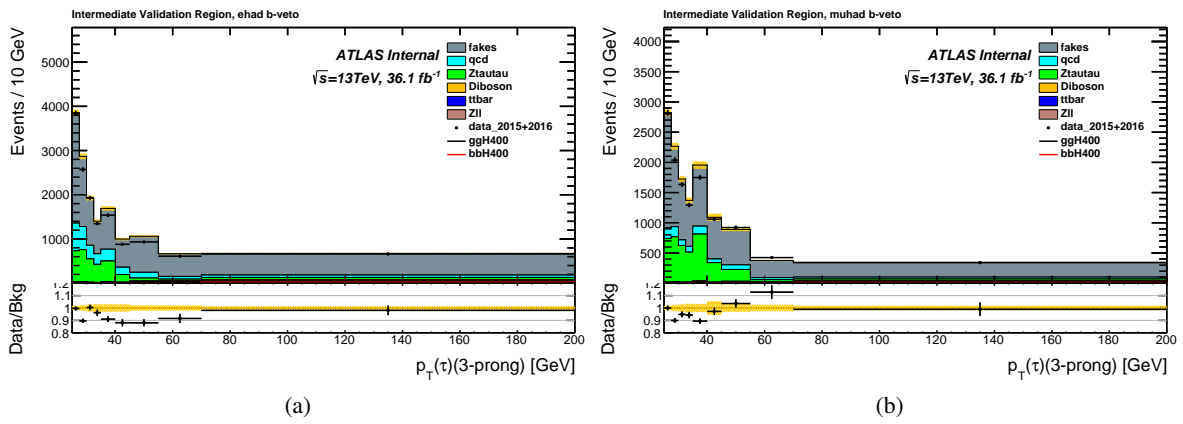


Figure 89: $p_T(\tau_{\text{had}})$ distributions of 3 prong tau in the b -veto (left) electron and (right) muon channel with requiring $40 < m_T(\ell, E_T^{\text{miss}}) < 60(70)$ GeV for muon(electron) channel. Backgrounds estimated from MC samples are truth matched.

1628 **F.4. muhad b -veto rQCD investigation**

1629 Figure 32 (b), in Section 5.2.4, shows a significant discrepancy between data and the prediction in the
1630 Anti-ID region muhad b -veto channel. A scaled rQCD is derived from the Anti-ID region, as shown in
1631 Figure 90. The underlying reason is not understood yet. This scaled rQCD is applied to the signal region
1632 to estimate the total fake background contribution. The comparison on the fake estimation between this
1633 scaled rQCD and default rQCD is shown in Figure 91. We can see that the difference between the scaled
1634 rQCD and default rQCD is negligible, which is due to the closeness between QCD fake factor and W +jet
1635 fake factor. In such a case, no further procedure is taken on the muhad b -veto rQCD in this analysis. The
1636 followup study will be performed in the future analysis.

Not reviewed, for internal circulation only

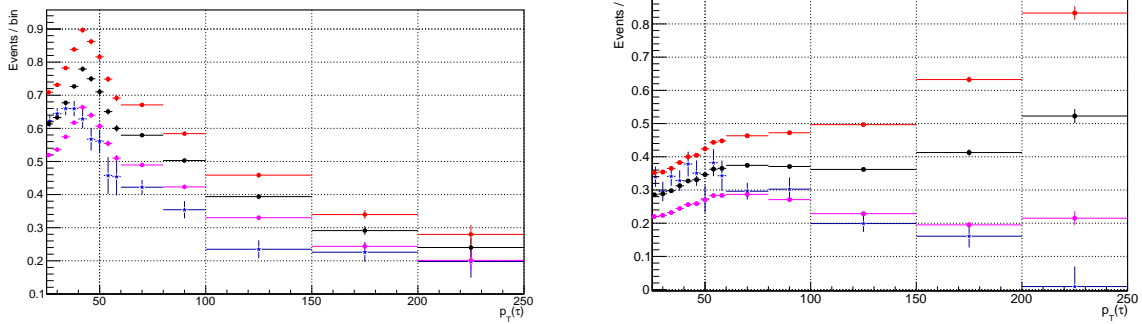


Figure 90: Lepton FF vs. $p_T(\text{lepton})$. Black is with the default nominal rQCD with red as sys up and Magenta as sys down, while blue is with the alternative rQCD.

Not reviewed, for internal circulation only

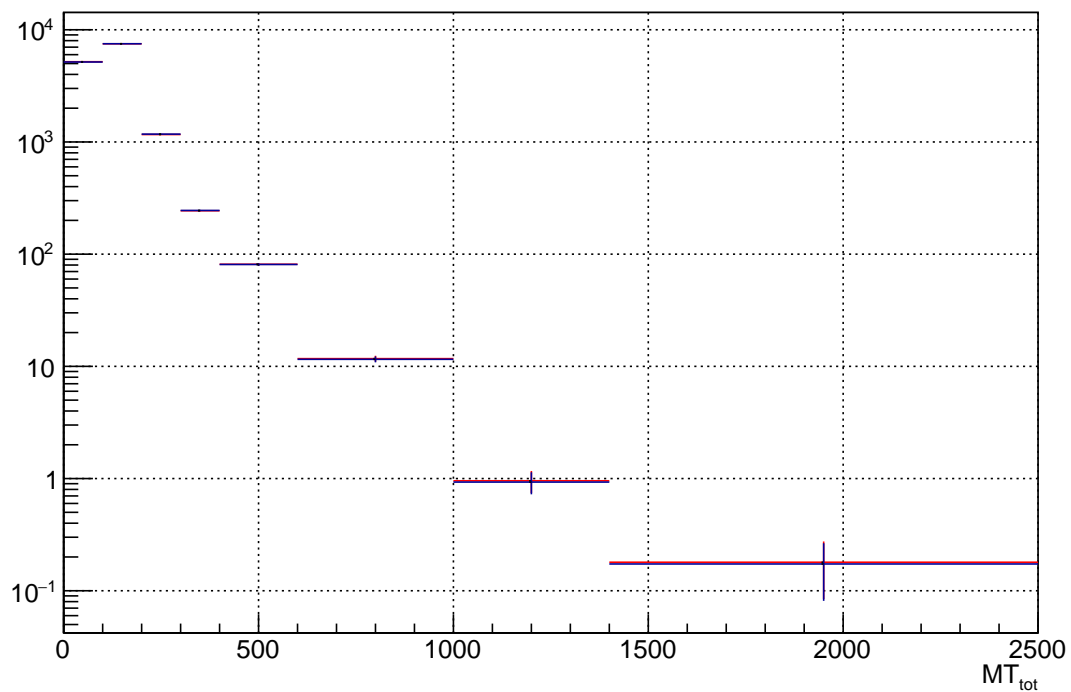


Figure 91: Distribution of $p_T(\text{lepton})$ in the Fake Lepton region for muhad channel. Black is with the default nominal rQCD, while red is with the alternative rQCD.

1637 **F.5. $W+jets$ control region with $\Delta\phi(\tau, E_T^{\text{miss}})$ corrected Fake**

1638 Figure 92 shows the $\Delta\phi(\tau, E_T^{\text{miss}})$ distribution after $\Delta\phi(\tau, E_T^{\text{miss}})$ corrections. Figures 93 and 94 show
 1639 $p_T(\tau_{\text{had}})$ and m_T^{tot} distributions in the $W+jets$ CR after the $\Delta\phi(\tau, E_T^{\text{miss}})$ correction, respectively. The
 1640 modeling is generally good. Figures 95 and 96 show that before correction. Please note that the y-axis
 1641 range of the ratio plots are different. We also find there is about 1-3% overall normalization shift after
 1642 reweighting. This is because the ehad and muhad channels behave slightly different. This 1-3% is well
 1643 covered by the existed Fake and dPhi correction systematics. So we decide to use a combined dphi
 1644 correction for ehad and muhad.

1645 **F.5.1. Discussion on the potential difference between ehad and muhad**

1646 There is some concern on the potential Fake factor difference between ehad and muhad channels, especially
 1647 considering the discrepancy in bveto ehad validation region show in Figures 20 and 22. In this section,
 1648 Figures 93 and 95 show the data-prediction comparison in the Wjets control region where Fake is dominant.
 1649 Note: the Fake here is modeled by using e+mu combined fake factor. From these plots, we can see that the
 1650 difference between ehad and muhad is about 1-3% level which is smaller than the systematics uncertainties
 1651 associated to Fake modeling, e.g. background subtraction sys., dphi correction sys., extrolation sys., etc.
 1652 Also, in the selections for both the signal region and the control region, we request lepton and hadronic
 1653 tau back to back. It is unlikely that the lepton part could affect the hadronic tau part.

1654 In the future analysis, we plan to further investigate the Fake modeling, e.g. parameterizing the fake factor
 1655 in more dimensions than just pT. For this round analysis, we think the current uncertainties can cover
 1656 the potential difference. This is also the reason why we de-correlate Fake systematics between ehad and
 1657 muhad, as shown in Figure 40.

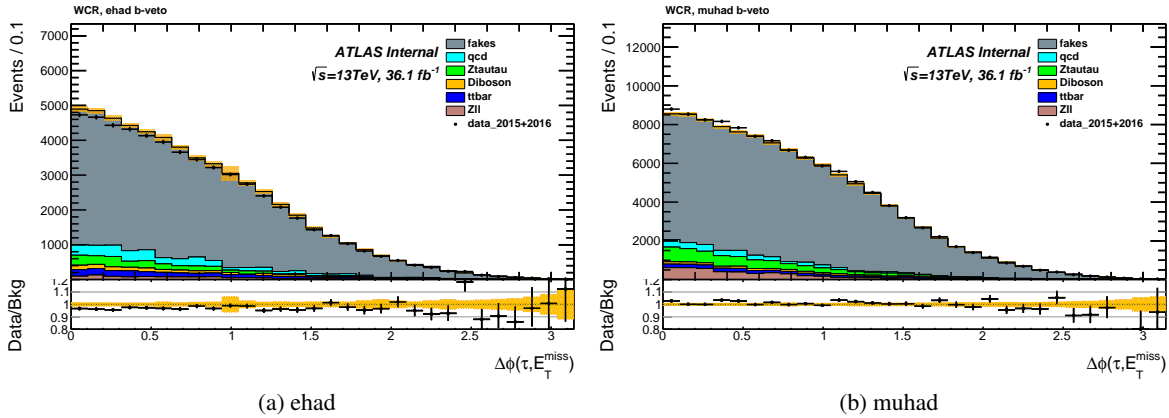


Figure 92: $\Delta\phi(\tau, E_T^{\text{miss}})$ in $W+jets$ control region after $\Delta\phi(\tau, E_T^{\text{miss}})$ corrections.

Not reviewed, for internal circulation only

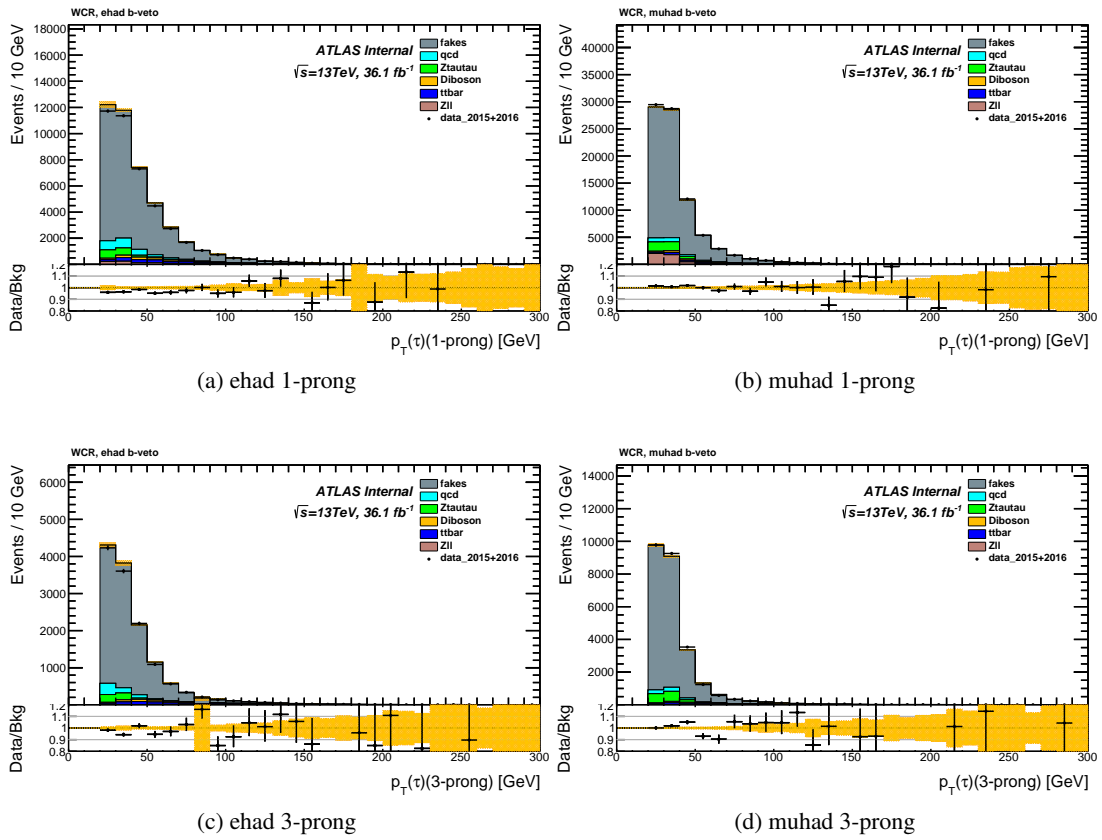


Figure 93: $p_T(\tau_{\text{had}})$ distributions in the b -veto $W+\text{jets}$ region after $\Delta\phi(\tau, E_T^{\text{miss}})$ corrections.

Not reviewed, for internal circulation only

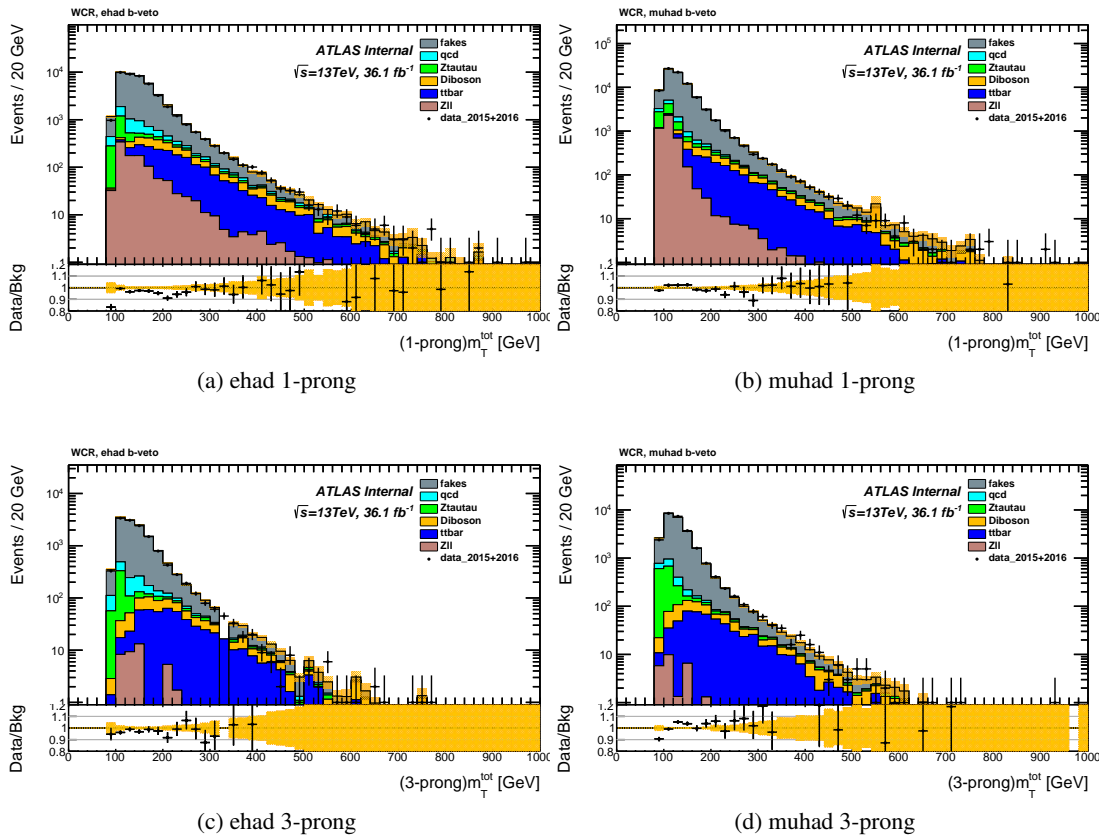


Figure 94: m_T^{tot} distributions in the b -veto $W + \text{jets}$ region after $\Delta\phi(\tau, E_T^{\text{miss}})$ corrections.

Not reviewed, for internal circulation only

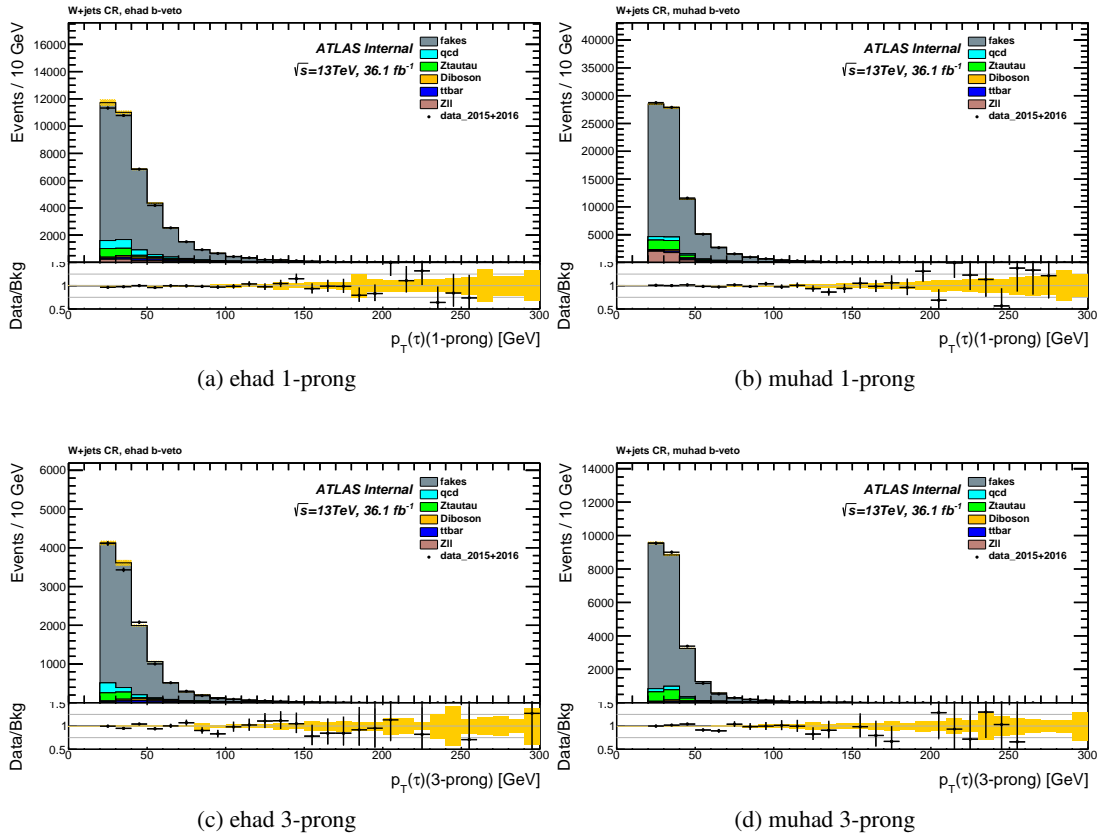


Figure 95: $p_T(\tau_{\text{had}})$ distributions in the b -veto $W+jets$ region before $\Delta\phi(\tau, E_T^{\text{miss}})$ corrections.

Not reviewed, for internal circulation only

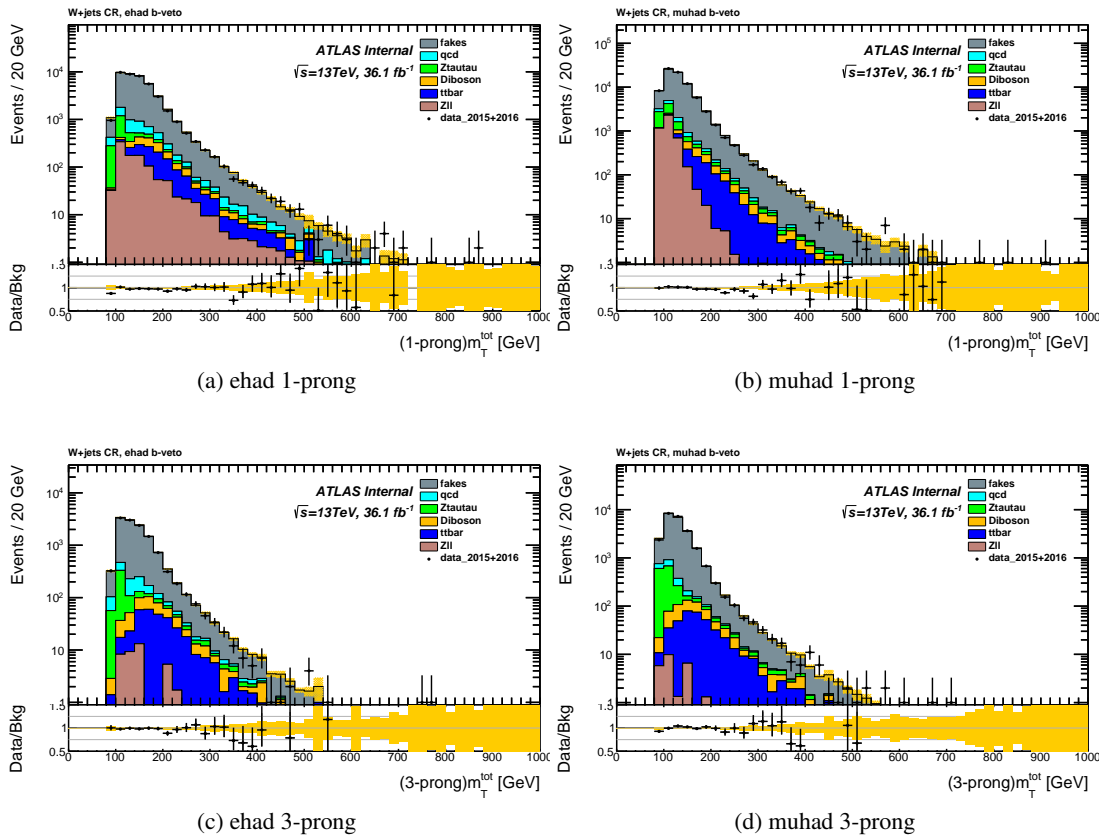


Figure 96: m_T^{tot} distributions in the b -veto $W+\text{jets}$ region before $\Delta\phi(\tau, E_T^{\text{miss}})$ corrections.

1658 F.6. Separated Intermediate Regions

1659 In order to investigate whether there is any systematical trend of mismodeling from the high m_T (control)
 1660 region to the low m_T (signal) region, the intermediate region is further split into two separated regions,
 1661 i.e. $40 < m_T < 55$ GeV and $55 < m_T < 70$ GeV for ehad; $40 < m_T < 50$ GeV and $50 < m_T < 60$ GeV
 1662 for muhad. Figures 97 and 98 show the $p_T(\tau_{\text{had}})$ distribution, while Figures 99 and 100 show the m_T^{tot}
 1663 distribution.

Not reviewed, for internal circulation only

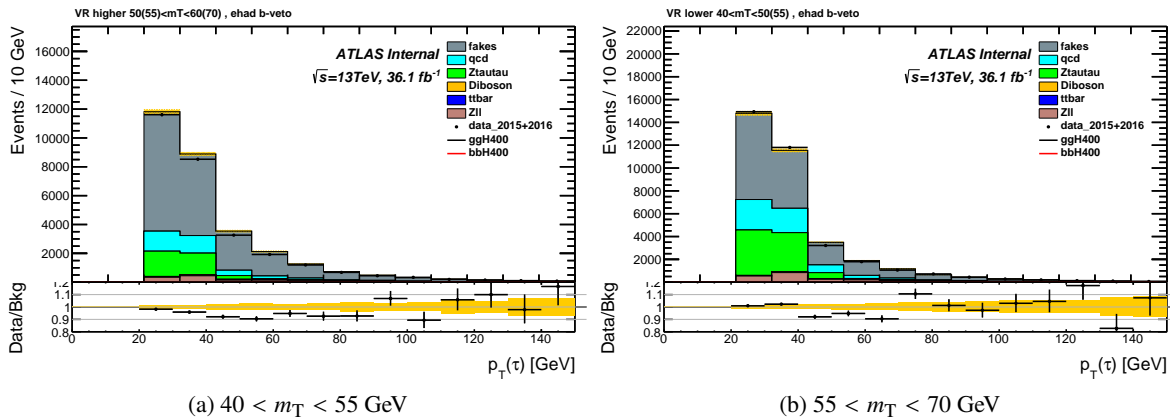


Figure 97: $p_T(\tau_{\text{had}})$ distributions in the b -veto electron channel with requiring (left) $40 < m_T < 55$ GeV and (right) $55 < m_T < 70$ GeV.

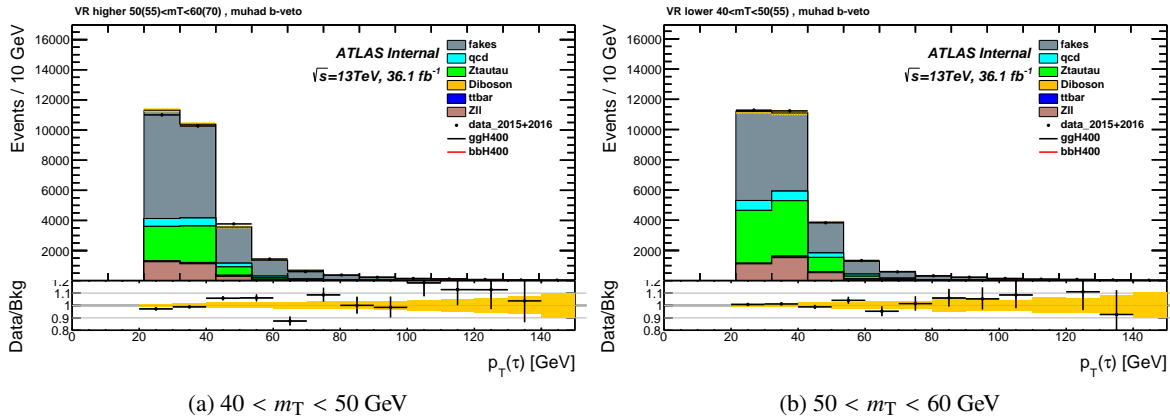


Figure 98: $p_T(\tau_{\text{had}})$ distributions in the b -veto muon channel with requiring (left) $40 < m_T < 50$ GeV and (right) $50 < m_T < 60$ GeV.

Not reviewed, for internal circulation only

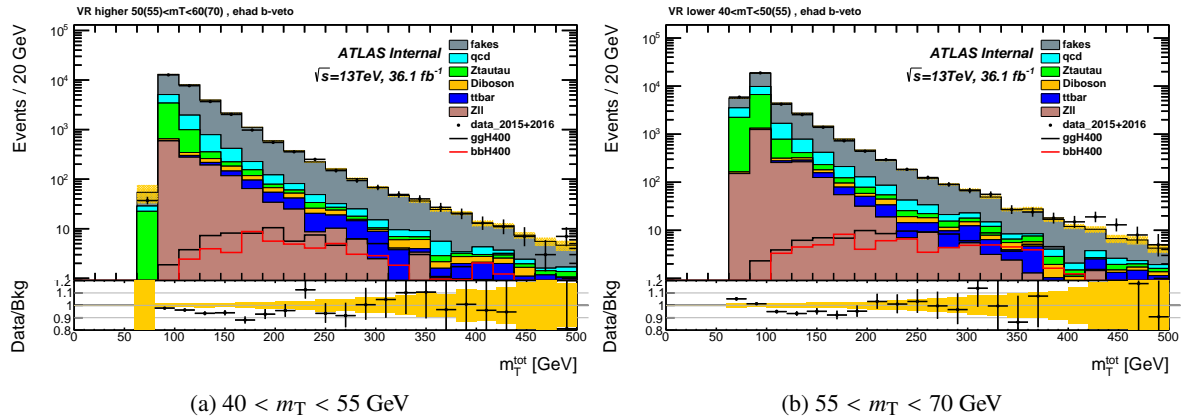


Figure 99: m_T^{tot} distributions in the b -veto electron channel with requiring (left) $40 < m_T < 55 \text{ GeV}$ and (right) $55 < m_T < 70 \text{ GeV}$.

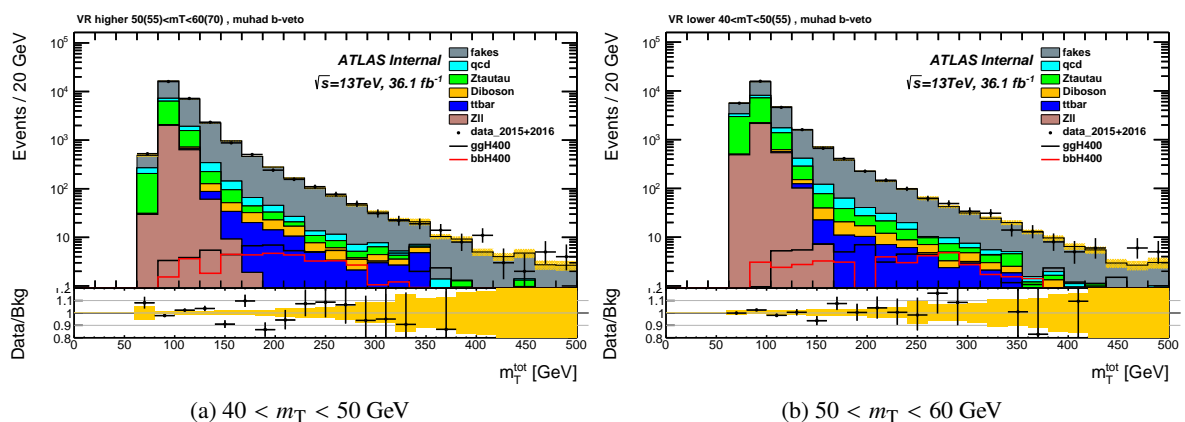


Figure 100: m_T^{tot} distributions in the b -veto muon channel with requiring (left) $40 < m_T < 50 \text{ GeV}$ and (right) $50 < m_T < 60 \text{ GeV}$.

1664 **F.7. Intermediate region with and without $\Delta\phi(\tau, E_T^{\text{miss}})$ corrected Fake**

1665 Figures 101 to 106 show the comparison on the validation region before and after $\Delta\phi(\tau, E_T^{\text{miss}})$ correc-
1666 tion.

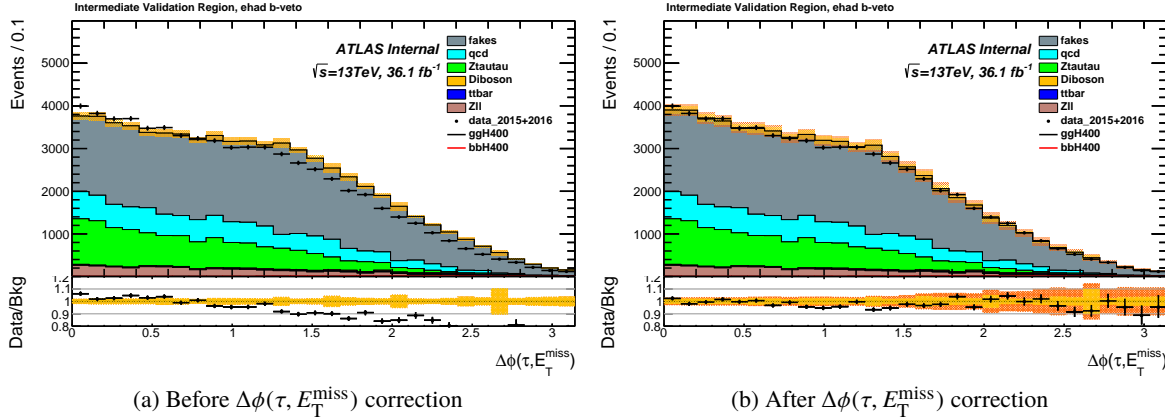


Figure 101: $\Delta\phi(\tau, E_T^{\text{miss}})$ distribution in the intermediate ehad b -veto region before and after $\Delta\phi(\tau, E_T^{\text{miss}})$ corrections.

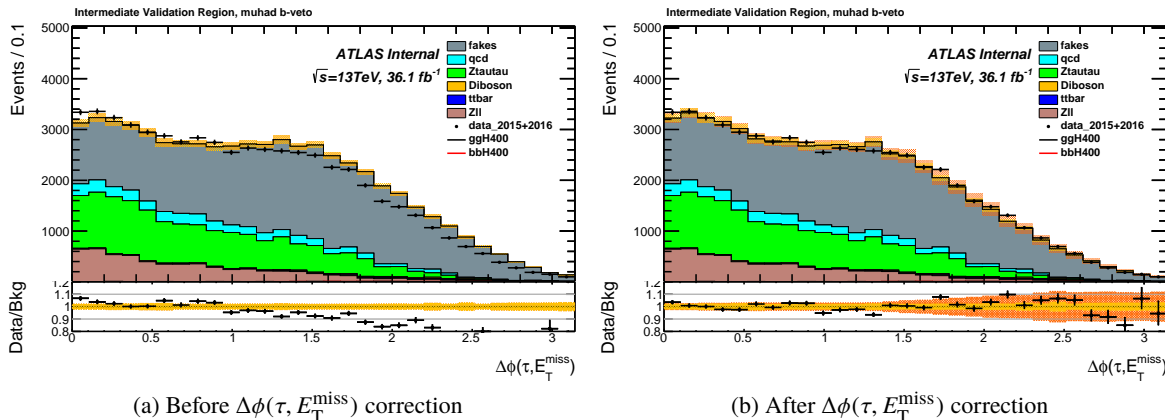


Figure 102: $\Delta\phi(\tau, E_T^{\text{miss}})$ distribution in the intermediate muhad b -veto region before and after $\Delta\phi(\tau, E_T^{\text{miss}})$ correc-
tions.

Not reviewed, for internal circulation only

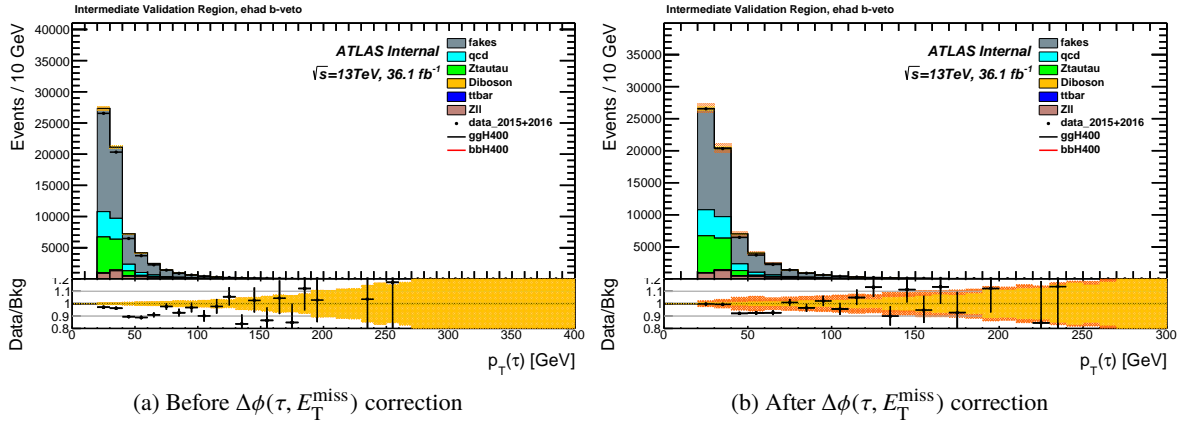


Figure 103: $p_T(\tau_{\text{had}})$ distribution in the intermediate ehad b -veto region before and after $\Delta\phi(\tau, E_T^{\text{miss}})$ corrections.

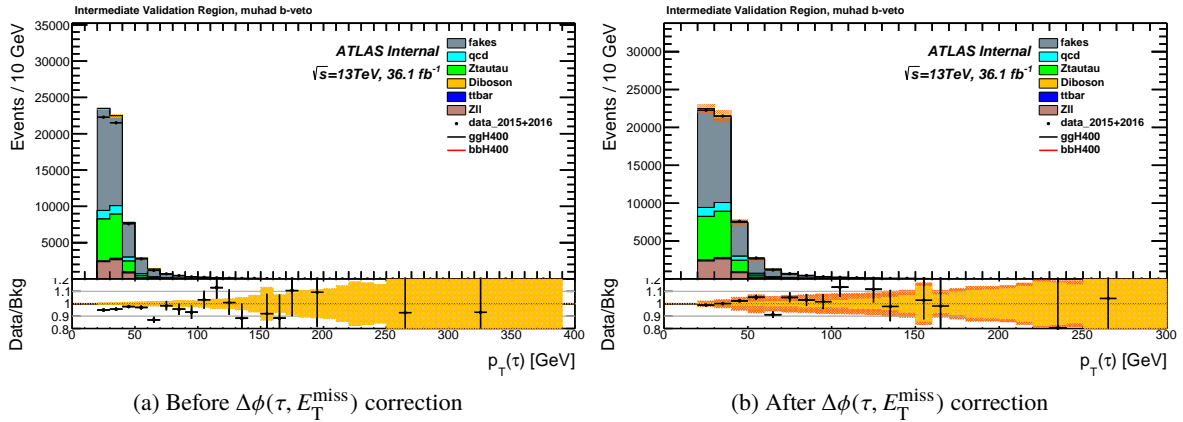


Figure 104: $p_T(\tau_{\text{had}})$ distribution in the intermediate muhad b -veto region before and after $\Delta\phi(\tau, E_T^{\text{miss}})$ corrections.

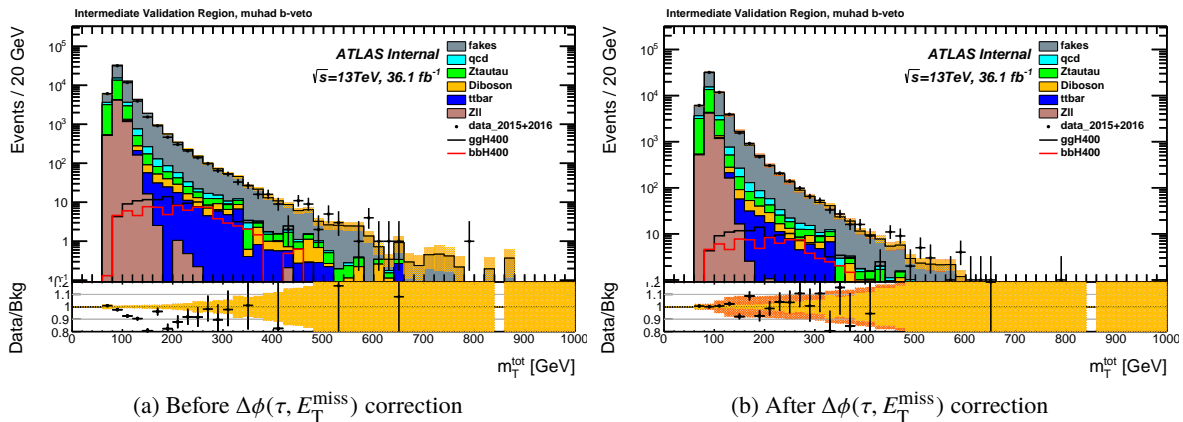


Figure 105: m_T^{tot} distribution in the intermediate ehad b -veto region before and after $\Delta\phi(\tau, E_T^{\text{miss}})$ corrections.

Not reviewed, for internal circulation only

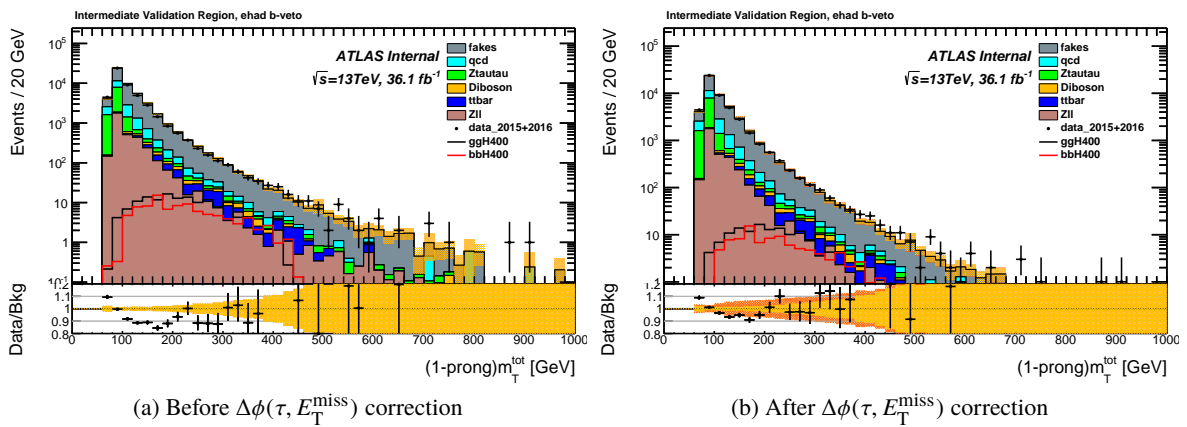


Figure 106: m_T^{tot} distribution in the intermediate muhad b -veto region before and after $\Delta\phi(\tau, E_T^{\text{miss}})$ corrections.

1667 F.8. $W+jets$ Fake factor calculation: original input distribution

1668 This section shows the detailed distribution plots that are used in the calculation of the W -jets FF. Figures
 1669 107 and 108 show the distribution used in calculating the b -veto fake factor. Figures 109 and 110 show
 1670 the distributions in the b -tag category. Here, the jet $\rightarrow\tau$ fake is modeled by using the MC simulation for
 1671 both fail and pass identification to demonstrate the event composition. Those items in the plots which
 1672 don't have (jet $\rightarrow\tau$) on the name are the events with either generated τ or lepton $\rightarrow\tau$ fake.

Not reviewed, for internal circulation only

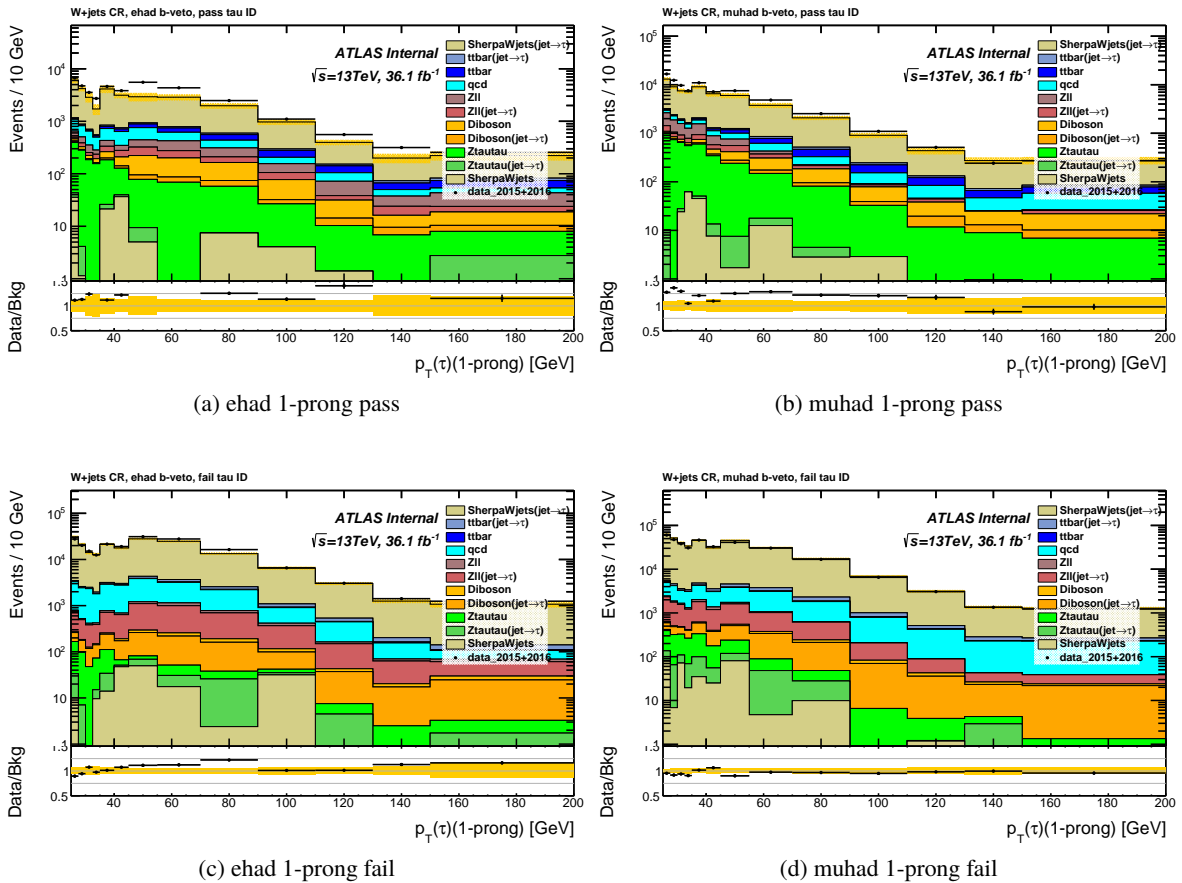


Figure 107: $p_T(\tau_{\text{had}})$ distribution of the $W+jets$ b -veto control region for 1-prong tau candidate. Here, the components in the legend without jet $\rightarrow\tau$ are with the tau candidate from the generated tau or lepton fake.

Not reviewed, for internal circulation only

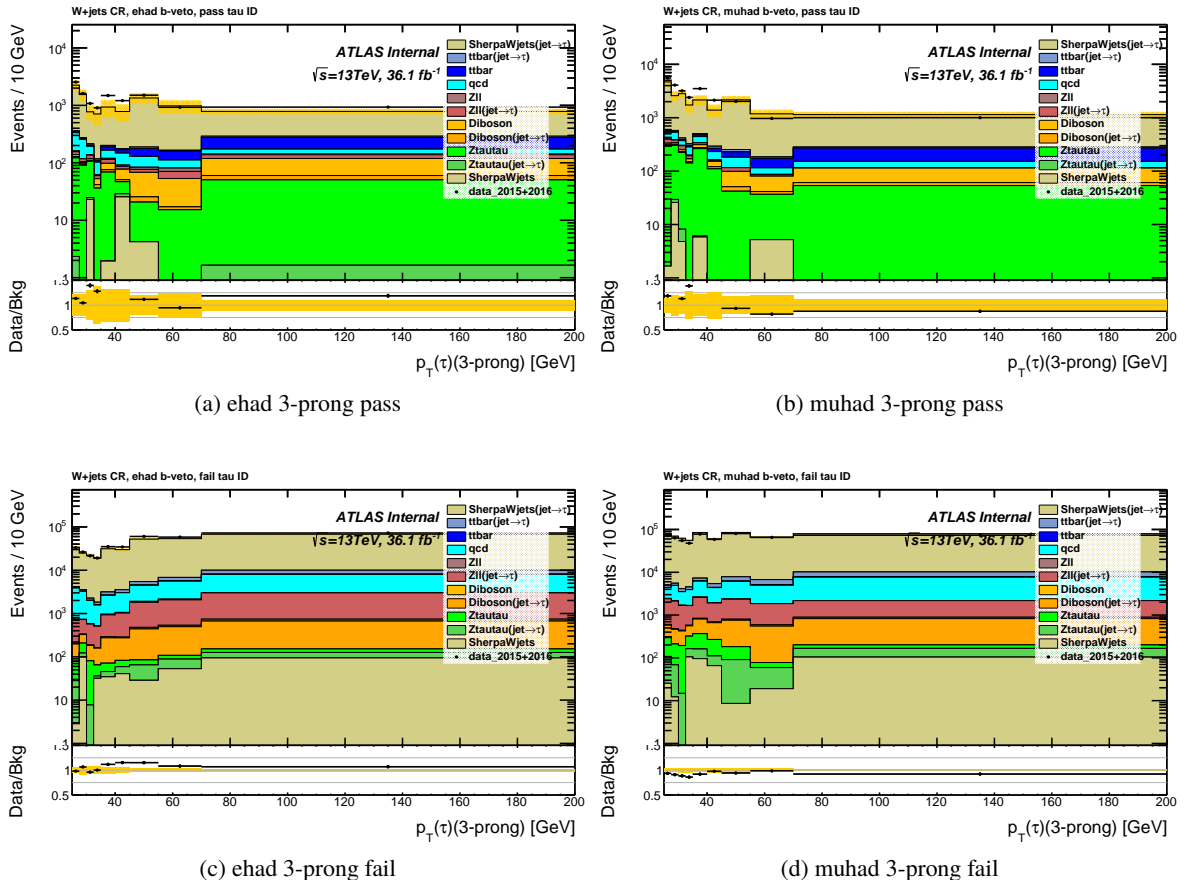


Figure 108: $p_T(\tau_{\text{had}})$ distribution of the $W+\text{jets}$ b -veto control region for 3-prong tau candidate. Here, the components in the legend without jet $\rightarrow\tau$ are with the tau candidate from the generated tau or lepton fake.

Not reviewed, for internal circulation only

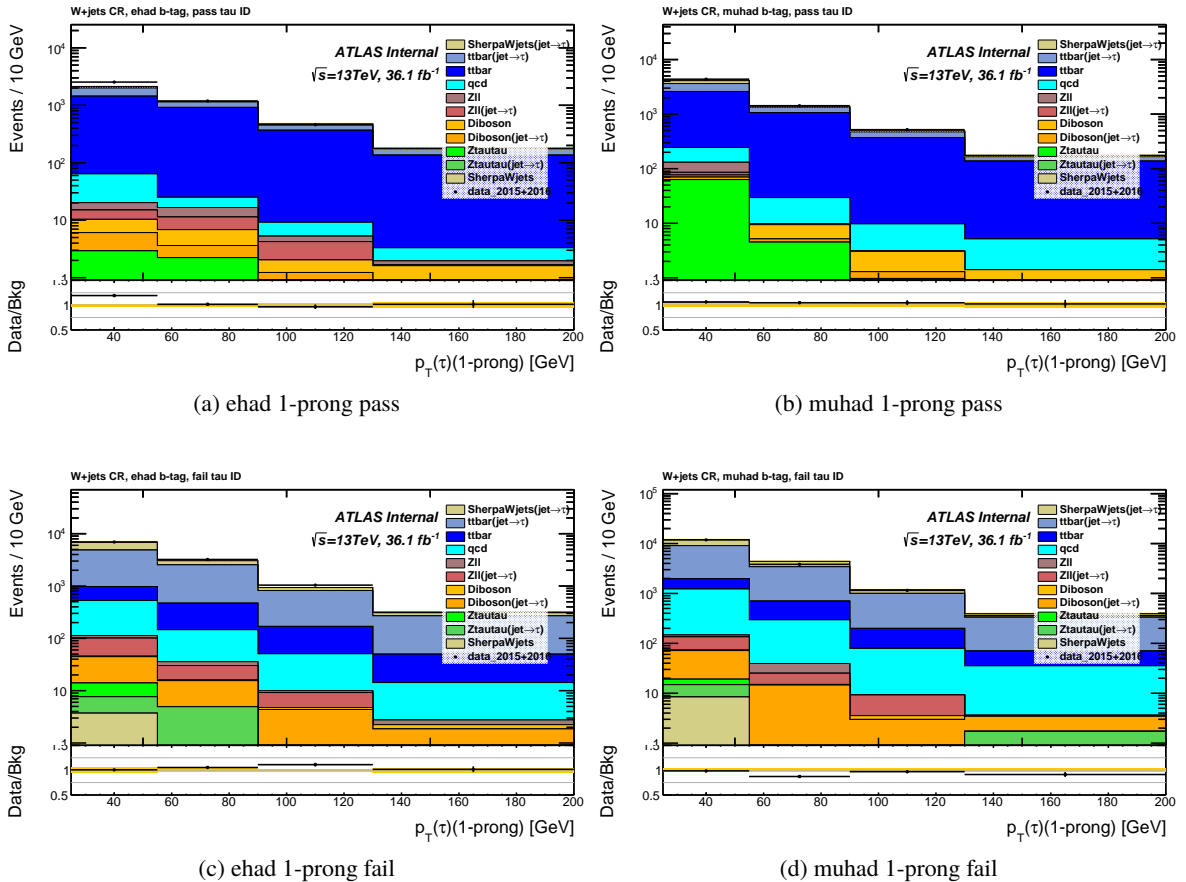


Figure 109: $p_T(\tau_{\text{had}})$ distribution of the $W+\text{jets}$ b -tag control region for 1-prong tau candidate. Here, the components in the legend without jet $\rightarrow\tau$ are with the tau candidate from the generated tau or lepton fake.

Not reviewed, for internal circulation only

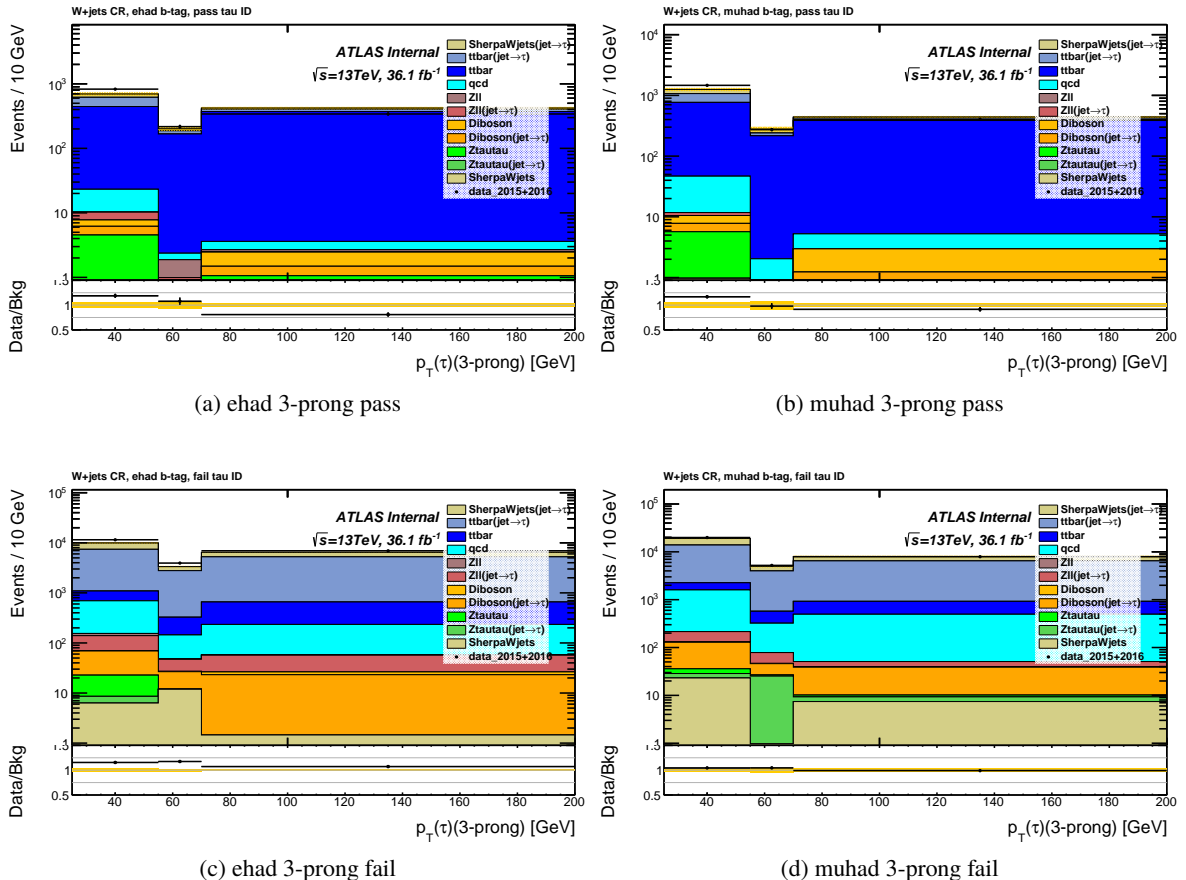


Figure 110: $p_T(\tau_{\text{had}})$ distribution of the $W+\text{jets}$ b -tag control region for 3-prong tau candidate. Here, the components in the legend without jet $\rightarrow\tau$ are with the tau candidate from the generated tau or lepton fake.

1673 **F.9. Lepton Fake factor calculation: original input distribution**

1674 This section shows the detailed distribution plots that are used in the calculation of the lepton FF. Figure
 1675 111 shows the distribution used in calculating the electron fake factor. Figures 112 and 113 show the
 1676 distributions in the muon low p_T and high p_T categories.

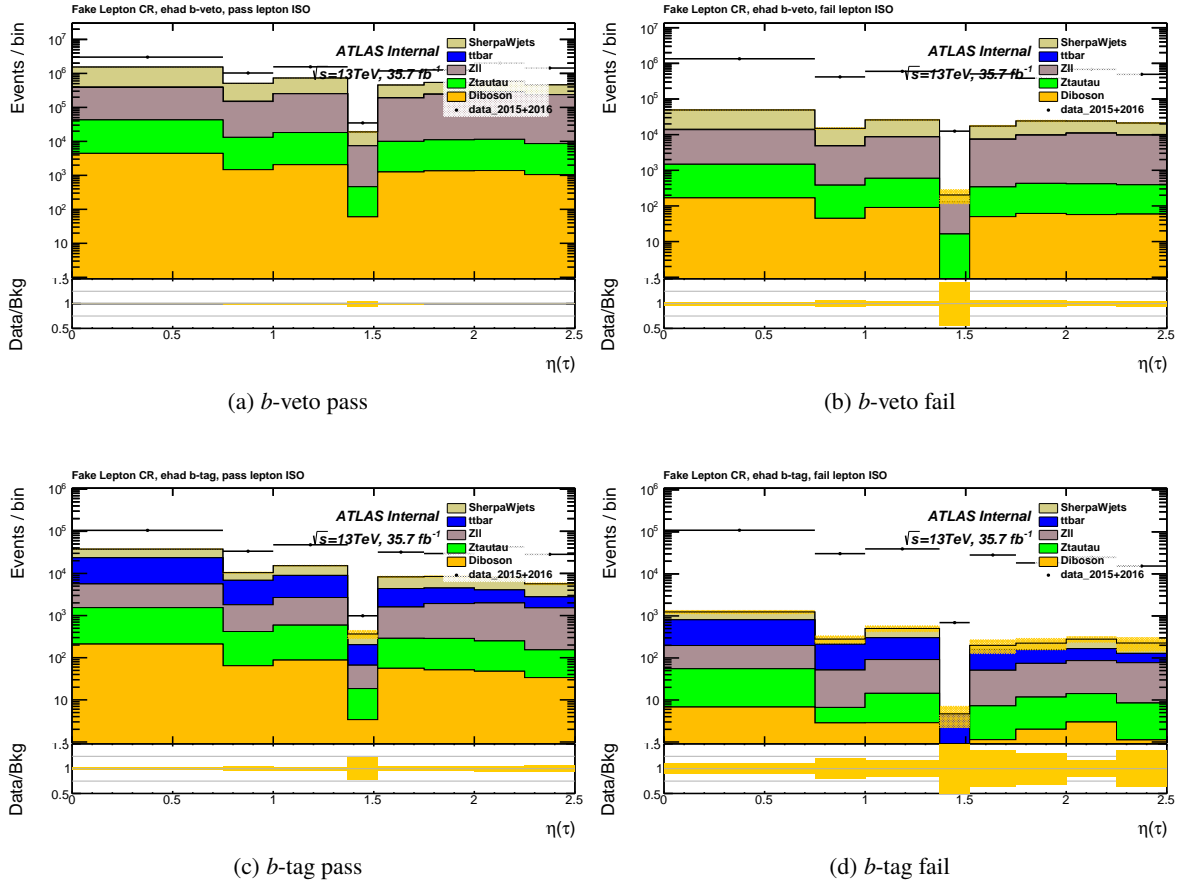


Figure 111: η (ℓ) distribution of the fake lepton control region of the electron channel.

Not reviewed, for internal circulation only

Not reviewed, for internal circulation only

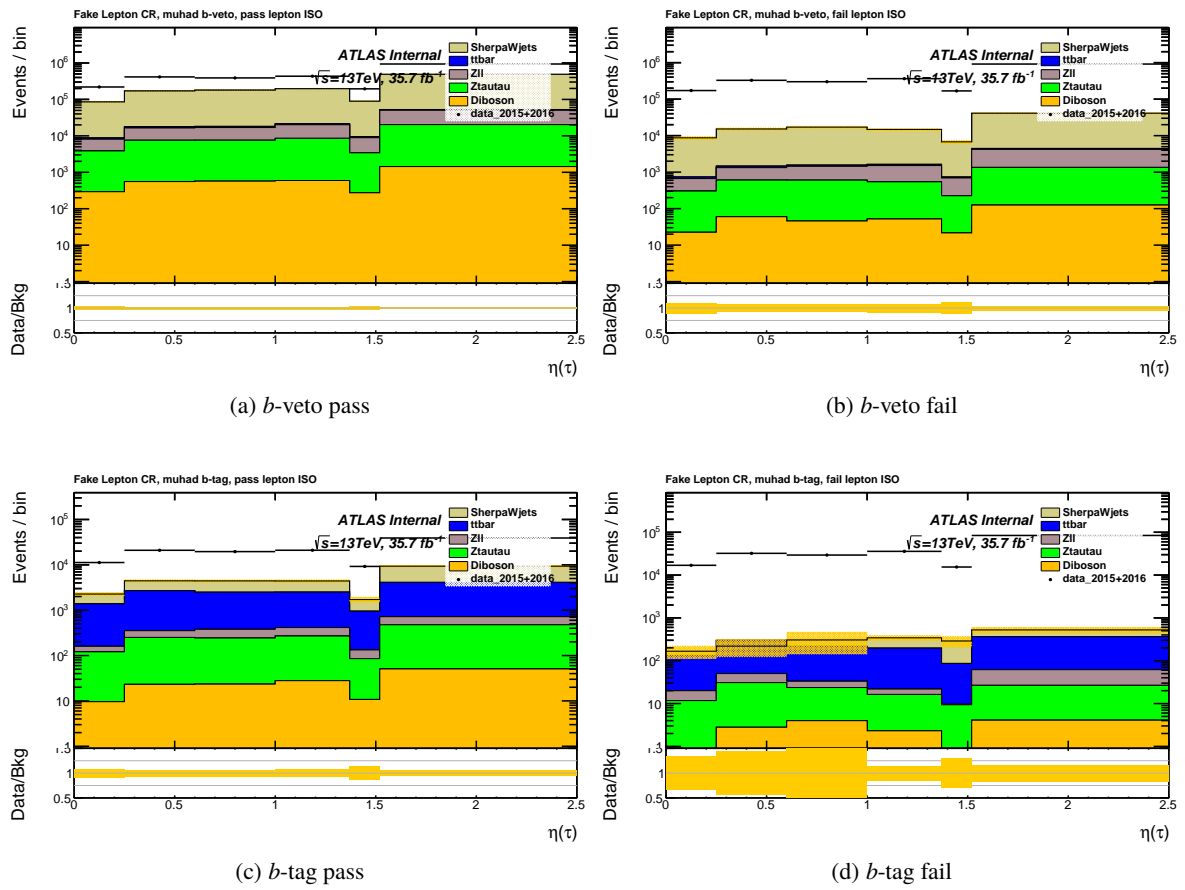


Figure 112: $\eta(\ell)$ distribution for the low p_T of the fake lepton control region of the muon channel.

Not reviewed, for internal circulation only

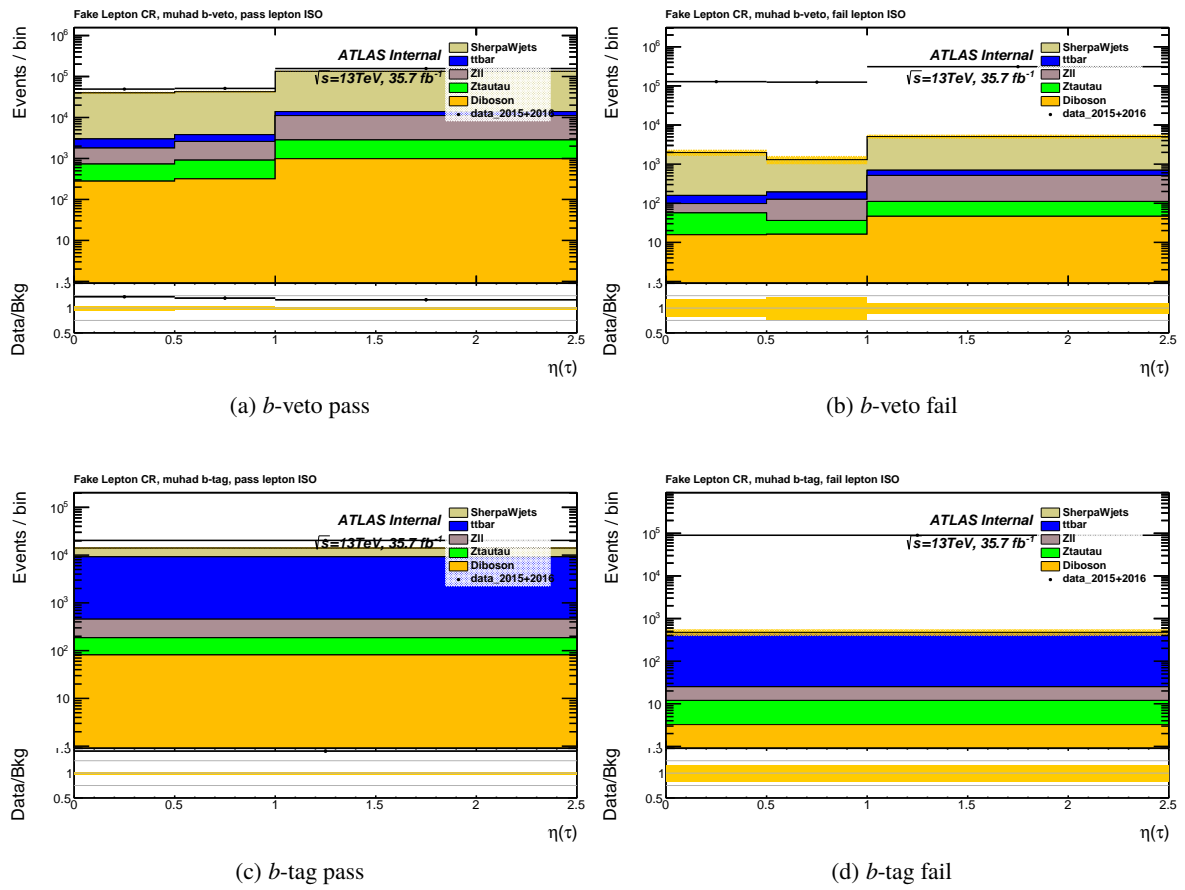


Figure 113: $\eta(\ell)$ distribution for the high p_T of the fake lepton control region of the high p_T muon channel.

1677 **F.10. Lepton fake factor study**

1678 Current version of the analysis uses lepton fake factors (FF) which are parametrised in channel (*ehad*,
 1679 *muhad*), *b*-tagging (*b-tag*, *b-veto*), lepton η and, additionally, muon FF is split into 2 lepton p_T bins due
 1680 to different isolation requirements in muon triggers.

1681 This parametrisation might be insufficient to fully capture the way in which jets fake leptons. One
 1682 would certainly expect FF to depend on the lepton p_T , which can be seen in Figure 114 (here FF are not
 1683 parametrised in lepton η and, also, one should look at fine structure of FF sceptically and, rather, focus on
 1684 the overall trend).

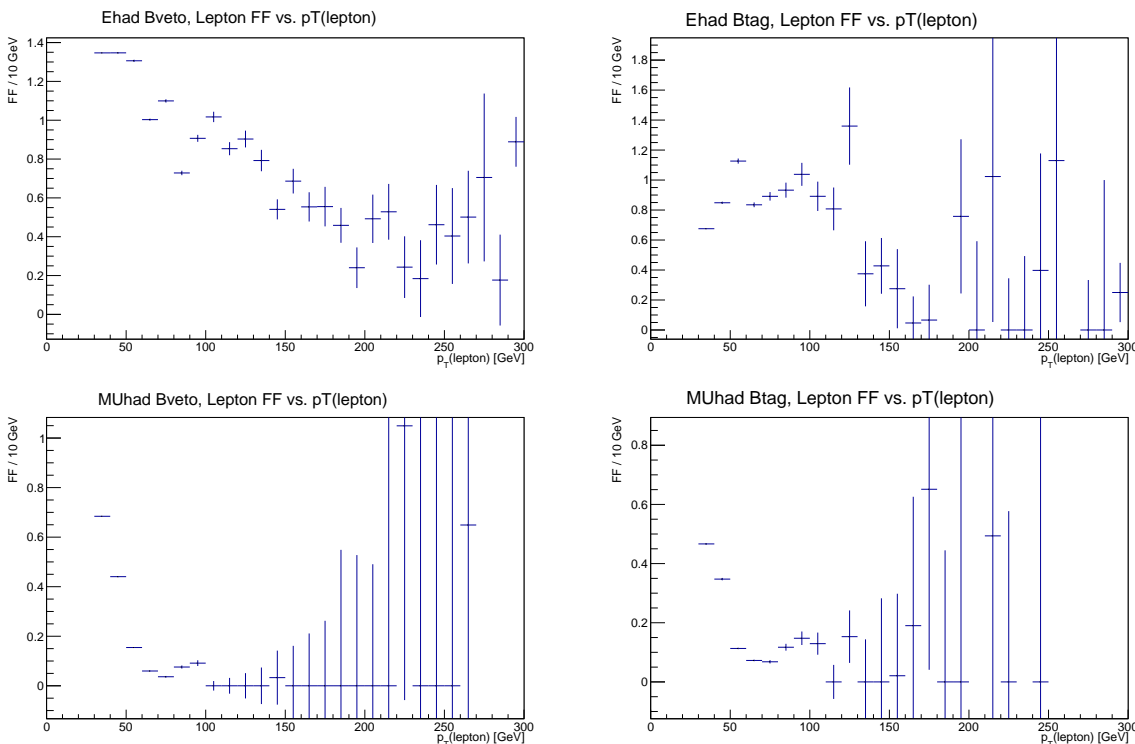


Figure 114: Lepton FF vs. $p_T(\text{lepton})$.

1685 One can also look at the distributions of variables in the Fake Lepton region including an estimate of QCD
 1686 using fake factors that have been measured in this region and infer how FF depend on those variables.
 1687 Figures 115-117 show distributions of lepton p_T , E_T^{miss} which seem to have biggest disagreements of
 1688 data and background. This both suggests and oblige us to parametrise FF with more variables. Number
 1689 of events in different categories allows us to do that: there are $O(10^6)$ events in *b-veto* categories and
 1690 $O(10^5)$ events in *b-tag*.

1691 The main goal of lepton fake factors in this analysis is to model QCD background in the Anti-ID region. All
 1692 other backgrounds can be taken from MC because there is only a loose requirement on the tau identification
 1693 which is expected to be modelled well. Therefore, the Anti-ID region should be a guideline for judging of
 1694 how well the fake factors are measured but also should not be used to adjust those fake factors to perfectly
 1695 fill in the difference between data and background. Figures 118-120 show distributions of variables in the

Not reviewed, for internal circulation only

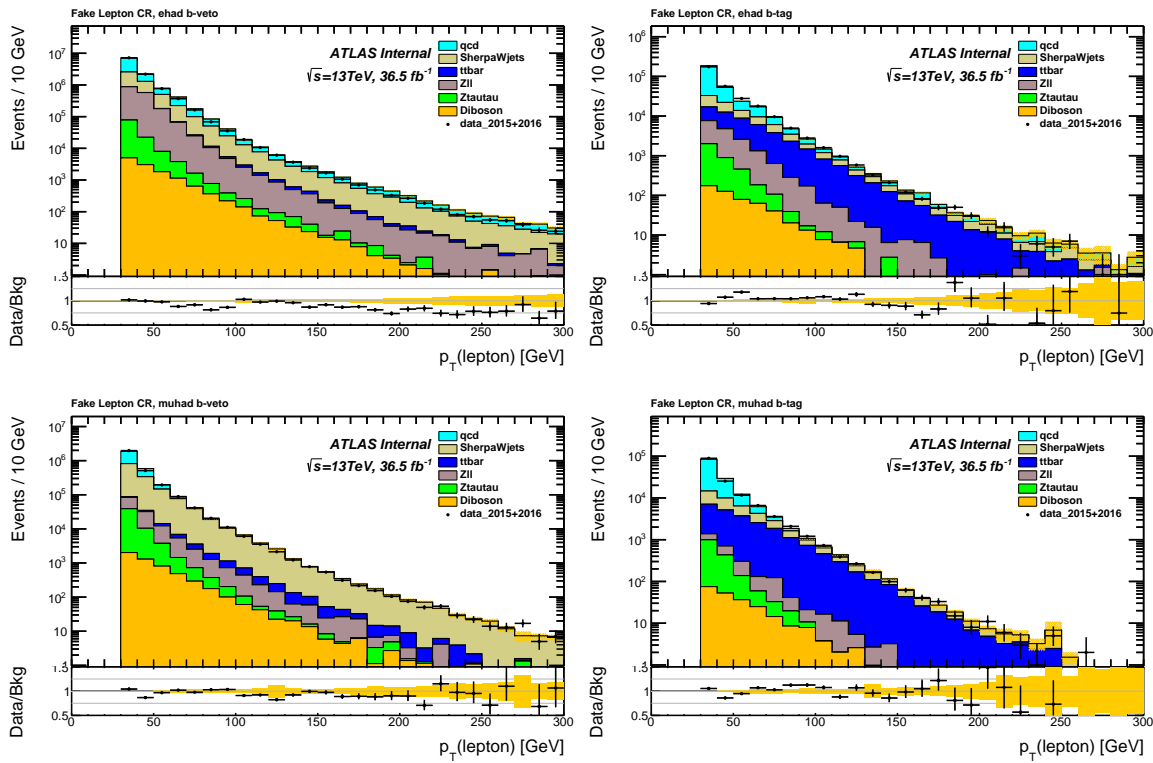


Figure 115: Distribution of $p_T(\text{lepton})$ in the Fake Lepton region.

1696 Anti-ID region (in those figures, the labels that do not have ($\text{jet} \rightarrow \tau$) in them are backgrounds where the
 1697 τ is truth matched or faked by a lepton).

1698 It is mostly important to model the distribution of the discriminating variable m_T^{tot} in the Anti-ID region.
 1699 As we mentioned before, the data and background might not agree perfectly but it should be clear when
 1700 there is a big inaccuracy in the model. Figures 121 show the m_T^{tot} distribution and one can see in the lower
 1701 end of the histograms in the *ehad* channel that the background is vastly underestimated. One then expects
 1702 that this disagreement is due to QCD estimate because it appears in a region where it dominates.

1703 An attempt to investigate possible improvements in fake factor measurement and resulting background
 1704 modelling was made and a second set of fake factors can be seen in Figures 122 and 123. Electron fake
 1705 factors are parametrised in E_T^{miss} , $p_T(\text{lepton})$ and $\eta(\text{lepton})$ while muon fake factors are parametrised
 1706 in $p_T(\text{lepton})$ and $\eta(\text{lepton})$ only. This parametrisation is not optimised and is intended to serve only
 1707 as an example. The m_T^{tot} distributions derived using new lepton fake factors are shown in Figure 124.
 1708 The lower end of the distribution in the *ehad* channel which previously was extensively mismodelled now
 1709 shows better agreement.

1710 however, in the end what matters is the m_T^{tot} distributions in the Signal region. Different background
 1711 models are due to different QCD and W+jets fake factors which are used to weigh events in the Anti-ID
 1712 region. Therefore, any big differences in models in the Anti-ID region due to improved lepton fake factors
 1713 will be much smaller in the final distributions in the Signal region. Employing old and new lepton fake
 1714 factors we show 125 m_T^{tot} distributions of fake backgrounds ($\text{jet} \rightarrow \tau$) in the Signal region *ehad* channel.
 1715 As a result, the biggest difference appears in the *b-veto* category and is around 5%.

Not reviewed, for internal circulation only

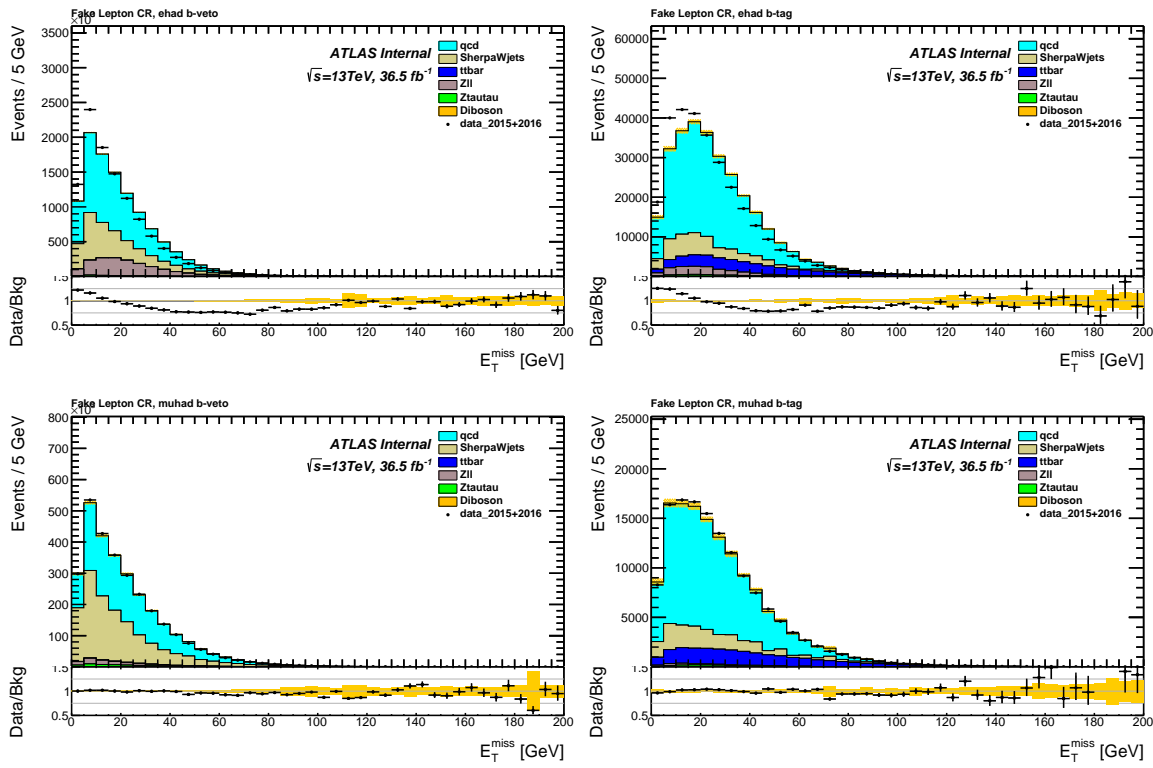


Figure 116: Distribution of E_T^{miss} in the Fake Lepton region.

1716 In conclusion, huge number of events in the Fake Lepton region allows us to improve measurement of
 1717 lepton fake factors which means extracting more information. In the future versions of the analysis it will
 1718 be important to revise which variables are needed to parametrise FF and also estimation of systematic
 1719 uncertainties, for example, by looking how FF depend on the recoiling leading jet p_T .

Not reviewed, for internal circulation only

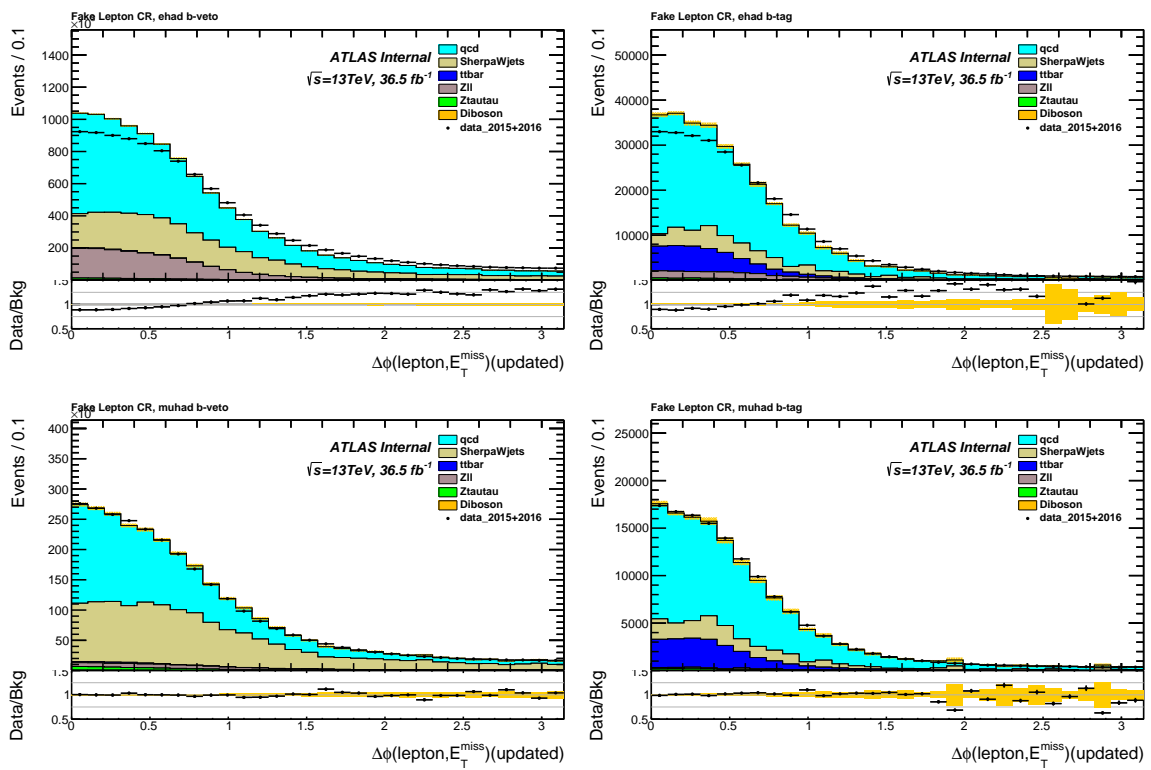


Figure 117: Distribution of $\Delta\phi(\text{lepton}, E_T^{\text{miss}})$ in the Fake Lepton region.

Not reviewed, for internal circulation only

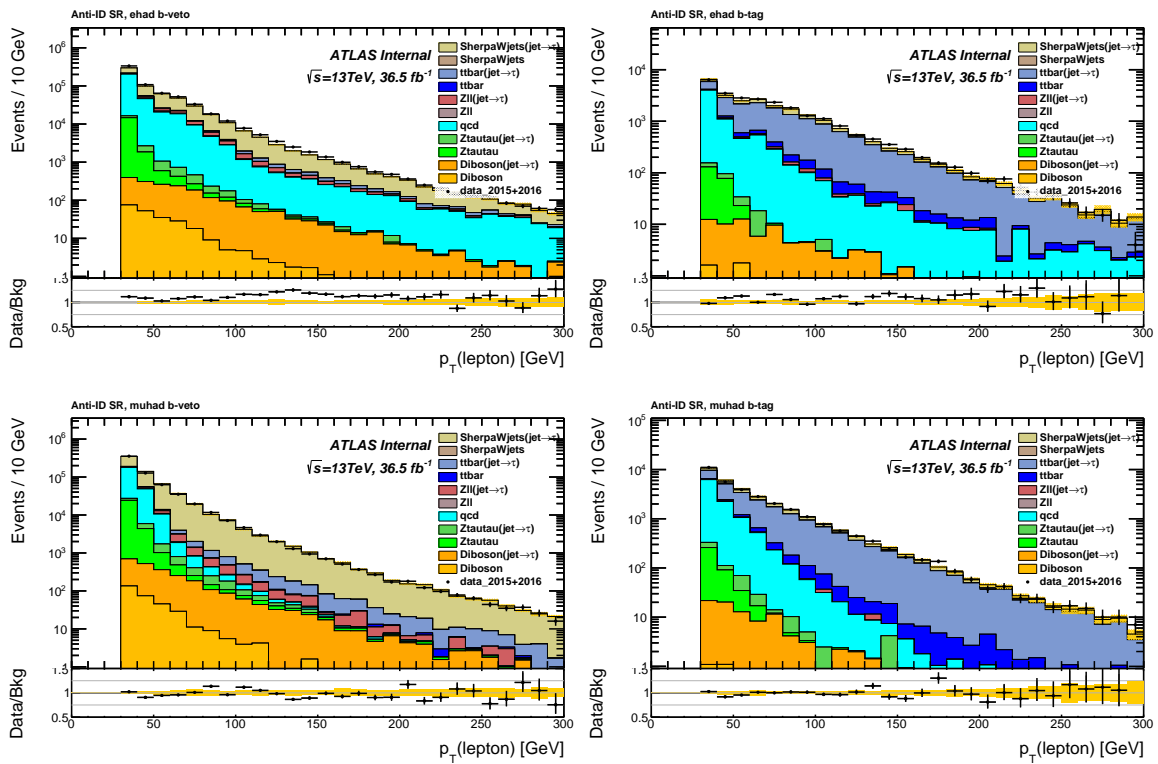


Figure 118: Distribution of $p_T(\text{lepton})$ in the Anti-ID region.

Not reviewed, for internal circulation only

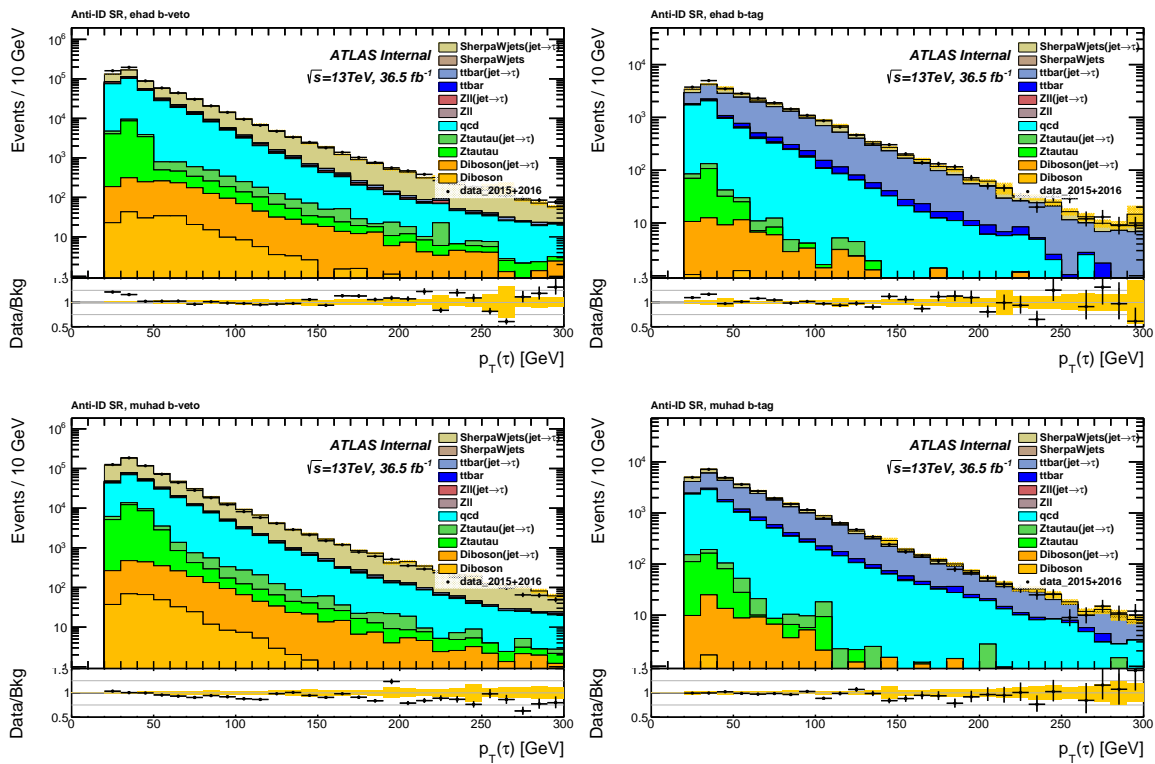


Figure 119: Distribution of $p_T(\tau)$ in the Anti-ID region.

Not reviewed, for internal circulation only

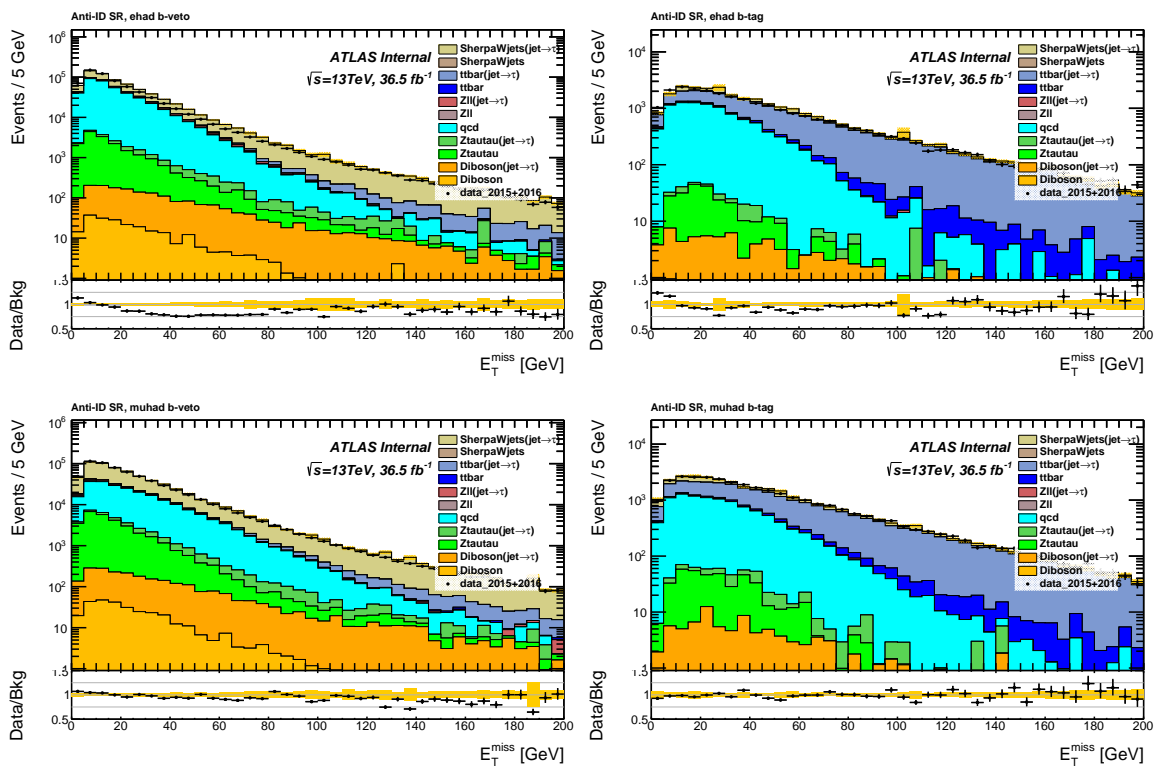


Figure 120: Distribution of E_T^{miss} in the Anti-ID region.

Not reviewed, for internal circulation only

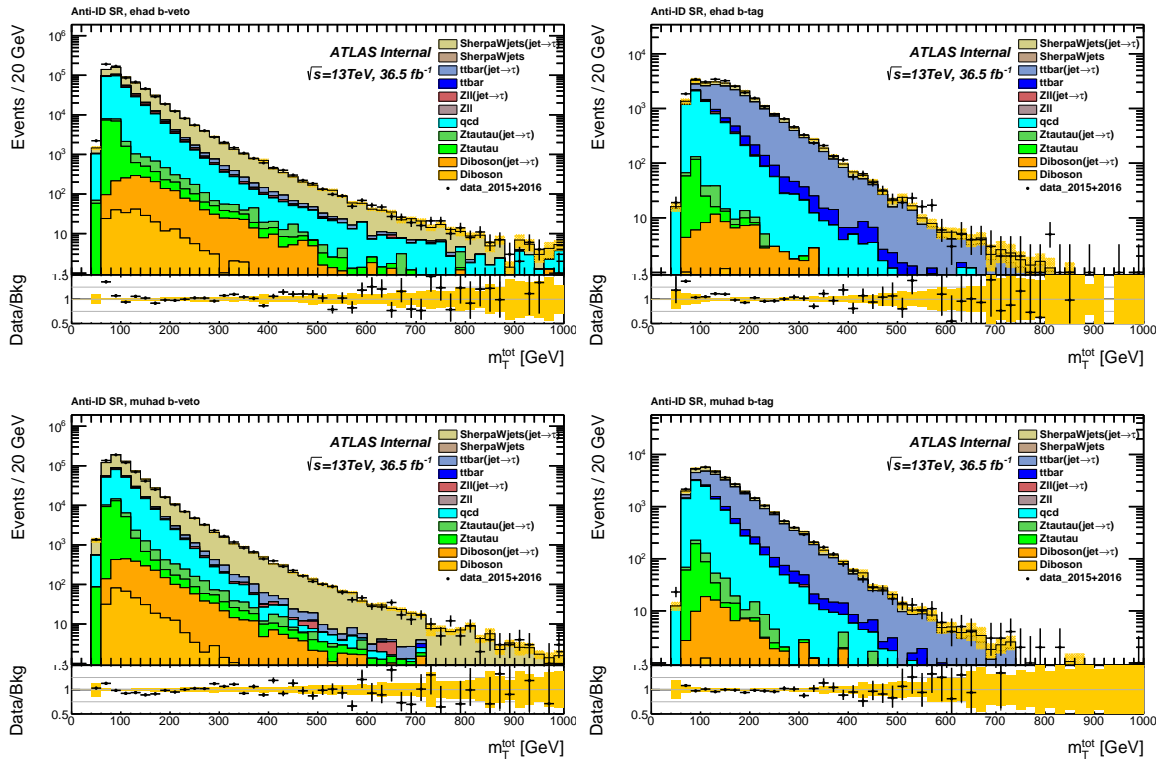


Figure 121: Distribution of m_T^{tot} in the Anti-ID region (nominal FF).

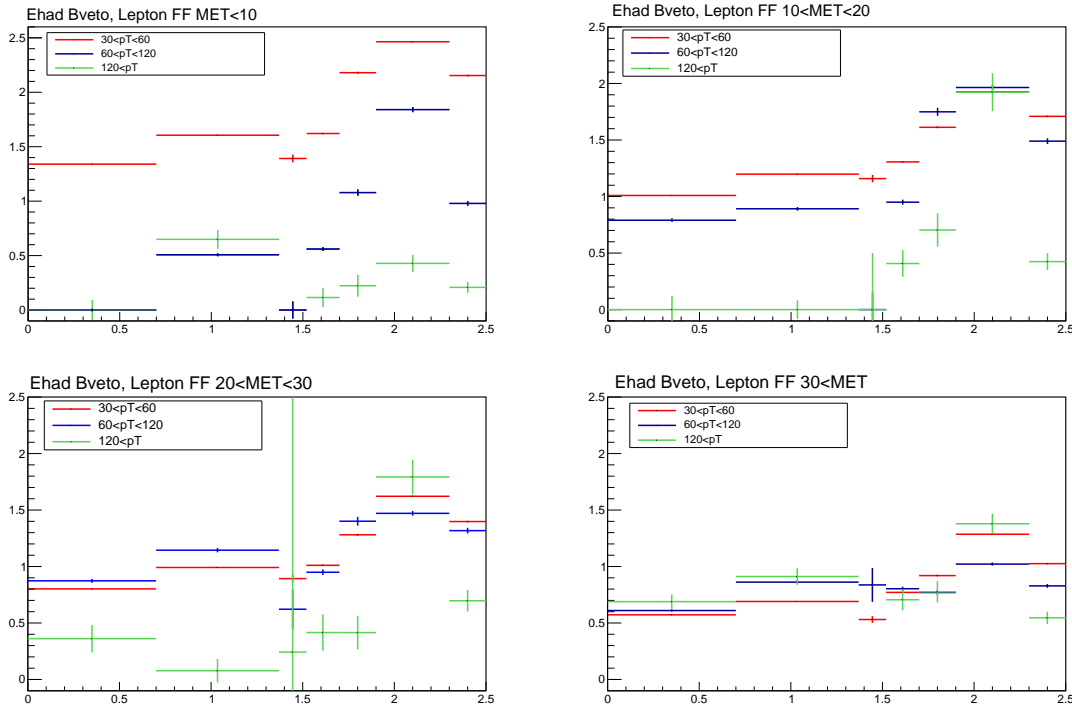


Figure 122: Electron fake factors parametrised in E_T^{miss} , $p_T(\text{lepton})$ and $\eta(\text{lepton})$.

Not reviewed, for internal circulation only

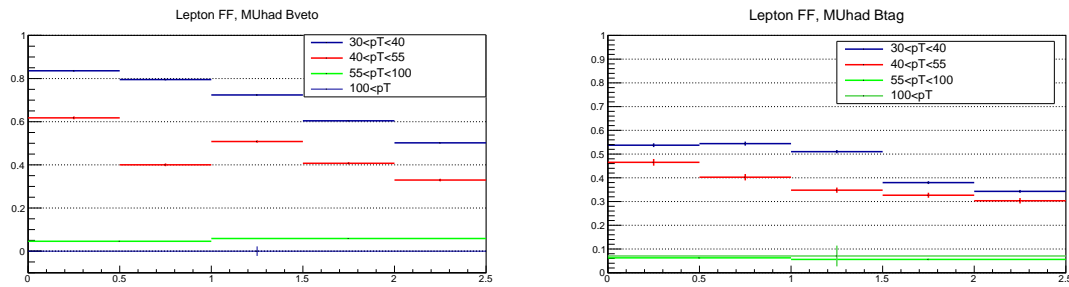


Figure 123: Muon fake factors parametrised in $p_T(\text{lepton})$ and $\eta(\text{lepton})$.

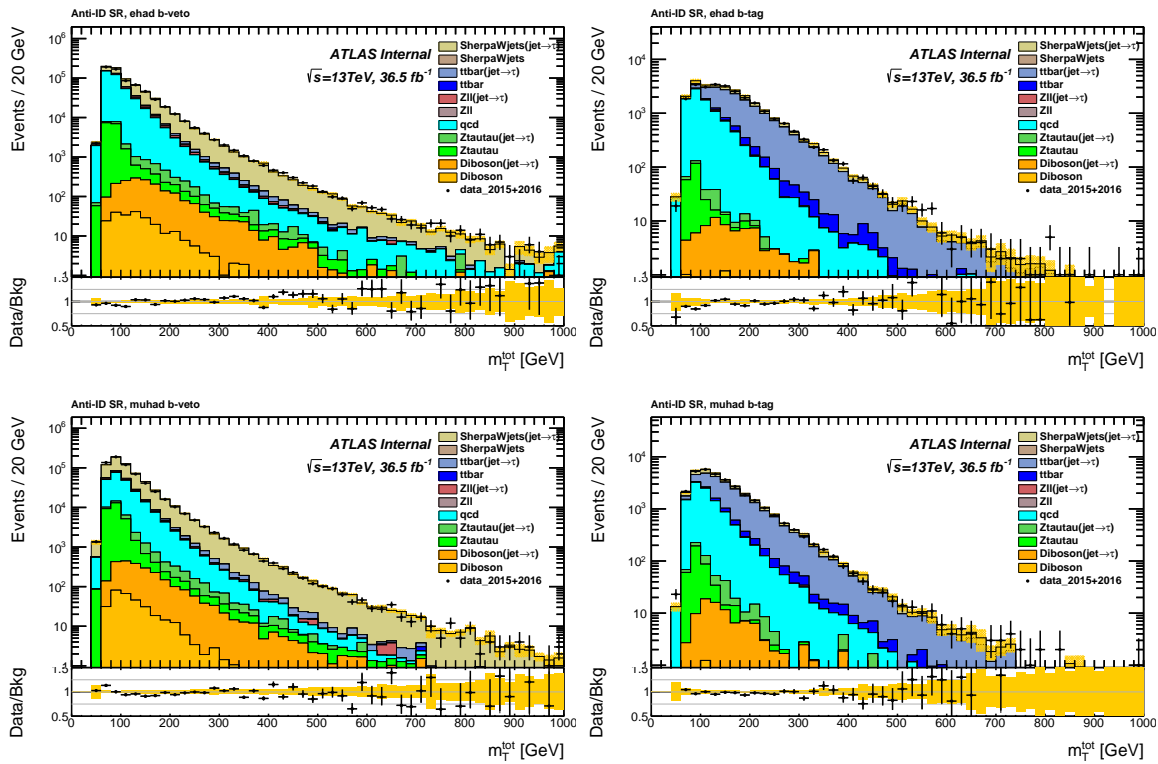


Figure 124: Distribution of m_T^{tot} in the Anti-ID region (improved FF).

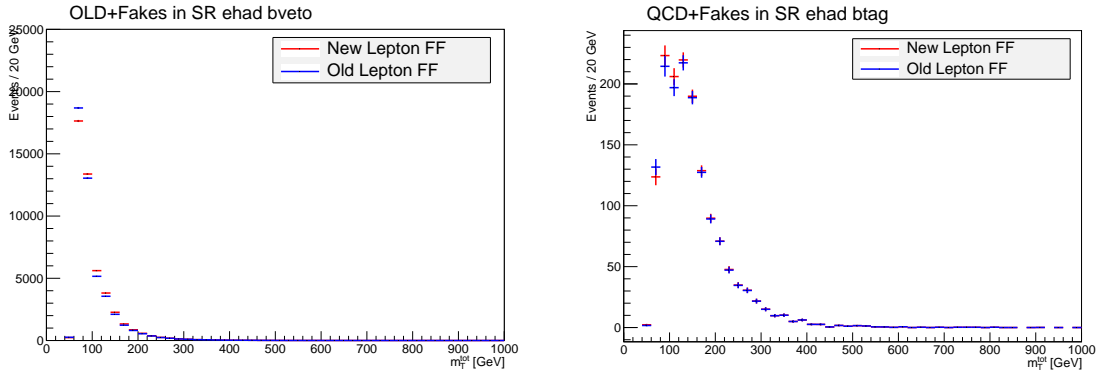
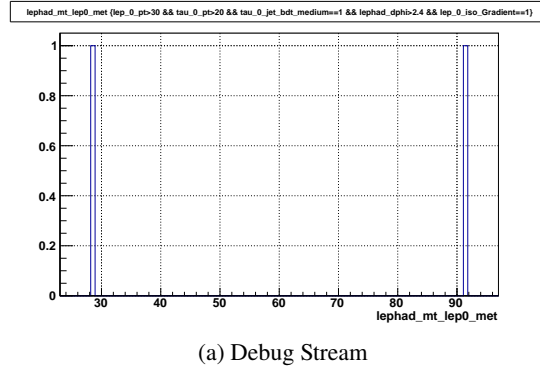


Figure 125: Distribution of m_T^{tot} of $\text{jet} \rightarrow \tau$ for ‘‘QCD+(Wjets)Fakes’’ in the Signal region.

1720 **G. Debug stream data check**



(a) Debug Stream

Figure 126: $m_T(\ell, E_T^{\text{miss}})$ after partial signal region selections: tauJetBdt is medium, lep Iso is Gradient, $p_T(\text{lepton}) > 30$, $p_T(\text{Tau}) > 20$, $\Delta\phi(\text{Tau}, \text{Lepton}) > 2.4$.

1721 As shown in Fig. 126, after partial signal region selections, only 2 events survive and only 1 is in the
1722 signal region. We conclude that the effect of debug stream could be ignored.

Not reviewed, for internal circulation only

1723 H. Different MSSM exclusion limit interpolation schemes

1724 The interpolation of the limit calculation in the parameter space of m_{Higgs} and production process composi-
1725 tion, as well as the comparison of this interpolated limit with the MSSM cross section predictions, result
1726 in very non-linear features between the considered signal mass points in parts of the $m_A - \tan \beta$ parameter
1727 space, as observed in Fig. 127. Therefore, the interpolation is not employed at $\tan \beta > 10$, which results
1728 in limits shown in Fig. 128. At low mass and low $\tan \beta$, in some cases there are multiple limit lines per
1729 mass, i.e. above the exclusion that is lowest in $\tan \beta$ a range of $\tan \beta$ appears which can not be excluded
1730 at 95 % CL. To explore the lateral extent of this hole in the exclusion space, the interpolation is especially
1731 interesting. Further studies are being performed to understand the interpolation effects, especially at
1732 $\tan \beta > 10$.

Not reviewed, for internal circulation only

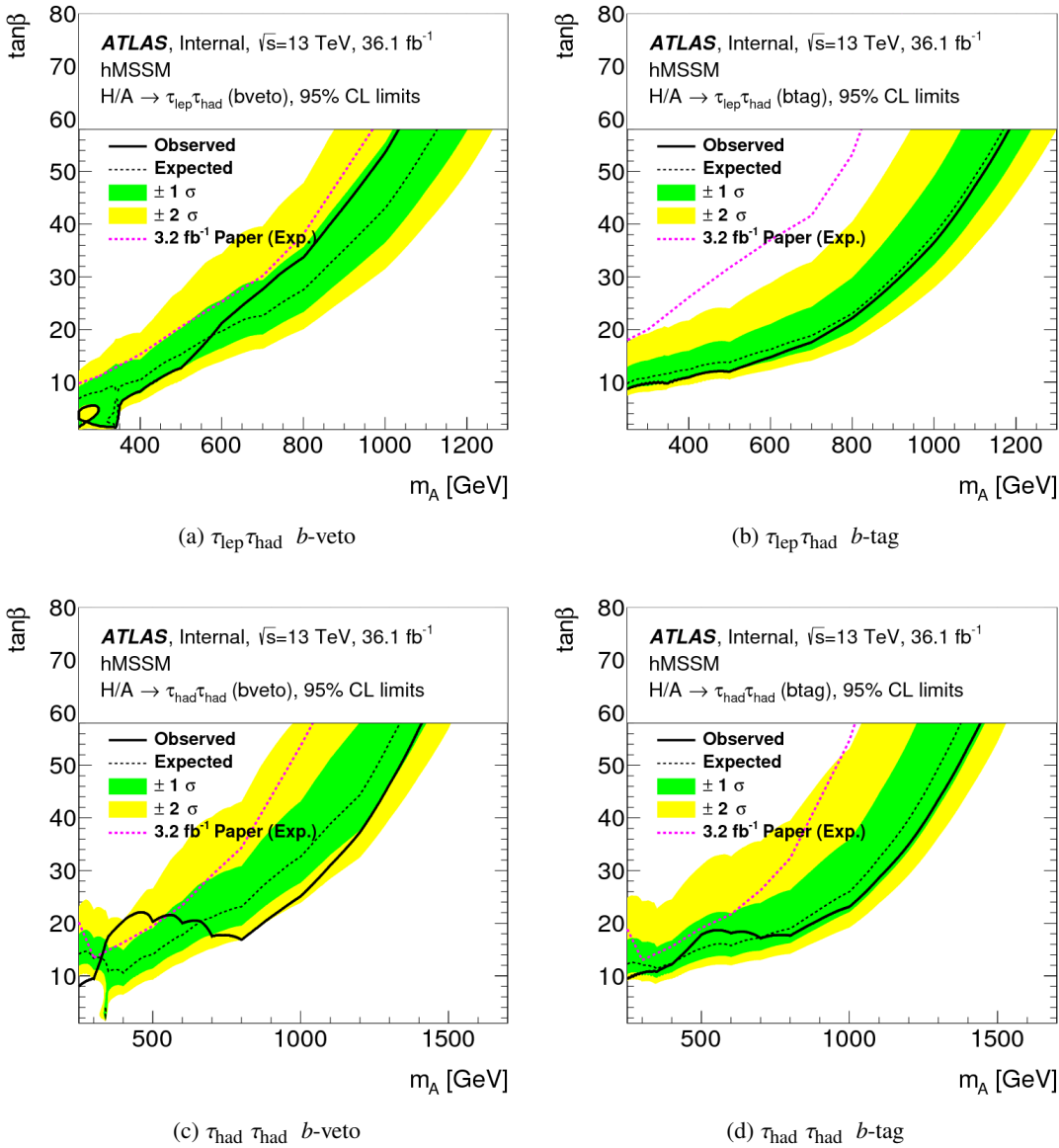


Figure 127: The 95% CL upper limit on the m_A - $\tan \beta$ plane of the hMSSM parameter space produced with the b-fraction interpolation in the different signal regions for 36.1 fb^{-1} of integrated luminosity at 13 TeV.

Not reviewed, for internal circulation only

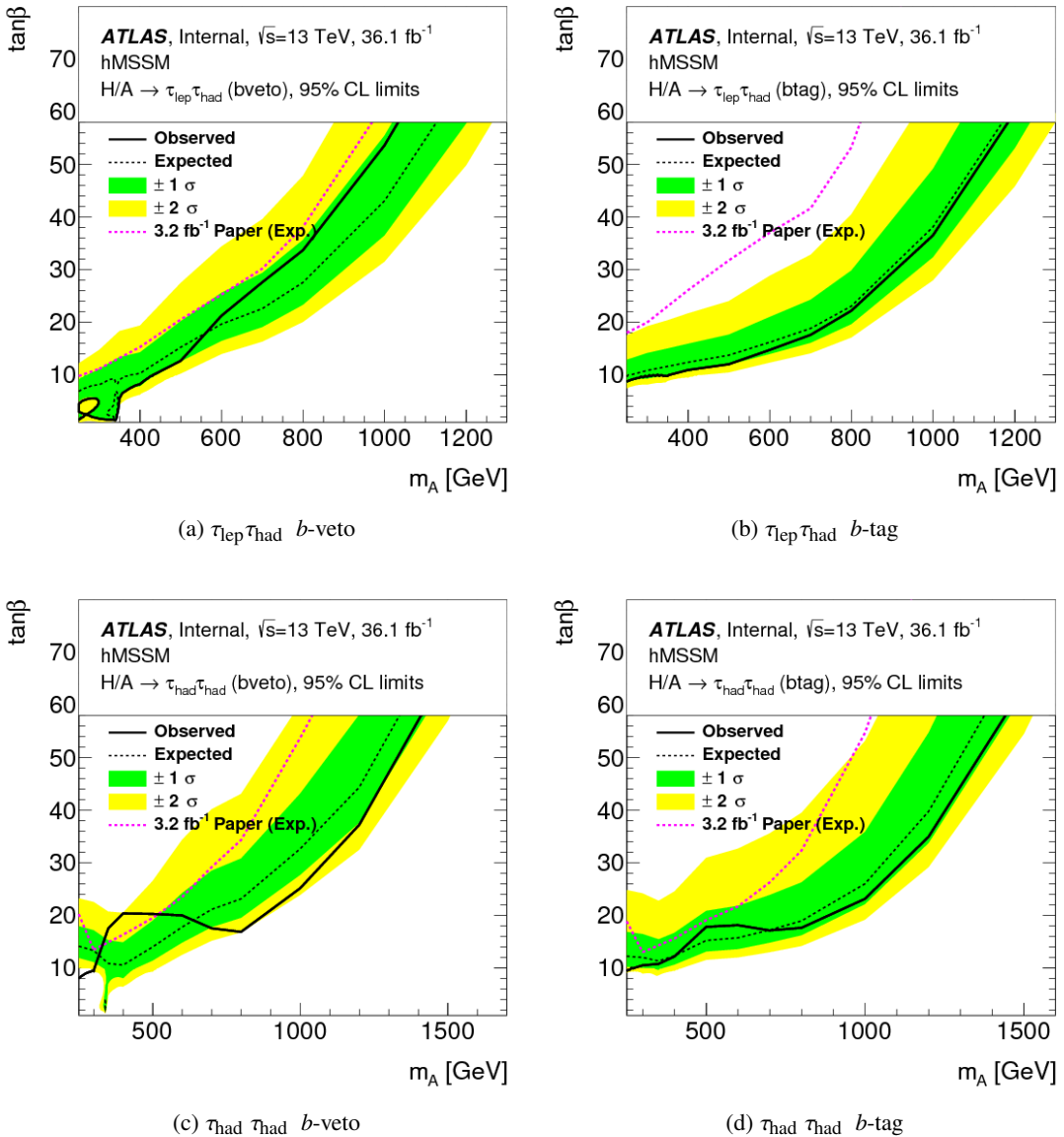


Figure 128: The 95% CL upper limit on the m_A - $\tan \beta$ plane of the hMSSM parameter space produced with the hybrid interpolation in the different signal regions for 36.1 fb^{-1} of integrated luminosity at 13 TeV.

1733 I. Central provided LPX systematics for Z+jets

1734 ATLAS has centrally provided the correction and systematics uncertainty on the W/Z+jets. Table 22 lists
 1735 the considered theoretical uncertainties. Figure 129 shows the effect of these systematic uncertainties.

Table 22: Theoretical systematic uncertainty of Z+jets

Systematic Uncertainty	Note
ALPHAS	
BEAM_ENERGY	
PDF	
CHOICE_NNPDF30	
PDF_EW	
PI	MultiParton Interation
SCALE_Z	QCD Scale

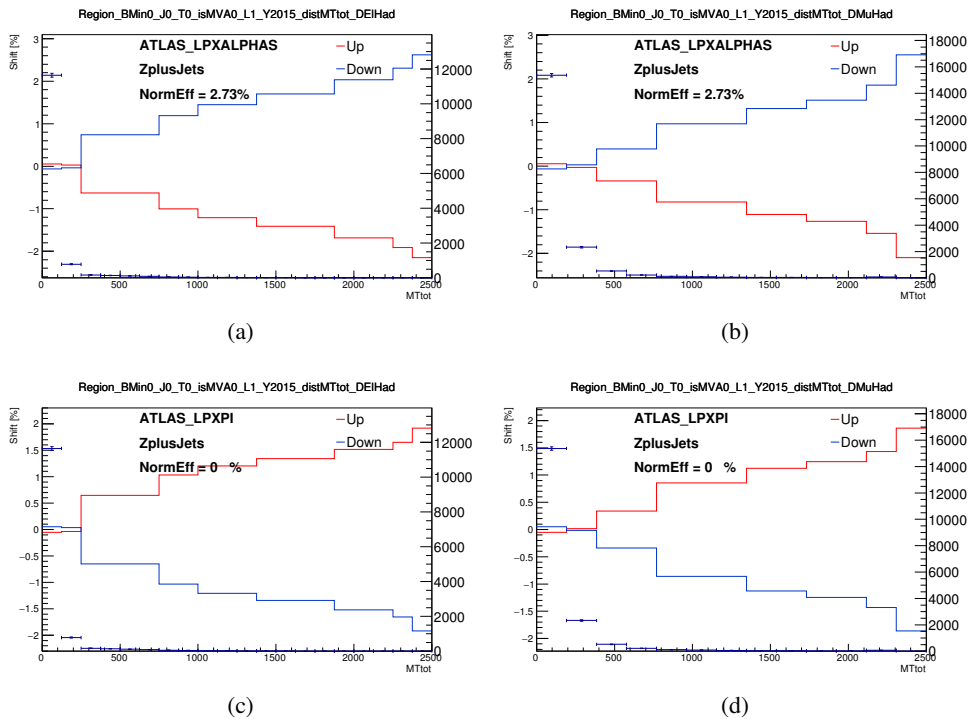


Figure 129: Theoretical systematic uncertainty of Z+jets

1736 J. Impact of the systematics on the expected limit

1737 Tables 23 and 24 show the expected limits when removing the given group of systematic uncertainties. It
 1738 can be seen that the signal uncertainty plays the dominant role on the limit.

Table 23: Summary of expected limit after removing a group of systematic uncertainties for ggH signal. “Default” is with the full default systematics, “all” means that all systematics are removed. “Fake” is all of the jet fake related sys, “AU” is signal acceptance uncertainties, “LPX sec” is background theoretical uncertainties, the meaning of the rest can be told from the names.

Mass	Default		Fake	AU	TES	LPX sec	Tau	TTBAR	JET JER MET			btag	EG
	all	Fake							PRW	LUMI	Jvt		
200	0.9576	0.5622	0.6869	0.8846	0.9523	0.9563	0.9574	0.9572	0.9489			0.9544	0.9574
300	0.2646	0.1682	0.2505	0.2423	0.2253	0.2625	0.2645	0.2639	0.2634			0.2621	0.2642
400	0.1340	0.0861	0.1298	0.1214	0.1084	0.1325	0.1340	0.1332	0.1326			0.1329	0.1336
500	0.0790	0.0529	0.0756	0.0713	0.0640	0.0780	0.0790	0.0783	0.0784			0.0787	0.0788
600	0.0555	0.0391	0.0533	0.0491	0.0470	0.0540	0.0554	0.0550	0.0553			0.0554	0.0554
700	0.0367	0.0272	0.0355	0.0322	0.0323	0.0356	0.0366	0.0363	0.0364			0.0366	0.0366
800	0.0265	0.0207	0.0260	0.0232	0.0244	0.0258	0.0264	0.0263	0.0264			0.0265	0.0265
1000	0.0221	0.0177	0.0218	0.0191	0.0210	0.0215	0.0221	0.0220	0.0220			0.0221	0.0221
1200	0.0206	0.0164	0.0203	0.0175	0.0197	0.0200	0.0205	0.0205	0.0205			0.0206	0.0206

Table 24: Summary of expected limit after removing a group of systematic uncertainties for bbH signal. “Default” is with the full default systematics, “all” means that all systematics are removed. “Fake” is all of the jet fake related sys, “AU” is signal acceptance uncertainties, “LPX sec” is background theoretical uncertainties, the meaning of the rest can be told from the names.

Mass	De- fault	all	Fake	AU	TES	LPX sec	Tau	TTBAR	JET JER MET			btag	EG
									PRW	LUMI	Jvt		
200	1.3251	0.5728	0.9924	0.9291	1.3154	1.3209	1.3199	1.3251	1.3136			1.3121	1.3245
300	0.4099	0.1730	0.3941	0.2936	0.3075	0.4089	0.4098	0.4079	0.4041			0.4082	0.4098
400	0.1921	0.0903	0.1897	0.1394	0.1432	0.1919	0.1920	0.1904	0.1901			0.1920	0.1920
500	0.1014	0.0568	0.0999	0.0746	0.0844	0.1012	0.1012	0.1008	0.1009			0.1014	0.1013
600	0.0628	0.0388	0.0619	0.0467	0.0555	0.0623	0.0626	0.0625	0.0626			0.0627	0.0627
700	0.0402	0.0269	0.0398	0.0299	0.0375	0.0398	0.0401	0.0401	0.0402			0.0402	0.0402
800	0.0313	0.0218	0.0310	0.0235	0.0297	0.0310	0.0312	0.0312	0.0313			0.0313	0.0313
1000	0.0256	0.0185	0.0255	0.0196	0.0248	0.0253	0.0256	0.0255	0.0256			0.0256	0.0256
1200	0.0245	0.0180	0.0243	0.0190	0.0238	0.0241	0.0244	0.0244	0.0244			0.0245	0.0245

1739 K. Fit study for Version (Latest production)

1740 This section shows some further detailed investigation on the fit results. The pull plot for the combined
 1741 conditional $\tau_{\text{lep}}\tau_{\text{had}}$ fit with real data and Asimov data are shown in Figure 130. The correlations of the
 1742 most correlated systematics are shown in Figures 131 (real data) and 132 (Asimov data). The fit results
 1743 in each individual region are shown in Figures 133 to 138. The fit results generally are understandable.
 1744 The error of *TES Detector* in the ehad b -veto fit is about 2 times larger than the pre-fit error. A dedicated
 1745 investigation is performed and can be found in the follow section K.1.

Not reviewed, for internal circulation only

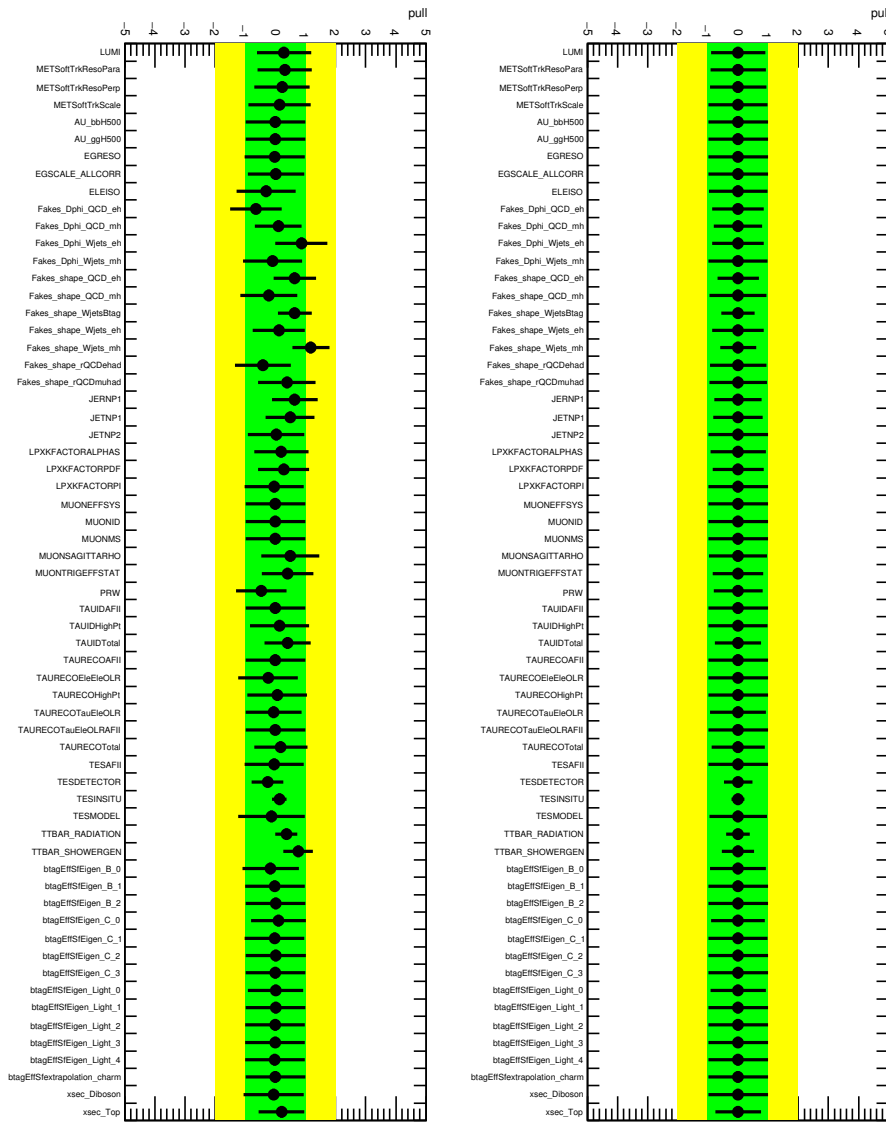


Figure 130: Pull plots for all nuisance parameters of the combined $\tau_{\text{lep}}\tau_{\text{had}}$ fit on (left) data and (right) Asimov data.

1746 Table 25 lists the suspicious systematics NPs which are either pulled or constrained. The ttbar sys has

Not reviewed, for internal circulation only

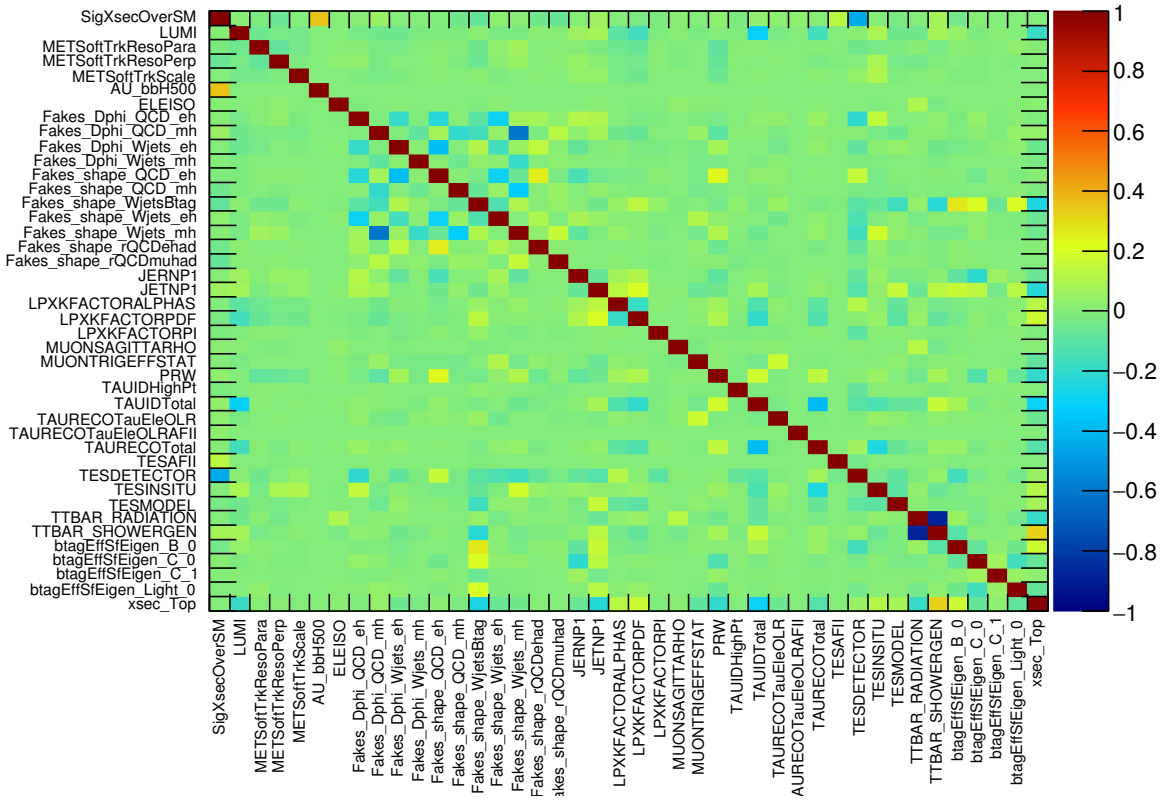


Figure 131: Correlation matrix of the highest correlated nuisance parameters of the combined $\tau_{\text{lep}} \tau_{\text{had}}$ fit on data.

1747 been well understood already. The shape of ttbar sys can be found in Sec. 6. Figures 139 to 145 show
 1748 the variation shape going to the fit. Note: some of them do not have shape since the effect is small and
 1749 prunned by the prunning algorithm.

Table 25: Summary of the suspicious systematics items show in the fit results.

Systematic Uncertainty	Note
Fakes_Dphi_QCD	
METSoftTrkResoPara	MET soft term
TESDETECTOR	Tau Energy scale
TESINSITU	Tau Energy scale

Not reviewed, for internal circulation only

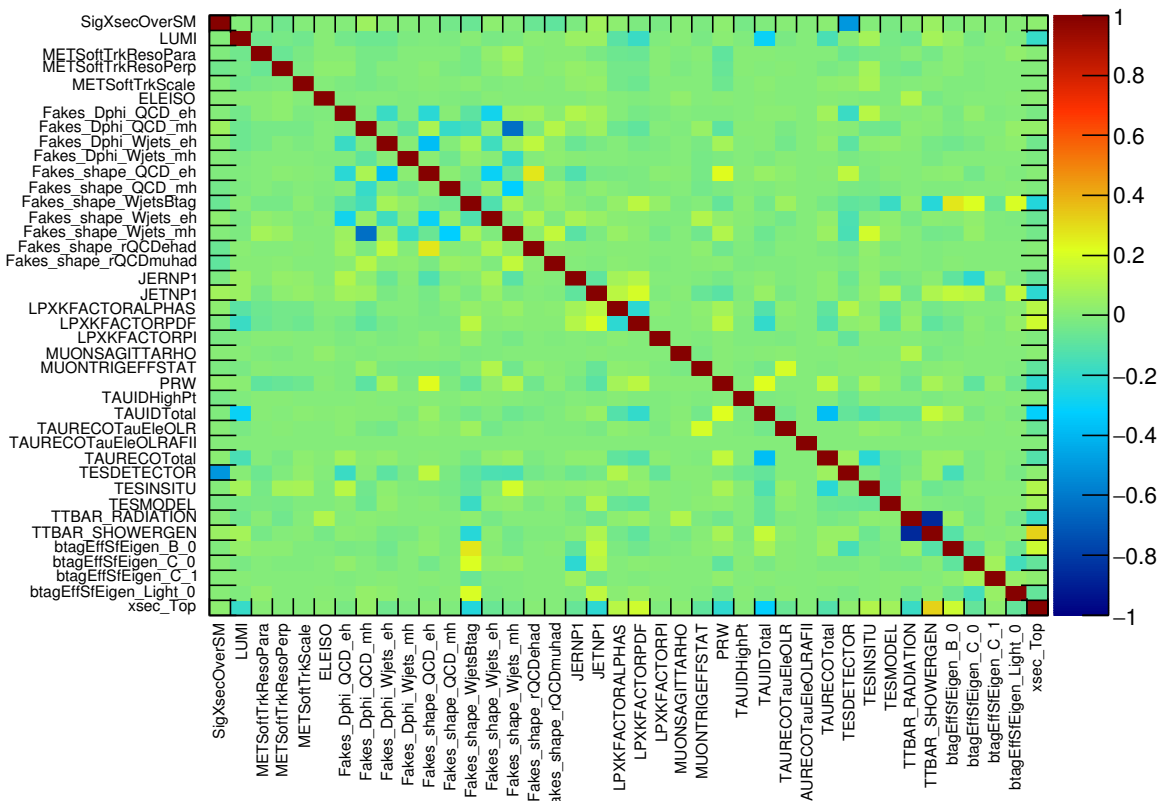


Figure 132: Correlation matrix of the highest correlated nuisance parameters of the combined $\tau_{\text{lep}}\tau_{\text{had}}$ fit on Asimov data.

Not reviewed, for internal circulation only

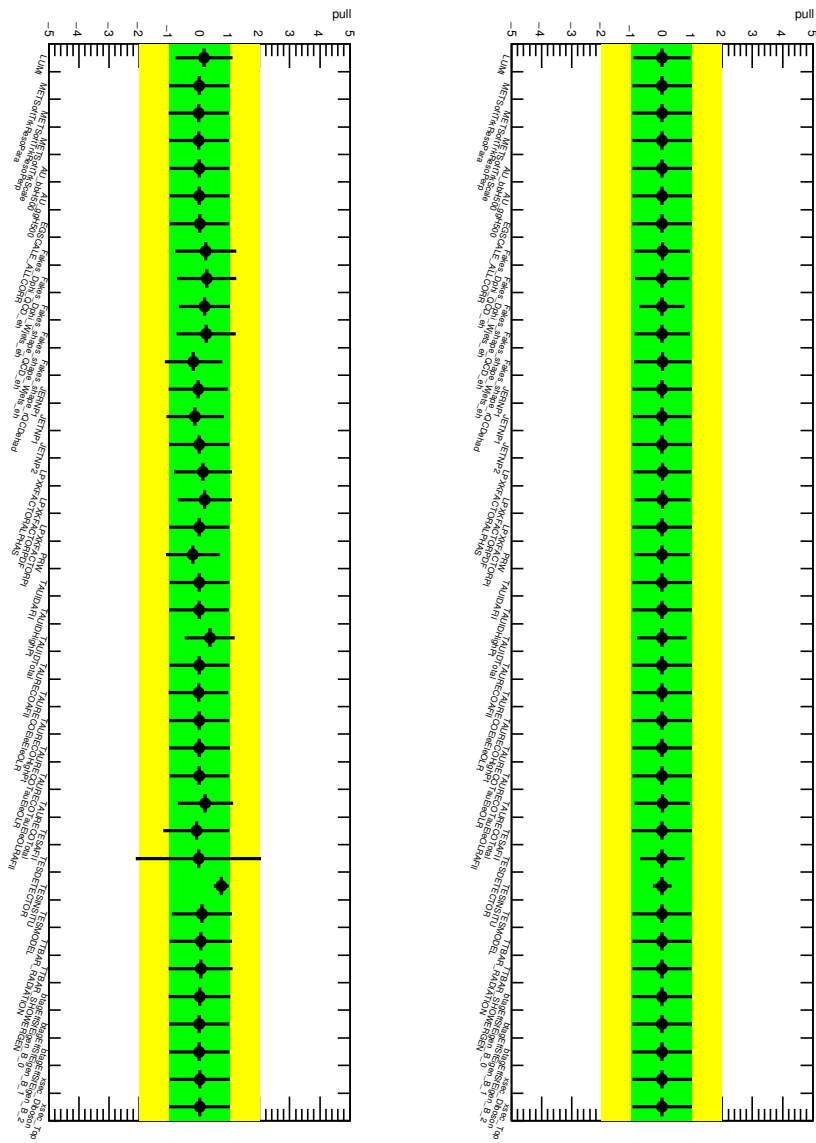


Figure 133: Pull plots for all nuisance parameters of the combined $\tau_{\text{lep}}\tau_{\text{had}}$ fit on (left) data and (right) Asimov data in the ehad bveto signal region.

Not reviewed, for internal circulation only

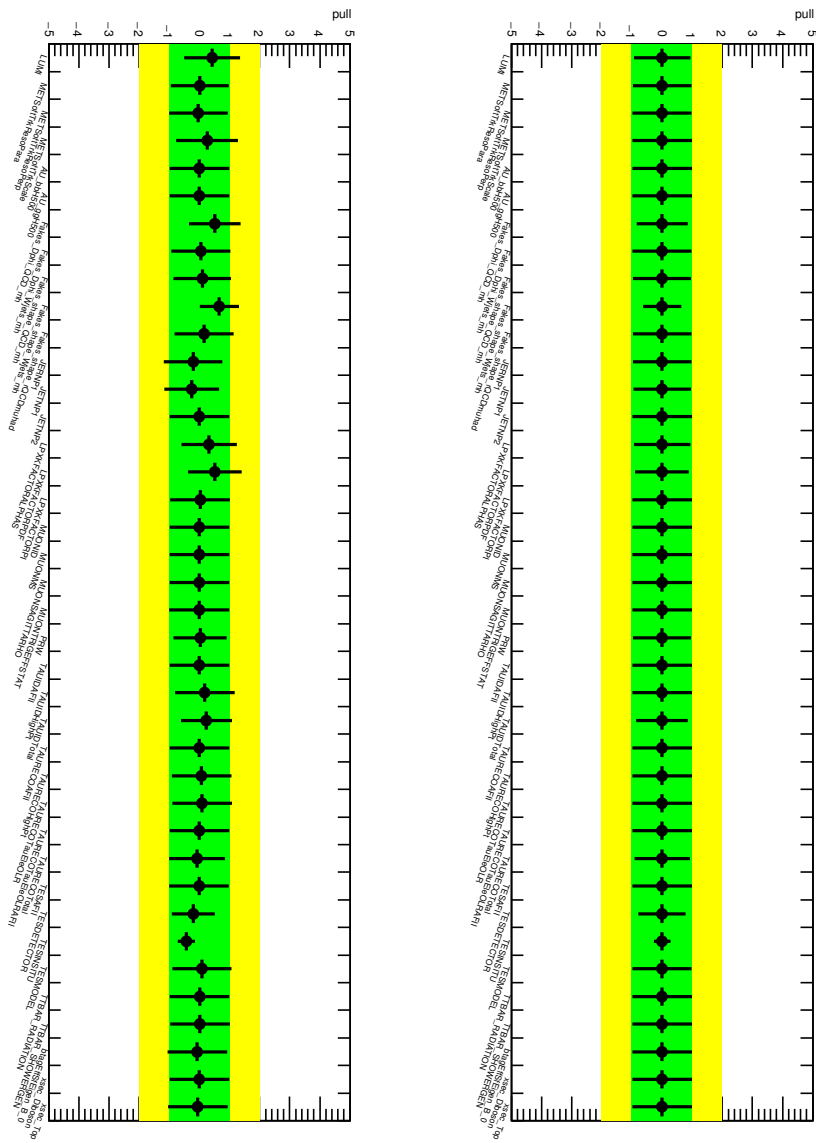


Figure 134: Pull plots for all nuisance parameters of the combined $\tau_{\text{lep}}\tau_{\text{had}}$ fit on (left) data and (right) Asimov data in the muhad bveto signal region.

Not reviewed, for internal circulation only

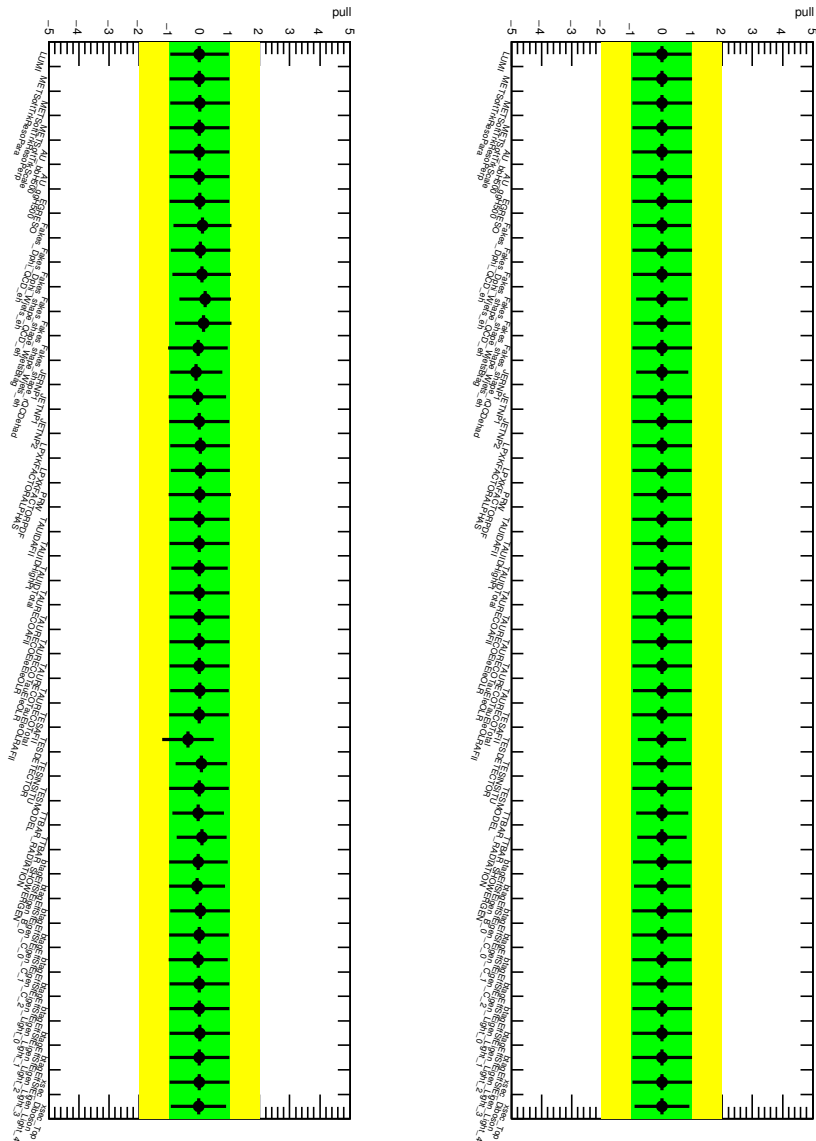


Figure 135: Pull plots for all nuisance parameters of the combined $\tau_{\text{lep}}\tau_{\text{had}}$ fit on (left) data and (right) Asimov data in the ehad btag signal region.

Not reviewed, for internal circulation only

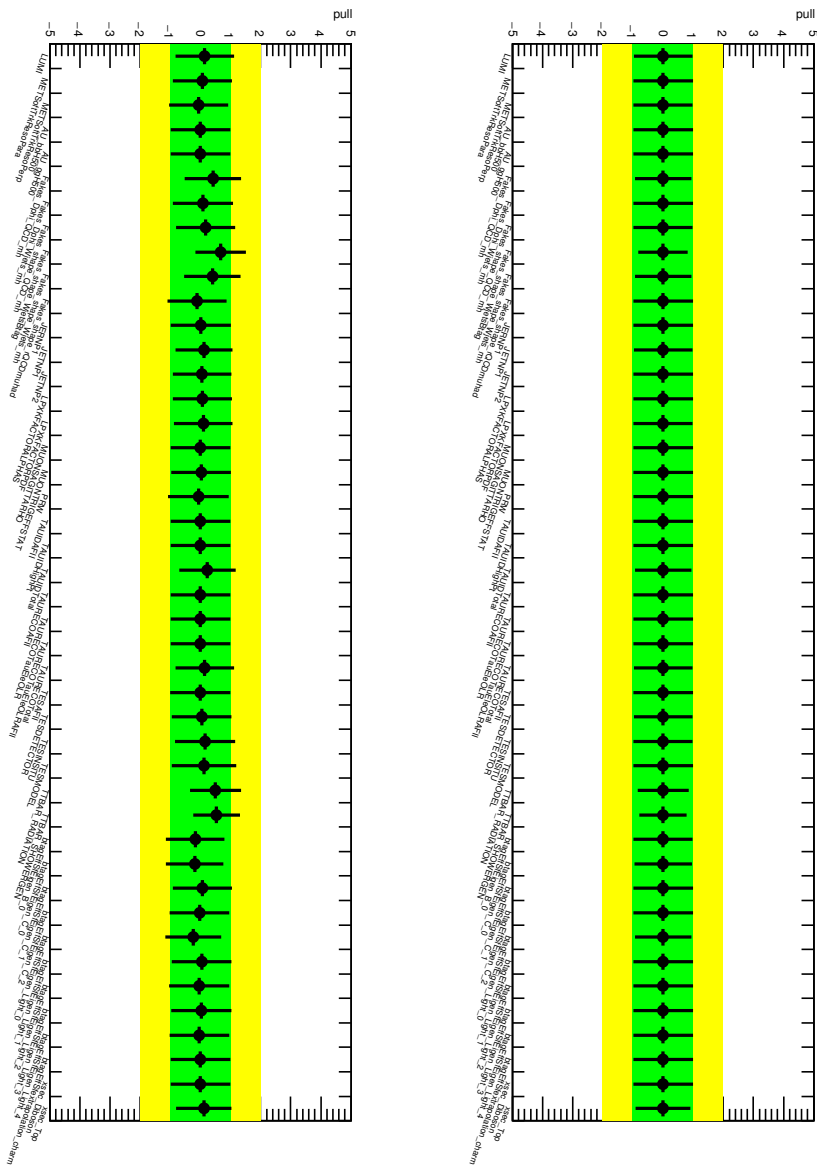


Figure 136: Pull plots for all nuisance parameters of the combined $\tau_{\text{lep}}\tau_{\text{had}}$ fit on (left) data and (right) Asimov data in the muhad btag signal region.

Not reviewed, for internal circulation only

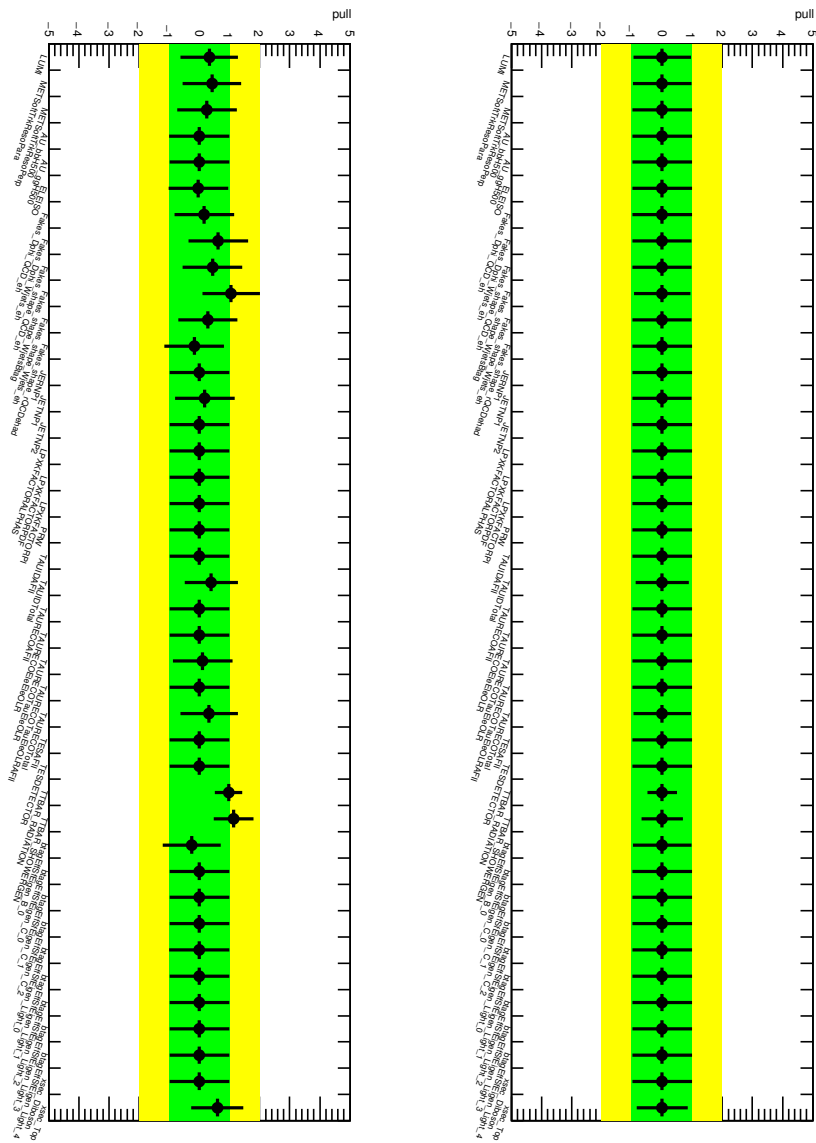


Figure 137: Pull plots for all nuisance parameters of the combined $\tau_{\text{lep}}\tau_{\text{had}}$ fit on (left) data and (right) Asimov data in the ehad top control region.

Not reviewed, for internal circulation only

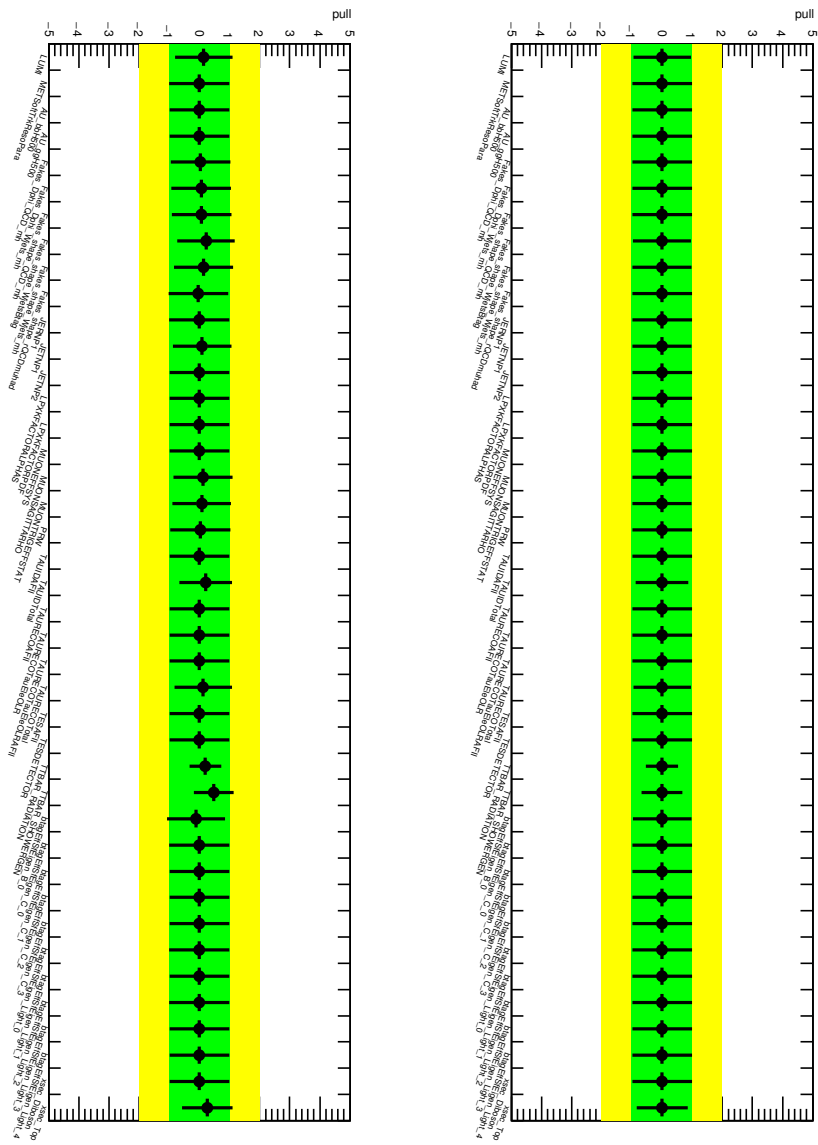


Figure 138: Pull plots for all nuisance parameters of the combined $\tau_{\text{lep}}\tau_{\text{had}}$ fit on (left) data and (right) Asimov data in the muhad top control region.

Not reviewed, for internal circulation only

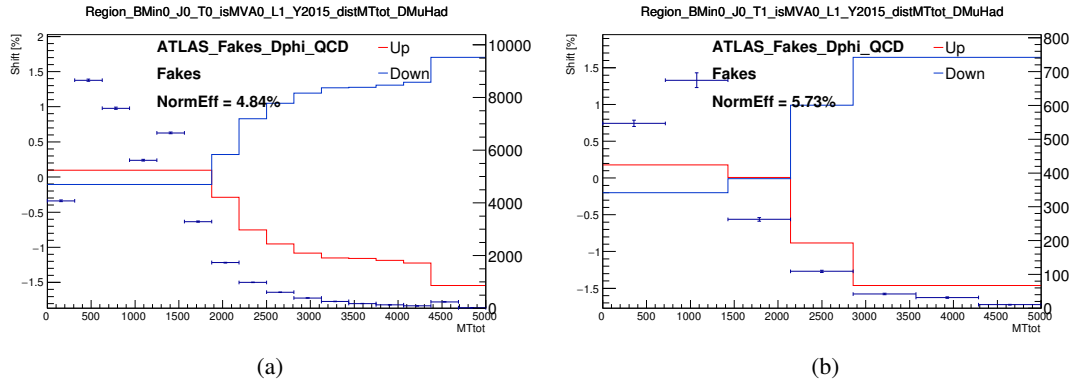


Figure 139: Important systematics shape for *Fakes_Dphi_QCD*

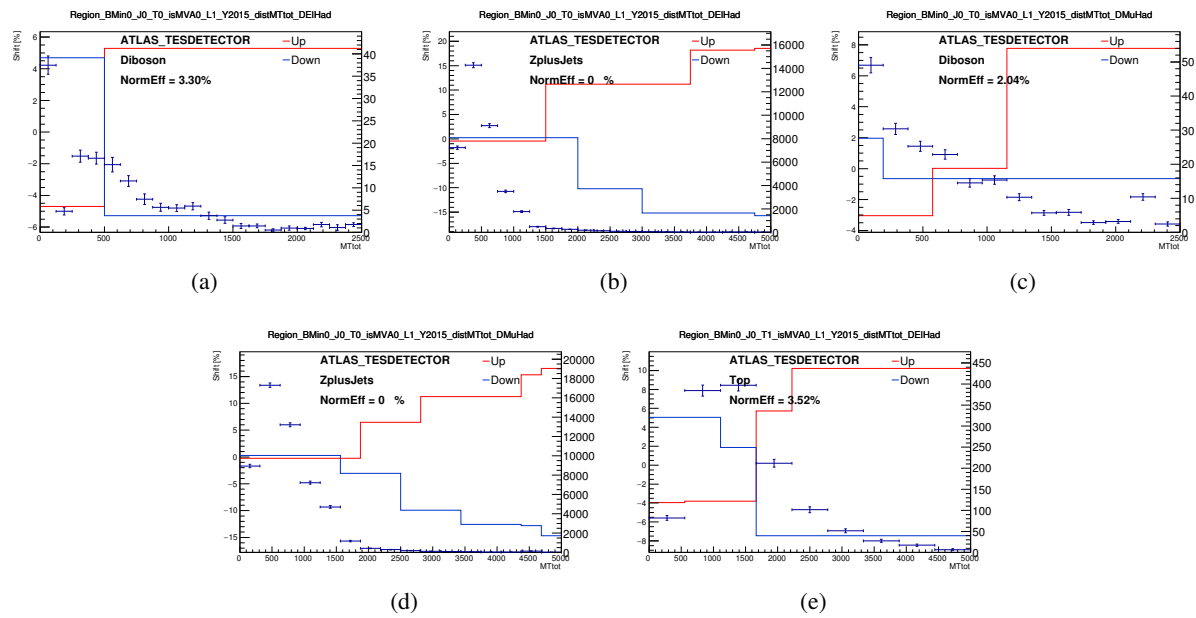


Figure 140: Important systematics shape for *TESDETECTOR*

Not reviewed, for internal circulation only

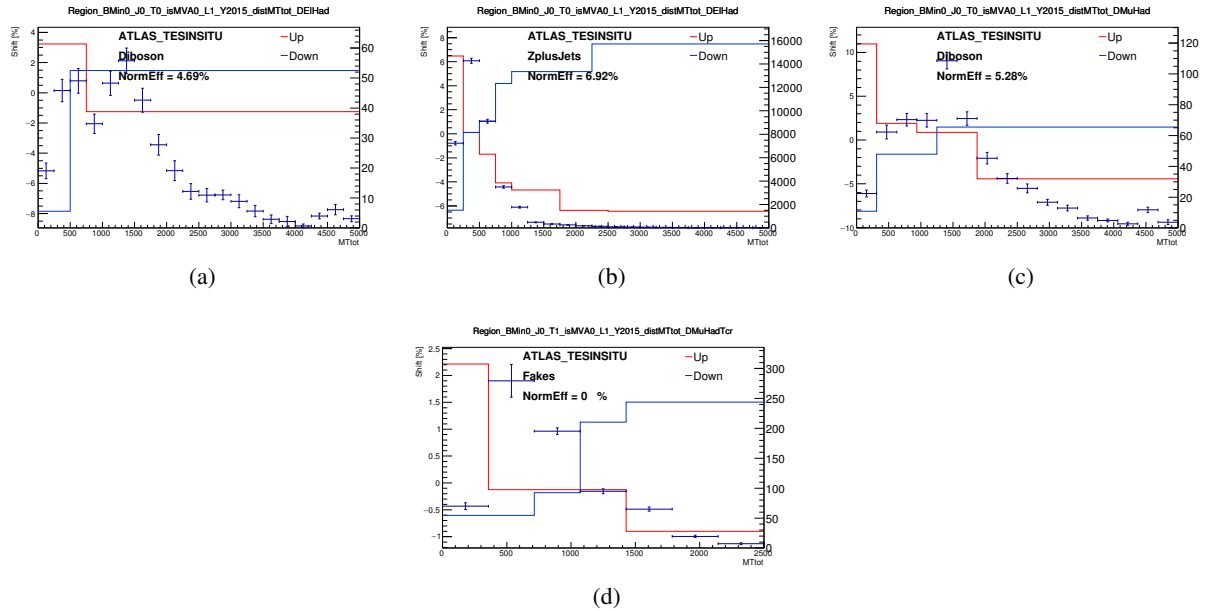


Figure 141: Important systematics shape for *TESINSITU*

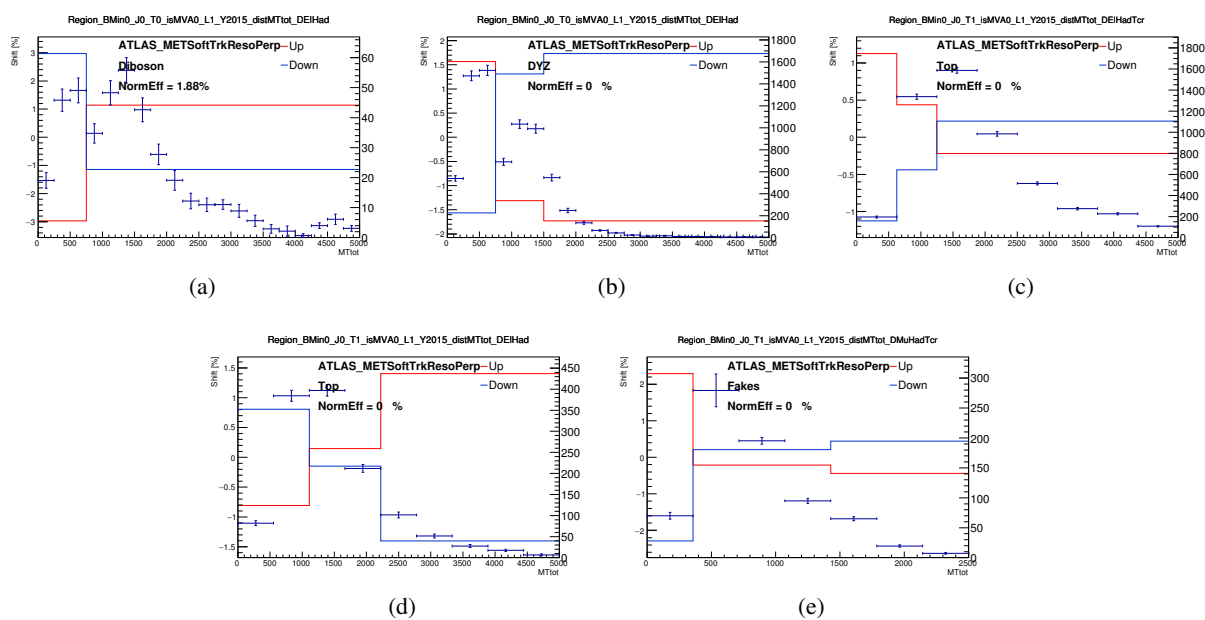


Figure 142: Important systematics shape for *METSoftTrkResoPerp*

Not reviewed, for internal circulation only

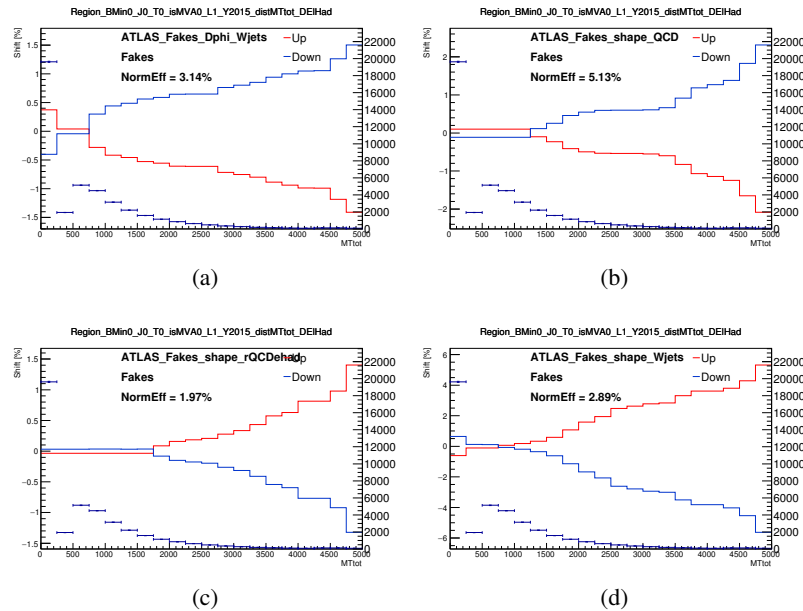


Figure 143: Important systematics shape for ehad fake b -veto

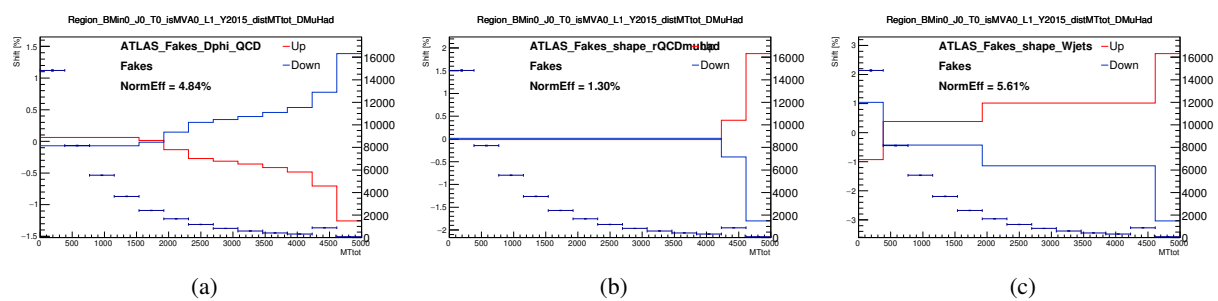


Figure 144: Important systematics shape for muhad fake b -veto

Not reviewed, for internal circulation only

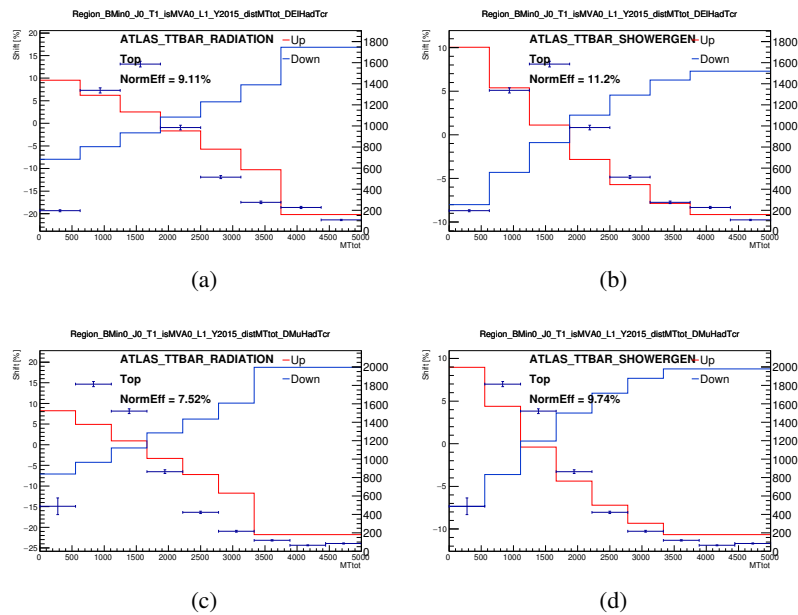


Figure 145: Important systematics shape for ttbar sys in Top CR

1750 K.1. Some detailed investigation on the Fit results

1751 The *TES Detector* in the left plot of Figure 133 has twice more error after fitting to data. This fit is
 1752 configured with the signal+background. Figure 146 shows the correlation matrix of this fit. It can be seen
 1753 that *TES Detector* is strongly correlated with several NPs, especially the signal strength. Figure 147 shows
 1754 the fit with the background only hypothesis where the *TES Detector* uncertainty is not under-constrained
 1755 anymore. This comparison proves the fact that the under-constraint of *TES Detector* NP comes from
 1756 the correlation with the signal strength. Since *TES Detector* NP in the combined fit has been properly
 1757 constrained by other regions, this under-constraint in the ehad *b*-veto only fit is expected to be harmless.

Not reviewed, for internal circulation only

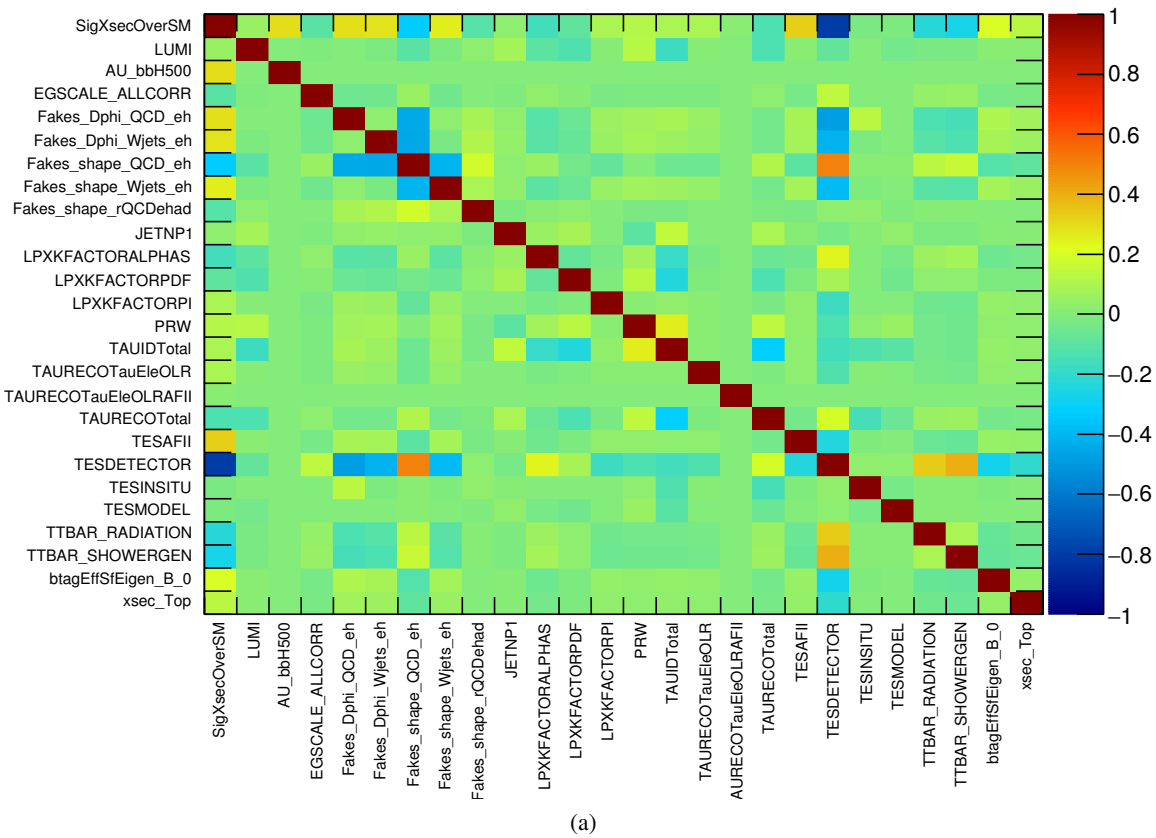


Figure 146: Correlation matrix of the *b*-veto ehad signal region fit.

Not reviewed, for internal circulation only

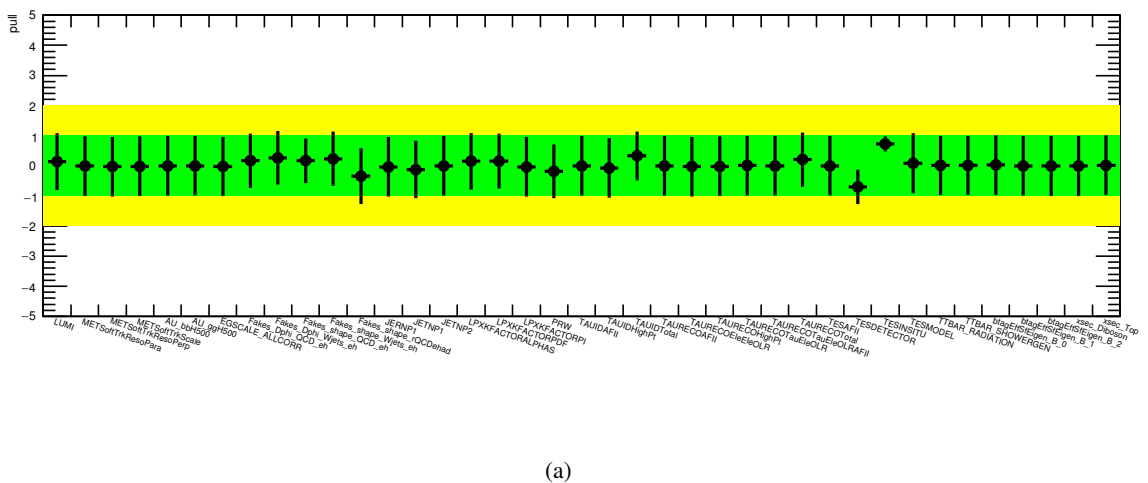


Figure 147: Pull plots for all nuisance parameters of the $\tau_{\text{lep}}\tau_{\text{had}}$ fit on data in the ehad bveto signal region.

1758 L. TES insitu systematics study

1759 In the previous results section and fit study section, a severe constraint of TES insitu systematics is
 1760 observed. This section shows some further detailed investigation on the fit results. The systematics norm
 1761 and shape templates are shown in Figure 148. The recommendation from TauWG is to apply the TES
 1762 insitu sys only for tau p_T less than 70 GeV, which only impact on the low mass region. This makes the
 1763 TES sys give a significant shape systematics in the fit. The pull plot for the combined conditional $\tau_{\text{lep}} \tau_{\text{had}}$
 1764 fit on Asimov data, with and without TES insitu shape systematics are shown in Figure 149. Norm only
 1765 fit has not significant constraint.

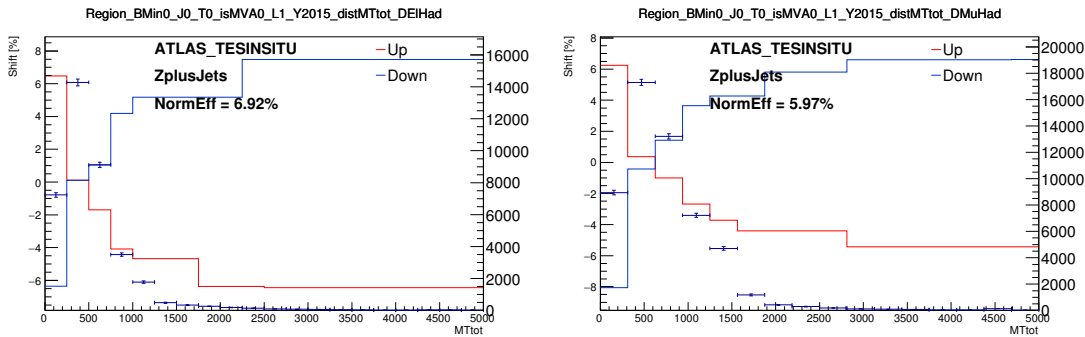


Figure 148: TES insitu systematics variation shapes for $Z \rightarrow \tau^+ \tau^-$ background in (left) ehad and (right) muhad b -veto channel.

1766 Figure 150 shows the comparison on the expected limit with and without TES insitu sys or only norm
 1767 effect for b -associated production, Figure 150 (a), and gluon-gluon fusion, Figure 150 (b). The nominal
 1768 limit, where the normalization and shape effects of the TES insitu are considered in the fit, is compared
 1769 to the case where the TES insitu is considered as a normalization systematic (norm) only, and the case
 1770 where the TES insitu is excluded from the fit (skip). The norm only limit shows slightly worse limit is
 1771 because the fit does not constrain the TES insitu sys in this fit configuration. The effect is only visible in
 1772 the gluon-gluon fusion signal, Figure 150 (b), for the b -veto and combined limits. However, the effect in
 1773 both cases is very small and considered negligible to a large extent. Figure 150 (a) shows no deviation of
 1774 the normalized and skipped cases from the nominal, and their graphs are superimposed and identical.

1775 Figures 151 and 152 show the NP pull and constrain for the b -veto region fit to the low mass spectrum
 1776 ($m_T^{\text{tot}} < 240$ GeV) and the high mass spectrum ($m_T^{\text{tot}} > 240$ GeV). During the unblind approval talk,
 1777 *TESDETECTOR* and *TESMODEL* are concerned that the low mass region constrains the high mass region
 1778 sys. From Figures 151 and 152, it can be seen that the *TESDETECTOR* and *TESMODEL* constraints are
 1779 more or less consistent between high and low mass fit. Note: the *TESINSITU* is pruned away in the high
 1780 mass fit in Figure 152 since it is applied only for $p_T < 70$ GeV.

Not reviewed, for internal circulation only

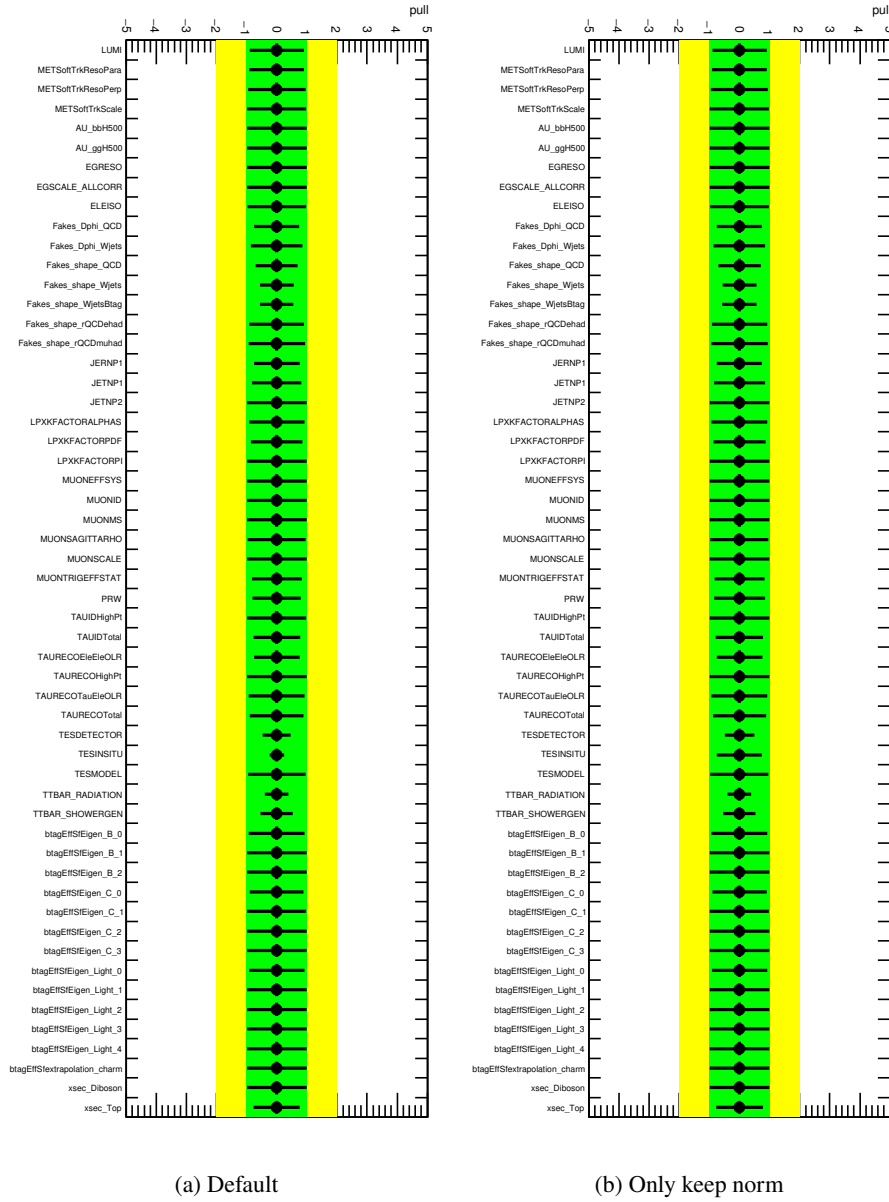
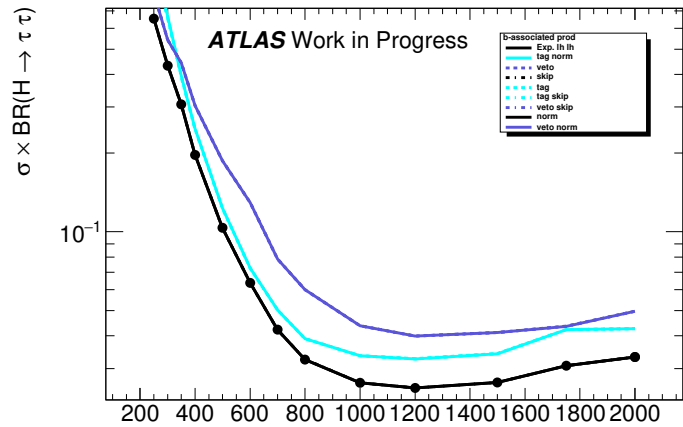
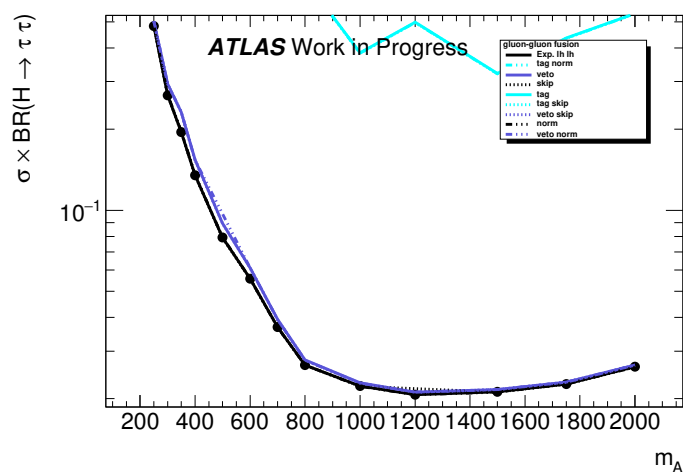


Figure 149: NP fit results with different *TESINSITU* systematics configurations

Not reviewed, for internal circulation only



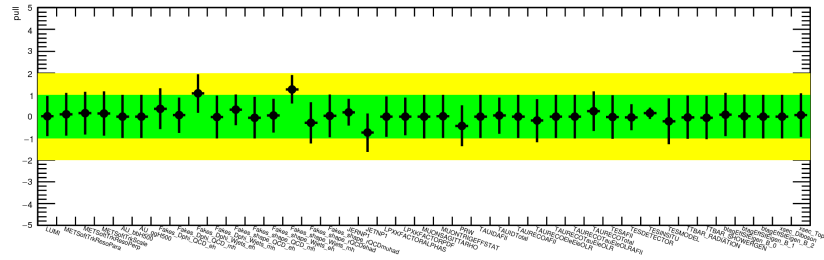
(a)



(b)

Figure 150: Impact on the expected limit from *TESINSITU* systematics for (a) b-associated production, and (b) gluon-gluon fusion production processes

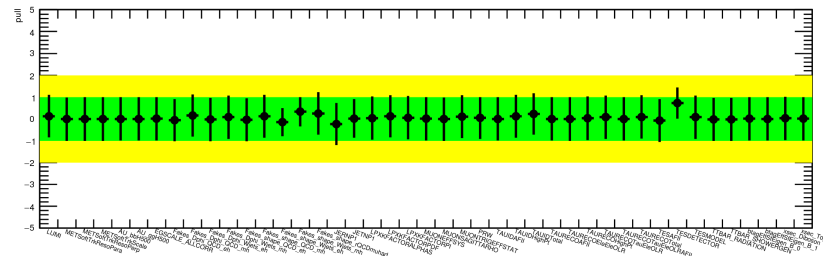
Low ($m_T < 240$ GeV)



(a) Low mass

Figure 151: NP pull and constrain of b -veto region fit for $m_T^{\text{tot}} < 240$ GeV .

Low ($m_T^{> 240 \text{ GeV}}$)



(a) High mass

Figure 152: NP pull and constrain of b -veto region fit for $m_T^{\text{tot}} > 240 \text{ GeV}$.

1781 M. Expected limit comparison between ICHEP and current analysis

1782 Table 26 shows the yield of ICHEP ntuple but with the same selection as the current analysis. Figure 153
 1783 shows the expected limit between ICHEP analysis and current analysis. At the low mass regime, the
 1784 sensitivity is limited by the systematics. The previous analysis did not give much shape systematics,
 1785 which lead to a constraint in the fit and effectively reduce the systematics on fake. The systematics
 1786 treatment in the current analysis is more solid comparing to the preliminary results in ICHEP. That is
 1787 why ICHEP expected limit is comparable at the low mass to the full lumi results. Another difference is
 1788 that, in the ICHEP analysis, a high E_T^{miss} signal region was introduced and brought sensitivity at the high
 1789 mass parameter. However, the background modeling in that region has been checked as carefully as other
 1790 regions. We did observe some tension between expected results and observed results. Considering the
 1791 fact that hadhad channel has better sensitivity at the high mass region, the final combined sensitivity at
 1792 high mass is expected to be better than ICHEP.

Not reviewed, for internal circulation only

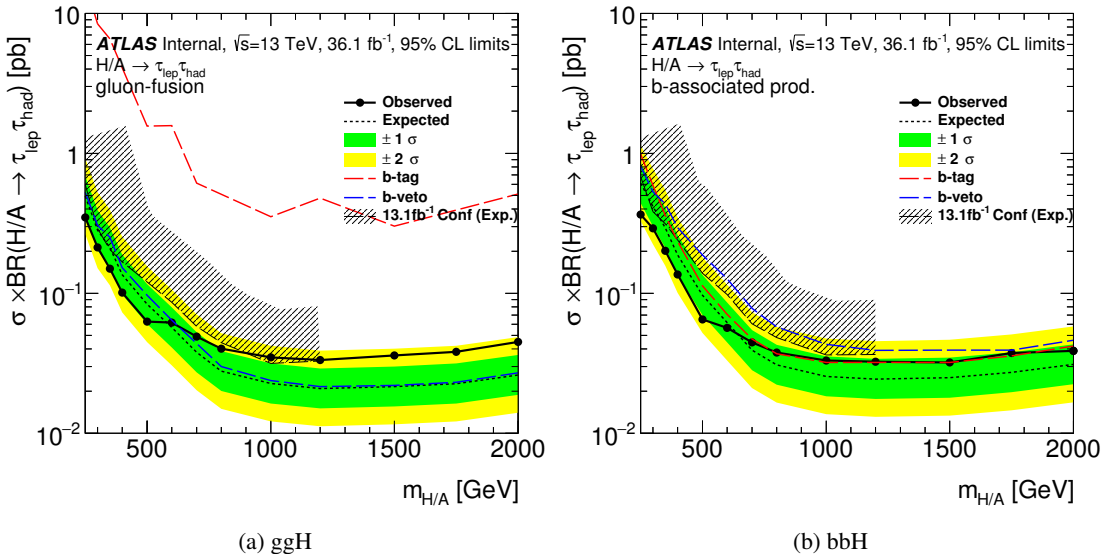


Figure 153: Expected Limit comparison with ICHEP results and current results

Table 26: Yield table for each category from ICHEP ntuple. The numbers correspond to the integrated luminosity of 36.1 fb^{-1} for signal regions. The signal normalization corresponds to an assumed cross section of 1 pb. The quoted uncertainties only contain the statistical uncertainty.

Regions	ggH200	ggH600	ggH1000	bbH200	bbH600	bbH1000
muhad b-veto	456.84 ± 17.08	1043.20 ± 27.38	1021.96 ± 27.05	318.85 ± 15.76	592.97 ± 13.29	511.49 ± 18.04
muhad b-tag	4.32 ± 2.03	32.37 ± 4.96	47.94 ± 6.78	135.80 ± 9.71	398.02 ± 11.20	436.37 ± 16.63
ehad b-veto	303.45 ± 13.58	1048.68 ± 28.26	972.85 ± 27.11	218.65 ± 12.91	550.28 ± 13.56	462.01 ± 17.71
ehad b-tag	4.92 ± 1.75	28.84 ± 5.52	39.87 ± 5.80	78.46 ± 7.88	389.77 ± 11.27	358.80 ± 16.15

1793 N. Extrap Plots

1794 Figures 154 and 155 show the m_T^{tot} distributions in b -tag region and $p_T(\tau_{\text{had}})$ distributions in the b -veto region with the x-axis is zoomed in.

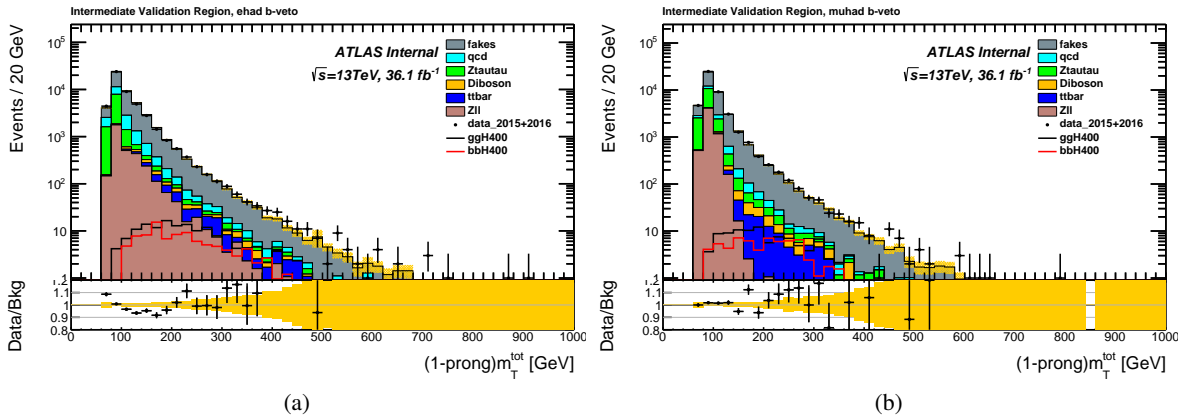


Figure 154: m_T^{tot} distributions in the b -tag (left) electron and (right) muon channel with requiring $40 < m_T(\ell, E_T^{\text{miss}}) < 60(70)$ GeV for muon(electron) channel. Backgrounds estimated from MC samples are truth matched.

1795

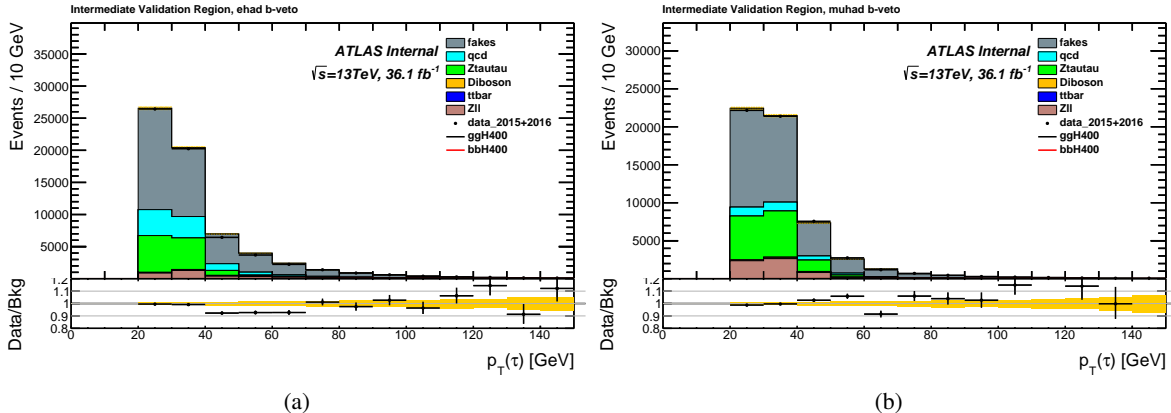


Figure 155: $p_T(\tau_{\text{had}})$ distributions in the b -veto (left) electron and (right) muon channel with requiring $40 < m_T(\ell, E_T^{\text{miss}}) < 60(70)$ GeV for muon(electron) channel. Backgrounds estimated from MC samples are truth matched.

1796 O. New and old m_T^{tot} reconstruction comparison

Figure 156 shows the comparison between new and old (to some extent “buggy”) m_T^{tot} reconstruction. The main difference is on the computation of “ $m_T^2(\tau_{\text{lep}}, \tau_{\text{had}})$ ”. The old m_T^{tot} uses the formula given in wikipedia “https://en.wikipedia.org/wiki/Transverse_mass”: $m_T^2 = m^2 + p_x^2 + p_y^2$. While the new m_T^{tot} uses the one listed in the note:

$$m_T(\vec{a}, \vec{b}) = \sqrt{2p_T(\vec{a})p_T(\vec{b})(1 - \cos \Delta\phi(\vec{a}, \vec{b}))}$$

1797 The later one is more consistent with the previous ICHEP and 2015 paper analysis, and also gives a better
1798 sensitivity. The new method tends to push the backgrounds, as well as the signal, to the low side.

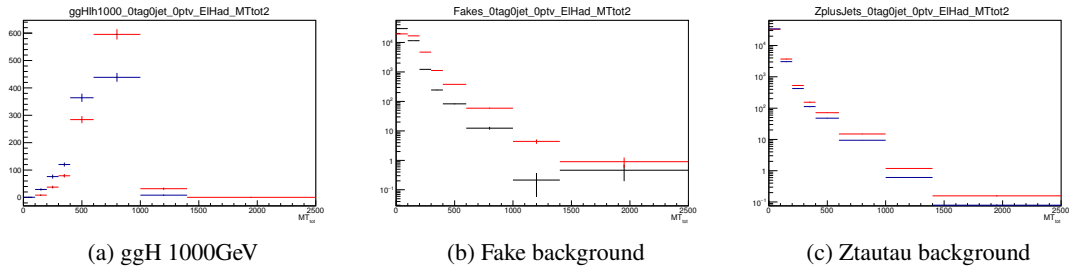


Figure 156: m_T^{tot} distribution in ehad bveto region. Red is the old method while blue is the new method.

1799 P. High MET category

1800 The High MET category was first introduced at ICHEP 2016. Its purpose was to recover signal events
 1801 that were lost due to inefficiency of the lepton triggers. Single lepton triggers are used in the nominal
 1802 analysis. At ICHEP, events were categorised based on their missing energy. In that case, some events from
 1803 the nominal categories were assigned to the High MET categories and any meaningful comparison of the
 1804 sensitivities of nominal and nominal+High MET categories could not be made. This time we keep the
 1805 nominal categories untouched and only further categorise those events which fail single lepton triggers.

1806 Only muon channel is considered because it is known that MET triggers are fully efficient at around
 1807 150GeV and in electron channel very few events have such high MET. On the other hand, muon channel
 1808 is different because at HLT muon momentum is not included in MET calculation and it contributes to
 1809 online MET. The estimate of online MET is therefore $|\vec{p}_T(\mu) + \vec{E}_T^{miss}|$ and MET trigger is fully efficient
 1810 when this variable reaches value of around 150GeV. Many events pass this requirement in muon channel
 1811 because the real MET is actually smaller than 150GeV.

1812 The definition of High MET category involves vetoing muon trigger which invoke a few complications:
 1813 how do we know the sampled luminosity and how can we measure MET trigger efficiency? Another issue,
 1814 probably much smaller, is how can we know muon trigger inefficiency for MC?

1815 The luminosity problem is solved by noticing that effectively we are using `HLT_xe*_vetomu*` "triggers"
 1816 and any combination of unprescaled triggers are sampling the full luminosity. This means that the
 1817 luminosity in this category is the same as in the nominal ones.

1818 Efficiency of MET trigger in MC is estimated in the following way: a looser event selection is defined and
 1819 then the data is compared to MC. The selection is as follows:

- 1820 • fail muon trigger (data and MC);
- 1821 • pass xe trigger (only data);
- 1822 • offline medium ID, gradient isolated muon;
- 1823 • number of taus > 0, no identification requirement;
- 1824 • $m_T(lep, met) > 60\text{GeV}$ (enriched in $W+jets$ events);

1825 The $|\vec{p}_T(\mu) + \vec{E}_T^{miss}|$ distribution in Fig.157 suggests that MET triggers are 100% efficient above 150GeV.
 1826 Note that there should be some uncertainty on muon trigger inefficiency in MC but it looks like it is not
 1827 playing any role here. Also there might be some multi-jet events passing this selection but not estimated
 1828 here (they are only important above 150GeV). Data/MC agreement is very good above 150GeV which
 1829 encourages us to define the High MET category:

- 1830 • fail SLT as used in the nominal categories;
- 1831 • pass MET triggers (lowest unprescaled, depending on period);
- 1832 • luminosity is the same as in nominal categories;
- 1833 • 100% MET trigger efficiency above 150GeV of the $|\vec{p}_T(\mu) + \vec{E}_T^{miss}|$ variable;
- 1834 • other cuts are the same as in the nominal category.

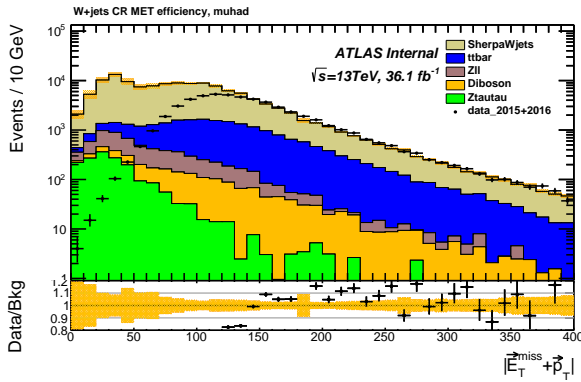


Figure 157: Distribution of $|\vec{p}_T(\mu) + \vec{E}_T^{miss}|$ with looser event selection.

Table 27: Signal yields in all categories, xsec=1pb.

	ggH200	ggH800	ggH1200	bbH200	bbH800	bbH1200
ehad bveto	300	1162	984	215	615	491
ehad btag	3	19	22	64	391	316
muhad bveto	463	1198	1035	316	624	570
muhad btag	4	24	24	109	406	352
hmet bveto	2	254	245	1	141	152
hmet btag	0	5	6	1	110	95

1835 This category helps to recover around 20% of events that are lost due to muon triggers (for high mass
 1836 points) as shown in Tab.27.

1837 Background estimation

1838 Background is estimated in the same way as in the nominal analysis except for multi-jet events. Compared
 1839 to the nominal analysis, the difference arises because quite a lot of multi-jet events are triggered with
 1840 muon triggers. Once the muon trigger is vetoed the event composition changes significantly. The Fake
 1841 Lepton region, modified to fit the High MET category definition, shows that $jet \rightarrow \mu$ fake factors are
 1842 equal to 0. Also, looking at the Anti-ID region in Fig.158, we see very small discrepancy between the data
 1843 and MC which suggests that multi-jet contribution is very small. We decided to take data minus MC in
 1844 the Anti-ID as multi-jet estimate and assigned a conservative 10% uncertainty on MC. We parametrised
 1845 multi-jet fraction ($rqcd$) in lepton p_T , Fig.159, which is similar to parametrising lepton fake factors in
 1846 lepton p_T .

Not reviewed, for internal circulation only

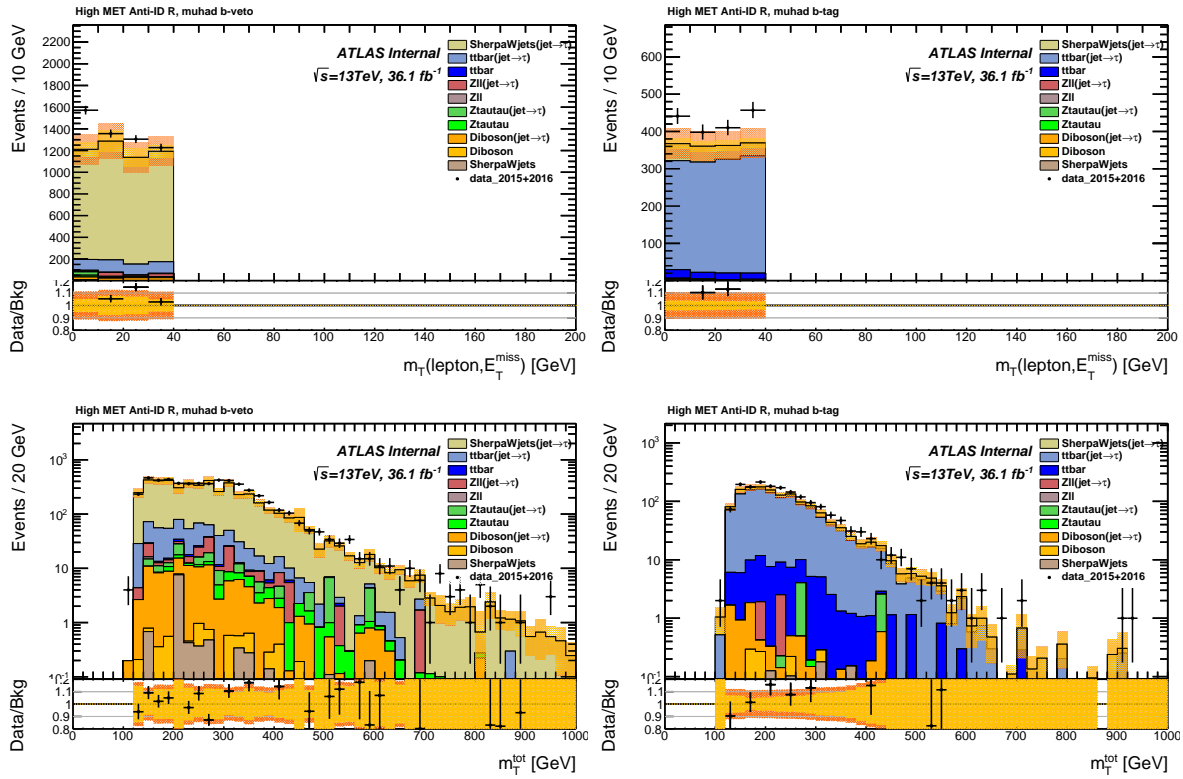


Figure 158: Distributions in the Anti-ID region.

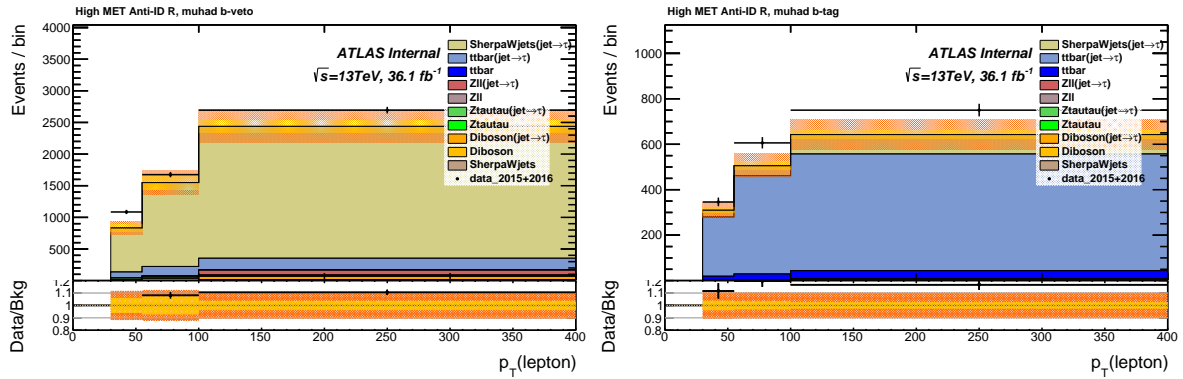


Figure 159: Muon p_T distribution in the Anti-ID region that is used to parametrise $rqcd$.

1847 Validation region

1848 High MET Validation region is modelled well, as shown in Fig.160-161. In this region multi-jet processes
1849 are negligible and, therefore, not included.

Not reviewed, for internal circulation only

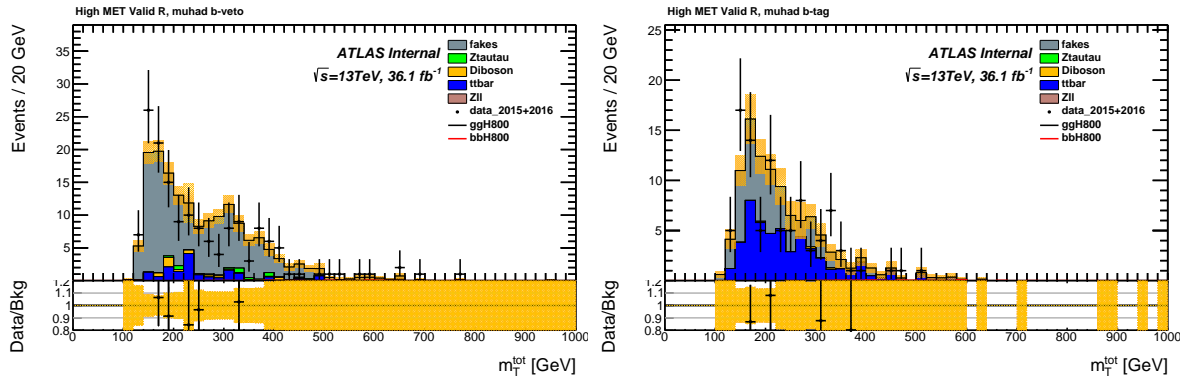


Figure 160: m_T^{tot} distributions in Validation region.

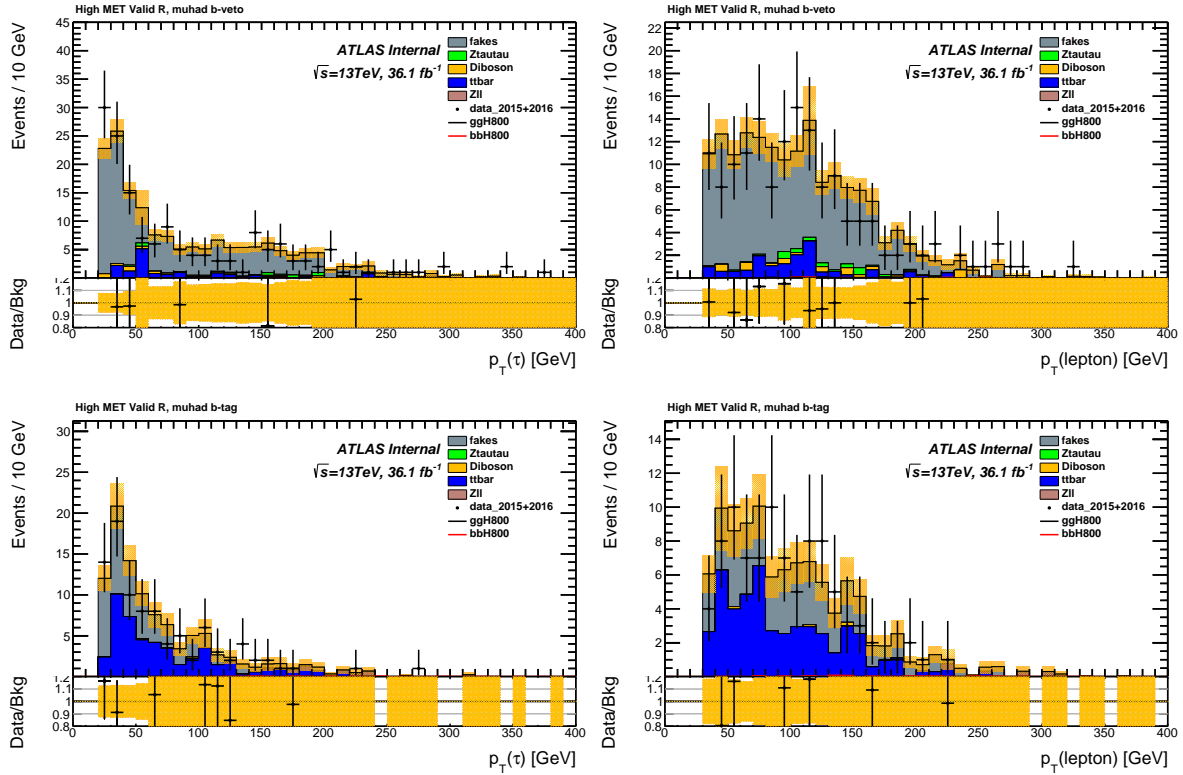


Figure 161: Distributions in Validation region.

1850 Signal Region

1851 Background yields in the High MET category are listed in Tab.28. Some distributions of this category are
 1852 shown in Fig.162. Expected 95% CL plots for High MET category only, Fig.163, and combined limits,
 1853 Fig.164, show that there is not much gain in sensitivity. This is understandable because at high transverse
 1854 mass there is very little background in all categories, but High MET category has 1/10 of signal events
 1855 compared to nominal.

Not reviewed, for internal circulation only

Table 28: Background yields in High MET category.

	$Z \rightarrow ll$	$Z \rightarrow \tau\tau$	Diboson	$t\bar{t}$ and single Top	QCD fakes	$W+jets$ and $t\bar{t}$ fakes
hmet bveto	0	56 ± 5	13 ± 3	25 ± 3	31 ± 1	255 ± 5
hmet btag	0	0.7 ± 0.3	0.7 ± 0.3	106 ± 7	10 ± 1	82 ± 3

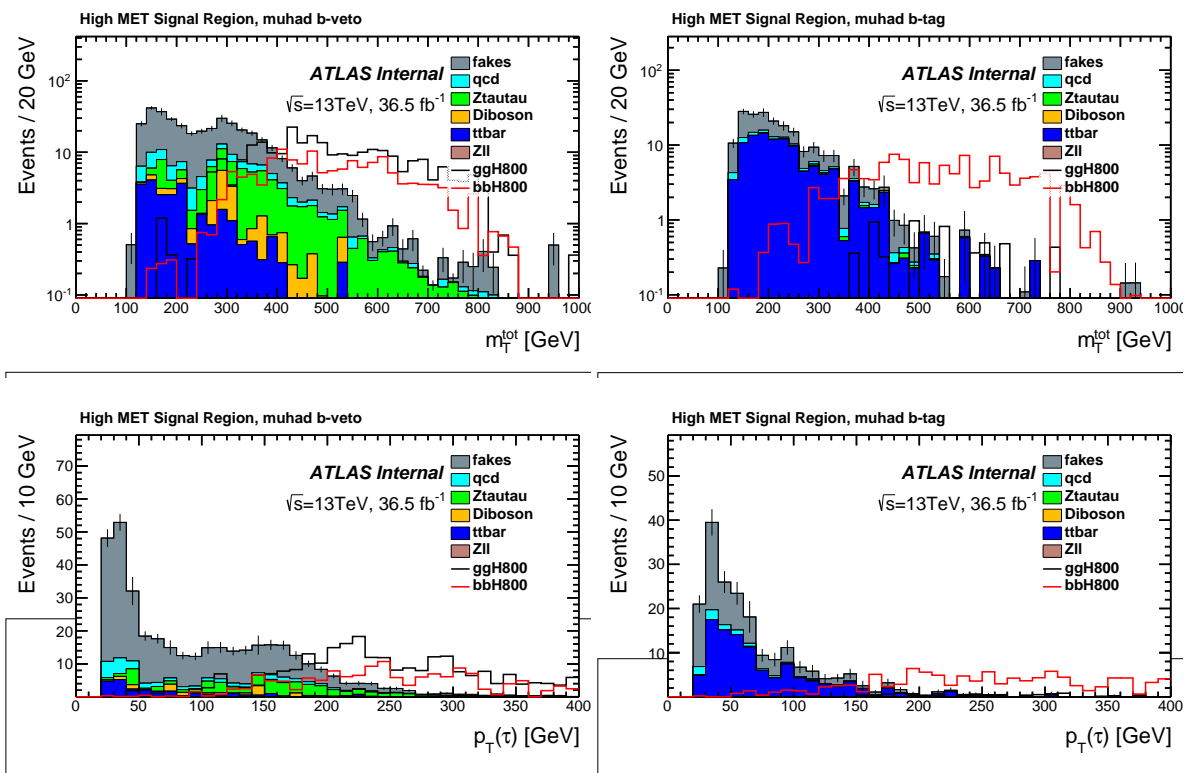


Figure 162: Distributions in Signal region, signal xsec=1pb.

Not reviewed, for internal circulation only

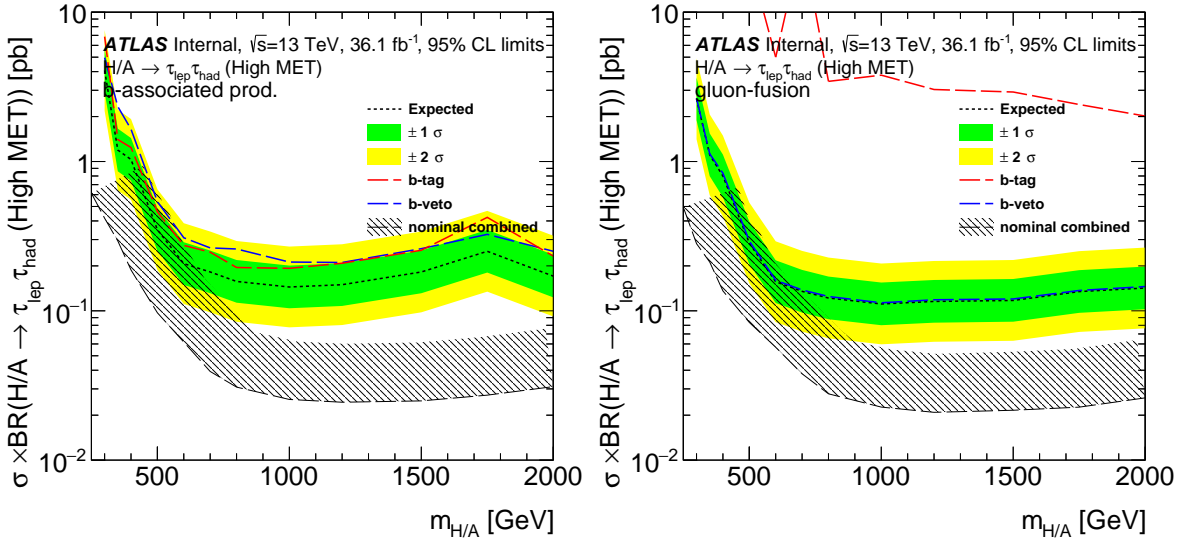


Figure 163: 95% CL limits on the cross section in High MET category compared to nominal categories.

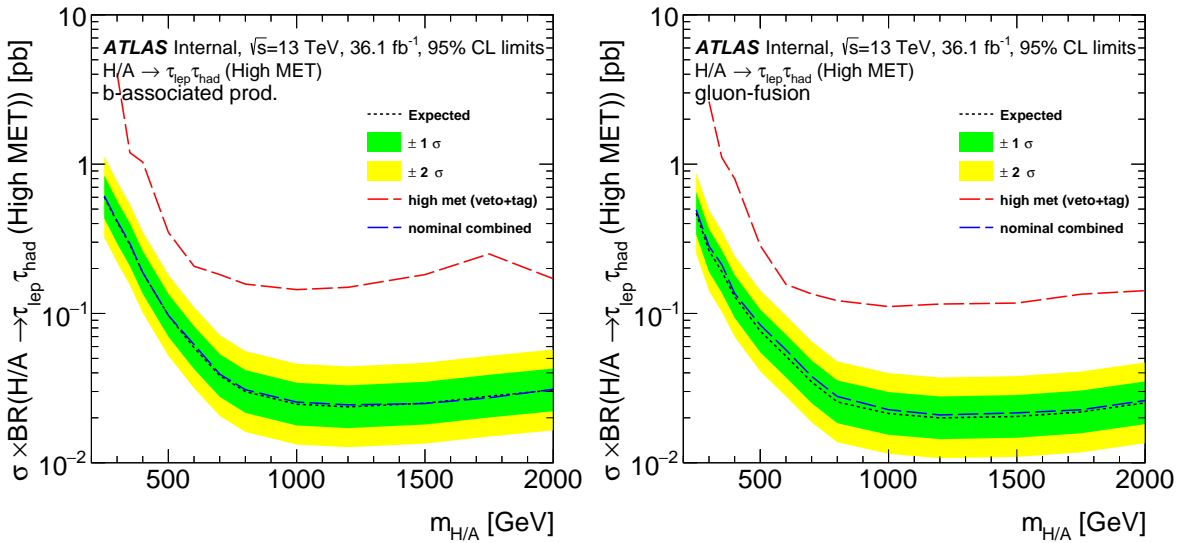


Figure 164: 95% CL limits on the cross section in all categories combined.

1856 Q. Investigation on Nbjet = 2

1857 Table 29 shows the yield of total background and each signal hypothesis for the btag category and the region
 1858 with number of bjets equal to 2, as well as muhad and ehad channels. Table 30 shows the corresponding
 1859 signal to background ratio, while Table 31 shows the corresponding signal to square root of background
 1860 ratio. It can be seen that the signal to background ratio is worse in the Nbjets= 2 region. Considering the
 1861 small fraction of Nbjets= 2 to the btag category, it is not worth to create a dedicated Nbjets= 2 region.

Table 29: The yield of the total background and each signal hypothesis with requiring Nbjets= 2 and Nbjets \geq 1 for muhad an ehad channels. The normalized luminosity corresponding to 35% of the total luminosity.

lephad	Total bkg	ggH200	bbH200	ggH600	bbH600	ggH1000	bbH1000	ggH1500	bbH1500
Muhad Nbjets=2	285 ± 6	0	4 ± 1	0 ± 0	17 ± 1	0 ± 0	20 ± 2	1 ± 0	16 ± 2
Muhad Nbjets \geq 1	1308 ± 19	1 ± 0	38 ± 3	6 ± 1	132 ± 3	9 ± 1	139 ± 5	14 ± 2	112 ± 5
Ehad Nbjets=2	246 ± 7	0	1 ± 1	0 ± 0	14 ± 1	1 ± 0	14 ± 2	1 ± 1	13 ± 2
Ehad Nbjets \geq 1	1050 ± 17	1 ± 0	22 ± 2	4 ± 1	120 ± 3	10 ± 2	119 ± 5	7 ± 1	85 ± 5

Table 30: The signal to background ratio (S/B) of each signal hypothesis with requiring Nbjets= 2 and Nbjets \geq 1 for muhad an ehad channels.

lephad	ggH200	bbH200	ggH600	bbH600	ggH1000	bbH1000	ggH1500	bbH1500
Muhad Nbjets=2	0	0.01	0	0.06	0	0.070	0.004	0.056
Muhad Nbjets \geq 1	0.0008	0.03	0.005	0.10	0.007	0.106	0.011	0.086
Ehad Nbjets=2	0	0.004	0	0.06	0.004	0.057	0.004	0.053
Ehad Nbjets \geq 1	0.0010	0.021	0.004	0.11	0.010	0.113	0.007	0.081

Table 31: The signal to square root of background ratio (S/ \sqrt{B}) of each signal hypothesis with requiring Nbjets= 2 and Nbjets \geq 1 for muhad an ehad channels.

lephad	ggH200	bbH200	ggH600	bbH600	ggH1000	bbH1000	ggH1500	bbH1500
Muhad Nbjets=2	0	0.24	0	1.0	0	1.2	0.06	0.95
Muhad Nbjets \geq 1	0.028	1.05	0.17	3.6	0.25	3.8	0.39	3.10
Ehad Nbjets=2	0	0.06	0	0.9	0.06	0.9	0.06	0.83
Ehad Nbjets \geq 1	0.031	0.68	0.12	3.7	0.31	3.7	0.21	2.62

1862 R. Useful plots and extra studies in paper

1863 The supporting note has been frozen after the unblinding approval. Some of the important studies and
 1864 plots are in the published paper but not in the supporting note. So, we document them here as a guide for
 1865 the future analysis.

1866 R.1. Background estimation

1867 The background estimation has been already documented in the supporting note in a great detail. However,
 1868 during writing the paper a clearer naming convention was invented as shown in Table 32.

Channel	Region	Selection
$\tau_{\text{lep}}\tau_{\text{had}}$	SR	ℓ (trigger, isolated), τ_1 (medium), $q(\ell) \times q(\tau_1) < 0$, $ \Delta\phi(\mathbf{p}_T^\ell, \mathbf{p}_T^{\tau_1}) > 2.4$, $m_T(\mathbf{p}_T^\ell, \mathbf{E}_T^{\text{miss}}) < 40 \text{ GeV}$, veto $80 < m(\mathbf{p}^\ell, \mathbf{p}^{\tau_1}) < 110 \text{ GeV}$ ($\tau_e\tau_{\text{had}}$ channel only)
	CR-1	Pass SR except: τ_1 (very-loose, fail medium)
	CR-2	Pass SR except: τ_1 (very-loose, fail medium), ℓ (fail isolation)
	MJ-FR	Pass SR except: τ_1 (very-loose), ℓ (fail isolation)
	W-FR	Pass SR except: $70(60) < m_T(\mathbf{p}_T^\ell, \mathbf{E}_T^{\text{miss}}) < 150 \text{ GeV}$ in $\tau_e\tau_{\text{had}}$ ($\tau_\mu\tau_{\text{had}}$) channel
	CR-T	Pass SR except: $m_T(\mathbf{p}_T^\ell, \mathbf{E}_T^{\text{miss}}) > 110(100) \text{ GeV}$ in the $\tau_e\tau_{\text{had}}$ ($\tau_\mu\tau_{\text{had}}$) channel, b -tag category only
$\tau_{\text{had}}\tau_{\text{had}}$	L-FR	ℓ (trigger, selected), jet (selected), no loose $\tau_{\text{had-vis}}$, $m_T(\mathbf{p}_T^\ell, \mathbf{E}_T^{\text{miss}}) < 30 \text{ GeV}$
	SR	τ_1 (trigger, medium), τ_2 (loose), $q(\tau_1) \times q(\tau_2) < 0$, $ \Delta\phi(\mathbf{p}_T^{\tau_1}, \mathbf{p}_T^{\tau_2}) > 2.7$
	CR-1	Pass SR except: τ_2 (fail loose)
	DJ-FR	jet trigger, $\tau_1 + \tau_2$ (no identification), $q(\tau_1) \times q(\tau_2) < 0$, $ \Delta\phi(\mathbf{p}_T^{\tau_1}, \mathbf{p}_T^{\tau_2}) > 2.7$ $p_T^{\tau_2}/p_T^{\tau_1} > 0.3$

Table 32: Definition of signal, control and fakes regions used in the analysis. The symbol ℓ represents the selected electron or muon candidate and τ_1 (τ_2) represents the leading (sub-leading) $\tau_{\text{had-vis}}$ candidate.

1869 R.1.1. Jet background estimate in the $\tau_{\text{lep}}\tau_{\text{had}}$ channel

1870 The estimation of the jet to tau fake background is quite complicated. Figure 165 is designed to describe
 1871 the procedure graphically.

Some of the equation could be useful to add in the next round supporting note. So, we also copy them here. The contribution from $W+\text{jets}$ (and $t\bar{t}$) events where the $\tau_{\text{had-vis}}$ candidate originates from a jet is estimated from events in CR-1 that remain after subtracting the multijetcontribution (estimated using the technique described below) and the real-lepton contribution (estimated using simulation). The events are weighted by the $W+\text{jetstau}$ fake-factor (f_W):

$$N_{W+\text{jets}}^{\text{SR}}(v; \mathbf{x}) = f_W(\mathbf{x}) \cdot [N_{\text{data}}^{\text{CR-1}}(v; \mathbf{x}) - N_{\text{multijet}}^{\text{CR-1}}(v; \mathbf{x}) - N_{\text{real-lepton}}^{\text{CR-1}}(v; \mathbf{x})],$$

1872 where v is the variable being modelled (e.g. m_T^{tot}) and \mathbf{x} is the set of auxiliary variables from the
 1873 f_W parameterisation: $\tau_{\text{had-vis}}p_T$, $\tau_{\text{had-vis}}$ track multiplicity and the azimuthal $\tau_{\text{had-vis}}-\mathbf{E}_T^{\text{miss}}$ separation,

Not reviewed, for internal circulation only

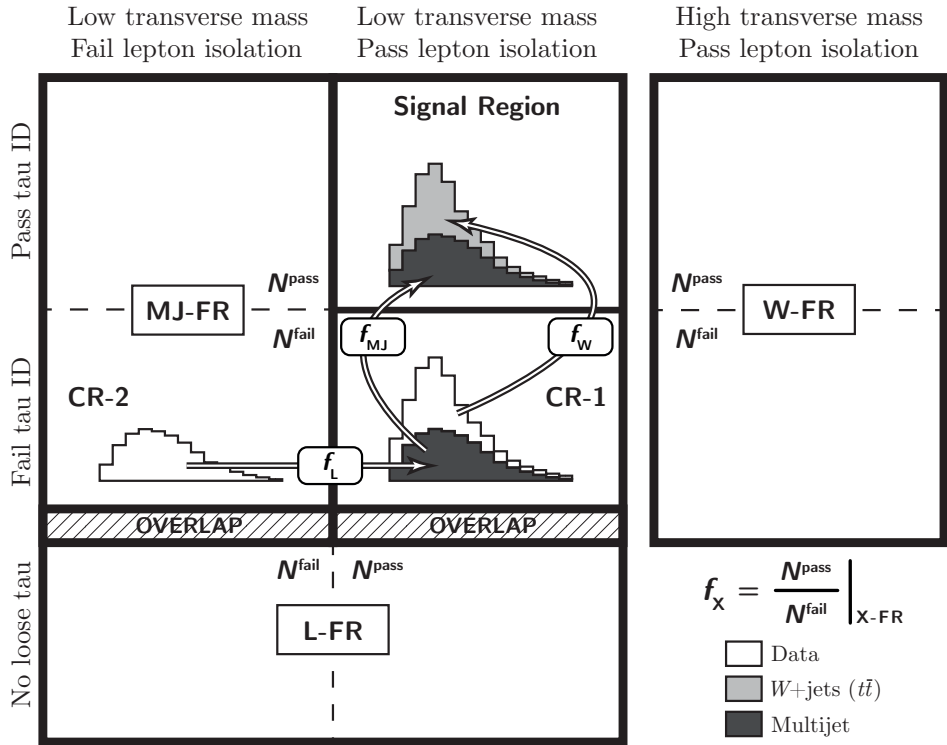


Figure 165: Schematic of the fake-factor background estimation in the $\tau_{\text{lep}}\tau_{\text{had}}$ channel. The fake-factors, f_X ($X = \text{MJ}, \text{W}, \text{L}$), are defined as the ratio of events in data that pass/fail the specified selection requirements, measured in the fakes-regions: MJ-FR, W-FR and L-FR, respectively. The multijetcontribution is estimated by weighting events in CR-2 by the product of f_L and f_{MJ} . The contribution from $W+\text{jets}$ and $t\bar{t}$ events where the $\tau_{\text{had-vis}}$ candidate originates from a jet is estimated by subtracting the multijetcontribution from CR-1 and then weighting by f_W . There is a small overlap of events between L-FR and the CR-1 and CR-2 regions. The contribution where both the selected $\tau_{\text{had-vis}}$ and lepton originate from leptons is estimated using simulation (not shown here).

¹⁸⁷⁴ $|\Delta\phi(\mathbf{p}_T^{\tau_{\text{had-vis}}}, \mathbf{E}_T^{\text{miss}})|$. The fake-factor f_W is measured in the $W+\text{jets}$ fakes-region (W-FR) defined in
¹⁸⁷⁵ Table 32.

The multijetcontributions in both CR-1 ($N_{\text{multijet}}^{\text{CR-1}}$) and SR ($N_{\text{multijet}}^{\text{SR}}$) are estimated from events where the $\tau_{\text{had-vis}}$ fails identification and the selected lepton fails isolation (CR-2). The non-multijetbackground is subtracted using simulation and the events are weighted first by the lepton-isolation fake-factor (f_L), yielding $N_{\text{multijet}}^{\text{CR-1}}$, and then by the multijettau fake-factor (f_{MJ}):

$$N_{\text{multijet}}^{\text{SR}}(v; \mathbf{x}, \eta^\ell) = f_{\text{MJ}}(\mathbf{x}) \cdot N_{\text{multijet}}^{\text{CR-1}}(v; \mathbf{x}, \eta^\ell),$$

$$N_{\text{multijet}}^{\text{CR-1}}(v; \mathbf{x}, \eta^\ell) = f_L(\eta^\ell) \cdot [N_{\text{data}}^{\text{CR-2}}(v; \mathbf{x}, \eta^\ell) - N_{\text{non-MJ}}^{\text{CR-2}}(v; \mathbf{x}, \eta^\ell)],$$

¹⁸⁷⁶ where η^ℓ is the pseudorapidity of the isolated lepton, which is used to parameterise f_L . The fake-factor
¹⁸⁷⁷ f_{MJ} is measured in the multijetfakes-region (MJ-FR) defined in Table 32 and the fake-factor f_L is measured
¹⁸⁷⁸ in the lepton fakes-region (L-FR) defined in Table 32.

¹⁸⁷⁹ The measured lephad fake factors are shown in Figure 166.

Not reviewed, for internal circulation only

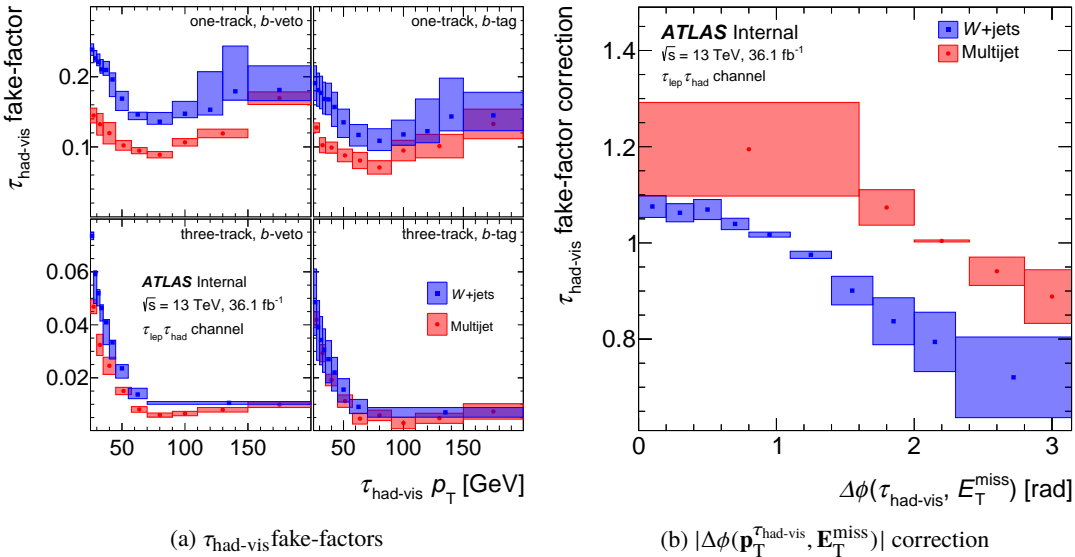


Figure 166: $\tau_{\text{had-vis}}$ identification fake-factors and the sequential $|\Delta\phi(\mathbf{p}_T^{\tau_{\text{had-vis}}}, \mathbf{E}_T^{\text{miss}})|$ correction in the $\tau_{\text{lep}}\tau_{\text{had}}$ channel. The multijet fake-factors are for the 2016 dataset only. The bands include all uncertainties.

1880 R.1.2. Jet background estimate in the $\tau_{\text{had}}\tau_{\text{had}}$ channel

1881 The fake-factor technique used to estimate the dominant multijet background in the $\tau_{\text{had}}\tau_{\text{had}}$ channel is
 1882 described in Section ???. The method used to weight simulated events to estimate the remaining background
 1883 containing events with $\tau_{\text{had-vis}}$ candidates that originate from jets is described in Table 32.

The contribution of multijet events in SR is estimated by weighting events in a control region that has the same selection as SR, but where the sub-leading $\tau_{\text{had-vis}}$ candidate fails identification (CR-1), by the dijet tau fake-factor (f_{DJ}), which is measured in the dijet fakes-region (DJ-FR):

$$N_{\text{multijet}}^{\text{SR}}(v; \mathbf{y}) = f_{\text{DJ}}(\mathbf{y}) \cdot [N_{\text{data}}^{\text{CR-1}}(v; \mathbf{y}) - N_{\text{non-MJ}}^{\text{CR-1}}(v; \mathbf{y})],$$

1884 where \mathbf{y} is the set of auxiliary variables from the f_{DJ} parameterisation: sub-leading $\tau_{\text{had-vis}} p_T$ and sub-
 1885 leading $\tau_{\text{had-vis}}$ track multiplicity. Unlike in the $\tau_{\text{lep}}\tau_{\text{had}}$ channel, CR-1 is completely dominated by mul-
 1886 tijet events, so a single fake-factor is sufficient. The non-multijet contamination in CR-1, $N_{\text{non-MJ}}^{\text{CR-1}}$, amounts
 1887 to $\sim 1.6\%$ ($\sim 7.0\%$) in the b -veto (b -tag) channel, and is subtracted using simulation.

1888 The fake-factors are shown in Figure 167.

1889 R.2. Results

1890 The number of observed events in the signal regions of the $\tau_{\text{lep}}\tau_{\text{had}}$ and $\tau_{\text{had}}\tau_{\text{had}}$ channels together with
 1891 the predicted event yields from signal and background processes are shown in Table 33. The numbers are
 1892 given before (pre-fit) and after (post-fit) applying the statistical fitting procedure described in Section ???.
 1893 The observed event yields are compatible with the expected event yields from SM processes, within
 1894 uncertainties. (NOTE by editors: Technically, the post-fit number are got from the full systematics

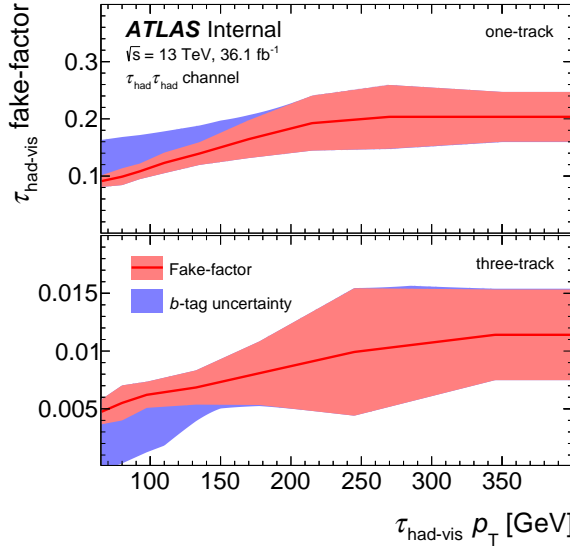


Figure 167: $\tau_{\text{had-vis}}$ identification fake-factors in the $\tau_{\text{had}} \tau_{\text{had}}$ channel. The red band indicates the total category inclusive uncertainty and the blue band indicates the additional uncertainty in the b -tag category.

1895 workspace after loading the final combined fit results, while the pre-fit numbers are got without loading
 1896 any fit results.) The m_T^{tot} distributions in the signal regions are shown in Figures 168(a)–168(d) and in the
 1897 CR-T in Figure 169.

1898 Figures 168 and 169 are the distributions used in the final fit. We decide to show the significance in the
 1899 lower panel. Those with usual ratio panel are also shown in the auxiliary materials after asked during the
 1900 circulation.

1901 R.2.1. Cross-section limits

1902 The limits are set using the standard ATLAS frequentist CL_s method as shown in Figures 170(a)–170(c).

1903 A small downward fluctuation at a mass of $\sim 0.3 \text{ TeV}$ is observed in all limits, while a small upward
 1904 fluctuation for gluon–gluon fusion and Z' bosons is seen around 0.5 TeV and a broad deficit is seen for
 1905 the b -quark associated production over the entire mass range. These features arise primarily because
 1906 of a deficit of events in the range 200 – 250 GeV followed by a mild excess in the range 300 – 400 GeV in
 1907 Figure 168(c), and by a consistent deficit of events across the whole range in Figure 168(d). Modifications
 1908 of the Z' chiral coupling structure can result in changes of up to 40% in the Z' cross-section limits.
 1909 Reducing the Z' width can improve the limits by up to $\sim 30\%$, while increasing the width to 36% can
 1910 degrade the limits by up to $\sim 70\%$. Figures 171(a) and 171(b) show the observed and expected 95% CL
 1911 upper limits on the production cross section times branching fraction for $\phi \rightarrow \tau\tau$ as a function of the ratio
 1912 of the gluon–gluon fusion to b -associated production strengths and the scalar boson mass.

1913 The impact of systematic uncertainties on the model-independent $\phi \rightarrow \tau\tau$ upper limits are calculated by
 1914 comparing the expected 95% CL upper limit in the case of no systematic uncertainties, μ_{stat}^{95} , with a limit
 1915 calculated by introducing a group of systematic uncertainties, μ_i^{95} . The systematic uncertainty impacts are
 1916 shown in Figure 172(a) for gluon–gluon fusion production and Figure 172(b) for b -associated production

Not reviewed, for internal circulation only

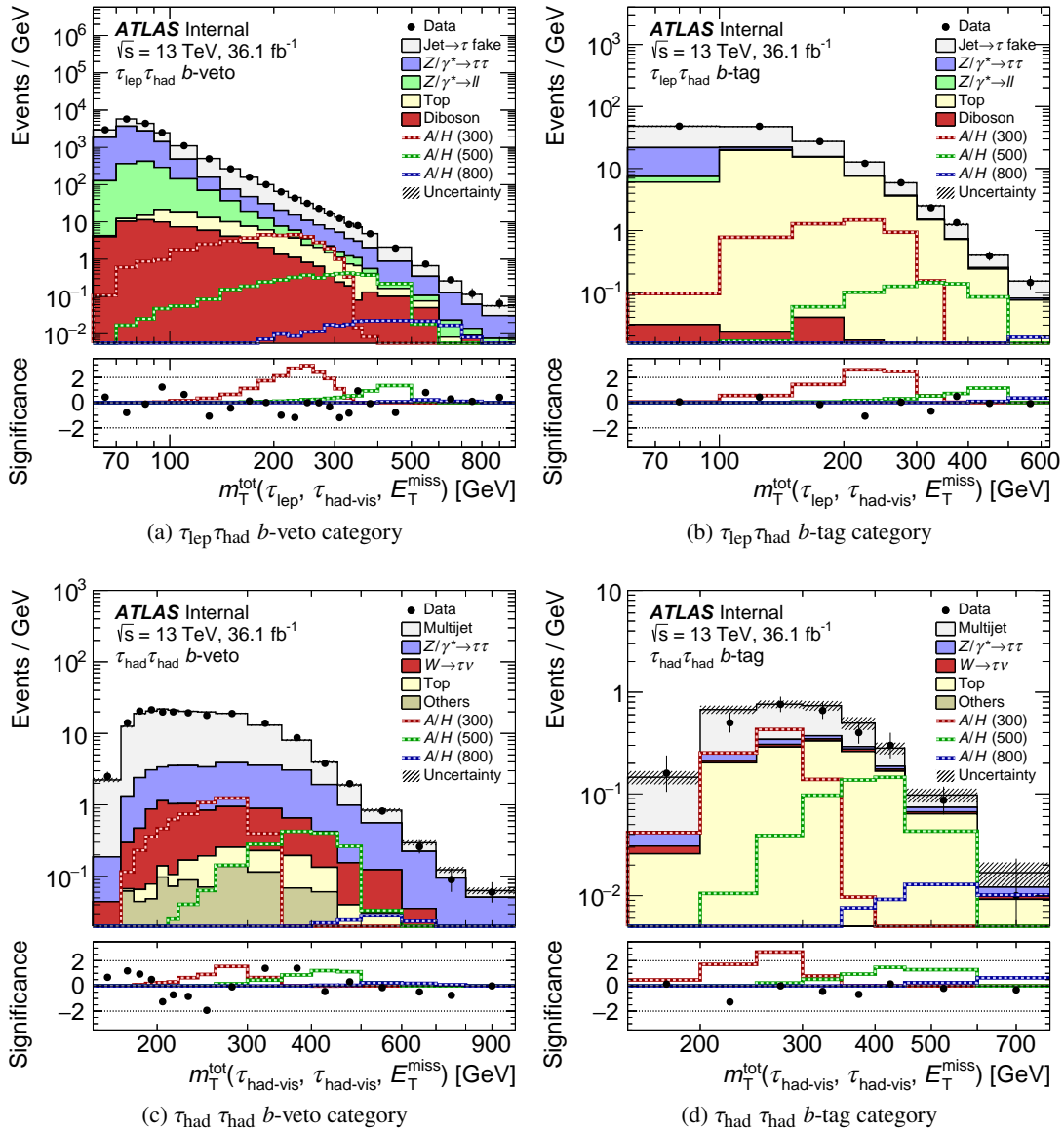


Figure 168: Distributions of m_T^{tot} for the (a) b -veto and (b) b -tag, categories of the $\tau_{\text{lep}}\tau_{\text{had}}$ channel and the (c) b -veto and (d) b -tag categories of the $\tau_{\text{had}}\tau_{\text{had}}$ channel. The label “Others” refers to contributions from diboson, $Z/\gamma^*(\rightarrow \ell\ell)$ +jets and $W(\rightarrow \ell\nu)$ +jets production. In the $\tau_{\text{lep}}\tau_{\text{had}}$ channel, events containing $\tau_{\text{had-vis}}$ candidates that originate from jets are removed from all processes other than Jet $\rightarrow \tau$ fake. The binning displayed is that entering into the statistical fit discussed in Section R.2, with minor modifications needed to combine the $\tau_{\text{lep}}\tau_{\text{had}}$ channels and with underflows and overflows included in the first and last bins, respectively. The predictions and uncertainties for the background processes are obtained from the fit under the hypothesis of no signal. The combined prediction for A and H bosons with masses of 300, 500 and 800 GeV and $\tan\beta = 10$ in the hMSSM scenario are superimposed. The significance of the data given the fitted model and its uncertainty is computed in each bin following Ref. [Diego:sig] and is shown in the lower panels. The expected significance of the hypothetical Higgs boson signals are also overlaid.

Not reviewed, for internal circulation only

Channel	Process	<i>b</i> -veto		<i>b</i> -tag	
		pre-fit	post-fit	pre-fit	post-fit
$\tau_{\text{lep}} \tau_{\text{had}}$	$Z/\gamma^* \rightarrow \tau\tau$	$92\,000 \pm 11\,000$	$96\,400 \pm 1\,600$	670 ± 140	690 ± 70
	Diboson	880 ± 100	920 ± 70	6.3 ± 1.7	6.5 ± 1.4
	$t\bar{t}$ and single top-quark	$1\,050 \pm 170$	$1\,090 \pm 130$	$2\,800 \pm 400$	$2\,680 \pm 80$
	Jet $\rightarrow \tau$ fake	$83\,000 \pm 5\,000$	$88\,800 \pm 1\,700$	$3\,000 \pm 400$	$3\,390 \pm 170$
	$Z/\gamma^* \rightarrow ll$	$15\,800 \pm 1\,200$	$16\,200 \pm 700$	86 ± 21	89 ± 16
	SM Total	$193\,000 \pm 13\,000$	$203\,400 \pm 1\,200$	$6\,500 \pm 600$	$6\,850 \pm 120$
$\tau_{\text{had}} \tau_{\text{had}}$	Data	$203\,365$		$6\,843$	
	A/H (300)	720 ± 80	–	236 ± 32	–
	A/H (500)	112 ± 11	–	39 ± 5	–
	A/H (800)	10.7 ± 1.1	–	4.8 ± 0.6	–
	Multijet	$3\,040 \pm 240$	$3\,040 \pm 90$	106 ± 32	85 ± 10
	$Z/\gamma^* \rightarrow \tau\tau$	610 ± 230	770 ± 80	7.5 ± 2.9	8.6 ± 1.3
$\tau_{\text{had}} \tau_{\text{had}}$	$W(\rightarrow \tau\nu) + \text{jets}$	178 ± 31	182 ± 15	4.0 ± 1.0	4.1 ± 0.5
	$t\bar{t}$ and single top-quark	26 ± 9	29 ± 4	60 ± 50	74 ± 15
	Others	25 ± 6	27.4 ± 2.1	1.0 ± 0.5	1.1 ± 0.4
	SM Total	$3\,900 \pm 400$	$4\,050 \pm 70$	180 ± 60	173 ± 16
	Data	$4\,059$		154	
	A/H (300)	130 ± 50	–	44 ± 19	–
$\tau_{\text{had}} \tau_{\text{had}}$	A/H (500)	80 ± 33	–	28 ± 12	–
	A/H (800)	11 ± 4	–	5.1 ± 2.2	–

Table 33: Observed number of events and predictions of signal and background contributions in the *b*-veto and *b*-tag categories of the $\tau_{\text{lep}} \tau_{\text{had}}$ and $\tau_{\text{had}} \tau_{\text{had}}$ channels. The background predictions and uncertainties (including both the statistical and systematic components) are obtained before (pre-fit) and after (post-fit) applying the statistical fitting procedure discussed in Section R.2. The individual uncertainties are correlated, and do not necessarily add in quadrature to the total background uncertainty. The label “Others” refers to contributions from diboson, $Z/\gamma^*(\rightarrow \ell\ell) + \text{jets}$ and $W(\rightarrow \ell\nu) + \text{jets}$ production. In the $\tau_{\text{lep}} \tau_{\text{had}}$ channel, events containing a $\tau_{\text{had-vis}}$ candidate that originate from jets are removed from all processes other than Jet $\rightarrow \tau$ fake. The expected pre-fit contributions from A and H bosons with masses of 300, 500 and 800 GeV and $\tan\beta = 10$ in the hMSSM scenario are also shown.

as functions of the scalar boson mass. The major uncertainties are grouped according to their origin, while minor uncertainties are collected as “Others”.

In the low mass range, the sensitivity is dominated by the $\tau_{\text{lep}} \tau_{\text{had}}$ channel, and the major uncertainties arise from the estimate of the dominant $W + \text{jets}$ background. Due to the large contribution the fit is able to significantly constrain the uncertainties in this background. In the intermediate mass range the tau energy scale uncertainty becomes dominant. The fit is able to effectively constrain this conservative uncertainty due to the large contribution from $Z/\gamma^* \rightarrow \tau\tau$ and $t\bar{t}$ in each of the categories. At very high masses, the uncertainty in the identification efficiency for high- p_T $\tau_{\text{had-vis}}$ candidates becomes dominant, and due to the lack of significant $Z/\gamma^* \rightarrow \tau\tau$ and $t\bar{t}$ at high mass, this uncertainty remains relatively unconstrained. The addition of the CR-T region distributions to the fit allows the uncertainties in the $t\bar{t}$ modelling to be well constrained and as such, they have little impact on the sensitivity.

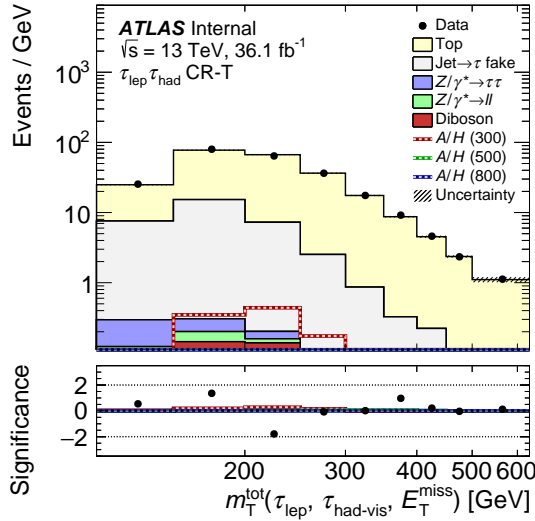


Figure 169: Distribution of m_T^{tot} in the $t\bar{t}$ -enriched control region (CR-T) of the $\tau_{\text{lep}}\tau_{\text{had}}$ channel. Events containing $\tau_{\text{had-vis}}$ candidates that originate from jets are removed from all processes other than $\text{Jet} \rightarrow \tau$ fake. The binning displayed is that entering into the statistical fit discussed in Section R.2, with minor modifications needed to combine the $\tau_{\text{lep}}\tau_{\text{had}}$ channels and with underflows and overflows included in the first and last bins, respectively. The predictions and uncertainties for the background processes are obtained from the fit under the hypothesis of no signal. The combined prediction for A and H bosons with masses of 300, 500 and 800 GeV and $\tan\beta = 10$ in the hMSSM scenario are superimposed. The significance of the data given the fitted model and its uncertainty is computed in each bin following Ref. [Diego:sig] and is shown in the lower panel. The expected significance of the hypothetical Higgs boson signals are also overlaid.

1928 R.2.2. MSSM interpretation

1929 The data are interpreted in terms of the MSSM. Figure 173 shows regions in the m_A – $\tan\beta$ plane excluded
 1930 at 95% CL in the $m_h^{\text{mod+}}$ and hMSSM scenarios. Constraints in the hMSSM scenario are stronger than
 1931 those in the $m_h^{\text{mod+}}$ scenario due to the presence of low-mass neutralinos in the $m_h^{\text{mod+}}$ scenario that reduce
 1932 the $H/A \rightarrow \tau\tau$ branching fraction and which are absent in the hMSSM scenario. In the hMSSM scenario,
 1933 the most stringent observed (expected) constraints on $\tan\beta$ for the combined search exclude $\tan\beta > 1.0$
 1934 (5.5) for $m_A = 0.25$ TeV and $\tan\beta > 42$ (48) for $m_A = 1.5$ TeV at 95% CL. The expected exclusion limit
 1935 and bands around $m_A = 350$ GeV reflect the behaviour of the $A \rightarrow \tau\tau$ branching fraction close to the
 1936 $A \rightarrow t\bar{t}$ kinematic threshold for low $\tan\beta$, allowing for some exclusion in this region. However, when
 1937 m_A is above the $A \rightarrow t\bar{t}$ production threshold, this additional decay mode reduces the sensitivity of the
 1938 $A \rightarrow \tau\tau$ search for low $\tan\beta$. In the MSSM $m_h^{\text{mod+}}$ scenario, the observed (expected) 95% CL upper
 1939 limits exclude $\tan\beta > 5.1$ (7.0) for $m_A = 0.25$ TeV and $\tan\beta > 51$ (57) for $m_A = 1.5$ TeV.

1940 R.2.3. Z' interpretations

1941 The data are also interpreted in terms of Z' models. As shown in Figure 170(c), the observed (expected)
 1942 lower limit on the mass of a Z'_{SSM} boson is 2.42 (2.47) TeV at 95% CL. Limits at 95% CL are also placed on
 1943 Z'_{SFM} bosons as a function of $m_{Z'}$ and the mixing angle between the heavy and light SU(2) gauge groups,

Not reviewed, for internal circulation only

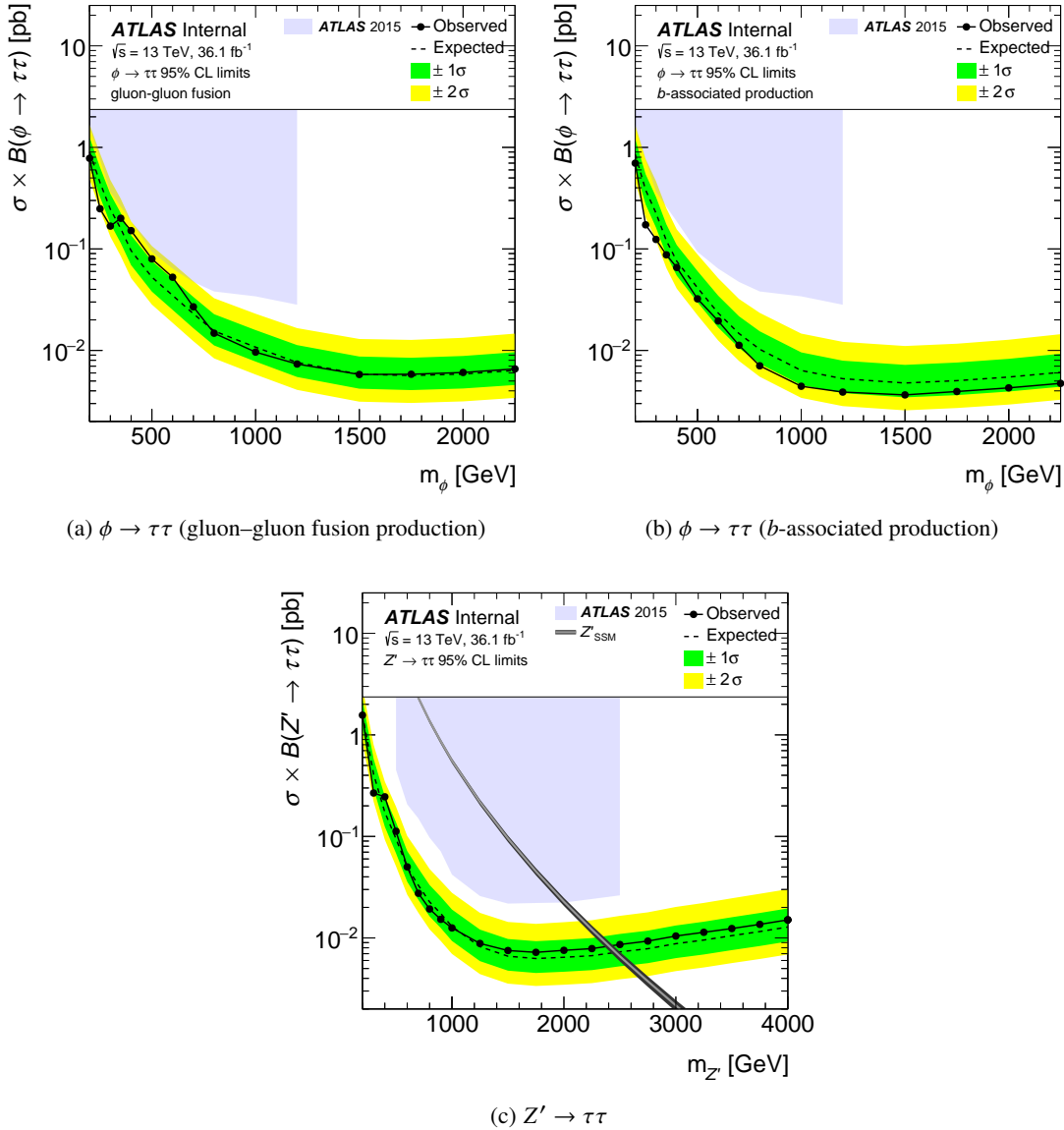


Figure 170: The observed and expected 95% CL upper limits on the production cross section times branching fraction for a scalar boson produced via (a) gluon–gluon fusion and (b) b -associated production, and for (c) gauge bosons. The limits are calculated from a statistical combination of the $\tau_{\text{lep}}\tau_{\text{had}}$ and $\tau_{\text{had}}\tau_{\text{had}}$ channels. The excluded regions from the 2015 ATLAS search [HIGG-2015-08] are depicted by the solid blue fill. The predicted cross section for a Z'_{SSM} boson is overlaid in (c), where the band depicts the total uncertainty.

Not reviewed, for internal circulation only

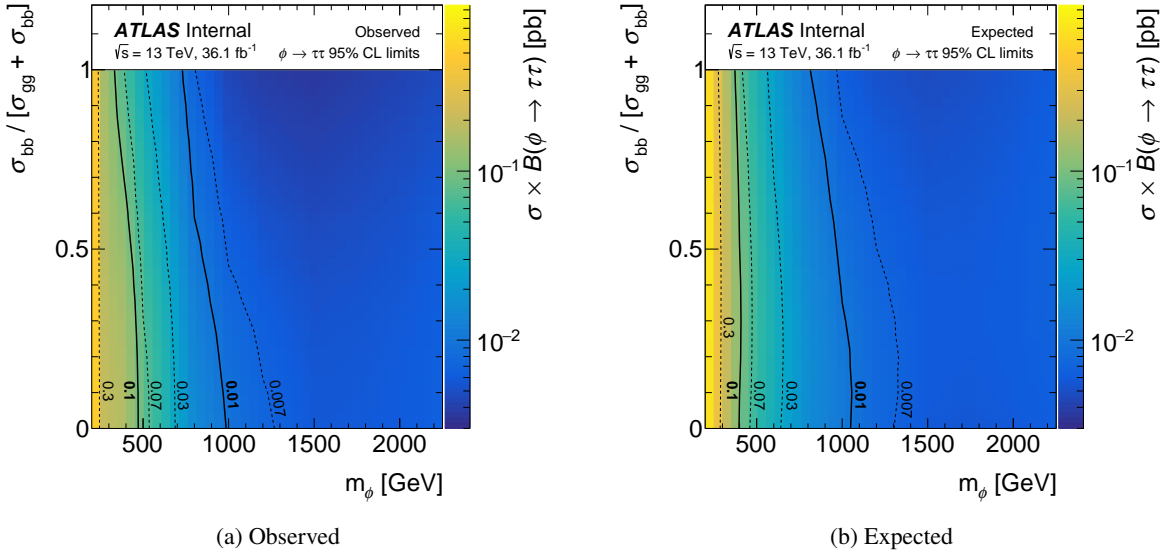


Figure 171: The (a) observed and (b) expected 95% CL upper limit on the production cross section times branching fraction for $\phi \rightarrow \tau\tau$ as a function of the ratio of the gluon–gluon fusion to b -associated production strengths and the scalar boson mass. The contours are overlaid.

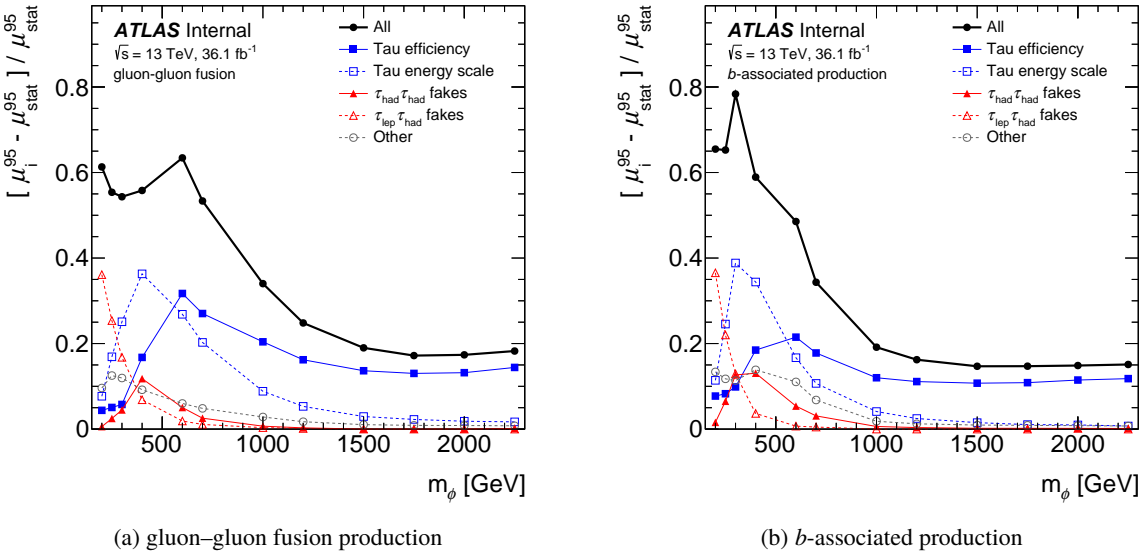


Figure 172: Impact of major groups of systematic uncertainties on the model-independent $\phi \rightarrow \tau\tau$ 95% CL upper limits on the cross section as a function of the scalar boson mass, separately for the (a) gluon–gluon fusion and (b) b -associated production mechanisms.

Not reviewed, for internal circulation only

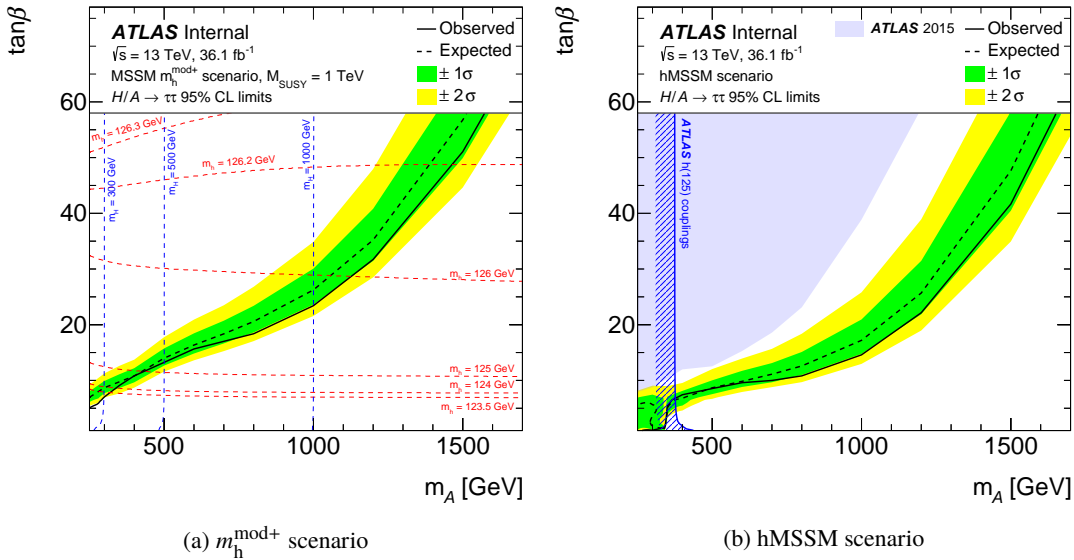


Figure 173: The observed and expected 95% CL limits on $\tan\beta$ as a function of m_A in the MSSM (a) $m_h^{\text{mod}+}$ and (b) hMSSM scenarios. For the $m_h^{\text{mod}+}$ scenario, dashed lines of constant m_h and m_H are shown in red and blue, respectively. For the hMSSM scenario, the exclusion arising from the SM Higgs boson coupling measurements of Ref. [Aad:2015pla] and the exclusion limit from the ATLAS 2015 $H/A \rightarrow \tau\tau$ search result of Ref. [HIGG-2015-08] are shown.

1944 ϕ , as shown in Figure 174. Masses below 2.25–2.60 TeV are excluded in the range $0.03 < \sin^2 \phi < 0.5$
 1945 assuming no μ - τ mixing.

1946 R.3. Auxillary plots in paper

1947 Figures 175 and ?? are with the data to predicted backgroundratio on the bottom since they are requested
 1948 during the ATLAS circulation.

1949 Figures 177 and ?? show the b-tagging inclusive distribution used in the Z' limit calculation. Figures
 1950 ?? and ?? show the p_T of the Higgs decay products in the lephad and hadhad channels, respectively.

1951 In order to make the re-interpretation of our data easier, the signal selection acceptance and the full
 1952 likelihood scan are provided in public. Figures 185 and 186 show the signal selection acceptance for
 1953 Higgs analysis and Z' analysis, respectively. Figures 187 to 189 show the negative log likelihood scan for
 1954 each 3D (ggH-bbH-mass) point. Technically, the scan is performed by fix the ggH and bbH cross section
 1955 for a give mass point, then retrieve the likelihood after fitting the full systematics model to data.

Not reviewed, for internal circulation only

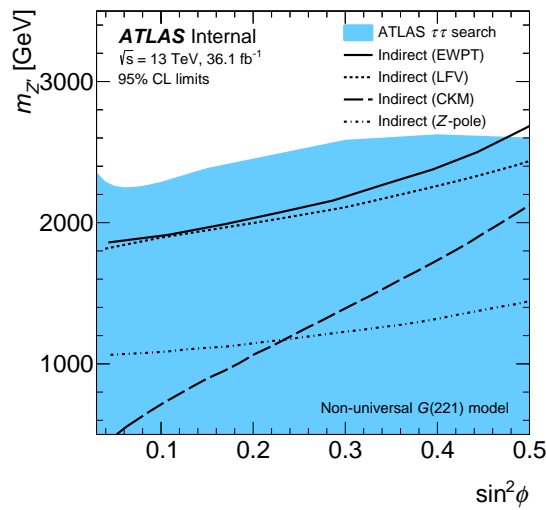


Figure 174: The 95% CL exclusion in the non-universal $G(221)$ parameter space overlaid with indirect limits at 95% CL from fits to electroweak precision measurements [100], lepton flavour violation [101], CKM unitarity [102] and Z-pole measurements [44].

Not reviewed, for internal circulation only

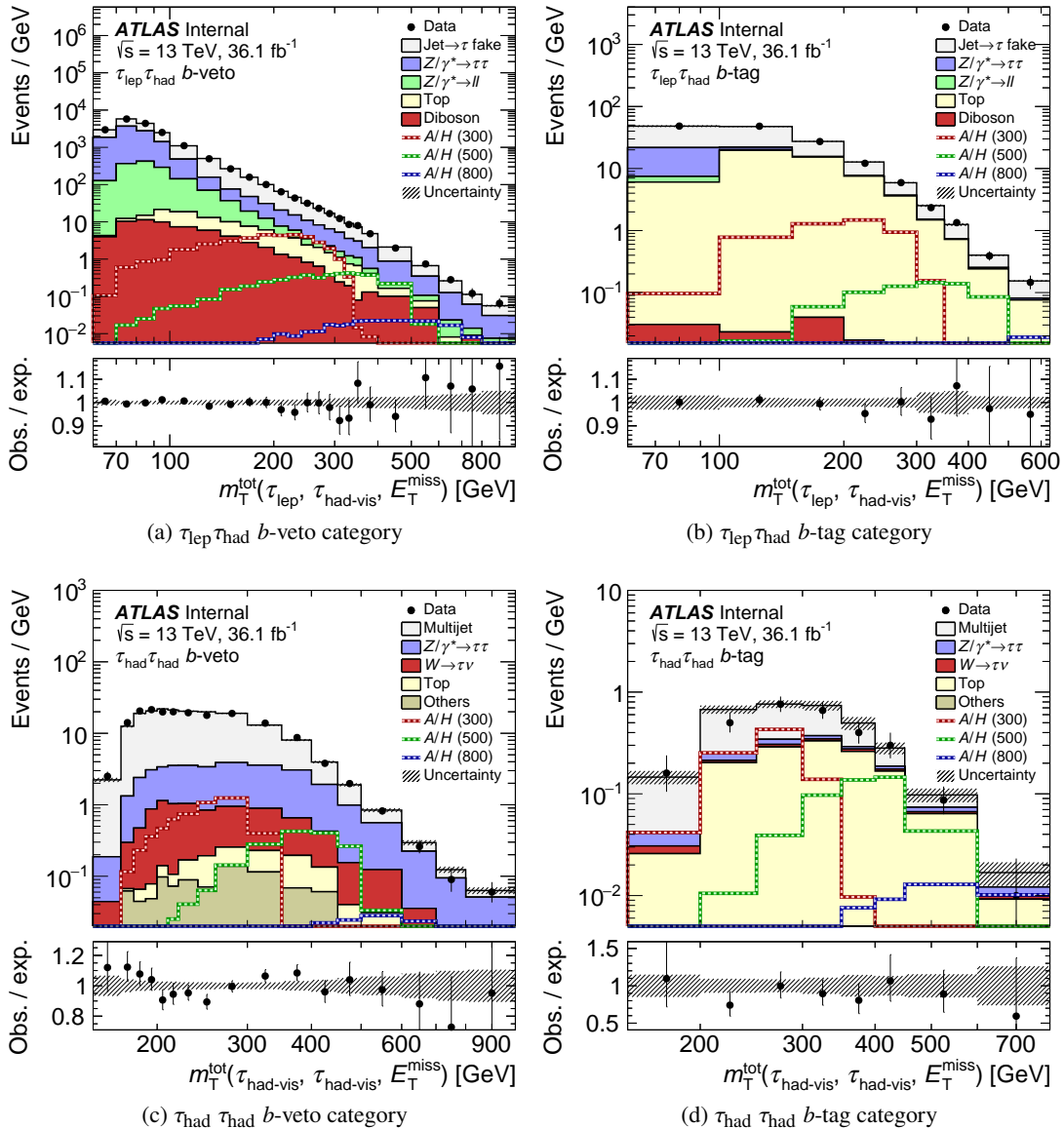


Figure 175: Distributions of m_T^{tot} for the (a) b -veto and (b) b -tag, categories of the $\tau_{\text{lep}}\tau_{\text{had}}$ channel and the (c) b -veto and (d) b -tag categories of the $\tau_{\text{had}}\tau_{\text{had}}$ channel. The label “Others” refers to contributions from diboson, $Z/\gamma^*(\rightarrow \ell\ell)$ +jets and $W(\rightarrow \ell\nu)$ +jets production. In the $\tau_{\text{lep}}\tau_{\text{had}}$ channel, events containing $\tau_{\text{had-vis}}$ candidates that originate from jets are removed from all processes other than $\text{Jet} \rightarrow \tau$ fake. The binning displayed is that entering into the statistical fit discussed in Section R.2, with minor modifications needed to combine the $\tau_{\text{lep}}\tau_{\text{had}}$ channels and with underflows and overflows included in the first and last bins, respectively. The predictions and uncertainties for the background processes are obtained from the fit under the hypothesis of no signal. The combined prediction for A and H bosons with masses of 300, 500 and 800 GeV and $\tan \beta = 10$ in the hMSSM scenario are superimposed. The ratio of the data to the fitted model is shown in the lower panels.

Not reviewed, for internal circulation only

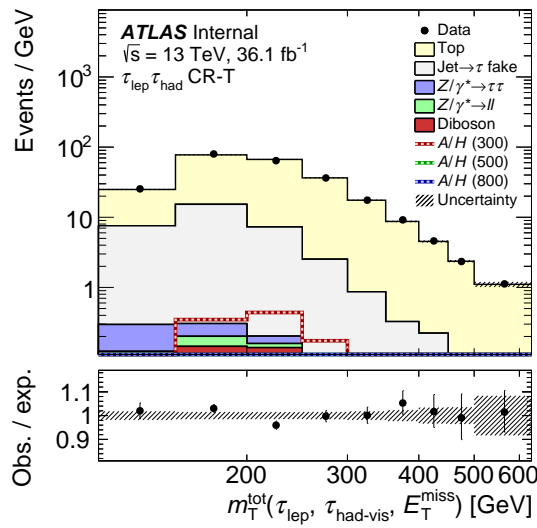


Figure 176: Distribution of m_T^{tot} in the $t\bar{t}$ -enriched control region (CR-T) of the $\tau_{\text{lep}}\tau_{\text{had}}$ channel. Events containing $\tau_{\text{had-vis}}$ candidates that originate from jets are removed from all processes other than $\text{Jet} \rightarrow \tau$ fake. The binning displayed is that entering into the statistical fit discussed in Section R.2, with minor modifications needed to combine the $\tau_{\text{lep}}\tau_{\text{had}}$ channels and with underflows and overflows included in the first and last bins, respectively. The predictions and uncertainties for the background processes are obtained from the fit under the hypothesis of no signal. The combined prediction for A and H bosons with masses of 300, 500 and 800 GeV and $\tan\beta = 10$ in the hMSSM scenario are superimposed. The ratio of the data to the fitted model is shown in the lower panel.

Not reviewed, for internal circulation only

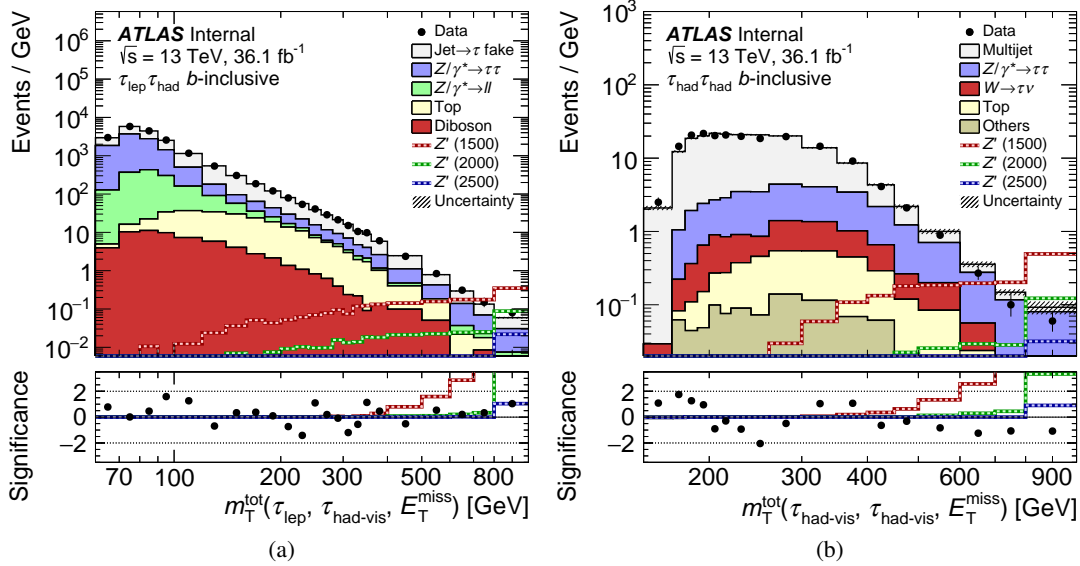


Figure 177: Distributions of m_T^{tot} for the b -inclusive selection in the (a) $\tau_{\text{lep}} \tau_{\text{had}}$ and (b) $\tau_{\text{had}} \tau_{\text{had}}$ channels. The label “Others” refers to contributions from diboson, $Z/\gamma^*(\rightarrow \ell\ell)$ +jets and $W(\rightarrow \ell\nu)$ +jets production. In the $\tau_{\text{lep}} \tau_{\text{had}}$ channel, events containing $\tau_{\text{had-vis}}$ candidates that originate from jets are removed from all processes other than Jet $\rightarrow \tau$ fake. The binning displayed is that entering into the statistical fit discussed in Section R.2, with minor modifications needed to combine the $\tau_{\text{lep}} \tau_{\text{had}}$ channels and with underflows and overflows included in the first and last bins, respectively. The predictions and uncertainties for the background processes are obtained from the fit under the hypothesis of no signal. The expectation from Z'_SSM with masses of 1500, 2000, and 2500 GeV are superimposed. The significance of the data given the fitted model and its uncertainty is computed in each bin following Ref. [Diego:sig] and is shown in the lower panels. The expected significance of the hypothetical Z' signals are also overlaid.

Not reviewed, for internal circulation only

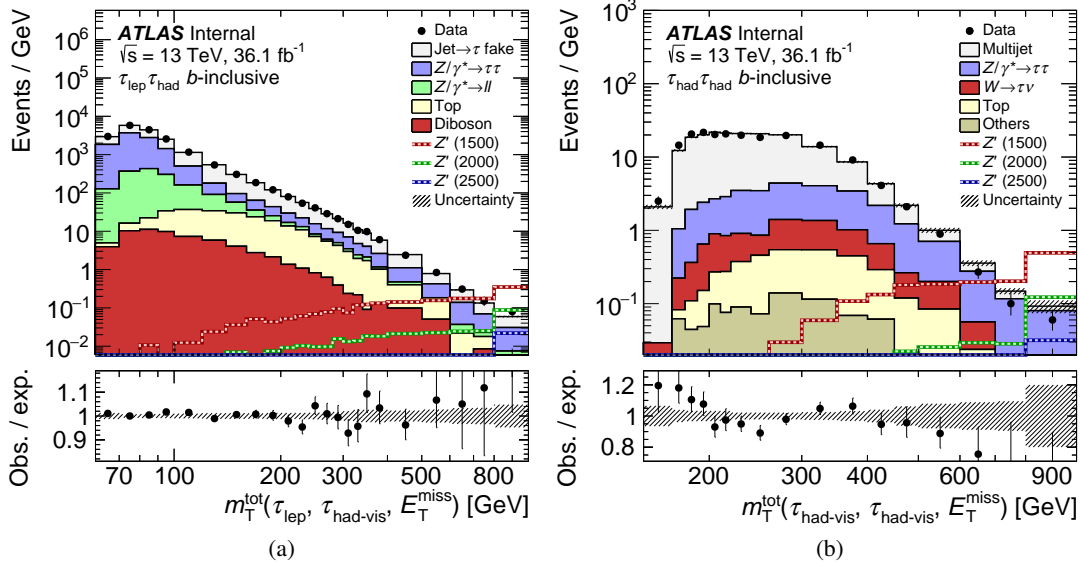


Figure 178: Distributions of m_T^{tot} for the b -inclusive selection in the (a) $\tau_{\text{lep}} \tau_{\text{had}}$ and (b) $\tau_{\text{had}} \tau_{\text{had}}$ channels. The label ‘‘Others’’ refers to contributions from diboson, $Z/\gamma^*(\rightarrow \ell\ell)$ +jets and $W(\rightarrow \ell\nu)$ +jets production. In the $\tau_{\text{lep}} \tau_{\text{had}}$ channel, events containing $\tau_{\text{had-vis}}$ candidates that originate from jets are removed from all processes other than Jet $\rightarrow \tau$ fake. The binning displayed is that entering into the statistical fit discussed in Section R.2, with minor modifications needed to combine the $\tau_{\text{lep}} \tau_{\text{had}}$ channels and with underflows and overflows included in the first and last bins, respectively. The predictions and uncertainties for the background processes are obtained from the fit under the hypothesis of no signal. The expectation from Z'_{SSM} with masses of 1500, 2000, and 2500 GeV are superimposed. The ratio of the data to the fitted model is shown in the lower panel.

Not reviewed, for internal circulation only

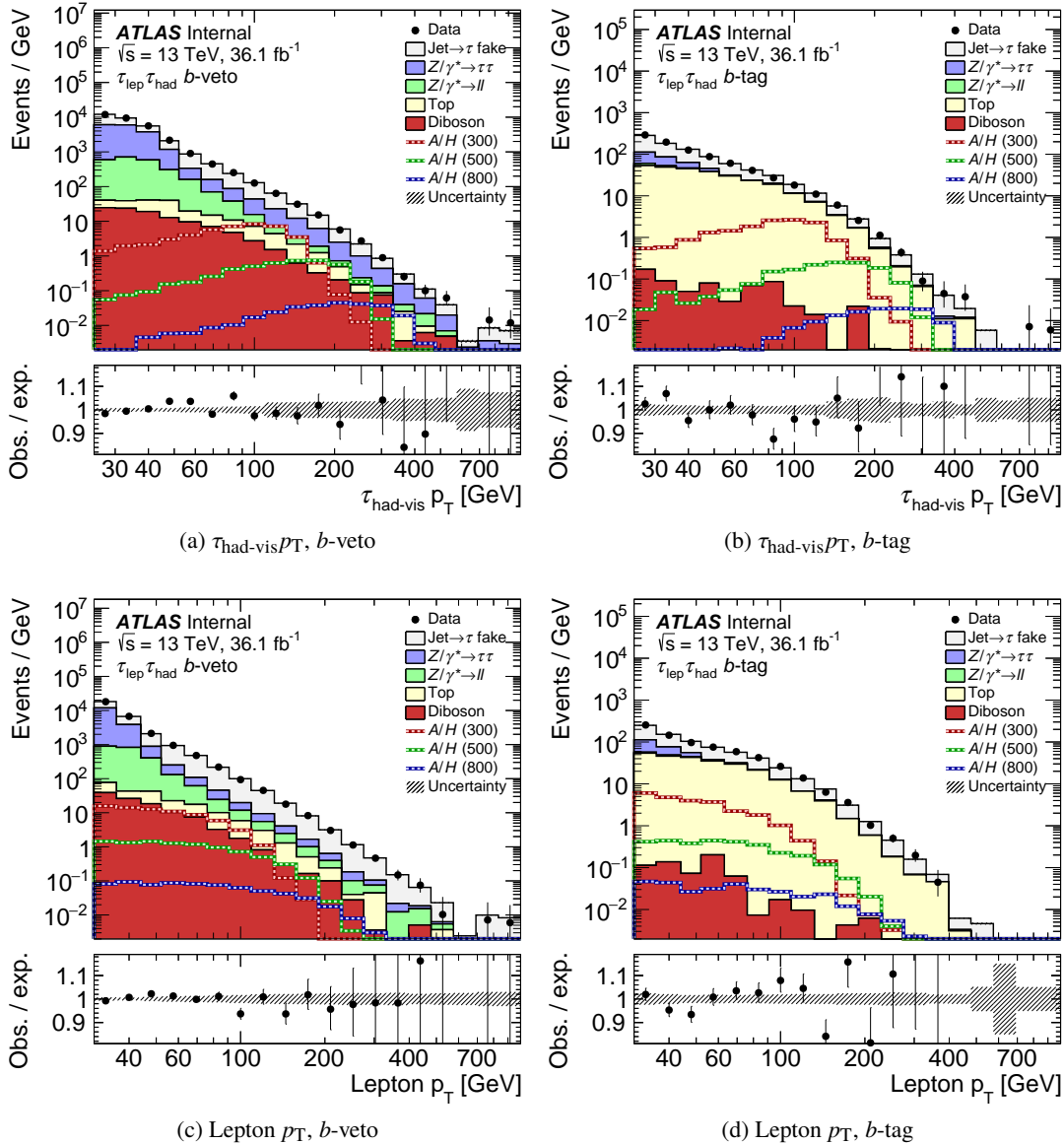


Figure 179: Distributions of (a+b) $\tau_{\text{had-vis}} p_T$ and (c+d) lepton p_T in the b -veto and b -tag categories of the $\tau_{\text{lep}} \tau_{\text{had}}$ channel. Events containing $\tau_{\text{had-vis}}$ candidates that originate from jets are removed from all processes other than Jet $\rightarrow \tau$ fake. The predictions and uncertainties for the background processes are obtained by applying the statistical fitting procedure (see Section R.2) to the m_T^{tot} distributions under the hypothesis of no signal. The combined prediction for A and H bosons with masses of 300, 500 and 800 GeV and $\tan \beta = 10$ in the hMSSM scenario are superimposed. The ratio of the data to the fitted model is shown in the lower panels.

Not reviewed, for internal circulation only

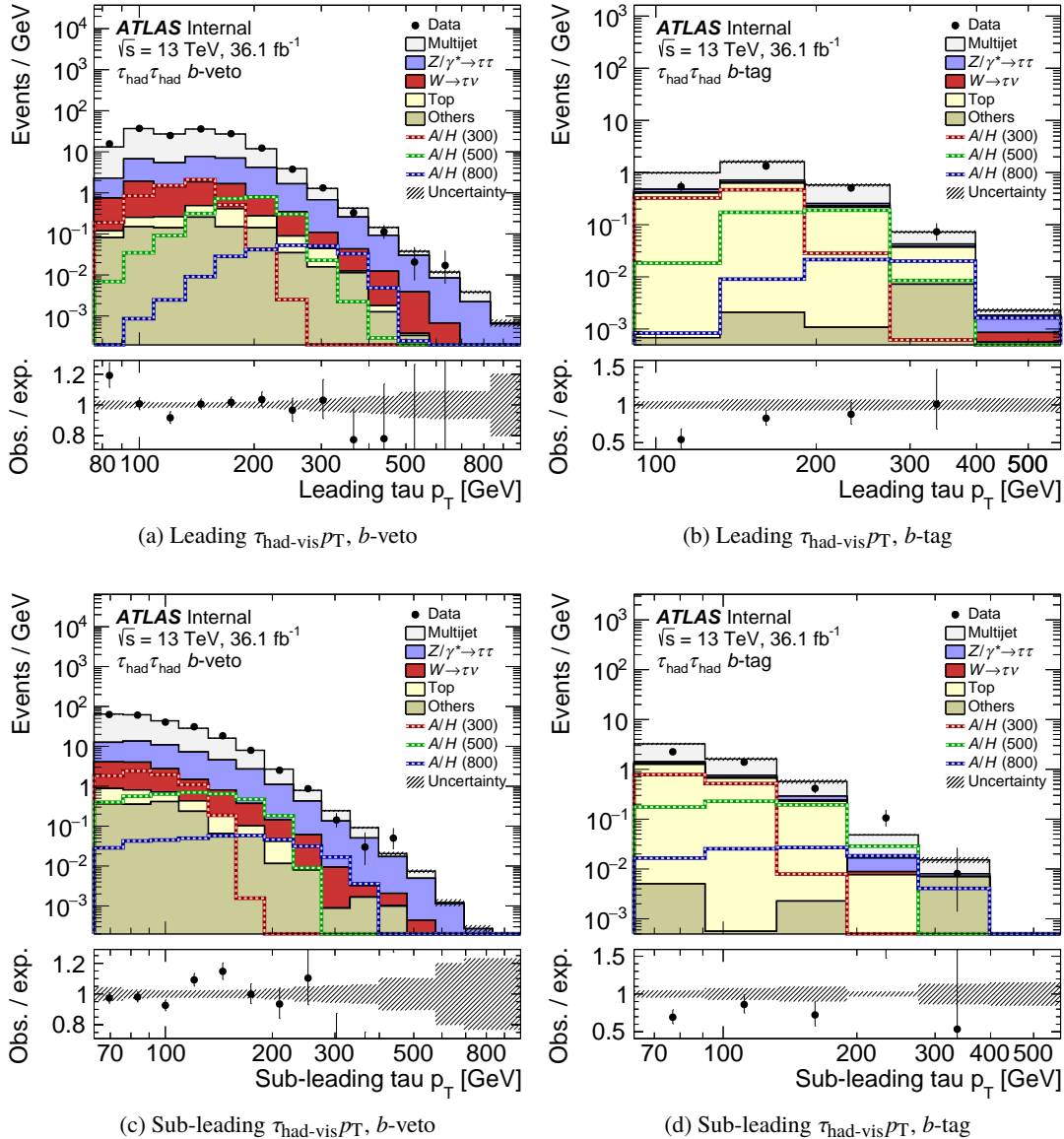


Figure 180: Distributions of (a+b) leading $\tau_{\text{had}} \tau_{\text{had}} p_T$ and (c+d) sub-leading $\tau_{\text{had}} \tau_{\text{had}} p_T$ in the b -veto and b -tag categories of the $\tau_{\text{had}} \tau_{\text{had}}$ channel. The label “Others” refers to contributions from diboson, $Z/\gamma^*(\rightarrow \ell\ell)$ +jets and $W(\rightarrow \ell\nu)$ +jets production. The predictions and uncertainties for the background processes are obtained by applying the statistical fitting procedure (see Section R.2) to the m_T^{tot} distributions under the hypothesis of no signal. The combined prediction for A and H bosons with masses of 300, 500 and 800 GeV and $\tan\beta = 10$ in the hMSSM scenario are superimposed. The ratio of the data to the fitted model is shown in the lower panels.

Not reviewed, for internal circulation only

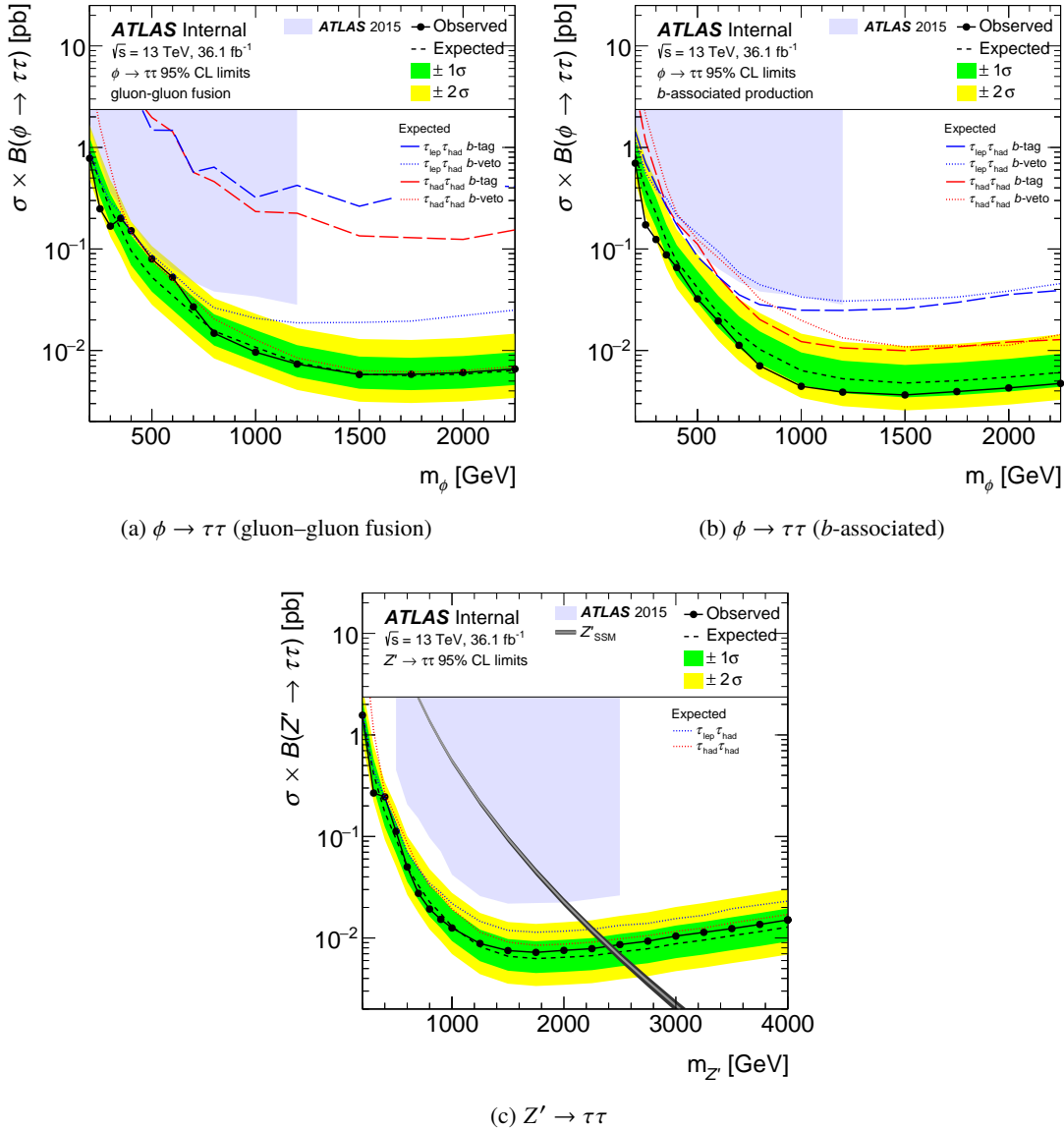


Figure 181: The observed and expected 95% CL upper limits on the production cross section times branching fraction for a scalar boson produced via (a) gluon–gluon fusion and (b) b -associated production and for (c) gauge bosons. The limits are calculated from a statistical combination of the $\tau_{\text{lep}}\tau_{\text{had}}$ and $\tau_{\text{had}}\tau_{\text{had}}$ channels. The predicted cross section for a Z'_{SSM} boson is overlaid in (c). For comparison, the expected limits for the individual channels and categories and the observed limit from the ATLAS 2015 search [HIGG-2015-08] are overlaid.

Not reviewed, for internal circulation only

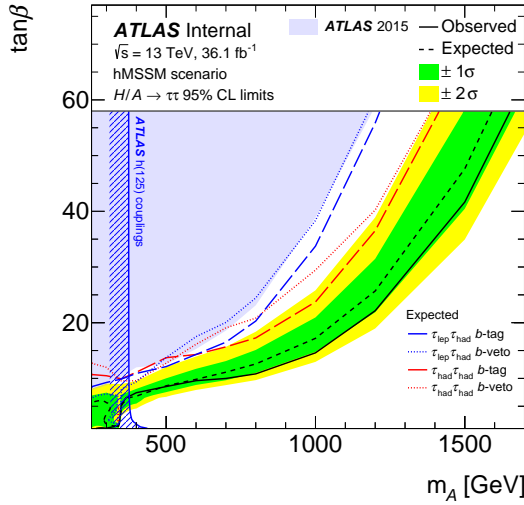


Figure 182: The observed and expected 95% CL limits on $\tan \beta$ as a function of m_A in the hMSSM scenario. The exclusion arising from the SM Higgs boson coupling measurements of Ref. [Aad:2015pla] is also shown. For comparison, the expected limits for the individual channels and categories and the observed limit from the ATLAS 2015 search [HIGG-2015-08] are overlaid.

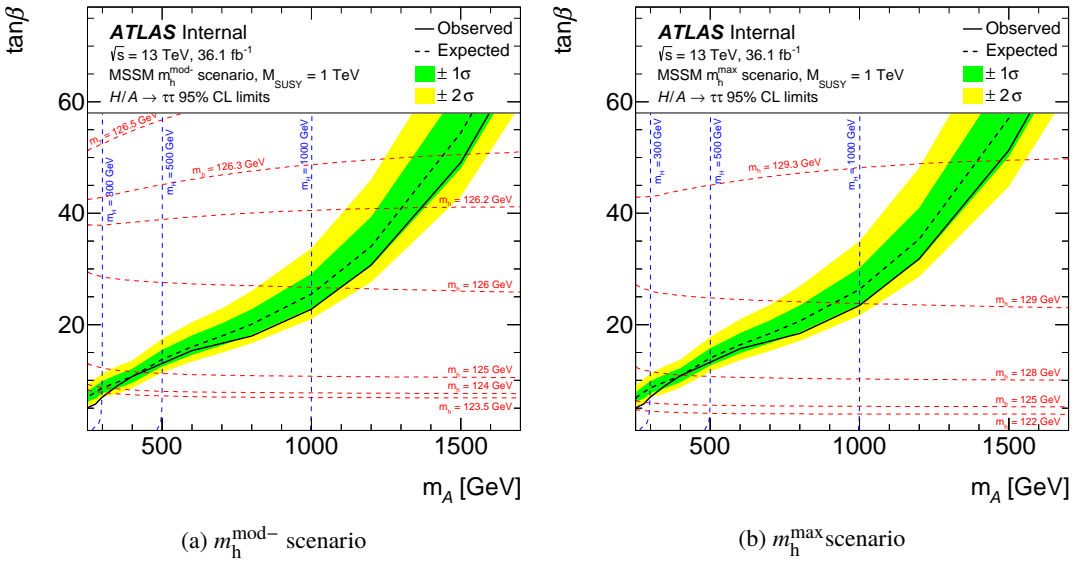


Figure 183: The observed and expected 95% CL limits on $\tan \beta$ as a function of m_A in the MSSM (a) $m_h^{\text{mod-}}$ and (b) m_h^{max} scenarios.

Not reviewed, for internal circulation only

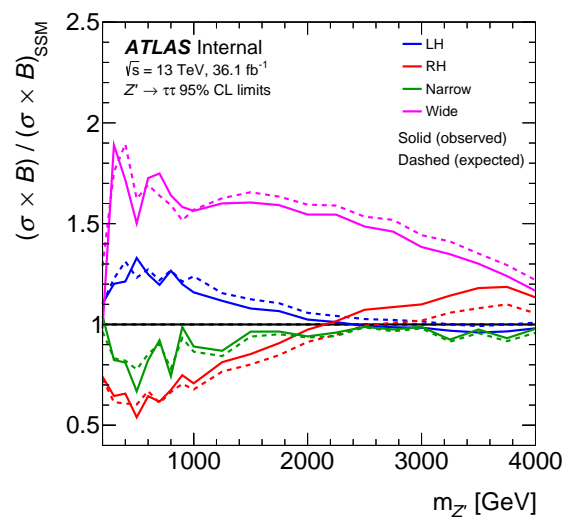


Figure 184: Ratio of the observed and expected 95% CL upper limits on the production cross section times branching fraction for Z' models with left-handed couplings (LH), right-handed couplings (RH), 0.5% natural width (Narrow) and 36% natural width (Wide) with respect to the SSM.

Not reviewed, for internal circulation only

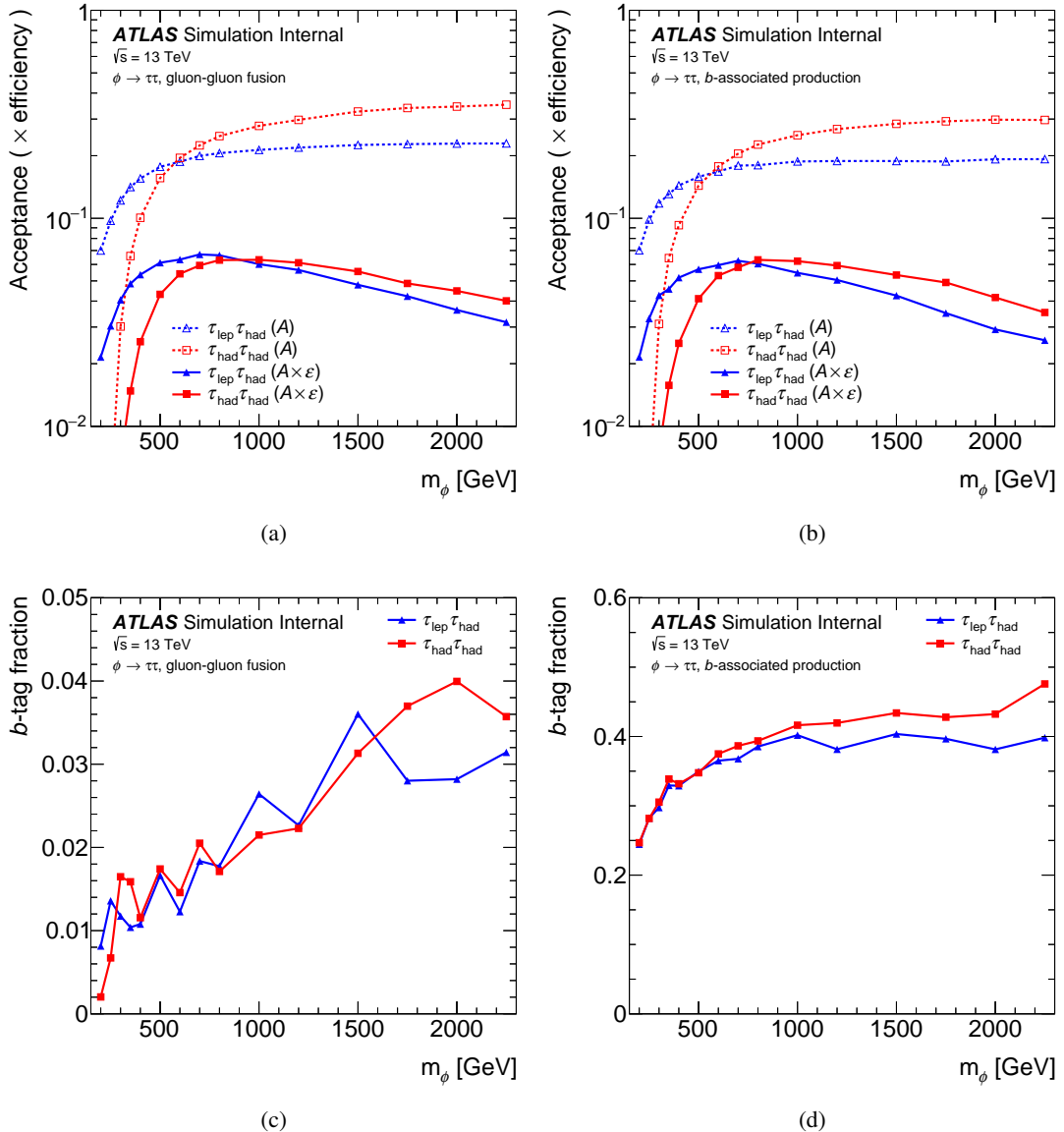


Figure 185: Acceptance (A) and acceptance times efficiency ($A \times \varepsilon$) for a scalar boson produced via (a) gluon–gluon fusion and (b) b -associated production and the fraction of events entering the b -tag category for (c) gluon–gluon fusion and (d) b -associated production.

Not reviewed, for internal circulation only

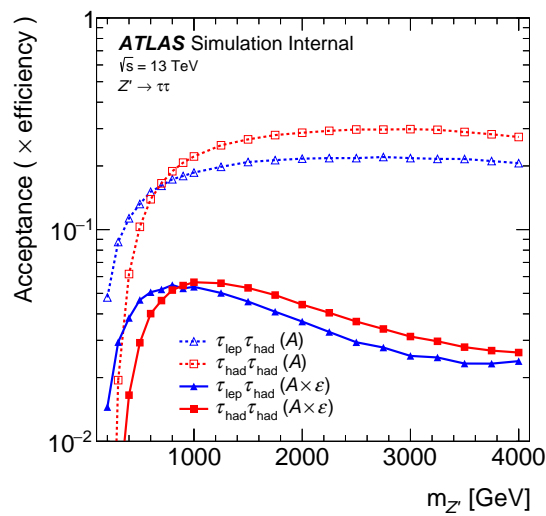


Figure 186: Acceptance (A) and acceptance times efficiency ($A \times \epsilon$) for a gauge boson.

Not reviewed, for internal circulation only

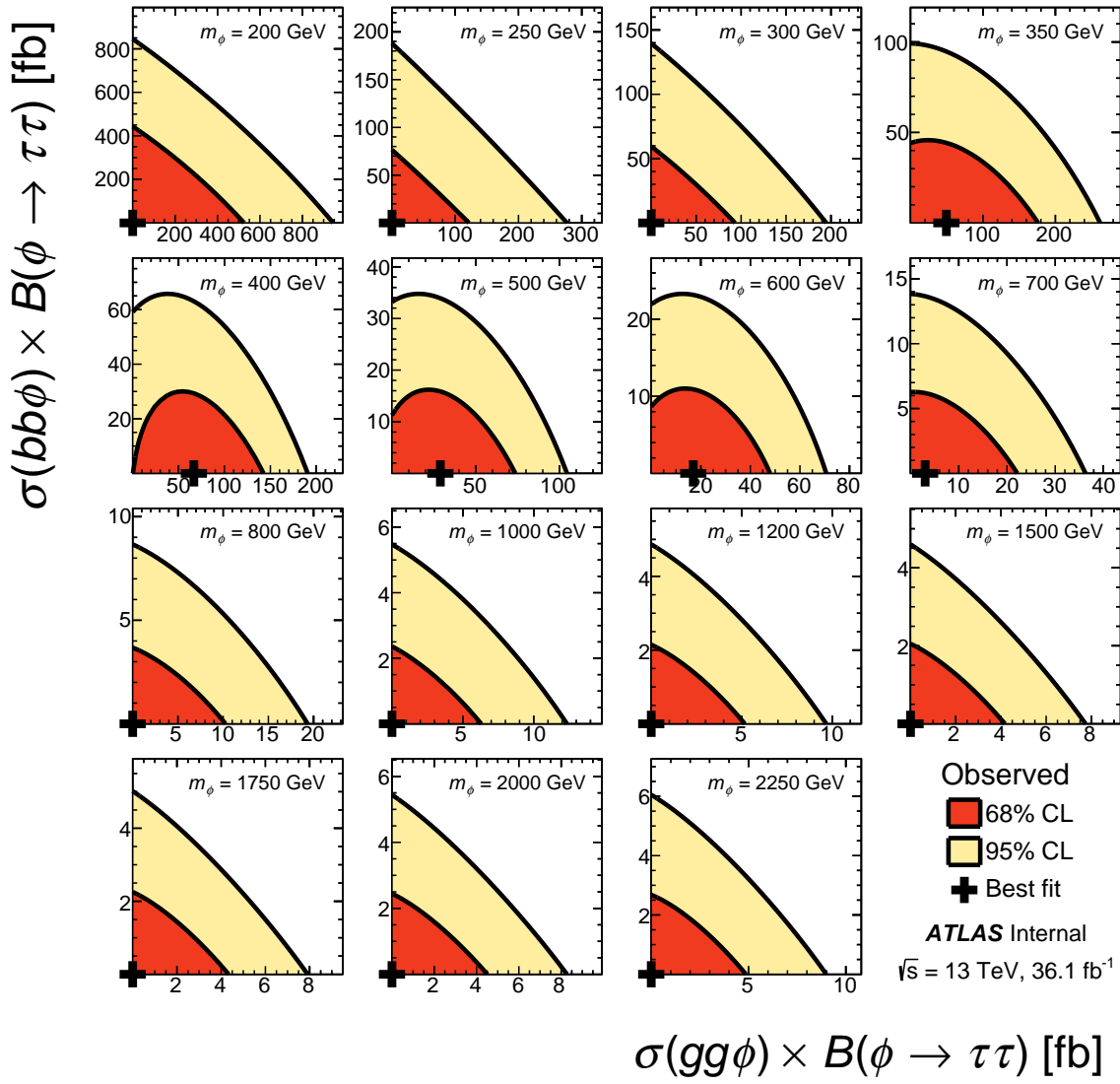


Figure 187: Observed two dimensional likelihood scans for each analysed Higgs boson mass in the $\phi \rightarrow \tau\tau$ search. The axes are the cross section times branching fraction for the gluon–gluon fusion and b -associated production processes. The best-fit point and preferred 68% and 95% CL regions are shown.

Not reviewed, for internal circulation only

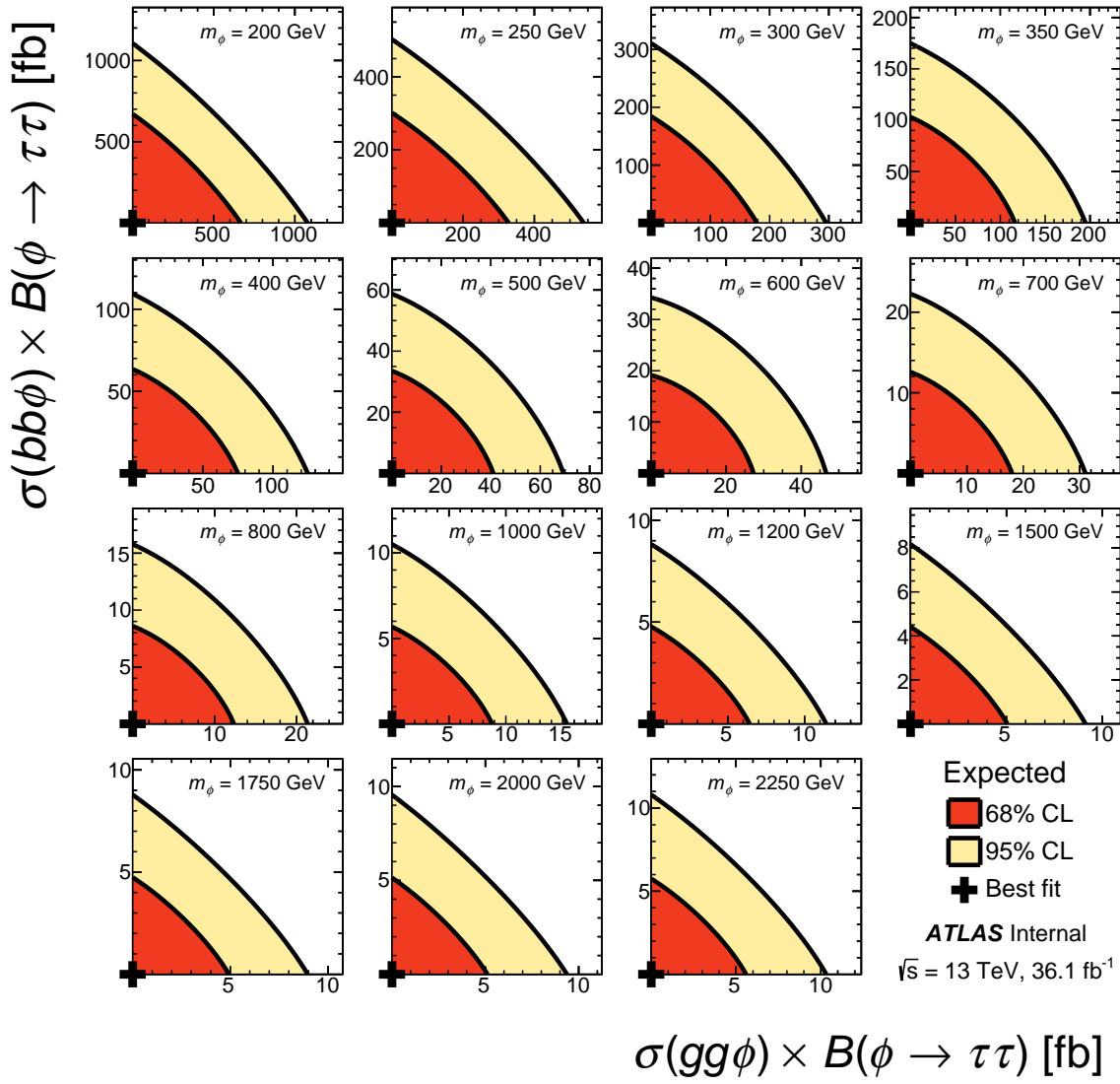


Figure 188: Expected two dimensional likelihood scans for each analysed Higgs boson mass in the $\phi \rightarrow \tau\tau$ search. The axes are the cross section times branching fraction for the gluon–gluon fusion and b -associated production processes. The best-fit point and preferred 68% and 95% CL regions are shown.

Not reviewed, for internal circulation only

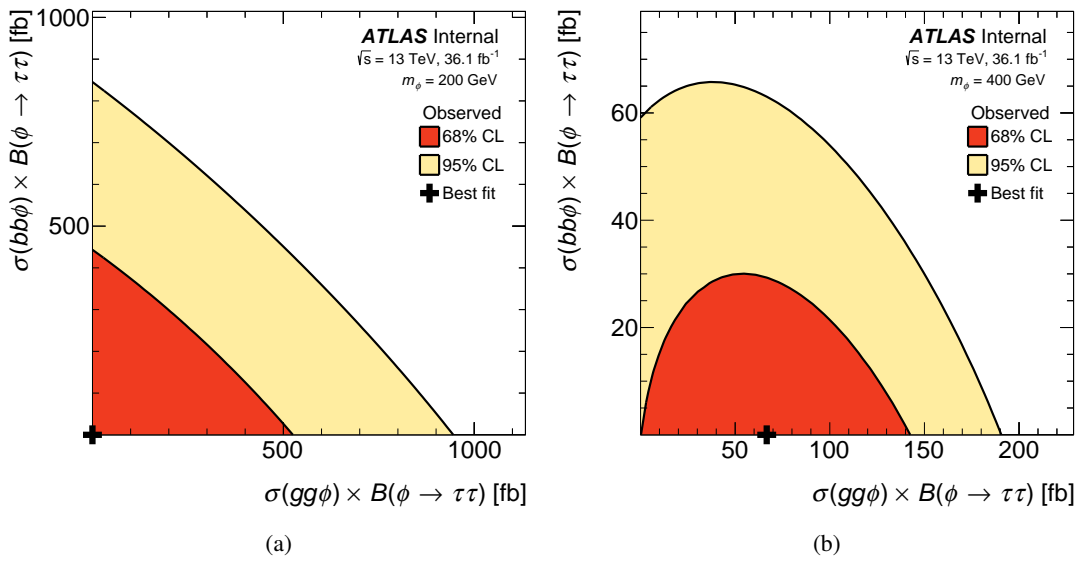


Figure 189: Observed two dimensional likelihood scan of the cross section times branching fraction of $\phi \rightarrow \tau\tau$ for the gluon–gluon fusion vs b -associated production processes, for Higgs boson masses of (a) 0.2 TeV and (b) 0.4 TeV. The best-fit point and preferred 68% and 95% CL regions are shown.